STATE-RESOLVED COLLISIONAL COUPLING OF EXCITED STATES OF THE CH RADICAL

Craig Murray

A thesis presented for the degree of Doctor of Philosophy

University of Edinburgh

2001

EX BIBL. UNIV. EDINBURGH

DECLARATION

I hereby declare that the work presented in this thesis is entirely my own, except where due acknowledgment has been made to the work of others, and has not been presented previously, in whole or in part, for any other degree or professional qualification.

ACKNOWLEDGEMENTS

First mention must go to Professor Ken McKendrick, to whom I am eternally grateful for his advice, expertise and, most importantly, his patience, which I know I tested. Also, thanks must go to Dr Colin J. Randall for a great deal of help while I was finding my feet in the lab, and to Dr Trevor Ridley for lending an assortment of bits and pieces, and, of course, for getting the beers in. I'd also like to acknowledge Professor Robert J. Donovan, for taking over as my supervisor, following Ken's mid-season transfer from UoE to H-WU.

I'd also like to thank everyone in the current McKendrick group at H-WU for an enjoyable few years. In alphabetical order, thanks to Florian Ausfelder, Dr Matthew L. Costen, Hilary J. Crichton, Dr David A. Henderson, Dr Stefan Himmelmann and Hailey Kelso. The sterling efforts of Stuart Mains and the team in the workshops at UoE, and of Iain Drummond, Alan Barton and Bill Stirling at H-WU also deserve a mention. Thanks for all the good work that has made this research possible.

A special mention must go to all my family for their continuous support, both financial and otherwise, during the more difficult times over the past four years. You've been fantastic. A dishonourable mention is required for the lads I've shared flats and (perhaps just a few) drinks with, and who have stood by me through thick and thin. You know who you are, I won't mention names (someone in authority may end up reading this...), so thanks for helping to make a PhD even more of a challenge.

Finally, no UoE thesis should be considered complete without a mention of Mags in the King's Buildings Union. Cheers for the banter, Mags, and roll on the next Edinburgh Derby.

I can't go on in any case. But I must go on. So I'll go on.

The Unnamable, by Samuel Beckett

ABSTRACT

The collisional coupling of the first two spin-conserved excited states of the CH radical, $A^2\Delta$ and $B^2\Sigma^-$, has been investigated using a combination of time- and wavelength-resolved laser-induced fluorescence spectroscopy. CH radicals, produced by UV multiphoton photolysis of $CHBr_3$, were state-selectively excited to specific rotational and fine-structure levels within the near-isoenergetic $A^2\Delta$, $v = 1$ and $B^2\Sigma^-$, $v = 0$ vibrational manifolds. CO_2, as a model collision partner, was found to efficiently couple the $A^2\Delta$ and $B^2\Sigma^-$ states at room temperature (~295 K). Vibrationally-resolved results showed the $A^2\Delta$, $v = 1 \leftrightarrow B^2\Sigma^-$, $v = 0$ coupling to be efficient and reversible, in addition to irreversible $A^2\Delta$, $v = 1 \rightarrow A^2\Delta$, $v' = 0$ vibrational relaxation and $B^2\Sigma^-$, $v = 0 \rightarrow A^2\Delta$, $v' = 0$ electronic energy transfer. For collisional transfer out of $B^2\Sigma^-$, $v = 0$, a branching ratio of ~2:1 in favour of the more nearly degenerate $A^2\Delta$, $v' = 1$ level was measured, which differs significantly from the predictions of energy-gap scaling laws. The $A^2\Delta$, $v' = 0$ level was found to be only very weakly quenched by CO_2, in accordance with previously reported rate constants.

Following excitation to a range of rotational levels in $A^2\Delta$, $v = 1$ and $B^2\Sigma^-$, $v = 0$, dispersed fluorescence spectra of the pumped and collisionally-populated levels have been recorded at rotational resolution with time-gating. Rates of rotational energy transfer within the initial state were found to be close to gas-kinetic. The $A^2\Delta$, $v = 1$ and $B^2\Sigma^-$, $v = 0$ levels did not show significantly different ΔN propensities, in contrast to previous reports. Electronic $A^2\Delta$, $v = 1 \rightarrow B^2\Sigma^-$, $v' = 0$ energy transfer shows a propensity for a relatively broad range of ΔN, with the product state distributions peaked in levels close in energy to the initial level. Analysis of the reverse process, $B^2\Sigma^-$, $v = 0 \rightarrow A^2\Delta$, $v' = 0$ and 1, is complicated by the spectral overlap of the A-X(0,0) and (1,1) bands. Nevertheless, a broad product state distribution, attributable unambiguously at high N' to $A^2\Delta$, $v' = 0$, was observed. The

distributions observed following electronic state-changing collisions are broader than those observed for pure rotational transfer within a state, suggesting that state-changing collisions sample more strongly interacting regions of the $CH\cdots CO_2$ intermolecular potential. The interaction, however, is not strong enough to cause complete rotational or vibrational redistribution of population.

TABLE OF CONTENTS

I GENERAL INTRODUCTION

I-1 PREAMBLE

Collisional processes affecting electronically excited states of small molecules and radicals are of enormous practical importance and of fundamental interest. By far the largest area of study has been electronic quenching rates of excited species, typically by measurements of the fluorescence decay lifetime in the presence of varying pressure of a collision partner. Electronic quenching affects the fluorescence quantum yield; hence, knowledge of collisional removal rates is essential in relating signal sizes to ground state populations in the application of optical techniques for the measurement of concentrations and temperatures in collisional environments [1,2]. Laser-based techniques, being non-intrusive and highly sensitive, are commonly applied to the detection of radical species for diagnostic purposes in high-energy environments such as flames and plasmas.

While measurements of electronic quenching rates have been common, studies of the fate of electronically quenched molecules are far rarer. Only in a few systems have the products of electronically inelastic collisions been determined, and in even fewer have the products been determined in a state-resolved manner. The current challenge to both experiment and theory is to study electronically inelastic collisions in which the population in the rovibrational and fine-structure levels is known in the initial and the product states as a means of gaining further understanding of the factors governing the collisional process.

I-2 ELECTRONICALLY INELASTIC COLLISIONS

The field of state-resolved electronically inelastic collisional processes has recently been comprehensively reviewed by Dagdigian [3]. A discussion of the factors determining the disposal of energy in the products of electronically inelastic collisions has been presented by McKendrick [4] in the form of a case study comparing observations made on the apparently similar SiCl and SiF systems (discussed in Section I-3.4). Discussion of electronic energy transfer processes in this chapter will be limited to state-resolved studies of open-shell molecules.

I-2.1 Theoretical models

I-2.1.1 Spectroscopic perturbations

That isolated-molecule spectroscopic perturbations might play a role in electronically inelastic collisions was proposed by Gelbart and Freed [5], and provided the first theoretical model. In this theory, perturbed levels, which share the electronic character of both the product and the initial states, are considered to act as 'gateway' levels through which population is transferred. For example, Broida and co-workers [6, 7] observed a pressure-dependent enhancement in the intensity of emission from perturbed levels in the $B^2\Sigma^+ - X^2\Sigma^+$ band which was at that time interpreted as being due to transfer from perturbed $A^2\Pi$ state levels of the CN radical. Based on these observations, Gelbart and Freed suggested that the transfer cross section be given by [8],

$$\sigma_{EJ,E'J'} \approx \sigma_{EJ,EJ'} c_{EE'} (J')^2 + \sigma_{E'J,E'J'} c_{EE'} (J)^2$$

Equation I.1

where $\sigma_{EJ,EJ'}$ and $\sigma_{E'J,E'J'}$ are cross-sections for collisional rotational relaxation within a single electronic state and $c_{EE'}(J')$ and $c_{EE'}(J)$ are the isolated-molecule $E \sim E'$ mixing coefficients. The transfer mechanism through the perturbed 'gateway' levels is essentially rotational relaxation, modulated by the electronic state mixing, rather than electronic quenching. Hence, the rate is almost gas kinetic. The importance of spectroscopic perturbations in collision-induced electronic energy transfer will be discussed in relation to specific systems below.

I-2.1.2 Franck-Condon factor and energy-gap dependence

Studies on the isoelectronic species CO^+ and CN led Bondybey and Miller [9] and Katayama *et al.* [10] to propose a simple model. Observing a strongly double exponential time-dependence for the emission from certain vibrational levels in the $A^2\Pi$ states, they suggested a mechanism involving rapid equilibration between the pumped vibrational levels of the $A^2\Pi$ state and nearly isoenergetic high vibrational levels of the $X^2\Sigma^+$ state. The model states that the thermal collisional transfer rates should depend on the Franck-Condon overlap between the vibrational levels involved, $q_{v,v'}$ and the vibronic energy gap, $\Delta E_{Ev,E'v'}$, such that,

$$k_{Ev,E'v'} \approx k^{el}_{E,E'} q_{v,v'} \exp\left(-\frac{\Delta E_{Ev,E'v'}}{kT}\right)$$

Equation I.2

where $k^{el}_{E,E'}$ is a pure electronic transfer rate. The applicability of the Franck-Condon factor/energy-gap model has been found to be very limited. This will be discussed further in relation to other systems below.

I-2.1.3 Electrostatic mixing

Facile collision-induced electronic transitions have been observed in systems for which isolated-molecule perturbations are either rigorously forbidden, for example in N_2^+, or are small, for example in certain vibrational manifolds of CN. These systems are discussed in detail in Section I-3 below. In these systems, the 'gateway' model clearly cannot apply. Alexander and Corey [11] have developed a fully quantum description of the dynamics of electronically inelastic transitions between $^2\Pi$ and $^2\Sigma^+$ states induced by a spherical perturber in the absence of spectroscopic perturbations in the isolated molecule. In this model, the approach of the collision partner causes electrostatic mixing of the collisionally coupled electronic states.

A spherical perturber approaching a Π state lifts the electronic degeneracy and the interaction can be described diabatically by symmetric (A') and antisymmetric (A'') potential energy surfaces (PESs) in C_S geometry. Similarly, the interaction of a Σ state with a spherical perturber results in a PES of A' symmetry. The electrostatic coupling will occur in this diabatic basis between the PESs of A' symmetry.

The interaction of the atom and the diatom can be expressed in terms of three PESs, V_Σ, V_Π, V_2 and a coupling potential, V_1,

$$\langle \Sigma | V_{el} | \Sigma \rangle = V_\Sigma(r,R,\theta)$$

Equation I.3

$$\langle \Sigma | V_{el} | \Pi(A') \rangle = V_1(r,R,\theta)$$

Equation I.4

$$\langle \Pi(A') | V_{el} | \Pi(A') \rangle = V_\Pi(r,R,\theta) - V_2(r,R,\theta)$$

Equation I.5

$$\langle \Pi(A'') | V_{el} | \Pi(A'') \rangle = V_{\Pi}(r,R,\theta) + V_2(r,R,\theta)$$

Equation I.6

which are functions of the co-ordinates, r, the diatom internuclear separation; $\boldsymbol{R}$, the vector connecting the atom and the diatom centre-of-mass; and θ, the angle between the diatom axis and $\boldsymbol{R}$. The splitting of the two $^2\Pi$ components by the approach of the collision partner is described by the repulsive V_2 potential. The V_1 potential describes the nonadiabatic coupling between the $^2\Pi$ and the $^2\Sigma^+$ states.

PESs controlling CN($A^2\Pi \rightarrow X^2\Sigma^+$) interactions with He [12,13] and, more recently Ar [14], and $N_2^+(^2\Pi_u \rightarrow {}^2\Sigma_g^+)$ with He [15] have been calculated and comparisons between the quantum scattering calculations and the experimental observations will be drawn later in the discussion of those systems (see Section I-3).

I-3 SYSTEMS

Electronic transitions between the $A^2\Pi_{(u)}$ and $X^2\Sigma_{(g)}^+$ states of N_2^+, CO^+ and CN induced by collisions with rare gas atoms have been most extensively studied and, despite the isoelectronic nature of these species, found to show varying behaviour as will be described in this section. Collision induced transitions between the C/$B'^2\Delta$ and $B^2\Sigma^+$ states in SiF/Cl will also be discussed. There are marked contrasts in the behaviour of the silicon halides in the presence of a range of collision partners. The observed propensities differ again from those of the CN, N_2^+, CO^+-rare gas systems. Discussion of electronically inelastic collisions in other systems (alkali dimers, N_2, CO, OH, NH and I_2) can be found in Dagdigian's review article [3]. These systems are selected to highlight the extremes of behaviour observed to accompany electronically inelastic collisions.

I-3.1 N_2^+ ($A^2\Pi_u \rightarrow X^2\Sigma_g^+$) transitions

As discussed previously, the first model proposed to describe electronically inelastic transitions was the presence of 'gateway' levels, caused by isolated-molecule spectroscopic perturbations. In the N_2^+ ion, however, such perturbations are rigorously forbidden because of the $g \leftrightarrow u$ selection rule for a homonuclear molecule [8]. Collision-induced transitions between the $A^2\Pi_u$ and the $X^2\Sigma_g^+$, however, are facile. Thus, while spectroscopic perturbations may play some role in collision-induced electronic state changes, they are not prerequisite.

Population transfer from the $A^2\Pi_u$ state to the $X^2\Sigma_g^+$ state in N_2^+ ions induced by He has been extensively studied by Katayama and co-workers [16, 17, 18, 19, 20, 21, 22], using an optical-optical double-resonance (OODR) technique. Following laser excitation to specific rovibrational and fine-structure levels in the $A^2\Pi_u$ state, the collisionally populated $X^2\Sigma_g^+$ state was probed using laser-induced fluorescence on the $B^2\Sigma_u^+ - X^2\Sigma_g^+$ band. The $g \leftrightarrow u$ selection rule for spectroscopic transitions [23] prevents the use of laser-induced fluorescence to monitor the rotational relaxation in the initially populated $A^2\Pi_u$ state.

The vibrational structure of the $A^2\Pi_u$ and $X^2\Sigma_g^+$ states is such that $A^2\Pi_u$ levels, v_A, are nearly isoenergetic with $X^2\Sigma_g^+$ levels with $v_X = v_A + 4$. Rotational and fine-structure levels in the $v_A = 3$ and 4 vibrational manifolds have been populated and found to collisionally populate the nearly isoenergetic $X^2\Sigma_g^+$ levels and the next lowest vibrational levels with $v_X = v_A + 3$, with a marked propensity for $\Delta J = 0$ transitions on both pathways. Large energy gap transitions (~1800 cm^{-1}) to levels with $v_X = v_A + 3$ were found to have rates only two to five times smaller than transitions to the nearly isoenergetic levels with $v_X = v_A + 4$, although predictions based on an exponential energy-gap scaling law would predict differences in the rates of nearly six orders of magnitude [18,21,22]. Clearly, the energy-gap

law completely fails to provide any predictive power for the vibrational branching in this system.

The rotational levels of the N_2^+ ion have well-defined *s/a* nuclear permutation symmetry [23]. Following initial excitation to an $A^2\Pi_u$ state level with specified symmetry, the OODR spectra probing the population distributions over the product $X^2\Sigma_g^+$ levels show clearly that the symmetry is conserved during the state-changing collision [17].

Generally, the fine-structure components of the $B^2\Sigma_u^+ - X^2\Sigma_g^+$ band system are not resolvable. However strong perturbations caused by the $A^2\Pi_u$ state exist in the $v_B = 5$ level allowing non-statistical populations in the different spin-rotation states of the collisionally-produced level to be observed [22].

Berning and Werner [15] have calculated $N_2^+(A^2\Pi_u, X^2\Sigma_g^+)$-He PESs and have carried out quantum scattering calculations of electronically inelastic collisions. For the near isoenergetic transitions in which $v_X = v_A + 4$, the calculated cross-sections were in good agreement with the experimental data and reflected the observed conservation of the permutation-inversion symmetry and the propensity for small changes in ΔJ. Cross-sections for transitions with large energy gaps, $v_X = v_A + 3$, disagreed significantly with experimental measurements, being around three orders of magnitude smaller. Attempts to resolve this discrepancy by including the vibrational motion of the N_2^+ ion in the scattering calculations were unsuccessful. This remains therefore one of the main areas of discrepancy between theoretical treatments and experiment.

I-3.2 CO^+ ($A^2\Pi \rightarrow X^2\Sigma^+$) transitions

CO^+, formed by Penning ionisation by metastable He atoms, has been selectively excited to specific vibrational levels in the $A^2\Pi$ state and the relaxation process studied. Time-resolved decays were found to show double exponential behaviour. The relaxation

was deduced to occur *via* collision-induced transitions to high vibrational levels of the $X^2\Sigma^+$ state in a cascade mechanism [9, 24], relaxation rates being higher for higher vibrational levels. Cross-sections for vibrational relaxation were found to decrease with temperature [25], implying an attractive interaction.

The $v_A = 0$ and $v_X = 10$ are nearly isoenergetic and are mixed by spectroscopic perturbations [26]. Levels of *e* symmetry in the $A^2\Pi_{1/2}$ (F_2) manifold are perturbed, mostly affecting levels with $J = 2.5 - 7.5$, for which the amount of Σ character is 20 – 30%. An OODR study of electronic energy transfer between $A^2\Pi$, $v = 0$ and $X^2\Sigma^+$, $v' = 10$ induced by collisions with He by Dentamaro and Katayama [27] found that significant transfer only occurred through the perturbed levels. This obviously contrasts with N_2^+, discussed above, in which spectroscopic perturbations are forbidden and rapid collision-induced electronic energy transfer is found to occur. It was suggested that although the energy gap is practically zero, the very small Franck-Condon factor connecting the $v_A = 0$ and $v_X = 10$ levels may play a role in enhancing the participation of gateway levels.

I-3.3 CN ($A^2\Pi \rightarrow X^2\Sigma^+$) transitions

Electronic energy transfer between the $A^2\Pi$ and $X^2\Sigma^+$ states induced by collisions with Ar atoms was first observed by Katayama *et al.* [10] (see Section I-2.1.2) and has been comprehensively studied by Dagdigian and co-workers using OODR [28, 29, 30, 31]. $CN(A^2\Pi)$ radicals were produced by collisional dissociation of C_2N_2 induced by metastable Ar atoms in a microwave discharge followed by selective laser excitation to specific rotational and fine-structure levels in the $v_A = 3$, 7 and 8 manifolds. Population distributions in the pumped and collisionally produced $v_X = v_A + 4$ levels were determined from spectra recorded on the $B^2\Sigma^+$–$A^2\Pi$ and $B^2\Sigma^+ - X^2\Sigma^+$ bands respectively. In contrast to the N_2^+-He system, no collisional transfer to lower $X^2\Sigma^+$ vibrational levels was detected.

The potential curves for the $X^2\Sigma^+$, $A^2\Pi$ and $B^2\Sigma^+$ states of CN are qualitatively similar to those of N_2^+, although spectroscopic perturbations in the rotational and fine-structure levels are no longer forbidden [32], most notably between the $v_A = 7$ and $v_X = 11$ levels. Product state rotational distributions show a distinct even/odd alternation when the $v_A = 3$ or 7 levels are initially populated [28, 29, 30], the phase of the oscillation depending on the *e* or *f* parity of the initial level. The enhanced final rotational states are those that would be populated were CN homonuclear (as is the case for the isoelectronic N_2^+-He system). This phenomenon is not observed, however, when levels in the $v_A = 8$ manifold are initially populated [31]. It was suggested that this was related to a vibrational state dependence of the V_1 coupling potential.

For all starting levels, relatively small ΔJ are observed for CN-Ar collisions, as in the N_2^+-He system. Despite the variation in the rotationless energy gaps, ranging from ~640 cm^{-1} for $v_A = 3$ to –80 cm^{-1} for $v_A = 8$, there appears to be no propensity for energy resonant transitions. Quantum scattering calculations [13] based on previously calculated CN-He PESs [12] were compared with the experimental CN-Ar observations. The scattering calculations neglected any non-Born-Oppenheimer mixing between the $A^2\Pi$ and $X^2\Sigma^+$ states and the calculated potentials were averaged over the CN vibrational motion.

The even/odd alternation observed experimentally in the product state distribution for transfer from $v_A = 3$ and 7 to $v_X = 7$ and 11 was reproduced in the calculated cross-sections. This is due to the near homonuclear symmetry of the V_1 coupling potential, shown in Figure I.1. Generally, small values of ΔJ were found to have the largest cross-sections, although the peak in the calculated product state distribution was at slightly higher *J* and showed a narrower range than the experiment. The most significant discrepancy was the magnitude of the cross sections for the large energy gap $v_A = 3 \rightarrow v_X = 7$ transitions. Experimentally, these are found to be similar in magnitude to those for transitions from $v_A =$ 7 and 8 but are predicted to be several orders of magnitude smaller in the scattering

calculations. Additional *ab initio* calculations for the CN-Ar system [13] found the change in the coupling potential to be too small to explain the discrepancy in the magnitudes of the cross-sections. This is similar to the problem found for N_2^+ for large energy gap transitions [15] and remains an outstanding problem of the theory.

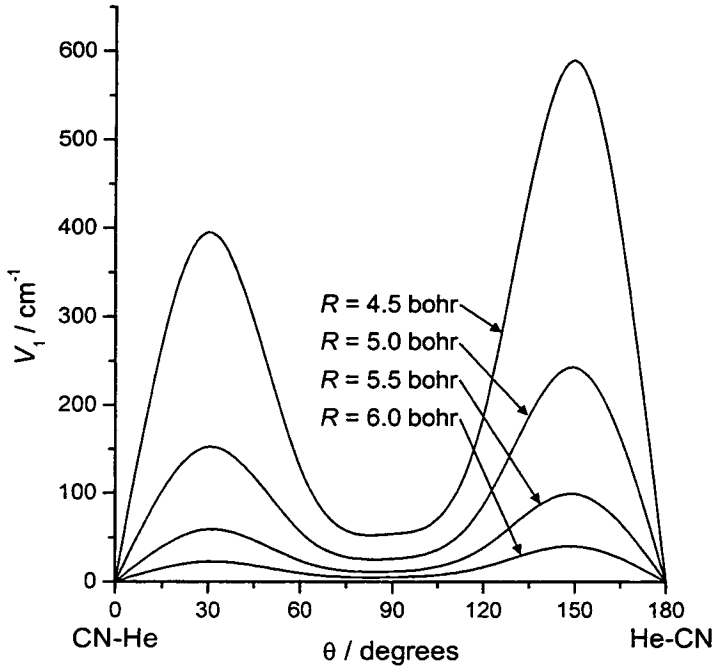

Figure I.1

Angular dependence of the V_1 coupling PES at various CN-He separations (R) for CN($A^2\Pi \rightarrow X^2\Sigma^+$) transitions. The near-symmetric quasi-homonuclear nature about $\theta =$ 90° results in the even/odd product state distribution (see text). Adapted from reference 12.

A joint experimental and theoretical study by Dagdigian *et al.* [33] measured cross-sections for transitions from individual fine-structure levels of the CN, $v_A = 7$ manifold into the $v_X = 11$ level induced by collisions with He. Scattering calculations in this work

included spectroscopic perturbations between the $A^2\Pi$ and $X^2\Sigma^+$ states but retained the rigid-rotor approximation from previous work [13]. Cross-sections for transitions from perturbed levels were calculated to be significantly enhanced although the most perturbed level, J = 13.5 F_1f, in v_A = 7 could not be pumped because of spectral congestion. Transitions from levels that lie far from the maximum perturbation show only slightly modified cross-sections. The calculated product state distribution peaked in the same J as was measured experimentally (*cf.* CN-Ar above). Electronically inelastic collisions were found to be a factor of two smaller relative to rotationally inelastic collisions in comparison with the CN-Ar experiments. Further work is required to determine the amount of influence isolated-molecule perturbations have on electronic state changes.

I-3.4 SiCl ($B'^2\Delta \rightarrow B^2\Sigma^+$) and SiF ($C^2\Delta \rightarrow B^2\Sigma^+$) valence-Rydberg transitions

The v' = 0 and 1 levels of the $B'^2\Delta$ valence state of SiCl were found to be very efficiently quenched by He, Ne and Ar in work by Jeffries [34], the $B^2\Sigma^+$ Rydberg state accounting for a significant fraction of the quenched molecules. The potential curves for the $B'^2\Delta$ and $B^2\Sigma^+$ states are shown in Figure I.2. State-resolved studies of this system are facilitated by the very short radiative lifetime of the $B^2\Sigma^+$ state (~10 ns). Thus, it is possible to select experimental conditions under which the collisionally-populated $B^2\Sigma^+$ state effectively undergoes no collisions prior to radiating, revealing the nascent population distribution. Work by Singleton and McKendrick [35] extended the range of quenching species to include diatomic and polyatomic molecules. The vibrational distribution over the product $B^2\Sigma^+$ (v' = 0, 1, 2) levels was found to be very strongly dependent on the identity of the collision partner, with the nearly isoenergetic channel not always being preferred. No obvious correlation with any single molecular property was found. For the larger quenchers

studied, the $B^2\Sigma^+$ state was found to account for almost all of the population collisionally removed from the $B'^2\Delta$ state.

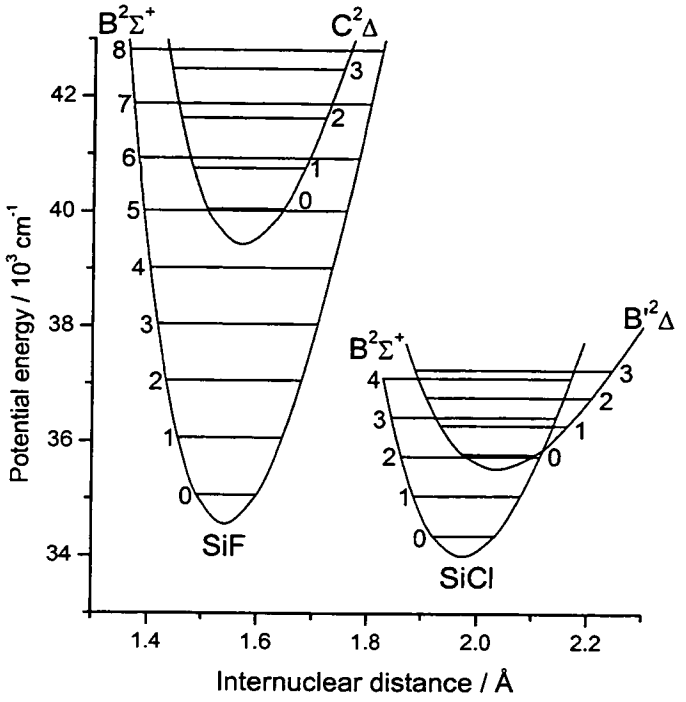

Figure I.2

RKR potential curves for the collisionally-coupled excited states of the silicon halides.

Studies on the silicon halides have been extended to include the corresponding collision-induced $C^2\Delta \rightarrow B^2\Sigma^+$ transition in the SiF molecule by McKendrick and co-workers [36, 37, 38, 39]. The relevant internuclear potential curves are shown in Figure I.2. As for SiCl, the valence $C^2\Delta$ state of SiF has a significantly longer lifetime than the Rydberg $B^2\Sigma^+$ state. In marked contrast to SiCl, the vibrational branching fractions are found to be independent of the identity of the perturber, and the $C^2\Delta$ state is only very inefficiently quenched by noble gases. Only the $v' = 0$, 1 and 2 vibrational levels of the $B^2\Sigma^+$ state are

found to be collisionally populated, despite the much larger energy gap, and the distribution correlated well with the calculated $C^2\Delta - B^2\Sigma^+$ Franck-Condon overlap [36].

In contrast to other systems such as $N_2^+(A^2\Pi_u \rightarrow X^2\Sigma_g^+)$, $CN(A^2\Pi \rightarrow X^2\Sigma^+)$ and $CO^+(A^2\Pi \rightarrow X^2\Sigma^+)$ for which there is a propensity for $\Delta J = 0$ transitions regardless of the magnitude of the energy gap, a large release of rotational energy is observed in $SiF(C^2\Delta \rightarrow B^2\Sigma^+)$ transitions following collisions with H_2 and N_2 [37, 38]. This was well described by a limiting impulsive model, consistent with 'sudden' collisions implicit in the Franck-Condon factor correlation, and accounted for by the valence-Rydberg nature of the transition. Put simply, the collision partner is assumed to approach closely enough to cause the electronic state-change from the valence $C^2\Delta$ state to the Rydberg $B^2\Sigma^+$ state. The much greater volume occupied by the Rydberg state means that the system finds itself on a highly repulsive part of the intermolecular PES, resulting in a large release of rotational and translational energy.

Polarised dispersed fluorescence measurements [40] have been carried out to investigate the degree of retention of alignment following a $C^2\Delta \rightarrow B^2\Sigma^+$ state changing collision in SiF, with H_2 as the collision partner. In directly prepared $B^2\Sigma^+$ levels, the retention of polarisation was found to be in agreement with theoretical predictions, attributable to the very short radiative lifetime of the $B^2\Sigma^+$ state. In the longer-lived $C^2\Delta$ state, the originally aligned sample was found to be marginally depolarised as a result of rotationally inelastic collisions. Following a state changing collision, the $B^2\Sigma^+$ product was found to be significantly less polarised than the $C^2\Delta$ state parent level, indicating a realignment of the plane of rotation. This is in accord with the mechanism of a large impulsive energy release concluded above, which predicts a substantial loss of alignment.

I-4 CONCLUSIONS

It remains clear yet that there is no universal model for electronically inelastic collisions. Systems can show behaviour ranging from small ΔE and a modest range of ΔJ to large ΔE accompanied by large rotational energy release, as in the $CN/N_2^+/CO^+$ and SiX cases discussed. Simple models based on Franck-Condon factors and energy gaps have been found to have limited qualitative applicability, and provide no quantitative predictive ability, even in analogous systems such as the silicon halides. The Franck-Condon dependence also has no rigorous theoretical basis [11].

Spectroscopic perturbations, caused by non-Born-Oppenheimer mixing of the electronic states have been shown to provide 'gateway' levels through which population can funnel efficiently as in the $CO^+(A^2\Pi \rightarrow X^2\Sigma^+)$-He. They may also make a more modest contribution for $CN(A^2\Pi \rightarrow X^2\Sigma^+)$-Ar, for example, where a slight enhancement over unperturbed levels is observed [33]. Such perturbations are certainly not a pre-requisite for electronic transitions, demonstrated by the $N_2^+(^2\Pi_u \rightarrow X^2\Sigma_g^+)$-He system which shows facile electronic energy transfer despite perturbations being rigorously forbidden.

The most advanced theoretical work has been carried out in tandem with experimental studies for $CN(A^2\Pi \rightarrow X^2\Sigma^+)$ transitions. Quantum scattering calculations based on the electrostatic mixing model are able to qualitatively reproduce experimental observations but are still unable at present to reproduce state-to-state cross-sections for transitions with larger energy gaps, for example the $v_A = 3 \rightarrow v_X = 7$ transition in CN. Predicting accurate cross-section for transitions with large energy gaps remains an unsolved problem of the theory.

I-5 SCOPE OF THIS WORK

The work described in this thesis extends the current body of data on electronically inelastic collisions by exploring transitions between the $A^2\Delta$ and $B^2\Sigma^-$ states of the technologically and fundamentally important CH radical. In Chapter IV, energy transfer between the near-isoenergetic $A^2\Delta$, $v = 1$ and $B^2\Sigma^-$, $v = 0$ levels will be shown to be facile and reversible in collisions with CO_2. $B^2\Sigma^-$, $v = 0 \rightarrow A^2\Delta$, $v' = 0$ transfer over a large energy gap will also be demonstrated to be efficient. These results will be shown to have important implications for previous measurements of electronic quenching [41]. Chapter V will present a rotational state-resolved study of $B^2\Sigma^-$, $v = 0 \rightarrow A^2\Delta$ and $A^2\Delta$, $v = 1 \rightarrow B^2\Sigma^-$, $v' = 0$ [42] electronic state changes under single-collision conditions.

I-6 REFERENCES

1 K. Kohse-Höinghaus, *Prog. Energy Combust. Sci.*, **20**, (1994), 203

2 D. R. Crosley, in "*Current Problems and Progress in Atmospheric Chemistry*", edited by J. R. Barker, World Scientific, Singapore, 1996

3 P. J. Dagdigian, *Annu. Rev. Phys. Chem.*, **48**, (1997), 95 and references therein

4 K. G. McKendrick, *J. Chem. Soc., Faraday Trans.*, **94**, (1998), 1921

5 W. M. Gelbart and K. F. Freed, *Chem. Phys. Lett.*, **18**, (1973), 470

6 H. E. Radford and H. P. Broida, *J. Chem. Phys.*, **38**, (1962), 644

7 D. W. Pratt and H. P. Broida, *J. Chem. Phys.*, **50**, (1968), 2181

8 H. Lefêbvre-Brion and R.W. Field, *"Perturbations in the Spectra of Diatomic Molecules"*, Academic Press, Orlando, 1986

9 V. E. Bondybey and T. A. Miller, *J. Chem. Phys.*, **69**, (1978), 3597

10 D. H. Katayama, T. A. Miller and V. E. Bondybey, *J. Chem. Phys.*, **71**, (1979), 1662

11 M. H. Alexander and G. C. Corey, *J. Chem. Phys.*, **84**, (1986), 100

12 H.-J. Werner, B. Follmeg and M. H. Alexander, *J. Chem. Phys.*, **89**, (1988), 3139

13 H.-J. Werner, B. Follmeg, M. H. Alexander and D. Lemoine, *J. Chem. Phys.*, **91**, (1989), 5425

14 M. H. Alexander, X. Yang, P J. Dagdigian, A. Berning and H.-J. Werner, *J. Chem. Phys.*, **112**, (2000), 781

15 A. Berning and H.-J. Werner, *J. Chem. Phys.*, **100**, (1994), 1953

16 D. H. Katayama, T. A. Miller and V. E. Bondybey, *J. Chem. Phys.*, **72**, (1980), 5469

17 D. H. Katayama, *J. Chem. Phys.*, **81**, (1984), 3495

18 D. H. Katayama, *Phys. Rev. Lett.*, **54**, (1985), 657

19 D. H. Katayama and A. V. Dentamaro, *J. Chem. Phys.*, **85**, (1986), 2595

20 D. H. Katayama, A. V. Dentamaro and J. A. Welsh, *J. Chem. Phys.*, **87**, (1987), 6983

21 D. H. Katayama and A. V. Dentamaro, *J. Chem. Phys.*, **91**, (1989), 4571

22 A. V. Dentamaro and D. H. Katayama, *Phys. Rev. A*, **43**, (1991), 1306

23 G. Herzberg, *"Molecular Spectra and Molecular Structure: Volume I – Spectra of Diatomic Molecules"*, 2nd Edition, Van Nostrand Reinhold, New York, 1950

24 D. H. Katayama and J. H. Welsh, *J. Chem. Phys.*, **79**, (1983), 3627

25 D. H. Katayama and J. A. Welsh, *Chem. Phys. Lett.*, **106**, (1984), 74

26 D. H. Katayama and J. A. Welsh, *J. Chem. Phys.*, **75**, (1981), 4224

27 A. V. Dentamaro and D. H. Katayama, *J. Chem. Phys.*, **90**, (1989), 91

28 N. Furio, A. Ali and P. J. Dagdigian, *Chem. Phys. Lett.*, **125**, (1986), 561

29 N. Furio, A. Ali and P. J. Dagdigian, *J. Chem. Phys.*, **85**, (1986), 3860

30 G. Jihua, A. Ali and P. J. Dagdigian, *J. Chem. Phys.*, **85**, (1986), 7098

31 A. Ali, G. Jihua and P. J. Dagdigian, *J. Chem. Phys.*, **87**, (1987), 2045

32 A. J. Kotlar, R. W. Field, J Steinfeld and J. A. Coxon, *J. Mol. Spetrosc.*, **80**, (1980), 86

33 P. J. Dagdigian, D. Patel-Misra, A. Berning, H.-J. Werner and M. H. Alexander, *J. Chem. Phys.*, **98**, (1993), 8580

34 J. B. Jeffries, *J. Chem. Phys.*, **95**, (1991), 1628

35 S. Singleton and K. G. McKendrick, *J. Phys. Chem.*, **97**, (1993), 1389

36 C. W. Watson and K. G. McKendrick, *Chem. Phys.*, **187**, (1994), 79

37 N. A. Jackson, C. W. Watson and K. G. McKendrick, *Chem. Phys. Lett.*, **243**, (1995), 564

38 N. A. Jackson, C. J. Randall and K. G. McKendrick, *J. Phys. Chem. A*, **102**, (1998), 51

39 N. A. Jackson, C. J. Randall and K. G. McKendrick, *Chem. Phys.*, **233**, (1998), 45

40 N. A. Jackson, C. J. Randall and K. G. McKendrick, Chem. Phys., **233**, (1998), 45

41 C. J. Randall, C. Murray and K. G. McKendrick, *Phys. Chem. Chem. Phys.*, **2**, (2000), 461

42 C. Murray, C. J. Randall and K. G. McKendrick, *Phys. Chem. Chem. Phys.*, **2**, (2000), 5553

II INTRODUCTION TO THE CH RADICAL

Since its discovery in 1918 [1], methylidyne has become one of the most studied free radical species in chemistry. CH is an important species in interstellar chemistry, is one of the most common molecules in the atmospheres of comets and is found in stars [2].

CH plays a role in the chemical vapour deposition of diamond. CH was one of the first molecules to be detected in a dc arcjet using laser-induced fluorescence (LIF) as a means of measuring the rotational temperature of the jet [3]. Subsequent work has also reported the measurement of CH rotational temperatures [4], absolute concentrations [5, 6] and spatial density distributions [7] in plasmas and two-dimensional imaging in a diamond-depositing oxyacetylene flame [8] by LIF.

Finally, and probably most importantly, CH is ubiquitous in the combustion chemistry of hydrocarbons. CH was the first radical species to be studied in a flame using LIF [9] and since that time has been the subject of much work. The use of LIF in flame diagnostics has recently been reviewed by Daily [10]. LIF provides a non-intrusive and highly spatially resolved means of measuring ground state radical rotational and vibrational temperatures [11, 12], concentrations [13, 14] and spatial distributions [15]. The use of LIF to measure rotational populations and hence the temperature of flames is complicated by collisional processes such as electronic quenching and vibrational and rotational energy transfer in the excited state, which affect the quantum yield, especially at higher pressures. Unless the effects of these processes can be assessed, large systematic errors in the measured temperatures can result. Studies of these processes [16, 17, 18, 19] have been reported, and means of assessing the effects of collisional processes have been suggested. CH radicals have also been detected in flames, for the same diagnostic purposes, by multiphoton ionisation [20], degenerate four-wave mixing [21] and wavelength modulation absorption spectroscopy [22].

The wide diversity of environments in which CH is to be found has resulted in an extensive literature. The majority of this introduction will cover the spectroscopy of CH and studies of collisional processes carried out under controlled, single quencher conditions.

The principal aim of this study was to investigate collision-induced electronic energy transfer between the $A^2\Delta$ and $B^2\Sigma^-$ states of the CH radical. More specifically, what was desired was an understanding of the factors that control the distribution of population among the various internal degrees of freedom of the product state, immediately after the collision, based on a narrow distribution over the rovibronic levels (ideally, a specific level) immediately before the collision. This can be achieved using the technique of LIF spectroscopy, since the collisionally coupled $A^2\Delta$ and $B^2\Sigma^-$ states are both optically connected to the $X^2\Pi$ ground state. However, a complete characterisation of the spectral line positions and transition probabilities is required if the product rotational population distributions are to be discerned.

CH is an ideal candidate for the study of energy transfer processes in open-shell molecules from both experimental and theoretical points of view, and as such can be used as a test for models of collisional processes. Experimentally, the large rotational constant of a hydride results in a broad spacing of the rotational energy levels, facilitating the collection of truly state-resolved data. The relatively small number of electrons in CH also makes *ab initio* calculations tractable, enabling the calculation of intermolecular potential surfaces for simple collision partners.

II-1 CH SPECTROSCOPY

The use of LIF spectroscopy to study the collisional energy transfer between the $A^2\Delta$ and $B^2\Sigma^-$ states requires the laser excitation of a CH radical to specific rovibrational levels in one electronic state and observation of the dispersed emission from the collisionally

populated state. Knowledge of the spectroscopy (transition frequencies and probabilities) of the radical is required to identify the transitions used in excitation and those observed in emission and to measure the populations of the emitting levels.

II-1.1 Previous work

The first observations of CH found that the spectrum consisted of three band systems, $A^2\Delta - X^2\Pi$, $B^2\Sigma^- - X^2\Pi$ and $C^2\Sigma^+ - X^2\Pi$, of which a complete analysis in absorption was carried out by Herzberg and Johns [23]. Subsequent refinements to the earlier analyses have also been performed [24, 25]. More recently, laser-magnetic resonance (LMR) and microwave-optical double resonance (MODR) spectroscopy have enabled accurate determination of the Λ-doubling in the $X^2\Pi$ state [26, 27, 28] and the $A^2\Delta$ state [29]. The Λ-doubling in the $A^2\Delta$ state has also been measured using LIF [30]. Measurements of the emission spectrum provide the most recent values of the molecular constants for the $A^2\Delta$ and $X^2\Pi$ states [31, 32, 33, 34], following a reduction of the spectrum with the effective Hamiltonian of Brown [35]. The $B^2\Sigma^- - X^2\Pi$ band system has also been investigated in emission [36, 37]. Investigations into the spectroscopy of the $^{13}C^1H$ radical have also been reported [38, 39].

II-1.2 Interatomic potentials and electronic structure

The potential energy curves for the states of interest are shown in Figure II.1. The $X^2\Pi$ and $A^2\Delta$ were derived using the Rydberg-Klein-Rees (RKR) method, using the published molecular constants of Zachwieja [34]. The $B^2\Sigma^-$ state is poorly represented by the RKR method, since it has only two bound vibrational levels, and is therefore based on the *ab initio* calculations of Lie *et al.* [40]. The energies of the vibrational levels in the $B^2\Sigma^-$ state

are those of Kepa *et al.* [37]. The relevant molecular constants are shown in Table II.1 [34, 37].

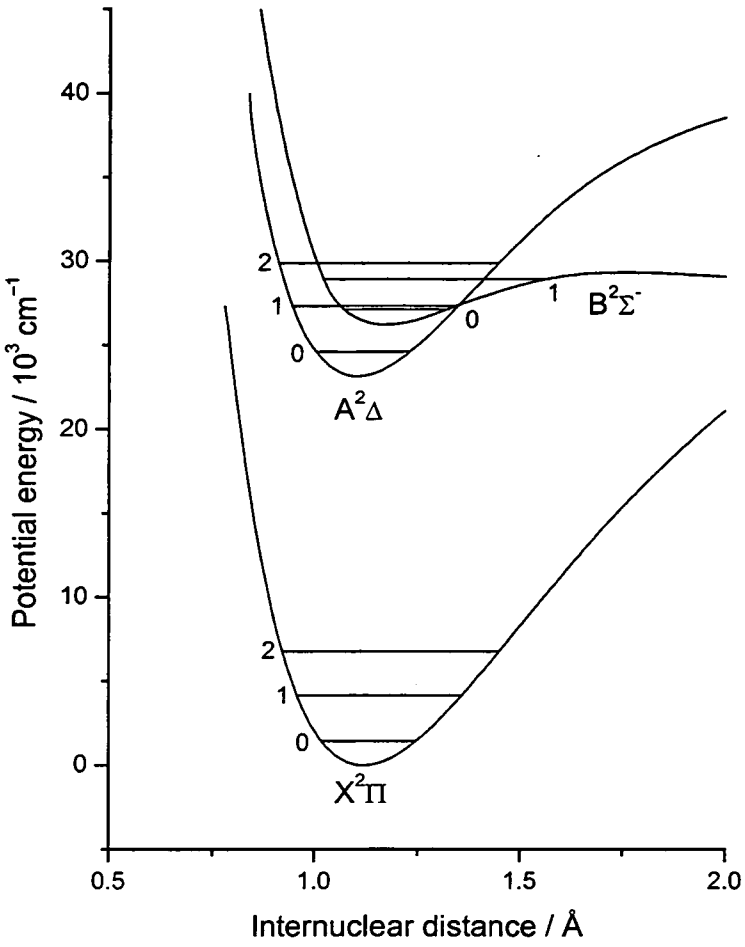

Figure II.1

Potential curves of the lowest electronic states of the CH radical. The lower vibrational levels in each state are indicated.

Table II.1

Equilibrium molecular constants in cm^{-1} (r_e in Å) for the $X^2\Pi$, $A^2\Delta$ and $B^2\Sigma^-$ states of CH. Taken from references 34 and 37.

Constant	$X^2\Pi$	$A^2\Delta$	$B^2\Sigma^-$
r_e [a]	1.1198	1.1031	1.1640
T_e [b]	–	23151.4925	26060.0376
ω_e [c]	2860.7508	2914.0990	2246.4153
$\omega_e x_e$ [c]	64.4387	81.4002	225.7
$\omega_e y_e$ [c]	0.3634	–3.3881	–
A_e [d]	28.0528	–1.1147	–
γ_e [e]	-2.6223×10^{-2}	4.340×10^{-2}	-2.953×10^{-2}
B_e [f]	14.4599	14.8997	13.3813
α_e [g]	0.5365	0.6354	1.4823
D_e [h]	1.4744×10^{-3}	1.5398×10^{-3}	1.6313×10^{-3}
H_e [h]	1.1922×10^{-7}	–	8.94×10^{-7}
p_e [i]	3.408×10^{-2}	3.1×10^{-7}	–
q_e [i]	3.936×10^{-2}	4.6×10^{-8}	–

[a] Equilibrium internuclear separation in Å

[b] Electronic term energy

[c] Harmonic oscillator vibrational frequency and first and second anharmonicity terms

[d] Spin-orbit coupling constant

[e] Spin-rotation coupling constant

[f] Equilibrium rotational constant

[g] Vibration-rotation interaction constant

[h] First and second order centrifugal distortion constants

[i] Λ-doubling parameters

The equilibrium internuclear distances and the potential curves for the $X^2\Pi$ (r_e = 1.1198 Å) and $A^2\Delta$ (r_e = 1.1031 Å) states are very similar, as can be seen in Table II.1. This results in highly diagonal overlap of the vibrational wavefunctions for each state and, hence, large Franck-Condon factors, $q_{v,v'}$, for transitions with $\Delta v = 0$. In the $A^2\Delta - X^2\Pi$ band system, $q_{v,v'} > 0.98$ for the (0,0), (1,1) and (2,2) bands [34,41], all of which lie at ~431 nm.

The $B^2\Sigma^-$ state has only a slightly longer r_e of 1.1640 Å, but the greater anharmonicity of the potential results in a poorer overlap integral for the diagonal bands, especially for $v' = 1$. Franck-Condon factors for the (0,0) and (1,1) bands are ~0.86 and ~0.5, respectively [37, 41]. The $B^2\Sigma^- - X^2\Pi$ (0,0) band lies at ~390 nm. As Figure II.1 shows, the $B^2\Sigma^-$ state potential is very shallow and can only support two vibrational levels. In addition, a barrier exists in the potential, first identified by Herzberg and Johns [23] who estimated it to lie at ~2 Å, with a height of around 500 cm^{-1}. Several authors have reported experimental values for the rotational dependence of the $B^2\Sigma^-$ state lifetimes and the onset of predissociation in CH [42, 43, 44] and CD [45]. The collision-free lifetime is found to increase with rotation and levels with $N' > 14$ in $v = 0$ and $N' > 6$ in $v = 1$ are predissociated.

Luque and Crosley have reported experimental transition moments for the $A^2\Delta - X^2\Pi$ and $B^2\Sigma^- - X^2\Pi$ band systems, derived from vibrational transition probabilities [46, 47]. They have found that the Einstein absorption and emission coefficients are highly dependent on the rotational quantum number in the $B^2\Sigma^-$ state.

The electronic configurations of the $X^2\Pi$, $A^2\Delta$ and $B^2\Sigma^-$ states at equilibrium internuclear separation have been determined by *ab initio* studies [2, 40, 48]. The $X^2\Pi$ state has a nominal electron configuration of $1\sigma^2 2\sigma^2 3\sigma^2 1\pi^1$ and dissociates to ground state atoms, namely $C(^3P)$ and $H(^2S)$. The $A^2\Delta$ state's electron configuration is $1\sigma^2 2\sigma^2 3\sigma^1(1\pi^2, {}^1\Delta)$, dissociating to $C(^1D)$ and ground state H. The ground state atoms also provide the dissociation limits for the $B^2\Sigma^-$ state which has an equilibrium configuration of

$1\sigma^2 2\sigma^2 3\sigma^1(1\pi^2, {}^3\Sigma^-)$. More recent *ab initio* calculations [49] have presented the bonding in terms of simple valence-bond Lewis diagrams the Mulliken populations of the atoms, given in Table II.2. These studies suggest that the *in situ* C atom in the $A^2\Delta$ state has an electron configuration corresponding to the excited ^3D state, which contributes ~70% to the σ-bond formation.

Table II.2

Calculated Mulliken populations for CH $X^2\Pi$, $A^2\Delta$ and $B^2\Sigma^-$, taken from reference 49.

	r_e		r_∞
State	C	H	C
$X^2\Pi$	$2s^{1.81}2p_z^{1.27}2p_x^{0.98}2p_y^{0.06}3d^{0.03}$	$1s^{0.79}2p_z^{0.01}2p_y^{0.02}$	$2s^{1.93}2p_z^{1.0}2p_x^{1.0}2p_y^{0.05}3d^{0.03}$
$A^2\Delta$	$2s^{1.55}2p_z^{0.73}2p_x^{0.97}2p_y^{0.97}3d^{0.05}$	$1s^{0.67}2p^{0.05}$	$2s^{1.93}2p_z^{0.05}2p_x^{1.0}2p_y^{1.0}3d^{0.03}$
$B^2\Sigma^-$	$2s^{1.74}2p_z^{0.55}2p_x^{0.98}2p_y^{0.98}3d^{0.03}$	$1s^{0.68}2p^{0.03}$	$2s^{1.93}2p_z^{1.0}2p_x^{1.0}2p_y^{0.05}3d^{0.03}$

II-1.3 Energy level structure

The rotational and fine-structure energy level structure of the $X^2\Pi$, $A^2\Delta$ and $B^2\Sigma^-$ states must be considered in order to understand the spectroscopic transitions exploited in this study. The level structure of each state is determined by the coupling of the various angular momenta. These angular momenta, neglecting nuclear spin, are

- ***L***, the total electronic orbital angular momentum
- ***S***, the total electron spin angular momentum
- ***R***, the nuclear framework rotation angular momentum.

They couple together to form J, the total angular momentum, neglecting nuclear spin. In this discussion, bold italic characters will be used to refer to angular momentum vectors and italic characters to the corresponding quantum numbers, according to convention.

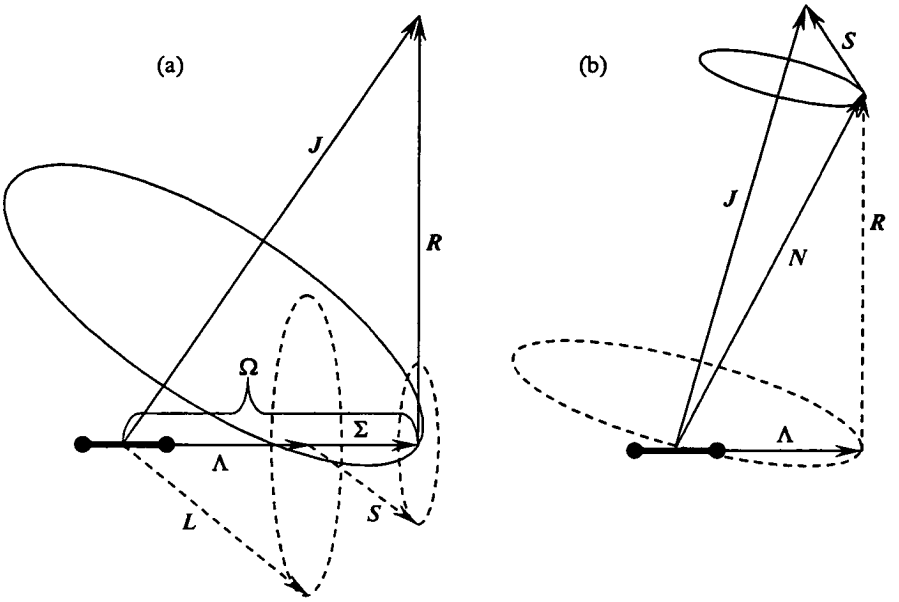

Figure II.2

Vector diagram showing the angular momentum coupling in Hund's case (a) and case (b). In case (a), the solid ellipse shows the nutation of the figure axis while the more rapid precessions of L and S about the internuclear axis are shown by the dashed ellipses. In case (b), the dashed ellipse shows the much faster nutation of the figure axis and the solid ellipse shows the slower precession of N and S about J.

II-1.3.1 The $X^2\Pi$ state

For low rotation, the $X^2\Pi$ state adheres quite closely to a Hund's case (a) description [50], as shown in Figure II.2. In this coupling case, the interaction between the rotation of the nuclear framework and the motion of the electrons is assumed to be weak. The axially symmetric electric field resulting from the charged nuclei results in the fast

precession of $\boldsymbol{L}$ about the internuclear axis. The magnetic field induced by this couples the electron spin, $\boldsymbol{S}$, in turn to the axis. The projections of $\boldsymbol{L}$ and $\boldsymbol{S}$ onto the internuclear axis, Λ and Σ, respectively, add to give Ω, the component of the total angular momentum along the internuclear axis. The quantum number, Ω, is given by

$$\Omega = |\Lambda + \Sigma|$$

Equation II.1

where Λ can take any integer value from 0 to L, while Σ can take any integer or half-integer value, depending on the number of unpaired electrons, from $+S$, $S - 1,\ldots, -S$. The total angular momentum, $\boldsymbol{J}$, is the resultant of $\boldsymbol{\Omega}$ and the nuclear rotation, $\boldsymbol{R}$. For a $^2\Pi$ state, Λ is 1 and Σ can take the values $+½$ or $-½$ causing a splitting of the rotational levels into two manifolds, $^2\Pi_{1/2}$ and $^2\Pi_{3/2}$. The magnitude of the splitting is determined by the spin-orbit constant, A_v. In the $X^2\Pi$ state of CH, the spin-orbit constant has a value of ~28 cm^{-1}. In a pure Hund's case (a) arrangement, the rotational term values in each spin-orbit manifold, neglecting centrifugal distortion, are given by

$$F_v(J) = B_v\left[J(J+1) - \Omega^2\right]$$

Equation II.2

Each J for states in which $\Lambda \neq 0$ is further split in energy due to a phenomenon known as Λ-doubling, the result of the interaction of the electronic orbital angular momentum and the rotation of the molecule. This arises because $\Lambda = \pm 1$ correspond classically to clockwise or anticlockwise circulation of the electrons about the internuclear axis. The Λ-doublets are different phased combinations of $\Lambda = \pm 1$, which, in the high-J limit, give electron densities either in the plane of rotation or perpendicular to it. The

respective electronic wavefunctions are either symmetric or anti-symmetric (labelled $\Pi(A')$ or $\Pi(A'')$ in effective C_s symmetry) with respect to reflection in the plane of rotation [51]. These wavefunctions are degenerate to a first approximation but split into two components as $\boldsymbol{R}$ increases. The Λ-doublets for a given J have different overall parities, indicated by + or –. Levels with + parity have molecular eigenfunctions which do not change sign upon inversion at the origin, while levels with – parity do. In the accepted notation [52] for molecules with half-integer J, rovibronic levels can be assigned as e or f according to

- levels with total parity $+(-1)^{J-½}$ are e levels
- levels with total parity $-(-1)^{J-½}$ are f levels

which represents the overall rotationless parity. In the $X^2\Pi$ state, the lower Λ-doublet has f parity in the F_1 manifold and e parity in the F_2 for all values of J.

In $CH(X^2\Pi)$, as rotation increases, the spin becomes uncoupled from the internuclear axis. This is the basis of the Hund's case (b) description. Here, Ω is no longer a good quantum number and it becomes useful to consider the total angular momentum apart from spin, $\boldsymbol{N}$, which is the resultant of $\boldsymbol{\Lambda}$ and $\boldsymbol{R}$. The total angular momentum, $\boldsymbol{J}$, is then the resultant of $\boldsymbol{N}$ and $\boldsymbol{S}$. The rotational term values are given by [53]

$$F_1(J) = B_v\left[(J+½)^2 - \Lambda^2 - ½\sqrt{4(J+½)^2 + Y(Y-4)\Lambda^2}\right] - D_v J^4$$

Equation II.3

$$F_2(J) = B_v\left[(J+½)^2 - \Lambda^2 + ½\sqrt{4(J+½)^2 + Y(Y-4)\Lambda^2}\right] - D_v (J+1)^4$$

Equation II.4

where $Y = A/B_v$. The transition to a case (b) description occurs at low rotation in the CH radical because of a combination of two complementary factors, both attributable to the low atomic masses of C and H. Firstly, the coupling of the electron spin, $\boldsymbol{S}$, to the internuclear axis by Λ is weak (small value of A_v), therefore the spin is readily uncoupled by the perpendicular rotation-induced magnetic field. Secondly, in a small reduced mass diatomic, the magnetic field increases quickly with $\boldsymbol{R}$ as a result of the large rotational constant. In the Hund's case (b) description, the label F_1 applies to those levels for which $J = N + ½$ and F_2 to levels with $J = N - ½$. N is not a good quantum number in the case (a) description but nominal labels can be attached to the lower lying rotational levels by extrapolation from above. Thus, the $^2\Pi_{1/2}$ manifold corresponds to F_1 and the $^2\Pi_{3/2}$ to F_2.

II-1.3.2 The $A^2\Delta$ state

The arguments applied to the level structure in the $X^2\Pi$ state apply similarly to the $A^2\Delta$ state. However, the strengths of the various angular momenta couplings are different, leading to a markedly different structure. The spin-orbit coupling constant is very small and negative ($A_v \approx -1.1$ cm^{-1}). This small magnitude of the spin-orbit coupling indicates that the $A^2\Delta$ state can essentially be considered as conforming to Hund's case (b) for all rotational levels. The negative sign means that the F_2 $^2\Delta_{5/2}$ manifold lies marginally lower in energy than the F_1 $^2\Delta_{3/2}$ manifold. Λ-doubling is much smaller in Δ states than in Π states and the energetic splitting is insignificantly small, except at very high rotation.

II-1.3.3 The $B^2\Sigma^-$ state

The $B^2\Sigma^-$ state has $\Lambda = 0$, and hence is accurately described by Hund's case (b). In a $^2\Sigma$ state, each N is split into two sub-levels by the spin-rotation coupling, with the

exception of the lowest level since J = – ½ cannot exist. The term values are given, in a first approximation by

$$F_1(N) = B_v N(N+1) + \tfrac{1}{2}\gamma N$$

Equation II.5

$$F_2(N) = B_v N(N+1) - \tfrac{1}{2}\gamma(N+1)$$

Equation II.6

where γ is the spin-rotation constant. In the $B^2\Sigma^-$ state, γ is negative so for a given N, the F_1 level lies below the F_2. The parity of each level can be assigned according to the convention described for the $X^2\Pi$ state, the rotationless level having negative parity.

II-1.3.4 Rovibronic selection rules and the $A^2\Delta - X^2\Pi$ and $B^2\Sigma^- - X^2\Pi$ band systems

For electric dipole transitions in a heteronuclear diatomic, selection rules determine which transitions are allowed. Some selection rules apply generally, while others are limited to the coupling cases of the states involved. For the total angular momentum, J,

$$\Delta J = 0, \pm 1 \textit{ with the restriction, } J = 0 \not\leftrightarrow J = 0$$

which holds rigorously. The symmetry selection rule is

$$+ \leftrightarrow -, + \not\leftrightarrow +, - \not\leftrightarrow -,$$

that is, only rovibronic levels of different parity can combine. These rules apply perfectly generally. For Hund's case (a) and (b) states as is the case with the $X^2\Pi$, $A^2\Delta$ and $B^2\Sigma^-$ states of CH, the electronic orbital angular momentum Λ is well-defined and the selection rule is

$$\Delta\Lambda = 0, \pm 1.$$

The electronic spin has the selection rule

$$\Delta S = 0$$

resulting in only states with the same multiplicity combining with one another. This rule holds less rigorously with increasing multiplet spin-orbit splitting, as is the case with increasing nuclear charge.

If both electronic states are represented by Hund's case (a), the components of spin and the total electronic angular momentum along the internuclear axis are well defined, leading to the rules

$$\Delta\Sigma = 0$$
$$\Delta\Omega = 0, \pm 1$$

This means that transitions of the type $^2\Pi_{1/2} - {}^2\Delta_{5/2}$ are forbidden in the pure case (a) coupling scheme. Similarly, if both electronic states are described by Hund's case (b), the total angular momentum apart from spin, N, is well defined with the selection rule

$$\Delta N = 0, \pm 1, \textit{ with the restriction } \Delta N = 0 \text{ for } \Sigma\text{–}\Sigma.$$

Thus, for branches in $^2\Sigma^- - {}^2\Pi$ and $^2\Delta - {}^2\Pi$ systems for which $\Delta N \neq \Delta J$, known as satellite branches, the intensity drops off rapidly with increasing rotation and progression towards Hund's case (b). With these selection rules in mind, it is therefore possible to rationalise all possible transitions between the $X^2\Pi$ ground state and the $A^2\Delta$ and $B^2\Sigma^-$ excited states. It follows that 24 branches arise in the $A^2\Delta - X^2\Pi$ band and 12 in the $B^2\Sigma^- - X^2\Pi$ band. These transitions are shown in Figure II.3-Figure II.6.

The transitions are labelled according to convention, such that the left superscript represents the value of ΔN and the main letter shows the value of ΔJ. The right subscripts symbolise the upper/lower state manifolds (F_1 or F_2) and rotationless parity (e or f).

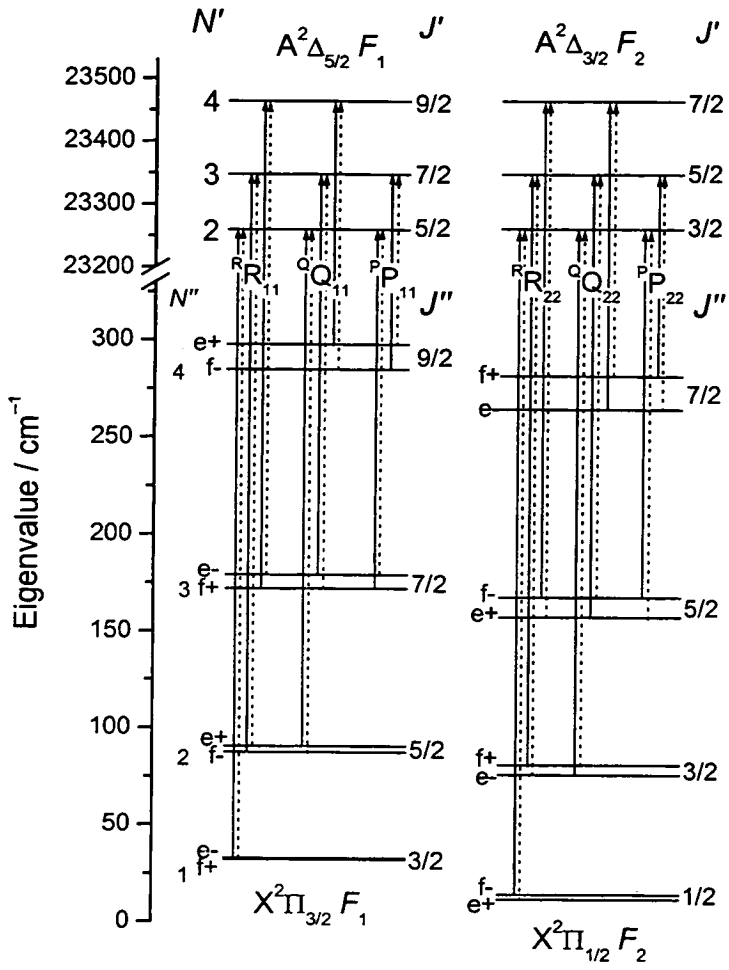

Figure II.3

Allowed main branch transitions of the $A^2\Delta - X^2\Pi$ band system. The Λ-doubling in the $X^2\Pi$ state has been greatly exaggerated, while that in the $A^2\Delta$ state has been omitted. Transitions indicated by solid arrows terminate in a level with *f* parity, dashed arrows indicate transitions terminating in a level with *e* parity.

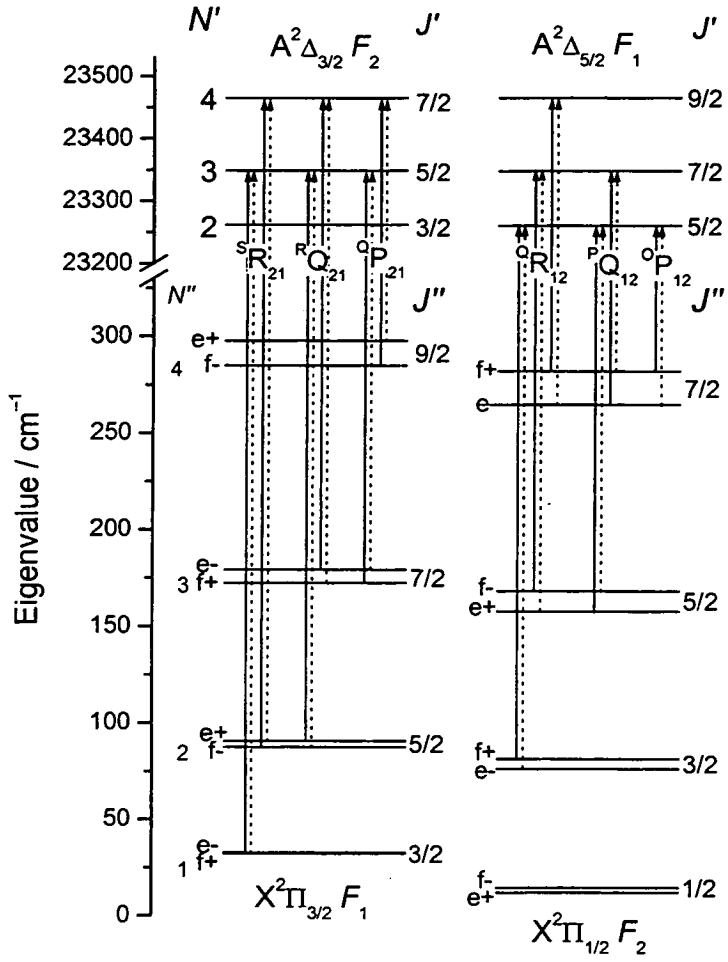

Figure II.4

Allowed satellite transitions of the $A^2\Delta - X^2\Pi$ band system. The Λ-doubling in the $X^2\Pi$ state has been greatly exaggerated, while that in the $A^2\Delta$ state has been omitted. Transitions indicated by solid arrows terminate in a level with *f* parity, dashed arrows indicate transitions terminating in a level with *e* parity.

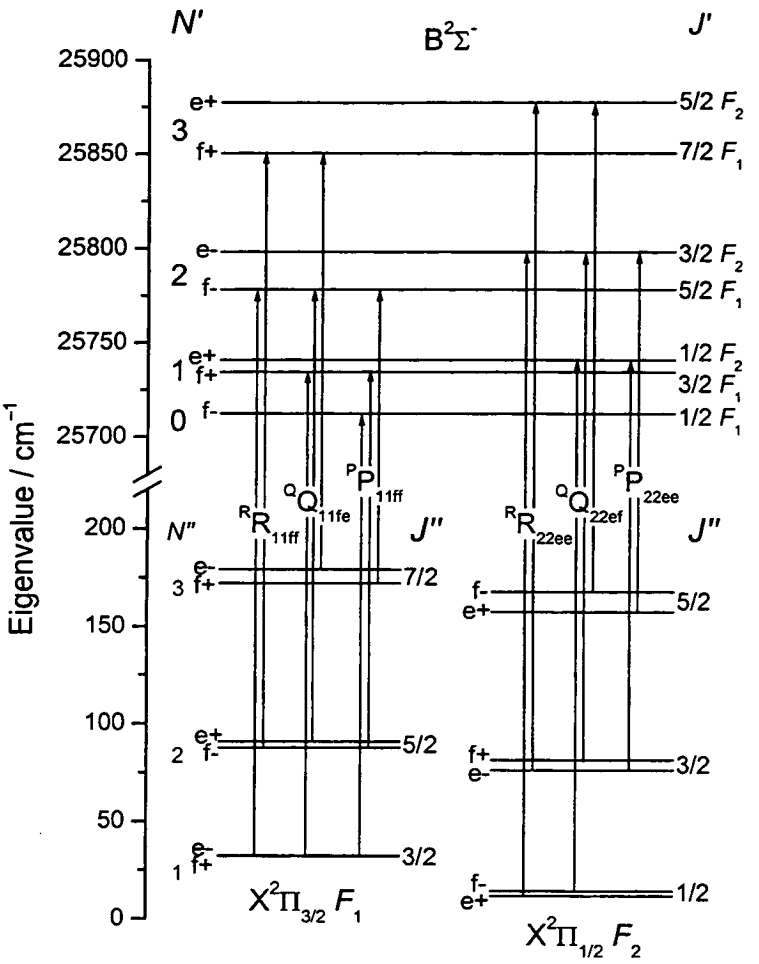

Figure II.5

Allowed main branch transitions in the $B^2\Sigma^- - X^2\Pi$ band system. The Λ-doubling in the $X^2\Pi$ state and the spin-rotation splitting in the $B^2\Sigma^-$ state have been greatly exaggerated for clarity.

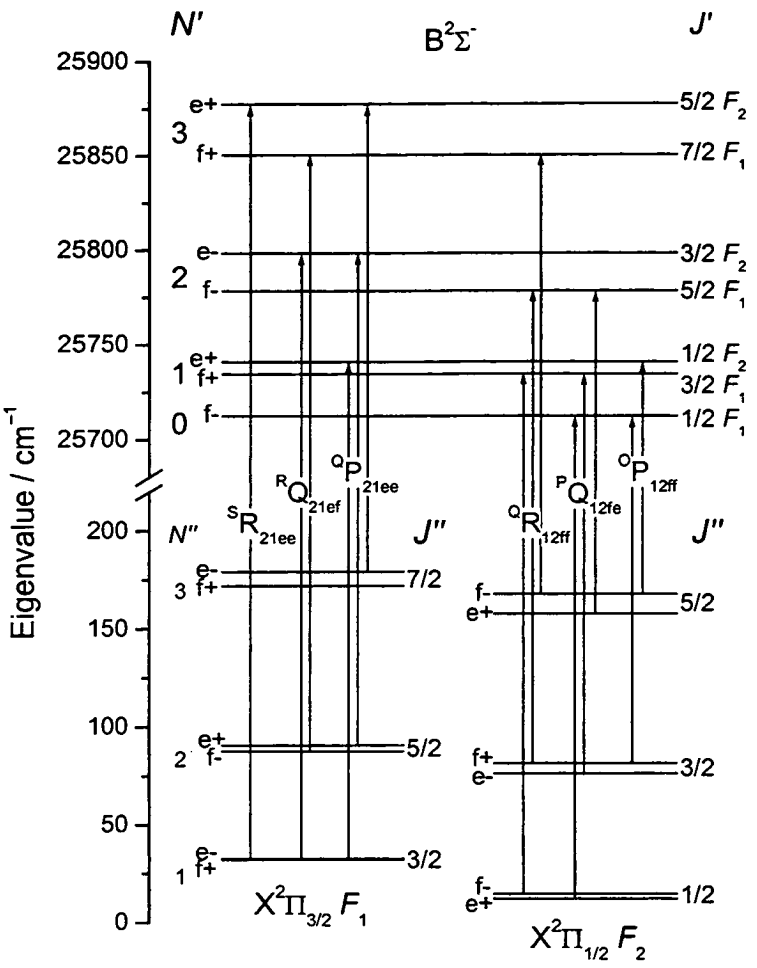

Figure II.6

Allowed satellite branch transitions in the $B^2\Sigma^-$ – $X^2\Pi$ band system. The Λ-doubling in the $X^2\Pi$ state and the spin-rotation splitting in the $B^2\Sigma^-$ state have been greatly exaggerated for clarity.

II-1.4 Spectral simulation

Line positions and intensities for the $A^2\Delta$ – $X^2\Pi$ and $B^2\Sigma^-$ – $X^2\Pi$ transitions required for spectral simulation were calculated using two different techniques. The dispersed fluorescence spectra that will be discussed in Chapter IV were simulated using a

program supplied by Zare *et al.* [54]. Using the molecular constants of Zachwieja and Kepa *et al.* [34, 37], the program carried out a matrix diagonalisation of the molecular Hamiltonian, based on Zare's Unique Perturber Approximation (UPA). The output of this program was coupled with a distribution over the rotational and fine-structure levels of the band to match the intensities of the spectral features to the experimental spectrum. The simulation was finally convoluted with a Gaussian line shape function, chosen to match the experimental bandwidth. The molecular constants used had to be corrected for use with the UPA Hamiltonian since the reduction of the experimental spectra had been carried out using the effective Hamiltonian of Brown *et al.* [29, 55, 56]. The necessary corrections are given by Amiot *et al.* [57].

The dispersed fluorescence spectra that will be discussed in Chapter V, were simulated using LIFBASE [58], a spectral simulation program. This slightly more user-friendly program, distributed by the SRI Chemical Physics Group, provides a database of spectroscopic quantities, most of which are calculated, but include experimentally optimised transition moments. Transition frequencies are generally calculated based on Brown's Hamiltonian [55]. These spectral quantities can then be used to simulate spectra under a range of different experimental conditions and allows the modelling of complex, non-Boltzmann distributions.

II-2 NON-REACTIVE COLLISIONAL PROCESSES

It is useful at this point to make clear explicitly what is meant by certain terms referring to various collisional processes that will be used in subsequent discussion. Rotational energy transfer (RET) refers to the redistribution of population among the rotational and/or fine-structure levels within a given vibronic state as the ensemble moves towards a thermal distribution. Vibrational energy transfer (VET) refers to a collisional

process that transfers population (which can be distributed over a range of rotational levels) into another vibrational level *within the same* electronic state. Electronic energy transfer (EET) will be used to refer to any collisional process that transfers population from one electronic state to another where the product state is explicitly identified. Finally, in the context of this work, quenching refers to a collisional process that removes population *irreversibly* from a given electronic state and deposits it in a 'dark state'. This can be the ground state, although quenching also covers all non-specifically identified EET processes, including reaction.

II-2.1 Total quenching rates

There have been a number of studies of the collisional removal of electronically excited states of the CH radical (in the most part, of the $A^2\Delta$ state, although there has been some work carried out on the $B^2\Sigma^-$ and $C^2\Sigma^+$ states) using a variety of techniques. Tabares and Ureña [59] measured the decrease in chemiluminescent intensity on the $A^2\Delta - X^2\Pi$ band as a function of collider pressure (N_2 and O_2) in a discharge flow apparatus. Their quenching rate constants are anomalously high. Donovan *et al.* used excimer laser photolysis at 193 nm of CH_2I_2, $(CH_3)_2CO$ and $CHBr_3$ [60, 61] to produce electronically excited $CH(A^2\Delta)$ radicals. They measured the pressure dependence of the fluorescence lifetime with a range of collision partners (H_2, O_2, NO, CO, N_2O and hydrocarbons) at 300 K. The removal rates were found to be smaller than the reaction rates for ground state $CH(X^2\Pi)$ with all collision partners used except CO [62, 63, 64]. In collisions with hydrocarbons, the rate constants are found to increase steadily with the number of C–H bonds present.

Similar room temperature fluorescence quenching measurements of the $A^2\Delta$ state have been made by Heinrich *et al.* [65], who also used 193 nm photolysis of acetone. The

two most polar collision partners used, H_2O and NH_3, were found to have the largest cross-sections.

Chen *et al.* [66, 67, 68, 69] extended the range of collision partners from small molecules and alkanes to include amines, alcohols, and chloromethane following 266 nm photolysis of $CHBr_3$. Quenching rate constants for the $A^2\Delta$ state of CH by alkanes were found to increase with increasing number of C–H bonds, as measured previously [60, 68]. For the series $CH_{(4-n)}Cl_n$, (n = 0 – 4), the quenching rate generally increases with increasing number of chlorine atoms although the rate for CCl_4 is smaller than $CHCl_3$. This is attributed to the zero dipole and quadrupole moments of CCl_4 [66]. For the $B^2\Sigma^-$ state, this trend is repeated but the absolute magnitude of the rate constants is larger [69] and in both cases, bromoform is a more effective quencher than chloroform. Measurements of $A^2\Delta$ and $B^2\Sigma^-$ state collisional removal rate constants showed no statistically significant differences between primary secondary and tertiary amines [67]. For the group of molecules $(CX_3)_2CO$, CF_3COOX and $CXCl_3$ where X is H or D, the measured rate constants were slightly greater with the deuterated collision partners for both the $A^2\Delta$ and $B^2\Sigma^-$ states [68]. This was accounted for by the greater density of states of the heavier molecules in terms of Rice-Rampsberger-Kassel-Markus (RRKM) theory after arguments by Zabarnick, Fleming and Lin [70]. Alcohol molecules were found [69] to quench the $A^2\Delta$ and $B^2\Sigma^-$ states of CH faster than the analogous alkanes, attributed to the greater polarity and the slightly weaker C–H bonds due to the presence of the hydroxyl group.

Cooper and Whitehead [71] provided the first systematic measurements of $B^2\Sigma^-$ and $C^2\Sigma^+$ state removal rate constants, by measuring the pressure-dependence of the photolytically produced fluorescence. Their work on the $B^2\Sigma^-$ state was extended by Chen *et al.* [67, 68, 69] as discussed above. For most collision partners, the $B^2\Sigma^-$ state is found to be quenched more effectively than the $A^2\Delta$ state.

In all these studies, the photolysis process produces rotationally and vibrationally hot CH radicals in the $A^2\Delta$, $B^2\Sigma^-$ and $C^2\Sigma^+$ states, regardless of the specific UV wavelength used. Rotational and translational thermalisation of the electronically excited radicals is assumed to occur quickly on the timescale of the fluorescence (within ~50ns [60, 65, 66] in the presence of a bath gas) although $B^2\Sigma^-$, $v = 0$ radicals remain slightly hotter [71]. Vibrational relaxation is generally a slower process than rotational relaxation for CH (see Section II-2.2). However, it is assumed not to affect measured quenching rates, which are presented as being for the $v = 0$ vibrational level in all electronic states. Collision induced coupling with other electronic states is considered only by Cooper and Whitehead [71] as a means of explaining the enhanced quenching rates of the $B^2\Sigma^-$ state with alkane molecules.

The radiative lifetime of the $A^2\Delta$ state of CH was first measured using LIF by Becker *et al.*, following the generation of ground state CH radicals in a microwave discharge [72] and later by 248 nm photolysis of $CHClBr_2$ [73]. They measured collision-free lifetimes for $A^2\Delta$, $v = 0$ of 537.5 ± 5 and 526 ± 11 ns and collisional removal rates for a range of small molecules which were generally in fairly good agreement with other room temperature measurements.

II-2.1.1 Temperature dependence of quenching

The temperature dependence of the collisional removal rates of the $A^2\Delta$ state of CH has been investigated in a number of studies. Garland and Crosley [74] used a combination of laser pyrolysis and laser-induced fluorescence to measure the quenching cross-sections for CH $A^2\Delta$, $v = 0$ at a temperature of 1300 K. Comparison with the results of Donovan *et al.* [61] found a positive temperature dependence, suggesting the involvement of repulsive forces or barriers in the collision process. *Ab initio* calculations of the potential energy surface between $CH(A^2\Delta)$ and H_2 have shown there to be a barrier on the reactive

surface [75]. Further work in the relatively low temperature regime (240 – 420 K) was carried out by Kenner *et al.* [76] by measuring the fluorescence lifetime in a heated reaction vessel. Chen *et al.* [77] used a similar technique over a wider range of temperatures (up to 653 K). Heinrich and Stuhl [78, 79] modified Garland and Crosley's technique [74] by using a pulsed CO_2 laser for heating prior to photolysis of a precursor at 193 nm. Altering the delay between the lasers allowed control of the temperature of the photolytically produced $CH(A^2\Delta)$ state radicals up to ~1000 K. In general, the quenching cross-sections are found for most collision partners to increase with increasing temperature, but Arrhenius plots are non-linear. Modification of the collision complex model of Fairchild *et al.* [80], which was successful at describing quenching of $OH(A^2\Sigma^+)$, by the inclusion of an activation barrier in the multipole attractive model has been attempted by several authors [68, 78, 79, 81] but its validity has been called into question [76]. As such, there remains no ideal model to explain the rates of collisional quenching of $CH(A^2\Delta)$.

II-2.1.2 Rotational level dependence of quenching

Rotational effects on the quenching of electronically excited diatomic hydrides have been reviewed by Crosley [82]. Following photolysis at 193 nm, the rotational dependence of the $A^2\Delta$ and $B^2\Sigma^-$ state quenching by the acetone precursor has been investigated [83, 84]. The quenching rates were found to decrease for $3 \leq N \leq 7$, while the rates increase steadily for higher N. $B^2\Sigma^-$ state quenching also showed a rotational dependence for levels with $N \geq 11$. Studies following the photodissociation of ketene [85] found that there was only a moderate increase in quenching rate with increasing N in the $A^2\Delta$ state while the $B^2\Sigma^-$ state was removed more quickly with increasing N. The $v = 2$ level of the $A^2\Delta$ state was collisionally removed faster than $v = 0$.

The effect of rotational and vibrational excitation on the collisional removal rates of CD($A^2\Delta$ and $B^2\Sigma^-$) by deuterated ketene, H_2 and Xe has been reported [86, 87, 88]. In this work, CD was produced by 193 nm photolysis of the deuterated ketene precursor and the resulting fluorescence decay was time-resolved for specific rotational lines. The quenching rates of CD($A^2\Delta$) by ketene showed the same trend as the same state of the protonated radical [85] although the absolute magnitudes were about a factor of two smaller. The $A^2\Delta$ state of CD is quenched more rapidly with increasing rotation by H_2 [87], while Xe shows an initial increase in quenching with greater rotation, followed by a decrease at high N [88]. Most recently [89], the rotational dependence of the collisional removal of the $A^2\Delta$ states of CD by CO and CH by CO, H_2 and Xe has been studied. The quenching efficiency of CO decreases with increasing CH/D rotation, suggesting an attractive interaction. The inefficient quenching by H_2 is consistent with a barrier in the intermolecular potential, as suggested by *ab initio* calculations [75], while Xe appears to show a more complex interaction.

II-2.2 Rotational and vibrational energy transfer

In marked contrast to measurements of total quenching rates described above, comparatively little work has been carried out on inelastic processes within a given electronic state. Dixon *et al.* [90] used time-resolution of dispersed fluorescence to measure the rate of RET within the $v = 0$ vibrational level of the $A^2\Delta$ state induced by He. A tuneable pulsed dye laser was used to excite CH radicals to several low N quantum states (different spin-orbit components were resolved but not individual Λ-doublets) and the resulting fluorescence was dispersed at rotational resolution. In this way, they found that the dominant RET transitions are those with $\Delta N = \pm 1$, although weak transfer was observed up to $\Delta N = \pm 3$ and that the total rates of removal from each level were close to gas-kinetic. The measured rates were compared to those predicted by the energy-corrected sudden

approximation incorporating a power-law dependence (ECS-P) [91] model, and were found to give a satisfactory but far from perfect fit.

Cooper and Whitehead [92, 93] have investigated RET and VET within the $A^2\Delta$ and $B^2\Sigma^-$ states of CH using Ar and N_2 as collision partners. Photolysis of $CHBr_3$ at 248 nm was used to produce vibrationally and rotationally hot CH in the $A^2\Delta$ ($v \leq 2$, $N \leq 25$) and $B^2\Sigma^-$ ($N \leq 15$ for $v = 0$ and $N \leq 6$ for $v = 1$, the predissociation onset) states and the resulting fluorescence was dispersed by a monochromator on the diagonal bands with a known pressure of quenching gas present. Spectral simulation was used to obtain the rotational population distributions, although fine-structure levels could not be resolved. The rate constants were obtained by solving the master equation for the level population, n_i

$$\frac{dn_i}{dt} = -k_f n_i - k_q n_i m + \sum_{j \neq i} [k_{j \to i} n_j - k_{i \to j} n_i] m$$

Equation II.7

where k_f is the reciprocal of the collision-free fluorescence lifetime, k_q is the collisional quenching rate constant and m is the added gas concentration. The RET rate constants $k_{j \to i}$ and $k_{i \to j}$ are related by microscopic reversibility. In the $A^2\Delta$ state, rate constants for RET were found to be close to gas-kinetic for both Ar and N_2 and decrease with increasing quantum number, although N_2 remains more effective at higher N. Transitions with relatively small ΔN (up to ± 2) were sufficient to account for the experimental observations. VET within the $A^2\Delta$ state was found to be about an order of magnitude slower, for which Ar was more efficient than N_2. In the $B^2\Sigma^-$, $v = 0$ state, RET rates were also found to be close to gas-kinetic, although multi-quantum changing collisions (up to $\Delta N = \pm 3$) were required to bring the experimental results into agreement with the model. A contrast with the $A^2\Delta$ state is apparent in the VET rates measured. For the $B^2\Sigma^-$ state, the measured VET rates are the

same order of magnitude as the RET rates, leading to suggestions that an attractive potential exists between the $B^2\Sigma^-$ state and the collision partner.

Wang *et al.* [94, 95] have used a Fourier transform spectrometer (FTS) to monitor RET in the $A^2\Delta$ and $B^2\Sigma^-$ states, following photolysis of $CHBr_3$ at 193 nm and 266 nm respectively. They resolved emission from individual rotational but not fine-structure levels. RET rate constants were derived, as in the work by Cooper and Whitehead [92, 93], by fitting to Equation II.7. In the $A^2\Delta$ state with He and Ar collision partners, only collisions with $\Delta N = \pm 1$ were found to be required to provide agreement with the experimental data. While the values for the rate constants obtained with Ar as the collision partner show the same trend as Cooper and Whitehead's (*i.e.* they decrease with increasing N), the values are consistently higher for low N and lower for high N. The same analysis was carried out for the $B^2\Sigma^-$ state in collisions with He, Ar, CO, N_2, N_2O, and $CHBr_3$, with collision-induced ΔN up to ± 3 found to be necessary for agreement with the experimental data. Values obtained for RET with Ar show the same trends as Cooper and Whitehead's measurements. However, the rate constants obtained for collisions with N_2 are significantly higher, especially at low N. Unsurprisingly, a general trend in the order of the RET rates was He ~ Ar < CO ~ N_2 < N_2O < $CHBr_3$. Once again, the multi-quantum changing collisions in the $B^2\Sigma^-$ state are interpreted as evidence for an attractive potential between it and the collision partner, while the small ΔN observed in the $A^2\Delta$ state is interpreted as evidence for a repulsive potential and hence sudden collisions.

RET in the $A^2\Delta$ state of CD caused by collisions with Ar has been investigated by Cerezo *et al.* [96]. Rate constants were deduced from the evolution of a hot photolytically-produced rotational distribution and the time-dependence of the fluorescence on individual rotational lines. The rate constants obtained for RET in $CD(A^2\Delta)$ were found to be smaller than those of Cooper and Whitehead [92] for $CH(A^2\Delta)$.

In Garland and Crosley's [16] atmospheric pressure methane-oxygen flame, the dominant processes removing population from the initially pumped level under the conditions used were RET and electronic quenching. Excited state rotational populations were non-thermal because of the electronic quenching arresting the RET process before equilibrium could be reached. In all states examined ($A^2\Delta$, $v = 0$ and 1 and $B^2\Sigma^-$, $v = 0$) a rotational level dependence was found for the ratio of RET rate and quenching rate. VET within the $A^2\Delta$ state was not observed, however in the $B^2\Sigma^-$ state, an upward vibrational transfer from $v = 0$ to $v = 1$ was found to occur at a rate two orders of magnitude smaller than the rotational redistribution. Unfortunately, the complexity of the flame environment means that various collision partners are responsible for the effects observed.

During the course of this work, Kind and Stuhl [97] have reported state-to-state rate constants for rotational transfer within $B^2\Sigma^-$, $v = 0$ in collisions with Ar. Dispersed florescence spectra were recorded, following initial state selection, at sufficient resolution to observe the individual fine-structure levels. They measured large rate constants approaching the collision frequency, which were in fairly good agreement with previous measurements [93, 94, 95]. At low N, the fine-structure changing transition, $F_1 \leftrightarrow F_2$, with $\Delta N = 0$ was found to dominate. This propensity decreases with increasing N. For transitions with a change in rotational quantum number, $\Delta N \neq 0$, there is a propensity to conserve the fine-structure label, which decreases with increasing initial N.

Using the same experimental approach, Dagdigian *et al.* have presented a combined experimental and theoretical study of rotationally inelastic collisions in CH($A^2\Delta$, $v = 0$) with resolution of the fine-structure at low N [98] and the Λ-doublets at high N [99]. As in the $B^2\Sigma^-$ state, RET rate constants were found to be large (for low N). A broader range in ΔN was observed compared to previous measurements [92, 95]. At low N [98], propensities for fine-structure changing/conserving transitions followed the same trends as described above for the $B^2\Sigma^-$ state [97]. The propensity for conservation of the fine-structure label is

interpreted as a consequence of the Hund's case (b) nature of the $A^2\Delta$ state, for which the spin is a spectator in the collision. At high N, where resolution of the Λ-doublets is possible, the dominant rotationally inelastic process is the symmetry-changing $A' \leftrightarrow A''$ transition for $\Delta N = 0$. A slight preference is observed (and predicted) for symmetry conservation in transitions with $\Delta N \neq 0$.

II-2.3 State-changing collisions

Garland and Crosley [16] observed collision-induced electronic energy transfer in their atmospheric flame. They noted that following excitation to either the $A^2\Delta$, $v = 1$ or $B^2\Sigma^-$,$v = 0$ levels, emission from the other was detected. No transfer from $B^2\Sigma^-$, $v = 0$ to $A^2\Delta$, $v = 0$ was observed. The $A^2\Delta$ state was found to account for approximately 20% of the removal of the $B^2\Sigma^-$ state. EET was also observed by Rensberger *et al.* in a low pressure flame [18] who found that the collision-induced $A^2\Delta$ state emission was between 30 and 50% of the initially populated $B^2\Sigma^-$ state signal.

The collisional coupling of the $A^2\Delta$ and $B^2\Sigma^-$ states in flames has formed the basis for recent planar laser-induced fluorescence (PLIF) measurements in flames by Carter *et al.* [100, 101, 102]. These authors excite to the $B^2\Sigma^-$, $v = 0$ level and collect the fluorescence emitted from the collisionally produced $A^2\Delta$ state.

These observations of collision-induced electronic energy transfer provided a stimulus to study this phenomenon under controlled conditions, in which the identity and the pressure of a selected collision partner is well defined.

II-3 REFERENCES

1 T. Heurlinger, Dissertation, University of Lund, 1918

2 E. F. van Dishoeck, *J. Chem. Phys.*, **86**, (1987), 196

3 G. A. Raiche and J. B. Jeffries, *Appl. Opt.*, **32**, (1993), 4629

4 E. A. Brinkmann, G. A. Raiche, M. S. Brown and J. B. Jeffries, *Appl. Phys. B*, **64**, (1997), 689

5 M. Engelhard, W.Jacob, W. Möller and A.W. Koch, *Appl. Opt.*, **34**, (1995), 4542

6 J. Luque, W. Luchmann and J. B. Jeffries, *Appl. Opt.*, **36**, (1997), 3261

7 J. Luque, W. Luchmann and J. B. Jeffries, *J. Appl. Phys.*, **82**, (1997), 2072

8 R. J. H. Klein-Douwel, J. J. L. Spaanjaars and J. J. ter Meulen, *J. Appl. Phys.*, **78**, (1995), 2086

9 R. H. Barnes, C. E. Moeller, J. F. Kircher and C. M. Berber, *Appl. Opt.*, **12**, (1973), 2531

10 J. W. Daily, *Prog. Energy Combust. Sci.*, **23**, (1997), 133

11 K. J. Rensberger, J. B. Jeffries, R. A. Copeland, K. Kohse-Höinghaus, M. L. Wise and D. R. Crosley, *Appl. Opt.*, **28**, (1989), 3556

12 J. Luque and D. R. Crosley, *Appl. Opt.*, **38**, (1999), 1423

13 M. Engelhard, W. Jacob, W. Möller and A. W. Koch, *Appl. Opt.*, **34**, (1995), 4542

14 J. Luque and D. R. Crosley, *Appl. Phys. B*, **63**, (1996), 91

15 L. G. Blevins, M. W. Renfro, K. H. Lyle, N. M. Laurendeau and J. P. Gore, *Combust. Flame*, **118**, (1999), 684

16 N. L. Garland and D. R. Crosley, *Appl. Opt.*, **24**, (1985), 4229

17 R. G. Joklik and J. W. Daily, *Combust. Flame*, **69**, (1987), 211

18 K. J. Rensberger, M. J. Dyer and R. A. Copeland, *Appl. Opt.*, **27**, (1988), 3679

19 J. Luque, R. J. H. Klein-Douwel, J. B. Jeffries and D. R. Crosley, *Appl. Phys. B*, **71**, (2000), 85

20 P. J. H. Tjossem and K. C. Smyth, *Chem. Phys. Lett.*, **144**, (1988), 51

21 S. Williams, D. S. Green, S. Sethuraman and R. N. Zare, *J. Am. Chem. Soc.*, **114**, (1992), 9122

22 K. A. Peterson and D. B. Oh, *Opt. Lett.*, **24**, (1999), 667

23 G. Herzberg and J. W. C. Johns, *Astrophys. J.*, **158**, (1969), 399 and references therein

24 I. Botterud, A. Lofthus and L. Veseth, *Phys. Scr.*, **8**, (1973), 218

25 B. N. Krupp, *Astrophys. J.* **189**, (1974), 389

26 K. M. Evenson, H.E. Radford and M. M. Moran, *Appl. Phys. Lett.*, **18**, (1971), 426

27 J. T. Hougen, J. A. Mucha, D. A. Jennings and K. M. Evenson, *J. Mol. Spectrosc.*, **72**, (1978), 463

28 J. M. Brown and K. H. Evenson, *J. Mol. Spectrosc.*, **98**, (1983), 392

29 C. Brazier and J. M. Brown, *Can. J. Phys.*, **62**, (1984), 1563

30 W. Ubachs, W. M. van Herpen, J. J. ter Meulen and A. Dymanus, *J. Chem. Phys.*, **84**, (1986), 6575

31 P. F. Bernath, *J. Chem. Phys.*, **86**, (1987), 4838

32 Z. Bembenek, R. Kepa, A. Para, M. Rytel and M. Zachwieja, *J. Mol. Spectrosc.*, **139**, (1990)

33 P.F. Bernath, C. R. Brazier, T. Olsen, R. Hailey, W. T.M. L. Fernando, C. Woods and J.L. Hardwick, *J. Mol. Spectrosc.*, **147**, (1991), 16

34 M. Zachwieja, *J. Mol. Spectrosc.*, **170**, (1995), 285

35 J. M. Brown, E. A. Colbourn, J. K. G. Watson and F. D. Wayne, *J. Mol. Spectrosc.*, **74**, (1979), 294

36 A. Para, *J. Phys. B: At. Mol. Phys.*, **24**, (1991), 3179

37 R. Kepa, A. Para, M. Rytel and M. Zachwieja, *J. Mol. Spectrosc.*, **178**, (1996), 189

38 A. Para, *J. Phys. B: At. Mol. Phys.*, **29**, (1996), 5765

39 M. Zachwieja, *J. Mol. Spectrosc.*, **182**, (1997), 18

40 G. Lie, J. Hinze and B. Liu, *J. Chem. Phys.*, **59**, (1973), 1872

41 N. L. Garland and D. R. Crosley, *J. Quant. Spectrosc. Radiat. Transfer.*, **33**, (1984), 591

42 R. A. Anderson, J. Peacher and D. M. Wilcox, *J. Chem. Phys.*, **63**, (1975), 5287

43 J. Brzozowski, P. Bunker, N. Elander and P. Erman, *Astrophys. J.*, **207**, (1976), 414

44 J. Luque and D. R. Crosley, *Chem. Phys.*, **206**, (1996), 185

45 M. Danielsson, P. Erman, A. Hishikawa, E. Rachlew-Källne and G. Sundström, *J. Chem. Phys.*, **98**, (1993), 9405

46 J. Luque and D. R. Crosley, *J. Chem. Phys.*, **104**, (1996), 2146

47 J. Luque and D. R. Crosley, *J. Chem. Phys.*, **104**, (1996), 3907

48 G. C. Lie, J. Hinze, B. Liu, *J. Chem. Phys.*, **59**, (1973), 1887

49 A. Kalemos, A. Mavridis and A. Metropoulos, *J. Chem. Phys.*, **111**, (1999), 9536

50 G. Herzberg, *"Molecular Spectra and Molecular Structure: Volume I – Spectra of Diatomic Molecules"*, 2nd Edition, Van Nostrand Reinhold, New York, 1950

51 M. H. Alexander, P. Andresen, R. Bacis, R. Bersohn, F. J. Comes, P. J. Dagdigian, R. N. Dixon, R. W. Field, G. W. Flynn, K.-H. Gericke, E. R. Grant, B. J. Howard, J. R. Huber, D. S. King, J. L. Kinsey, K. Kleinermanns, K. Kuchitsu, A. C. Luntz, A. J. McCaffery, B. Pouilly, H. Resiler, S. Rosenwaks, E. W. Rothe, M. Shapiro, J. P. Simons, R. Vasudev, J. R. Wiesenfeld, C. Wittig and R. N. Zare, *J. Chem. Phys.*, **89**, (1988), 1749

52 J. M. Brown, J. T. Hougen, K.-P. Huber, J.W. C. Johns, I Kopp, H. Lefëbvre-Brion, A. J. Merer, D. A. Ramsay, J. Rostas and R. N. Zare, *J. Mol. Spectrosc.*, **55**, (1975), 500

53 E. L. Hill and J. H. Van Vleck, *Phys. Rev.*, **32**, (1923), 250

54 R. N. Zare, A. L. Schmeltekopf, W. J. Harrop and D. L. Albritton, *J. Mol. Spectrosc.*, **46**, (1973), 37

55 J. M. Brown, E. A. Colbourn, J. K. G. Watson and F. D. Wayne, *J. Mol. Spectrosc.*, **74**, (1979), 294

56 J. M. Brown, A. S.-C. Cheung and A. J. Merer, *J. Mol. Spectrosc.*, **124**, (1987), 464

57 C. Amiot, J.-P. Maillard and J. Chauville, *J. Mol. Spectrosc.*, **87**, (1981), 196

58 J. Luque and D. R. Crosley, *"LIFBASE: Database and Spectral Simulation Program (Version 1.6)"*, SRI International Report MP 99-009 (1999)

59 F. L. Tabares and A. G. Ureña, *J. Photochem.*, **21**, (1983), 289

60 C. J. Nokes and R. J. Donovan, *Chem. Phys.*, **90**, (1984), 167

61 C. Nokes, G. Gilbert and R. J. Donovan, *Chem. Phys. Lett.*, **99**, (1983), 491

62 M. R. Berman, J. W. Fleming, A. B. Harvey and M. C. Lin, *Chem. Phys.*, **73**, (1982), 27

63 M. R. Berman and M. C. Lin, *Chem. Phys.*, **82**, (1983), 435

64 S. S. Wagal, T. Carrington, S. V. Filseth and C. M. Sadowski, *Chem. Phys.*, **69**, (1982), 61

65 P. Heinrich, R. D. Kenner and F. Stuhl, *Chem. Phys. Lett.*, **147**, (1988), 575

66 C. Chen, X. Wang, S. Yu, Q. Lu and X.Ma, *Chem. Phys. Lett.*, **197**, (1992), 286

67 C. Chen, Q. Ran, S. Yu and X. Ma, *Chem. Phys. Lett.*, **203**, (1993), 307

68 C. Chen, Q. Ran, S. Yu and X. Ma, *J. Chem. Phys.*, **99**, (1993), 1070

69 C. Chen, Y. Sheng, S. Yu, X. Ma, *J. Chem. Phys.*, **101**, (1994), 5727

70 S. Zabarnick, J. W. Fleming and M. C. Lin, *Chem. Phys.*, **150**, (1991), 109

71 J. L. Cooper and J. C. Whitehead, *J. Chem. Soc., Faraday Trans.*, **88**, (1992), 2323

72 K. H. Becker, H. H. Brenig and T. Tatrczyk, *Chem. Phys. Lett.*, **71**, (1980), 242

73 W. Bauer, B. Engelhardt, P. Wiesen and K. H. Becker, *Chem. Phys. Lett.*, **158**, (1989), 321

74 N. L. Garland and D. R. Crosley, *Chem. Phys. Lett.*, **134**, (1987), 189

75 A. Vegiri and S. C. Farantos, *Chem. Phys. Lett.*, **167**, (1990), 278

76 R. D. Kenner, S. Pfannenberg, P. Heinrich and F. Stuhl, *J. Phys. Chem.*, **95**, (1991), 6585

77 C. Chen, F. Wang, Y. Chen, X. Ma, *Chem. Phys.*, **230**, (1998), 317

78 P. Heinrich and F. Stuhl, *Chem. Phys.*, **199**, (1995), 105

79 P. Heinrich and F. Stuhl, *Chem. Phys.*, **199**, (1995), 297

80 P. W. Fairchild, G. P. Smith and D. R. Crosley, *J. Chem. Phys.*, **79**, (1983), 1795

81 C. Chen, F. Wang, Y. Chen and X. Ma, *Chem. Phys.*, **230**, (1998), 317

82 D. R. Crosley, *J. Phys. Chem.*, **93**, (1989), 6273

83 E. Hontzopoulos, Y. P. Vlahoyannis and C, Fotakis, *Chem. Phys. Lett.*, **147**, (1988), 321

84 S. Couris, N. Anastasopoulou and C. Fotakis, *Chem. Phys. Lett.*, **223**, (1994), 561

85 J. Luque, J. Ruiz and M. Martin, *Laser Chem.*, **14**, (1993), 207

86 A. Alonso, M. Ponz and M. Martin, *Chem. Phys. Lett.*, **258**, (1996), 465

87 M. Martin and M. Castillejo, *Chem. Phys. Lett.*, **266**, (1997), 111

88 M. Martin and C. Cerezo, *Chem. Phys. Lett.*, **288**, (1998), 799

89 C. Cerezo and M. Martin, *J. Photchem. Photobio. B*, **134**, (2000), 127

90 R. N. Dixon, D. P. Newton and H. Rieley, *J. Chem. Soc., Faraday Trans. 2*, **83**, (1987), 675

91 A. E. DePristo, S. D. Augustin, R. Ramaswamy and H. Rabitz, *J. Chem. Phys.*, **71**, (1979), 850

92 J. L. Cooper and J. C. Whithead, *J. Chem. Soc., Faraday Trans.*, **89**, (1993), 1287

93 J. L. Cooper and J. C. Whitehead, *J. Phys. Chem.*, **98**, (1994), 8274

94 C.-C. Wang, T.-L. Chin and K.-C. Lin, *J. Chem. Phys.*, **107**, (1997), 10348

95 C.-C. Wang, Y.-P. Chen, T.-L. Shin, H.-Y. Huang and K.-C. Lin, *J. Chem. Phys.*, **112**, (2000), 10204

96 C. Cerezo, R. Torres, J. Ruiz and M. Martin, *J. Photochem. Photobio. B*, **132**, (2000), 19

97 M. Kind and F. Stuhl, *J. Chem. Phys.*, **114**, (2001), 6160

98 M. Kind, F. Stuhl, Y.-R. Tzeng, H. H. Alexander and P. J. Dagdigian, *J. Chem. Phys.*, **114**, (2001), 4479

99 B. Nizamov, P. J. Dagdigian, Y.-R. Tzeng and M. H. Alexander, *J. Chem. Phys.*, **115**, (2001), 800

100 C. D. Carter, J. M. Donbar and J. F. Driscoll, *Appl. Phys. B*, **66**, (1998), 129

101 K. A. Watson, K. M. Lyons, J. M. Donbar and C. D. Carter, *Combustion and Flame*, **123**, (2000), 252

102 J. M. Donbar, J. F. Driscoll and C. D. Carter, *Combustion and Flame*, **122**, (2000), 1

III EXPERIMENTAL

III-1 INTRODUCTION

This section will describe in detail the apparatus used to carry out this study. The experimental equipment must be able to perform several distinct tasks. CH, as a radical species, is highly reactive and must therefore be produced *in situ*, in this case by laser photolysis of bromoform ($CHBr_3$). It was necessary to subsequently excite the radicals to specific rovibronic (and fine-structure) parent levels and observe the collision-induced product levels under controlled conditions of known pressures of the collision partner. This was achieved using the established technique of laser-induced fluorescence (LIF) spectroscopy in a high-vacuum reaction chamber. The relatively short timescale (ranging from ns to μs) of collisional and fluorescence processes required the use of specialised electronics and computer software to gather data. A schematic diagram of the experimental apparatus is shown in Figure III.1

III-2 VACUUM SYSTEM AND GAS HANDLING

A cryo-baffled diffusion pump (Edwards Diffstak 100/300M) backed by a rotary pump (Edwards E2M8) was used to evacuate a stainless steel, six-way cross reaction chamber (Vacuum Generators UK Ltd.) to a typical base pressure of the order of 10^{-6} mbar. Pirani (Edwards PR10K) and ion (Vacuum Generators VIG 8) gauges were used to monitor the backing and absolute chamber pressures respectively, through a gauge controller (Vacuum Generators IGC 17F). Chamber pressures during the course of experiments were measured with two capacitance manometers (MKS Baratrons 627, 0-10 Torr and 127, 0-1 Torr). The photolysis and probe laser beams counter-propagated into the reaction chamber

EX BIBL. UNIV. EDINBURGH

through two quartz flats, mounted at Brewster's angle, and along arms fitted with baffles to reduce the amount of scattered laser light detected. The laser entrance windows were rotated 90° with respect to each other due to the orthogonal polarisations of the beams (see Section III-3 below). Regular cleaning of the windows was required to remove a dark residue that was deposited over time, most markedly on the photolysis laser entrance.

Flow of gases into the reaction chamber was controlled via a custom-made gas supply manifold. This enabled the flow of the quenching gases to be controlled and the preparation of mixtures of gases and their storage. Since the vapour pressure of $CHBr_3$ at room temperature is ~4.6 Torr, a steady flow of precursor in the pressure regime of interest was ensured by using a pre-prepared mixture of $CHBr_3$ and 30 Torr of Ar carrier gas. The pre-mixture was stored in a stainless steel reservoir (Whitey). A capacitance manometer (MKS Baratron 222, 0-100 Torr) was used to monitor the rate of loss of the pre-mixture and hence maintain the partial pressure of the precursor in the chamber. The manifold was designed such that the precursor mixture and the quenching gas could be independently flowed through an inlet in the top flange of the chamber, the rates being controlled by separate needle valves (Whitey SS 22RS4). In later stages, inlets adjacent to the laser entrance windows were used to admit the quenching gas reducing the deposition of the residue described above by ensuring a steady flow of gas towards the centre of the chamber. The $CHBr_3$ precursor was stored as a liquid in a stainless steel finger (Whitey) and was purified by repeated freeze-pump-thaw cycles. Quenching gases were used directly from the cylinders without further purification. The total pressure within the chamber was regulated using the butterfly valve to partially throttle the diffusion pump, the precursor mixture being set to 40 mTorr before the quencher gas was introduced at a sufficient flow rate to achieve the desired total pressure.

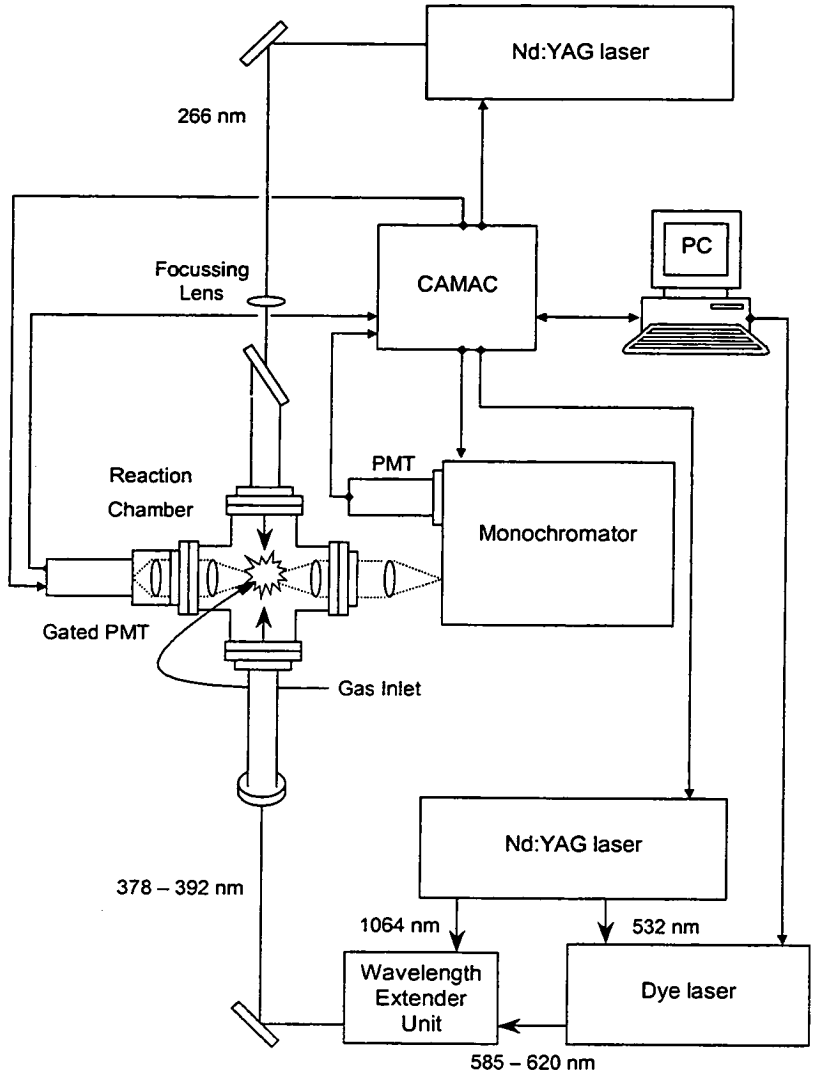

Figure III.1

Schematic diagram of the most commonly used experimental configuration. In later stages, a KrF excimer laser at 248 nm was used to photolyse and 355 nm light from a Nd:YAG was used to pump a dye laser to produce 420-440 nm probe light.

III-3 LASER SYSTEMS

III-3.1 Photolysis lasers

The mechanism for the ultraviolet photolysis of $CHBr_3$ is poorly understood, although it is clear that a multiphoton process is required on thermodynamic grounds. Mechanisms suggested [1, 2, 3] involve the sequential loss of Br atoms or the loss of a Br_2 molecule from a superexcited $CHBr_2^{**}$ radical. In either situation, the production of CH radicals in the $A^2\Delta$, $B^2\Sigma^-$ and $C^2\Sigma^+$ excited electronic states, as observed experimentally by large spontaneous fluorescence signals, requires the absorption of three photons at either 248 or 266 nm. The electronically excited CH is also vibrationally and rotationally hot. The fluorescence from the photolytically produced excited radicals must be allowed to decay prior to any subsequent state-selective excitation, hence a delay of a few μs was introduced between the firing of the photolysis laser and the probe laser.

Three different laser systems were used to photolyse $CHBr_3$ during the course of this work. In the early stages, a Nd:YAG laser (Spectron Laser Systems, SL803) configured to generate the fourth harmonic at 266 nm was used. This device was originally supplied as the pump laser for a dye laser system, which will be discussed in Section III-3.2 below. The laser consisted of independent oscillator and amplifier flashlamp-pumped Nd:YAG rods and the oscillator was equipped with a Pockels cell, polariser and λ/4 plate to provide Q-switching. The horizontally polarised fundamental output at 1064 nm gave a power output of ~1 J operating at a repetition rate of 10 Hz with a pulse duration of ~15 ns. The laser design enabled the use of up to two non-linear crystals, fitted in temperature-regulated housings, and hence the generation of the second, third and fourth harmonics at 532, 355 and 266 nm. Following 45° rotation of the fundamental beam polarisation, the use of a type II potassium dideuterium phthalate (KD*P) crystal enabled generation of the vertically polarised second harmonic 532 nm radiation which was subsequently doubled in frequency

again by the use of a type I KD*P crystal to generate the horizontally polarised 266 nm radiation required.

In practice, self-absorption within the second doubling crystal led to instability in the ultimate power achieved as a result of the induced temperature change in the crystal, varying the optimum phase-matching angle. In order to maintain reliable pulse energy, the second frequency doubling crystal was fitted within a wavelength extender unit (Spectron Laser Systems, SL4000D-FM4A), originally intended for use with the dye laser. Within the wavelength extender unit, the crystal could be angle tuned by a stepper motor controlled by a dedicated autotracker PC running custom software (Spectron Laser Systems, Auto2). By monitoring the power of a small fraction of the quadrupled beam with a photodiode, the PC was used to optimise the orientation of the crystal and provide typical, stable pulse energies of ~40 mJ. An assembly of two Pellin-Broca prisms within the wavelength extender unit separated the residual fundamental and second harmonic light from the 266 nm beam, which was then directed into the reaction chamber with a Pellin-Broca prism.

During later periods of the study, a Continuum Surelite II-10 Nd:YAG laser was used, also operating at 266 nm. This laser contained a single Nd:YAG rod, closely coupled with a linear flashlamp and was fitted with a Q-switch to produce short, high energy pulses. Fourth harmonic generation was achieved by initially frequency doubling the Nd:YAG fundamental with a type II KD*P crystal, and subsequently doubling the second harmonic with a β-barium borate (BBO) crystal. The advantage of this type of crystal was a greater stability in the 266 nm output power. Operationally, this meant that continual angle tuning of the crystal to optimise the phase-matching was not required as in the SL803 described above. Optimally, the Surelite produced horizontally polarised 266 nm laser radiation with pulse energies of ~80 mJ and pulse duration of ~5 ns. In practice, however, the delay between the firing of the flashlamp and the Q-switch was reduced to provide stable pulses of ~50 mJ typically, in order to minimise the rate of residue deposition on the windows and

prolong their usable lifetime. Wavelength separation to isolate the UV light was achieved in a small housing (Surelite Separation Package SSP-3) located outside the laser containing dichroic mirrors. The beam was steered into the reaction chamber by two Pellin-Broca prisms. Whilst photolysing at 266 nm, a spherical quartz lens (f = 50 cm) was used to mildly focus the beam near the centre of the chamber. This arrangement was found to noticeably enhance the LIF signal.

Latterly, a Lambda Physik COMPex 102 was used to provide 248 nm light, operating with a KrF gas mixture. This device was capable of delivering maximum pulse energies of ~300 mJ, although it was operated in "Energy Constant" mode, wherein the high voltage setting was automatically controlled to maintain pulse energies of ~150 mJ. Flowing the quenching gas in adjacent to the laser entrance windows significantly lengthened the window lifetime, allowing the use of higher pulse energies with the excimer laser. The non-polarised, divergent beam was collimated using a combination of positive and negative cylindrical quartz lenses before being directed into the reaction chamber using high reflectivity mirrors. As with 266 nm photolysis, mild focussing using a spherical quartz lens (f = 1 m) was found, to enhance the LIF signal. The system was equipped with a halogen generator module eliminating the need for external halogen cylinders.

III-3.2 Probe lasers

The technique of LIF requires the use of a tuneable source of laser radiation. To this end, two very similar pulsed Nd:YAG-pumped dye laser systems operating in different spectral regions were used for different phases of the work.

The probe laser system used for the majority of this study was supplied by Spectron Laser Systems, and consisted of a Q-switched Nd:YAG pump laser (SL803S), a dye laser unit (SL400G) and a wavelength extender unit (SL400EX). Mixing the fundamental dye laser output with the residual fundamental output of the Nd:YAG laser

generated light of the required wavelength in the near UV. The Nd:YAG laser was essentially identical to the SL803 described in section 3.3.1, configured to produce 532 nm light with typical pulse energies of ~300 mJ.

The lasing action of the dye laser is rooted in the oscillator cavity, with the total output power enhanced (if required) by two longitudinally pumped amplifier dye cells. The oscillator consists of a transversely pumped dye cell, a prism beam expander, a holographic grating, a tuning mirror mounted on a sine drive and an output coupler. The scanning of the tuning mirror and hence of the fundamental output wavelength was controlled *via* a scan controller unit (Spectron Laser Systems, SL4000SC), interfaced to the central control PC through a RS-232 serial connection. The arrangement of the oscillator cavity resulted in horizontally polarised light.

The dye solution provides the gain medium for the laser. A mixture of Rhodamine 610 (Rhodamine B) and Rhodamine 640 (Rhodamine 101) dissolved in methanol (HPLC grade), with ratios adjusted to provide a peak in the gain curve at the desired wavelength, was used. These solutions were constantly circulated through the cuvettes. The fundamental output from the dye laser typically spanned the range 585 – 620 nm and was subsequently mixed with the 1064 nm radiation from the Nd:YAG laser. This mixing process took place in a type II KD*P crystal to produce vertically polarised light in the near UV, tuneable over the range 378 – 392 nm, with maximum pulse energies of ~20 mJ and a linewidth of 0.4 cm^{-1}. The mixing crystal housing in the wavelength extender unit was temperature-controlled and fitted with a quartz compensating block to correct for any deviation in the beam path caused by the angle tuning of the crystal. A small fraction of the mixed beam was detected by a photodiode to monitor the power which allowed an autotracker unit (Spectron Laser Systems, SL400) connected to a BBC microcomputer running custom software to angle tune the crystal to ensure that optimum phase-matching was achieved. Two dichroic mirrors, coated to be highly reflecting in the UV, separated the

frequency-mixed output from the residual fundamental outputs of the dye and the Nd:YAG lasers. The beam was directed into the reaction chamber and spatially overlapped with the photolysis beam using quartz prisms.

The second dye laser system employed consisted of the Nd:YAG laser (SL803) described previously in Section III-3.1configured to produce a pump beam at 355 nm and a dye laser unit (Spectron Laser Systems, SL4000). The Nd:YAG pump laser used a type I KD*P frequency doubling crystal to generate vertically polarised 532 nm radiation that was subsequently mixed with the 1064 nm fundamental to produce the horizontally polarised third harmonic in a type II KD*P crystal with typical pulse energies of ~160 mJ. Operation utilising 355 nm pumping required that the dye laser oscillator and amplifier cells be transversely pumped. The oscillator cavity was essentially the same as in the SL4000G described above but contained the option to include an intra-cavity etalon for narrow linewidth operation, although this option was not used. The tuning mirror was controlled in this laser by a dedicated PC, running custom software (Spectron Laser Systems, Autotracker Version 8.10) *via* an AT101 scan controller rather than directly via the control PC.

The dye used in this laser system was a solution of Stilbene 420 in methanol (HPLC grade). The fundamental output of this dye spanned the region 420 – 440 nm, with typical maximum pulse energies of ~12 mJ.

III-4 FLUORESCENCE RESOLUTION AND DETECTION

Neglecting any effects caused by the polarisation of the probe laser and owing to the isotropic nature of the gas mixture, laser-induced fluorescence is emitted evenly in all directions. As shown in Figure III.1, the fluorescence was collected perpendicular to the direction of propagation of the laser beams in both directions and ultimately detected by two photomultiplier tubes (PMTs). By positioning two plano-convex quartz lenses at distances

equal to their focal lengths from the region in which the photolysis and probe laser beams were overlapped, the maximum number of emitted photons could be collected and collimated.

In one direction the transmitted fluorescence was focussed into a 1 m monochromator (Hilger and Watts, Monospek 1000 D400) by a second quartz lens chosen to match the device's effective *f*-number (~7). In this way, the grating of the monochromator should have been completely filled, maximising the resolution and the number of photons transmitted to the detector. Wavelength dispersion of the laser-induced fluorescence was achieved using this instrument, which used a 1200 groove mm^{-1} grating mounted in the Czerny-Turner configuration. Scanning of the wavelength was performed by a stepper motor (Hytec, KS 500, 0.72° per step) retro-fitted to the manual drive and controlled by a Hytec SMC 1066 stepper motor drive system. The spectral resolution of the monochromator was determined by the width of the entrance and exit slits. The wavelength-resolved light was detected by a PMT (EMI 9789QB, power supply EMI PM28B) supplied with quartz windows. This PMT features a 10 mm effective diameter CsSb photocathode with the Venetian blind arrangement of 13 dynodes, giving high sensitivity and low dark current.

In the opposite direction, wavelength discrimination was accomplished by means of a wide bandpass interference filter (FWHM 10 nm) centred on the band of interest. Since the fluorescence emitted on a give vibronic band is directly proportional to the total excited state population, measuring the intensity of the laser-induced fluorescence through the interference filter provided a means of normalising the signal during dispersed fluorescence measurements with respect to any fluctuations in the power of either the photolysis or probe lasers, the overlap of the beams, or the excitation laser wavelength. The transmitted fluorescence was detected by means of a gated PMT (EMI 9813QB, gating circuit GB1B, power supply Stanford Research Systems Model PS350). As described in Section III-3.1, the photolysis process produced electronically excited CH radicals that were allowed to

spontaneously emit before the excitation step takes place. When viewed through the interference filter, this spontaneous signal could be many times larger than the laser-induced fluorescence signal. The gating circuit enabled the PMT to be switched on for the duration of a switching pulse only. In this way, careful timing of the pulse meant that the PMT could remain effectively switched off during the spontaneous photolysis signal enabling the desired laser-induced fluorescence signal to be detected without prior saturation of the PMT. PMT output signals were amplified ×5 or ×25 prior to digitising by a Stanford Research Systems 240 unit.

III-5 DATA ACQUISITION AND EXPERIMENTAL CONTROL

Experimental timing and control and signal processing were achieved in the most part by various modules incorporated in a CAMAC (Computer Aided Monitoring And Control, IEEE-583) system (DSP optima 860 crate, DSP 6001 crate controller module) coupled to a dedicated control PC *via* an interface card (DSP PC6004). Communication between the PC and the CAMAC apparatus was achieved by the use of custom-written software previously developed in this laboratory [4], 'IO'.

The experimental timing sequence was controlled by a LeCroy 4222 Pulse Delay Generator (PDG), programmable in IO over the CAMAC system, although the overall 10 Hz repetition rate was maintained by the control PC. The LeCroy 4222 was capable of producing four completely independent, positive-going 5 V pulses of 100 ns duration, up to a maximum delay of 16.7 ms in 1 ns increments with very low jitter. Since these pulses are incompatible with the trigger logic of the lasers, a custom-made line driver module was used to provide pulses of the correct amplitude and duration with the same relative delays. As both lasers used for the majority of this work required two trigger pulses (flashlamp and Q-switch in the Nd:YAG systems), all available channels on the PDG were occupied. Hence,

some pulses were also used to trigger other devices, most importantly a Farnell PDG (PG102), which provided a further two independent channels, the uses of which will be discussed later.

The amplified analogue signal from the PMT mounted on the monochromator was digitised by the use of a 100 MHz transient digitiser (DSP 2001A) with a minimum sample interval of 10 ns. The module continuously digitises and stores data until it receives a trigger pulse (typically synchronously with the Q-switch of the photolysis laser) forcing it to output data to the PC. The sampling interval and record length were controlled from within IO. The gated PMT received a switching pulse from the Farnell PDG, timed to coincide with the laser-induced fluorescence signal. The analogue output was integrated over a 100 ns gate, set just after the probe laser fired, using a Stanford Research Systems, SR250 Gated Integrator and Boxcar Averager. The last sample averaged output was digitised by one of the four channels of an analogue to digital converter (Hytec ADC 520), triggered by the remaining channel on the Farnell PDG. It was recorded by IO for signal normalisation during dispersed fluorescence measurements. Similarly, a pyroelectric joulemeter (Molectron, J3-09DW) or a custom-built photodiode could be used to sample a small part of the probe beam during excitation scans to normalise the signal. The timing sequence is summarised schematically in Figure III.2.

The IO interface controlled the wavelength stepping of the monochromator in recording dispersed fluorescence spectra. In addition, IO was used to control the scanning of the dye laser wavelength while using the 532 nm-pumped SL400G laser to record excitation spectra. While using the 355 nm-pumped SL4000 dye laser, scanning of the wavelength was carried out by an independent PC as described in Section III-3.2 above. Approximate synchronisation was achieved by using a Stanford Research Systems Model DG535 Digital Delay/Pulse Generator to produce a trigger pulse instructing the dye laser to step after the required number of shots had been averaged in IO. This arrangement, while not providing

complete synchronisation, was found to provide very satisfactory results with the wavelength deviation between the PC's being of the order of only ~0.05 %. Integration of the fluorescence signal was carried out in IO with the useful feature of being able to set up multiple temporal gates, enabling the time dependence of the signal to be observed during dispersed fluorescence measurements. Other features of the IO software utilised in the course of this work were the ability to record spectra with multiple delay sets, which allowed any contribution from the photolytically produced fluorescence to be subtracted from the desired probe-induced signal, and a facility to average and save time-resolved fluorescence decay traces.

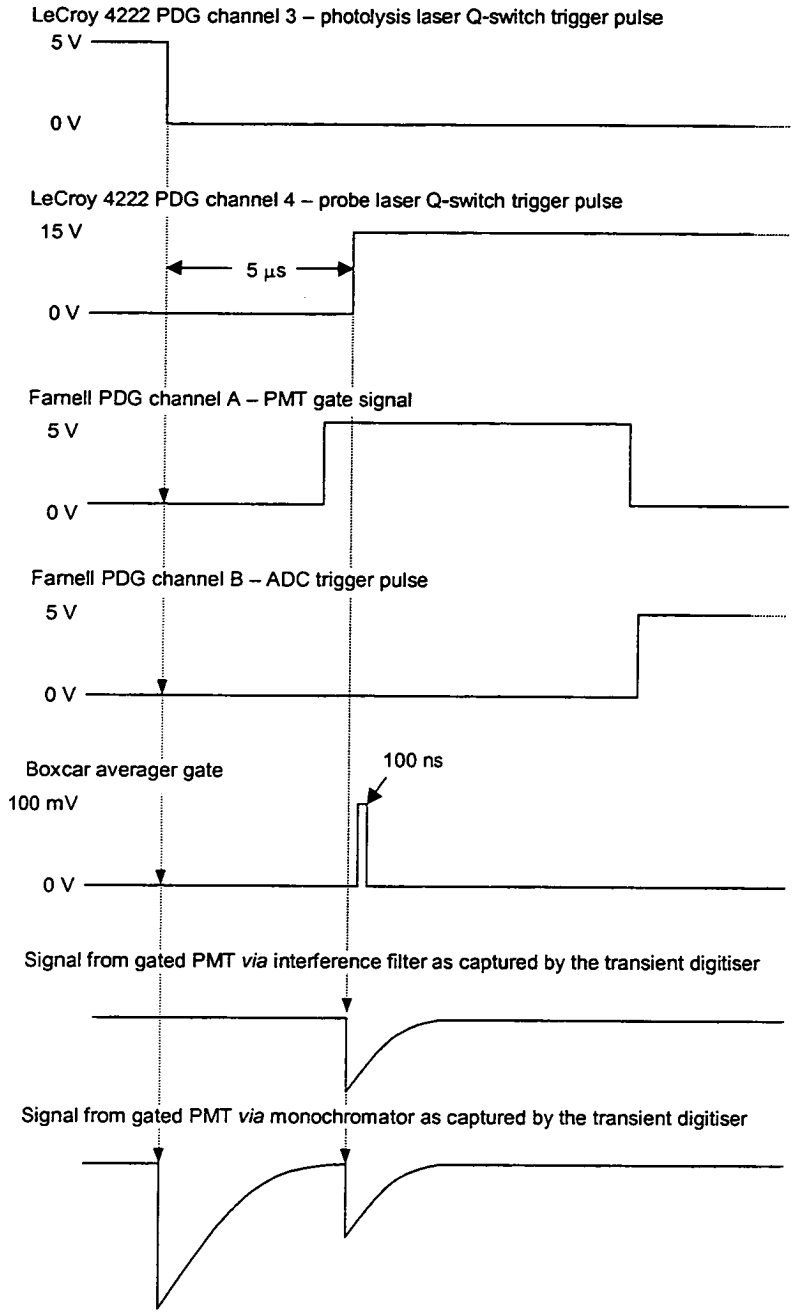

Figure III.2

The typical experimental timing sequence. Pulses to fire the Nd:YAG laser flashlamps preceded the Q-switch pulses by ~200 μs and are not shown.

III-6 REFERENCES

1 D.A. Lichtin, M. R. Berman and M. C. Lin, *Chem. Phys. Lett.*. **108**, (1984), 18

2 C. Chen, Q. Ran, S. Yu and X. Ma, *Chem. Phys. Lett.*, **203**, (1993), 307

3 J. Lindner, K Ermisch and R. Wilhelm, *Chem. Phys.*, **238**, (1998), 329

4 G. Maitland, PhD Thesis, University of Edinburgh, 1993

IV VIBRATIONALLY-RESOLVED ELECTRONIC ENERGY TRANSFER

IV-1 INTRODUCTION

This chapter presents results demonstrating the collisional coupling of the $A^2\Delta$ and $B^2\Sigma^-$ states of the CH radical and describes the kinetic modelling of the energy transfer processes in this system at vibrational resolution. Previously, electronic energy transfer between these electronic states had only been observed in flames [1, 2], conditions under which a variety of collision partners are present. Earlier work in this laboratory [3] had established that CO_2 was efficient at inducing interconversion of the $A^2\Delta$ and $B^2\Sigma^-$ states. It also reacts relatively slowly with the ground state [4], which minimises the loss of ground state radicals during the delay between the photolysis and probe lasers firing. In this chapter, CO_2 is used exclusively as the collision partner.

Tuneable laser radiation was used to selectively excite ground state CH radicals to the $A^2\Delta$, $v = 1$ and $B^2\Sigma^-$, $v = 0$ vibrational levels, which are nearly isoenergetic, and the resulting fluorescence from both the initially pumped and collisionally populated states was resolved in a time- and wavelength-resolved manner. It will be shown in this chapter that analysis of time-resolved decay traces alone is insufficient to obtain reliable microscopic rate constants for collisional processes which transfer population between the $A^2\Delta$ and $B^2\Sigma^-$ states of the CH radical. Inclusion of ratios of the total integrated fluorescence from the initially prepared and collisionally produced levels is required.

IV-2 EXCITATION SPECTRA

An essential preliminary part of this work was to identify transitions which would enable specific rotational levels of the $A^2\Delta$, $v = 1$ and $B^2\Sigma^-$, $v = 0$ levels to be populated cleanly. It is desirable to choose transitions that are both isolated, that is, will result in population being excited only to specific rotational and/or fine-structure levels, and which are also strong in absorption. Obviously, the rotational levels which are accessible and which bands can be used are ultimately determined by the population distribution in the ground state. It should be noted that the highly diagonal nature of the CH electronic band systems is an important factor in selecting suitable transitions as will be discussed later in this chapter. Table IV.1 and Table IV.2 show the Franck-Condon Factors and band origins for the A-X and B-X bands of relevance to this work.

Table IV.1

Franck-Condon factors for the A-X and B-X band systems of the CH radical taken from references 7 and 8.

		$A^2\Delta - X^2\Pi$			$B^2\Sigma^- - X^2\Pi$
v''	v'	0	1	2	0
0		0.9913	8.5223×10^{-3}	–	0.8768
1		8.0100×10^{-3}	0.9802	1.0356×10^{-2}	0.1036
2		–	9.4111×10^{-3}	0.9808	1.6723×10^{-2}

IV-2.1 Excitation to $B^2\Sigma^-$, $v = 0$

An obvious choice for excitation to the $B^2\Sigma^-$, $v = 0$ state is the B-X(0,0) band at ~ 390 nm since the majority of the ground state population resides in the $v = 0$ level and the

band is rather diagonal, carrying most of the transition probability (see Table IV.1). A relatively low-power excitation spectrum of the R-branch of this band, in which the transitions are indicated, is shown in Figure IV.1.

Table IV.2

Band origins, in nm, of the A-X and B-X band systems of the CH radical [5].

		$A^2\Delta - X^2\Pi$			$B^2\Sigma^- - X^2\Pi$
v''	v'	0	1	2	0
0		431.4	385.8	–	388.8
1		489.1	431.3	388.4	435.0
2		–	485.8	432.1	490.9

Additional features appear in this spectral region when higher probe laser powers are used. These additional lines have been successfully assigned to very weak $\Delta v = +1$, off-diagonal bands of the A-X system. These A-X(1,0) and A-X(2,1) bands lie slightly to the blue and red of the B-X(0,0) band, respectively. The presence of the A-X(2,1) band obviously indicates that vibrationally excited $CH(X^2\Pi)$ survives on the time scale of the experiment, typically ~5 μs.

The presence of the off-diagonal A-X bands underlying the B-X(0,0) diagonal band clearly requires that care be taken in selecting transitions for excitation to the $B^2\Sigma^-$ state, especially in studies of the electronic energy transfer between the $A^2\Delta$ and $B^2\Sigma^-$ states. The B-X(0,0) $^RR_{11}(N''= 3)$ line is suitably isolated and has been used throughout the work described in this chapter.

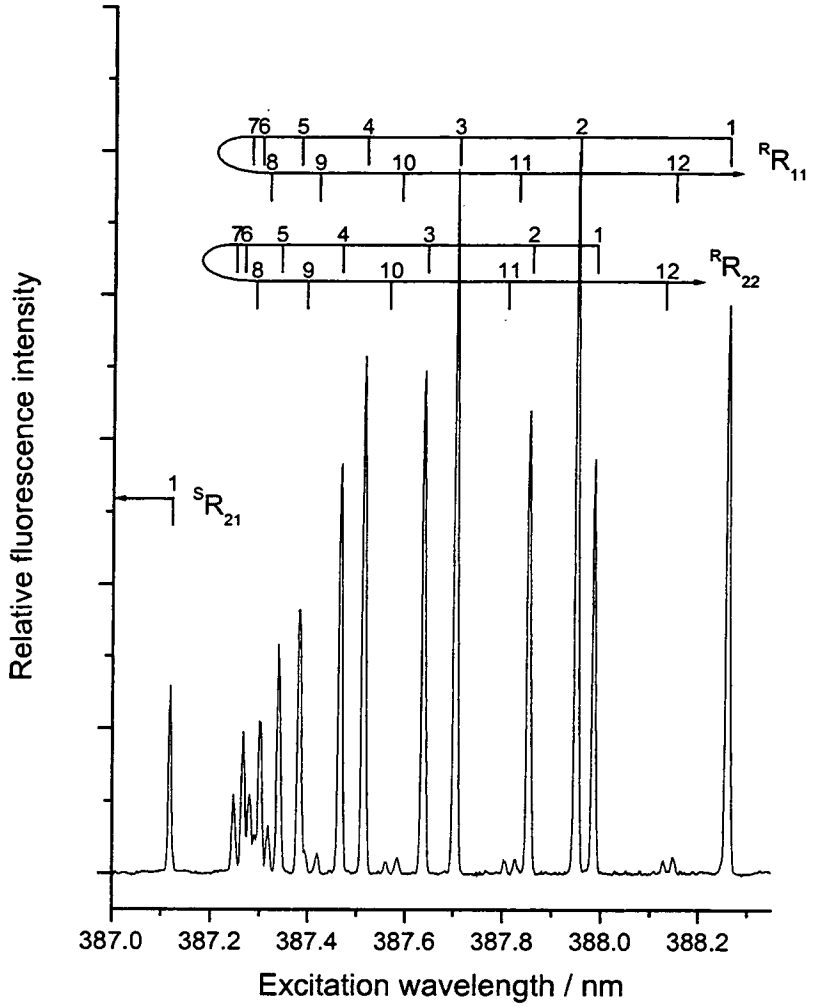

Figure IV.1

Relatively low-power LIF excitation spectrum of the B-X(0,0) R-branch of the CH radical. CH radicals were produced by UV multiphoton photolysis of $CHBr_3$ in the presence of ~1 Torr CO_2 with a photolysis – probe delay of 5 μs. Probe laser pulse energy ~0.5 mJ resulting in a partially saturated spectrum. Fluorescence observed using monochromator set at 388.8 nm.

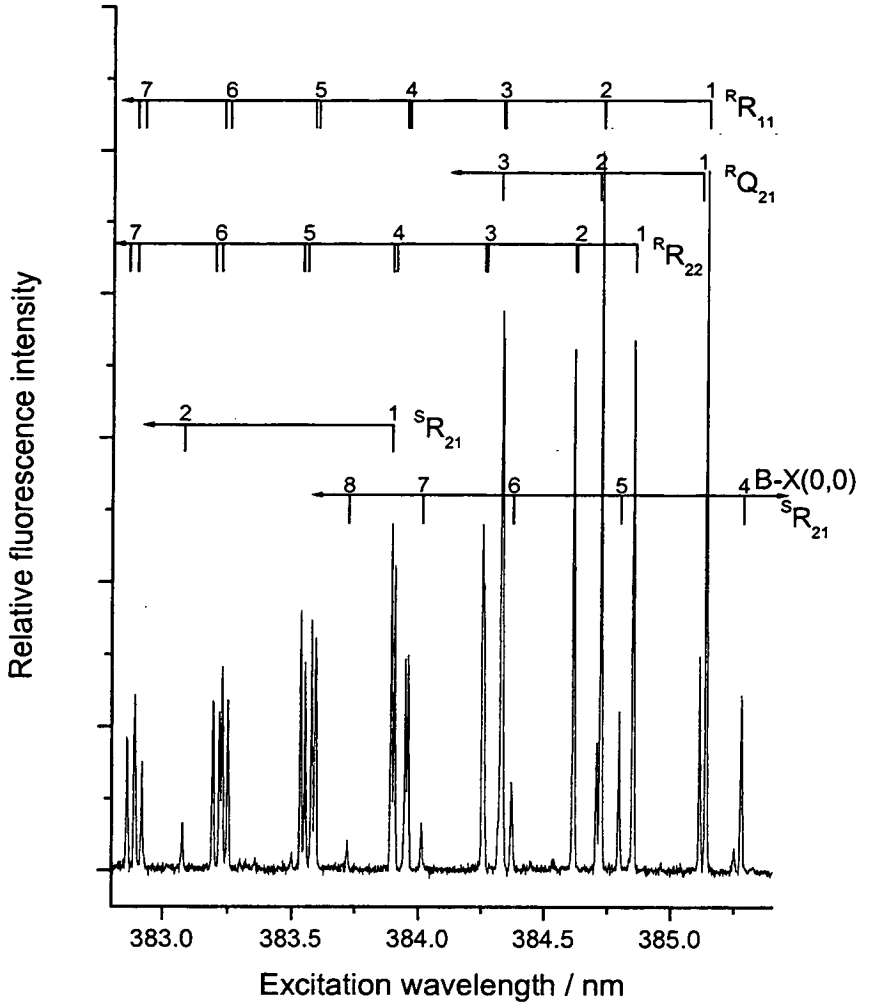

Figure IV.2

Relatively high-power LIF excitation spectrum of a section of the A-X(1,0) R-branch. CH radicals produced by UV multiphoton photolysis of $CHBr_3$ in the presence of ~1 Torr CO_2 with a photolysis – probe delay of 5 μs. Probe laser pulse energy ~15 mJ. Fluorescence observed using monochromator centred at 431.4 nm.

IV-2.2 Excitation to $A^2\Delta$, $v = 1$

The accidental clustering of the B-X(0,0), A-X(1,0) and (2,1) bands can be advantageous, however, since it provides a means of producing $A^2\Delta$ and $B^2\Sigma^-$ state CH radicals with probe laser wavelengths in the same spectral region. The R-branch of the A-X(1,0) band is spectrally isolated and can be used to state-selectively excite to $A^2\Delta$, $v = 1$. Part of this branch is shown in Figure IV.2. As mentioned previously, the highly diagonal nature of the A-X band system results in the A-X(1,0) carrying only a very small fraction of the transition probability. It is therefore necessary to use much higher laser pulse energies than for $B^2\Sigma^-$, $v = 0$ to excite a comparable amount of population to the $A^2\Delta$, $v = 1$.

In this chapter, the A-X(1,0) $^RR_{11}(N' = 1)$ line has been used throughout. It should be noted however, that as a result of the Λ-doubling of the $A^2\Delta$ state, both the *e* and *f* components of the $N = 2$ level are populated by pumping the unresolved $^RR_{11ee}(1)$ and $^RR_{11ff}(1)$ lines.

IV-3 DISPERSED FLUORESCENCE SPECTRA

A series of dispersed fluorescence spectra were recorded following initial excitation of the $A^2\Delta$, $v = 1$ and the $B^2\Sigma^-$, $v = 0$ levels at room temperature (~295 K). These measurements confirm conclusively that the $A^2\Delta$ and $B^2\Sigma^-$ states are coupled as a result of collisions with CO_2.

IV-3.1 The diagonal bands

Low-resolution (bandwidth ~0.9 nm) dispersed fluorescence spectra of the A-X($\Delta v = 0$) and B-X(0,0) diagonal bands were obtained by scanning the monochromator with

the probe laser fixed to excite to the $A^2\Delta$, $v = 1$ or $B^2\Sigma^-$, $v = 0$ level. The fluorescence was integrated over the whole of the time-resolved waveform. The spectra were normalised by simultaneously measuring undispersed fluorescence from the pumped level on its diagonal band through an interference filter (A-X, centred at 431.7 nm, FWHM 8 nm or B-X, centred at 390.9 nm, FWHM 10 nm). This provided a correction for any fluctuations in the experimental conditions experienced during the course of the scan.

Dispersed fluorescence spectra over the A-X and B-X diagonal bands following initial excitation to $A^2\Delta$, $v = 1$ on the $R_1(1)$ line are shown in Figure IV.3. The directly returning A-X(1,1) band at ~431 nm accounts for essentially all of the emission from the initially pumped level. The diagonal nature of the $A^2\Delta - X^2\Pi$ system also means that the (0,0) and (1,1) bands cannot be resolved at this experimental bandwidth preventing the identification of any vibrationally relaxed $A^2\Delta$ state emission. The band observed at ~390 nm can be assigned unambiguously as B-X(0,0) emission only. The A-X(1,0) band which is also found in this region of the CH emission spectrum as described above can be safely neglected. It is almost vanishingly weak in emission, with a Franck-Condon Factor three orders of magnitude smaller than the (1,1) band, as can be seen in Table IV.1. The B-X(1,1) band which lies to the high wavelength side of the B-X(0,0) band cannot be expected as a product level by energy conservation and is not seen in the spectra.

Figure IV.3 clearly shows that as the pressure of the CO_2 collision partner is increased, the amount of fluorescence detected on the B-X(0,0) band increases, proving that collisions transfer population from the initially populated $A^2\Delta$, $v = 1$ level to $B^2\Sigma^-$, $v = 0$.

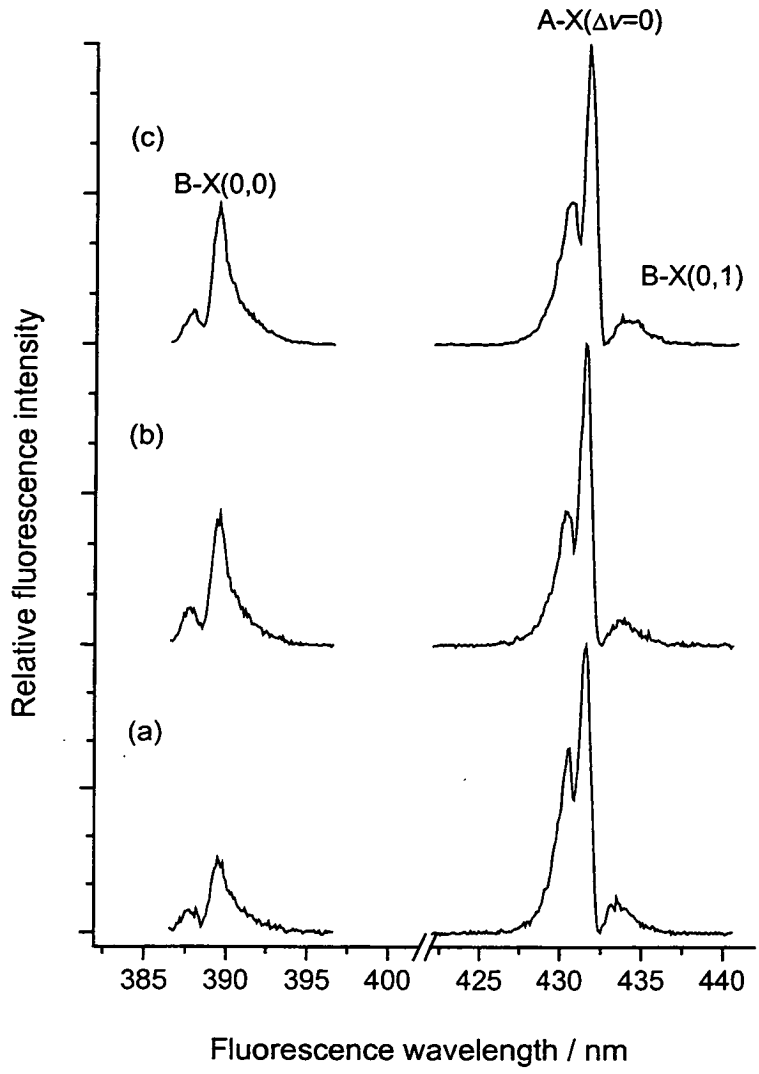

Figure IV.3

Dispersed fluorescence spectra on the CH B-X(0,0) and A-X(Δv = 0) bands following excitation on the $R_1(1)$ line of the A-X(1,0) band. The panels show the spectra recorded at CO_2 pressures of (a) 1.23 Torr, (b) 4.07 Torr, and (c) 6.15 Torr using an experimental bandwidth of 0.93 nm. Signals have been scaled to the peak of the A-X(Δv = 0) band at each pressure.

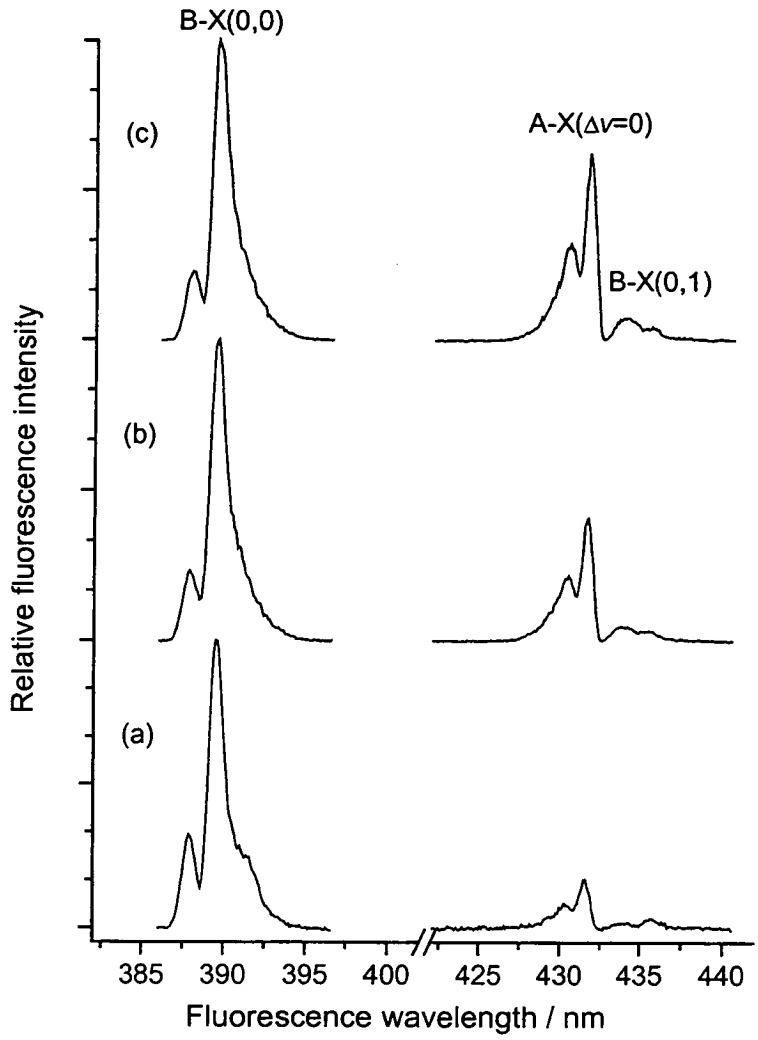

Figure IV.4

Dispersed fluorescence spectra on the CH B-X(0,0) and A-X(Δv = 0) bands following excitation on the $R_1(3)$ line of the B-X(0,0) band. The panels show the spectra recorded at CO_2 pressures of (a) 1.24 Torr, (b) 4.08 Torr, and (c) 6.07 Torr using an experimental bandwidth of 0.93 nm. Signals have been scaled to the peak of the B-X(0,0) band at each pressure.

Corresponding dispersed fluorescence spectra recorded following initial excitation to $B^2\Sigma^-$, $v = 0$ on the $R_1(3)$ line are shown in Figure IV.4. The magnitude of the collisionally populated $A^2\Delta$ state emission can be seen to increase as the pressure of CO_2 is increased. As was the case for initial excitation of $A^2\Delta$, $v = 1$, the A-X (0,0) and (1,1) diagonal bands cannot be resolved and there is no means of determining from these measurements whether either or both of these bands are responsible for the collisionally produced fluorescence. The B-X(0,1) band is also visible in these spectra, underlying the P-branch of the A-X($\Delta v = 0$) emission. The $B^2\Sigma^- - X^2\Pi$ system is marginally less diagonal than the $A^2\Delta - X^2\Pi$, and as a result, the B-X(0,1) band does have some intensity in emission.

The total integrated fluorescence ratios from the collisionally produced state to the initially populated state (I_A/I_B or I_B/I_A, depending on which level was originally populated) are shown as a function of CO_2 pressure in Figure IV.5. Emission on the $A^2\Delta - X^2\Pi$ diagonal bands can be safely assumed to account for all the emission from the $A^2\Delta$ state, as discussed previously and that emission on the B-X(0,0) band is free from contamination from the A-X(1,0) band. The inability to resolve the (0,0) and (1,1) bands means that only the total integrated fluorescence from the $A^2\Delta$ state, I_A, can be measured, however. The means by which the branching between the $v = 0$ and $v = 1$ levels of the $A^2\Delta$ state can be discerned will be discussed in the next section. Since emission on the B-X(0,1) band is included in the A-X spectra, its contribution has been subtracted from the total integrated fluorescence from the $A^2\Delta$ state, based on previously measured relative transition probabilities [6]. The ratios displayed in Figure IV.5 are thus those of the total emission from the collisionally populated state to the initially populated state, without vibrational level discrimination. Figure IV.5 clearly shows that there is a rather linear increase in I_A/I_B following excitation to $B^2\Sigma^-$, $v = 0$, while the I_B/I_A ratio following excitation to $A^2\Delta$, $v = 1$ rises more sharply but shows greater curvature. Qualitatively, this is because of vibrational

relaxation within the $A^2\Delta$ state, as will be demonstrated more quantitatively through kinetic modelling below.

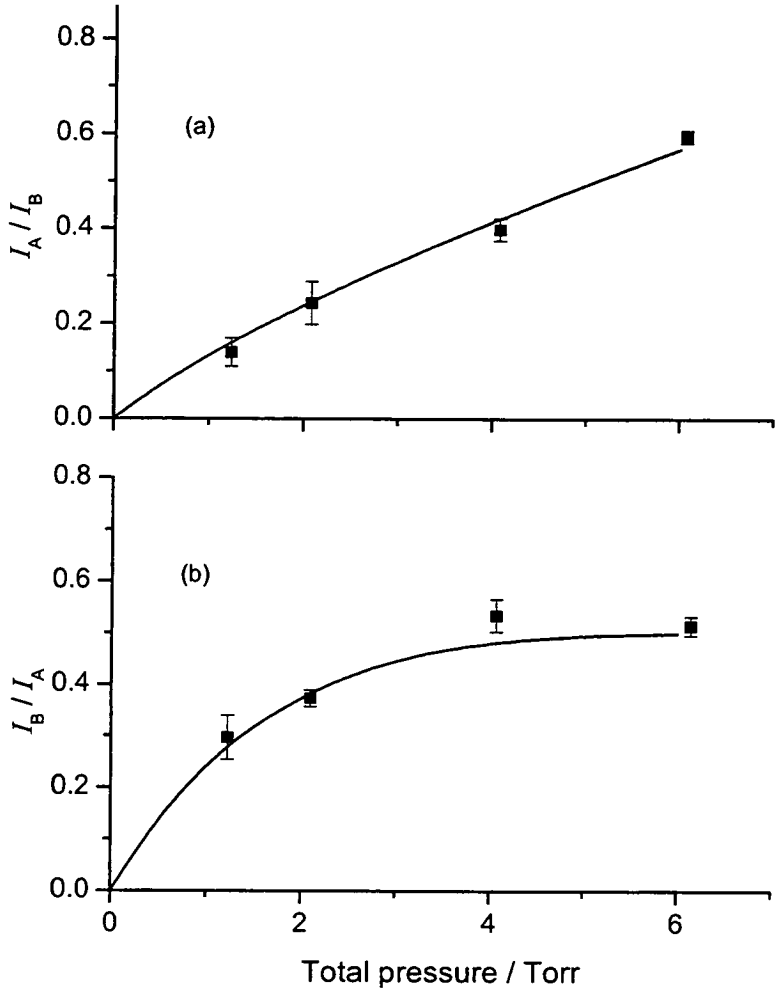

Figure IV.5

Variation with CO_2 pressure of product : initial state ratios of integrated signal on the A-X (I_A) and B-X (I_B) diagonal bands. Initial excitation of (a) $B^2\Sigma^-$, $v = 0$ and (b) $A^2\Delta$, $v = 1$. Each panel shows the experimental results (■) with error bars (1σ) estimated from variations in repeated measurements; solid lines are the predictions of the four-level kinetic model described in the text.

The data displayed in Figure IV.5 do however, closely reflect true relative emission intensities since the diagonal B-X(0,0) and the A-X(0,0) and (1,1) bands carry the vast majority of the transition probability. Corrections would amount to, at most, a few percent, and have therefore been neglected. A further factor which must be considered, in principle, is the relative detection sensitivity of the apparatus, due mostly to the monochromator transmission and the PMT response, at ~390 nm and ~430 nm. This was investigated using a calibrated standard lamp and was not found to vary more than a few percent over the wavelength range of interest. Hence, the detection sensitivity was assumed to be constant with wavelength and no corrections to the signal intensities were made.

IV-3.2 The off-diagonal bands

As described above, dispersed fluorescence spectra recorded over the A-X(0,0) and (1,1) bands cannot be used to determine the relative populations in the $A^2\Delta$, $v = 0$ and $A^2\Delta$, $v = 1$ levels as the bands are unresolved. To determine the branching between these levels, two further series of dispersed fluorescence spectra were recorded, observing in this case the off-diagonal A-X(0,1) and (1,2) bands found at ~490 nm. Transition probabilities on these off-diagonal bands are approximately two orders of magnitude smaller than the diagonal bands, which clearly results in reduced signal-to-noise. The B-X(0,2) band, which also happens to fall in this spectral region, is a further order of magnitude weaker.

Typical spectra can be seen in Figure IV.6 and Figure IV.7 recorded with varying pressures of CO_2 after excitation to $A^2\Delta$, $v = 1$ and $B^2\Sigma^-$, $v = 0$ respectively. In the case of initial excitation of $B^2\Sigma^-$, $v = 0$ (Figure IV.7), with increasing CO_2 pressure, the collisionally produced A-X(0,1) and (1,2) bands can be seen to grow in at the expense of the directly returning B-X(0,2) band. It should be noted, however, that the A-X(0,1) band is present even at low pressures. In the reciprocal experiment in which the $A^2\Delta$, $v = 1$ level is initially

populated, the A-X(0,1) band can be seen (Figure IV.6) to increase in size relative to A-X(1,2), suggesting that vibrational relaxation occurs at a rate comparable to other processes.

Quantitative measurements of the relative intensities of each band were obtained by carrying out an iterative simulation procedure and decomposing the recorded spectrum into the respective contributions from the A-X(0,1) and (1,2) and B-X(0,2) bands. Rotational line positions and transition probabilities were calculated from the molecular constants [7, 8] using a computer program, based around the work of Zare *et al.* [9] and subsequently convoluted with the instrumental bandwidth and the rotational population distribution as has previously been described in Chapter II. The rotational population distribution was adjusted manually to give the best agreement with the experimental spectra. Assumed initial conditions were that collisionally populated vibrational levels had a room temperature (~295 K) Boltzmann distribution over the rotational levels while the initially prepared level had a distribution which was sharply peaked in the initially pumped rotational level. Broadening the distribution over more rotational levels in the initially pumped level was found to have a more beneficial effect on the quality of the fit than adjusting the collisionally populated levels. Rotationally resolved spectra recorded later, which will be discussed in Chapter V, were found to be qualitatively consistent with the population distributions assumed for the low-resolution spectra.

The total integrated fluorescence from each vibrational level was then corrected for the relative transition probabilities of the A-X(0,1) and (1,2) bands [10]. The result can conveniently be thought of as a measure of the total population that has emitted from a given level, since the radiative lifetimes of the $v = 0$ and 1 levels of the $A^2\Delta$ state are almost identical [10, 11]. The resulting ratios of $A^2\Delta$, $v = 0$ to $A^2\Delta$, $v = 1$ emission, I_{A0}/I_{A1}, can be plotted as a function of CO_2 pressure, as shown in Figure IV.8. There is a moderately large systematic uncertainty in these ratios caused by the uncertainties in the independently

measured bandstrengths [10], indicated by the error bars in Figure IV.8. This is considered to be significantly larger than any statistical uncertainties in the results.

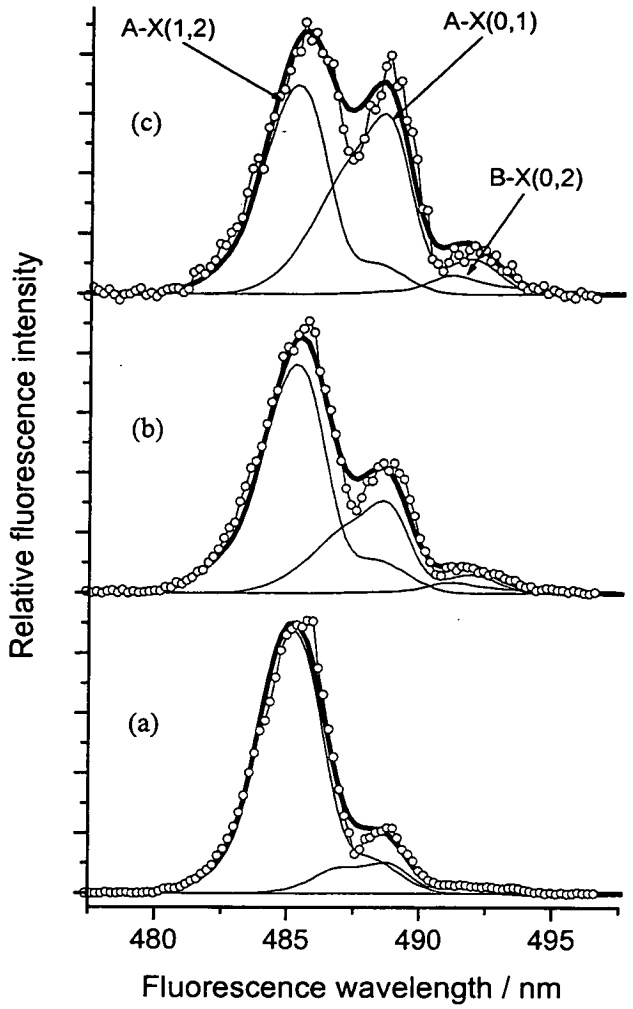

Figure IV.6

Dispersed fluorescence spectra on the A-X(1,2) and (0,1) and B-X(0,2) off-diagonal bands following excitation on the $R_1(1)$ line of the A-X(1,0) band. The panels show the spectra recorded at CO_2 pressures of (a) 1.04 Torr, (b) 3.98 Torr, and (c) 8.02 Torr using an experimental bandwidth of 1.86 nm. Experimental points are shown by (o); fine lines are the best-fit decompositions into component bands; bold lines are the sum of the best-fit components. Signals have been scaled to the peak of the A-X(1,2) band at each pressure.

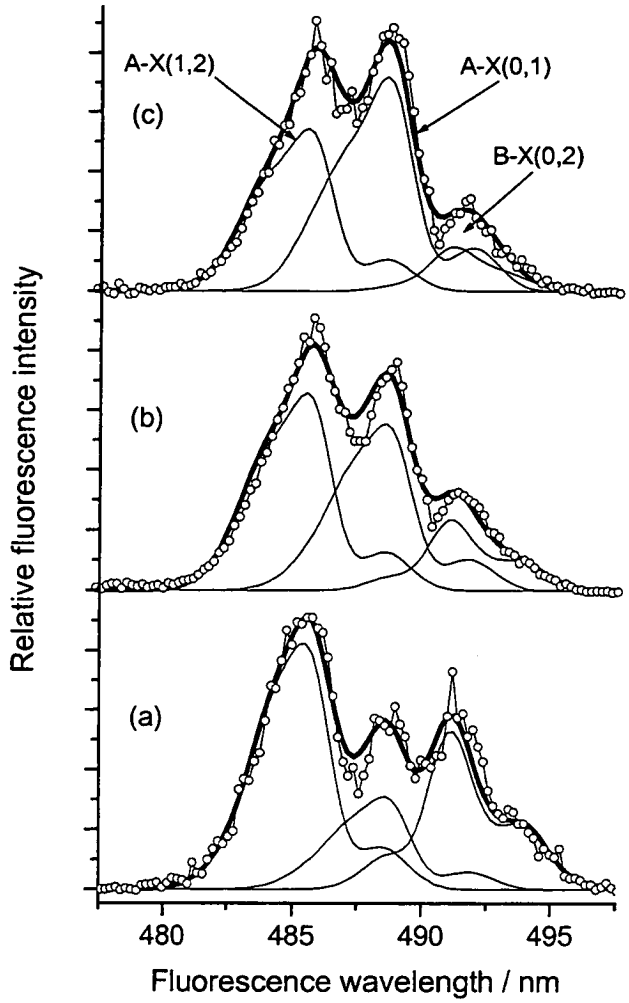

Figure IV.7

Dispersed fluorescence spectra on the A-X(1,2) and (0,1) and B-X(0,2) off-diagonal bands following excitation on the $R_1(3)$ line of the B-X(0,0) band. The panels show the spectra recorded at CO_2 pressures of (a) 1.06 Torr, (b) 4.03 Torr, and (c) 8.13 Torr using an experimental bandwidth of 1.86 nm. Experimental points are shown by (○); fine lines are the best-fit decompositions into component bands; bold lines are the sum of the best-fit components. Signals have been scaled to the peak of the A-X(1,2) band at each pressure.

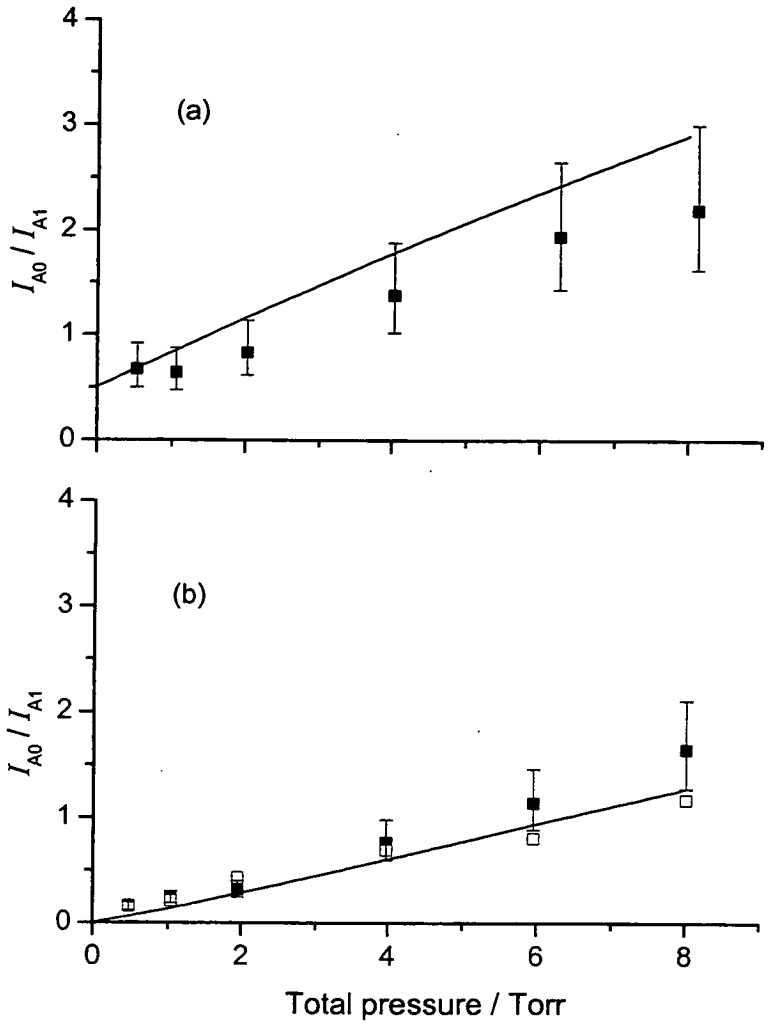

Figure IV.8

Variation with CO_2 pressure of the ratio of integrated emission intensities, I_{A0}/I_{A1}, from the $A^2\Delta$, $v = 0$ and 1 levels. Initial excitation of (a) $B^2\Sigma^-$, $v = 0$ and (b) $A^2\Delta$, $v = 1$. The panels show the experimental measurements (■) on the off-diagonal bands, corrected for the relative transition probabilities of the A-X(1,2) and (0,1) bands; from integration of the waveforms (□); solid lines are the predictions of the model. Error bars indicate the systematic uncertainty in the correction factor.

After initial excitation to $A^2\Delta$, $v = 1$, the ratio I_{A0}/I_{A1} starts from the origin and increases approximately linearly with CO_2 pressure. The slope is mainly determined by the rate of vibrational relaxation from $A^2\Delta$, $v = 1$ to $v' = 0$. Starting in $B^2\Sigma^-$, $v = 0$ results in a slightly different variation of with pressure. While the ratio of $A^2\Delta$, $v' = 0$ to $A^2\Delta$, $v' = 1$ emission intensity also increases approximately linearly with CO_2 pressure, extrapolation reveals that in the limit of zero pressure, I_{A0}/I_{A1} has a value of ~½.

In principle, these measurements of the off-diagonal bands could also be used to determine the relative $A^2\Delta$ and $B^2\Sigma^-$ state populations since the B-X(0,2) band is also simulated. In practice, however, this was not done, as the combination of the fairly significant uncertainties in the strengths of the weak bands observed would result in a far greater systematic uncertainty. Since the collision-induced B-X(0,2) band is very difficult to distinguish following excitation to $A^2\Delta$, $v = 1$ with any degree of accuracy, especially at low CO_2 pressures, this was not a realistic prospect.

IV-4 TIME-RESOLVED FLUORESCENCE WAVEFORMS

The time dependence of fluorescence emitted from the initially populated level and the collisionally produced state was measured by fixing the wavelengths of the pump laser and the monochromator and capturing the decay traces using the transient digitiser. After pumping to both the $A^2\Delta$, $v = 1$ and $B^2\Sigma^-$, $v = 0$ levels, decay traces of directly returning and collision-induced fluorescence were recorded with varying pressures of the CO_2 collision partner.

IV-4.1 Initial excitation to $A^2\Delta$, $v = 1$

Following excitation to $A^2\Delta$, $v = 1$, the fluorescence emitted was recorded by positioning the monochromator at the Q-head of the strong A-X diagonal bands at ~430 nm. Excitation was carried out on the spectrally distant A-X(1,0) off-diagonal band's $R_1(1)$ transition, therefore the measured decay traces are free from scattered laser light. At low pressures of CO_2, the time dependence of the A-X($\Delta v = 0$) emission appears to be approximately single-exponential. However, with increasing pressure of the collision partner, the decay traces adopt a more bimodal appearance with a clearly noticeable long-lived component in addition to a sharper initial decrease. Sample decay traces with varying CO_2 pressures are shown in Figure IV.9 to illustrate this. Qualitatively, this provides further evidence of vibrational relaxation from $A^2\Delta$, $v = 1$ to $A^2\Delta$, $v' = 0$, the population being effectively pooled in the robust $v = 0$ level, which is believed to be only very slowly quenched by CO_2 [12].

As the dispersed fluorescence spectra of the A-X off-diagonal bands showed, the A-X(1,2) and (0,1) are not perfectly overlapped. It is therefore possible to isolate the emission from $A^2\Delta$, $v = 1$ by positioning the monochromator to the short-wavelength side of the A-X(1,2) band at 485 nm, at the cost of a decrease in signal-to-noise. While the best-fit simulations of the off-diagonal bands retain some residual uncertainty, the fluorescence observed can relatively safely be assumed to contain only negligible contamination from emission on the A-X(0,1) and B-X(0,2) bands. Typical decay traces are shown in Figure IV.9, showing a definite contrast to the behaviour of the A-X($\Delta v = 0$) waveforms at longer times.

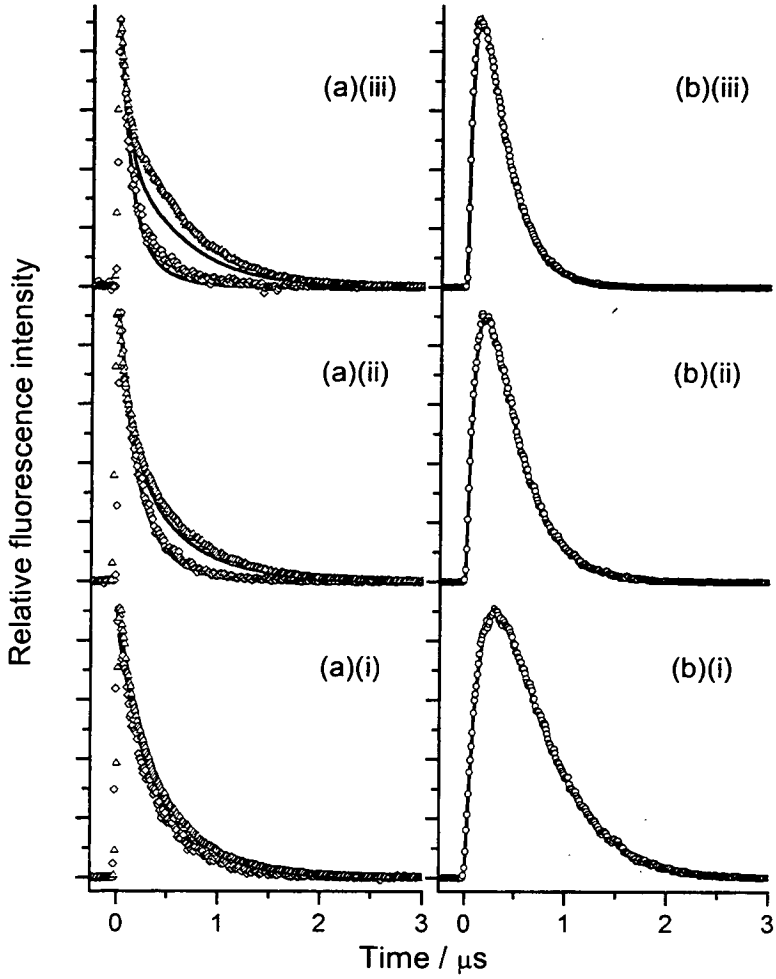

Figure IV.9

Fluorescence decay traces following pumping on the $R_1(1)$ line of the CH A-X(1,0) band in the presence of (i) 1.0 Torr, (ii) 4.0 Torr, and (iii) 8.0 Torr of CO_2. Experimental results show (a) directly returning $A^2\Delta$ emission on (△) A-X(Δv = 0) bands, (◇) A-X(1,2) band; (b) collision-induced emission on (○) B-X(0,0) band. All traces have been scaled to the same peak value. The solid lines are (a) predictions of the kinetic model and (b) non-linear least squares fits of a difference of exponentials (see Equation IV.9) to the experimental data.

Unfortunately, there is no way to directly isolate the emission from the $A^2\Delta$, v = 0 level experimentally, but an indirect route does exist, utilising both the A-X(1,2) and A-X(Δv = 0) waveforms. The A-X(1,2) waveforms can be scaled to have the same initial intensity as the A-X(Δv = 0) traces, and subsequently subtracted from them. The residual fluorescence, while suffering from marginally worse signal-to-noise, can be attributed solely to the A-X(0,0) band. An example of this is shown in Figure IV.10, in which the difference waveform can clearly be seen to show a rise-and-fall profile, characteristic of a collisional product.

Another useful aspect of this approach is that it provides an estimate of the I_{A0}/I_{A1} ratio independent of that obtained from analysis of the off-diagonal dispersed fluorescence spectra by integrating the time-resolved waveforms. The results of this are shown in Figure IV.8 and show a reasonable agreement, falling just within the systematic error limits imposed as a result of the uncertainty in the vibrational bandstrengths used in the analysis.

Finally, following excitation to $A^2\Delta$, v = 1, fluorescence decay traces were recorded observing the collisionally produced B-X(0,0) band as a function of CO_2 pressure. These traces can be observed without any problems of spectral congestion with excellent signal-to-noise. Typical waveforms are shown for several collision partner pressures in Figure IV.9. It is apparent that the rates of both the rising and falling portions of the decay traces increase with pressure.

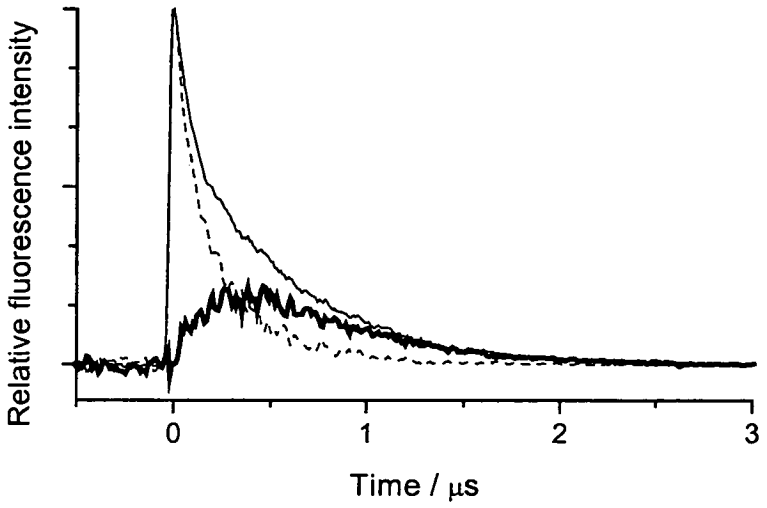

Figure IV.10

Extraction of the time-dependence of CH A-X(0,0) emission following pumping on the $R_1(1)$ line of the A-X(1,0) band at 6.0 Torr of CO_2. The bold line shows the A-X(0,0) component obtained after subtracting a scaled multiple of the A-X(1,2) waveform (dotted line) from the A-X($\Delta v = 0$) diagonal emission (solid line).

IV-4.2 Initial excitation to $B^2\Sigma^-$, $v = 0$

The reciprocal of the time-resolved measurements described above involved laser excitation to the $B^2\Sigma^-$, $v = 0$ level on the $R_1(3)$ transition and observation of the directly returning and collisionally produced fluorescence under conditions of varying pressure of CO_2. The fluorescence directly returning from $B^2\Sigma^-$, $v = 0$ was observed on the spectrally isolated diagonal B-X(0,0) band. The monochromator wavelength was set to transmit the Q- and P-branches to avoid scattered laser light in the R-branch. Typical decay traces can be seen in Figure IV.11. Initial examination of these waveforms would appear to suggest that

they exhibit simple mono-exponential decay as a function of time. The extent to which they do, however, will be considered further in Section IV-5.

Corresponding collisionally produced fluorescence was observed on the A-X(Δv = 0) bands and typical traces are displayed in Figure IV.11, showing the expected rise-and-fall profile of collisional products. A long-lived component, attributable to A-X(0,0) emission can be observed. While in principle these decay traces could be decomposed into A-X(1,1) and (0,0) components by measuring the time-dependence of the collision-induced A-X(1,2) waveforms, this was not pursued. Decomposition would not in this case be as straightforward as when $A^2\Delta$, $v = 1$ was initially populated since both the A-X(1,1) and (0,0) components should show similar time dependence causing a correctly scaled subtraction to be problematic. There would also be significant signal-to-noise difficulties in observing a collisional product on so weak a band as the A-X(1,2) in a time-resolved manner. There is, in any case, sufficient redundancy in the current set of data to allow a kinetic analysis of the collisional coupling of the $A^2\Delta$, $v = 1$, $v = 0$ and $B^2\Sigma^-$, $v = 0$ levels to be carried out.

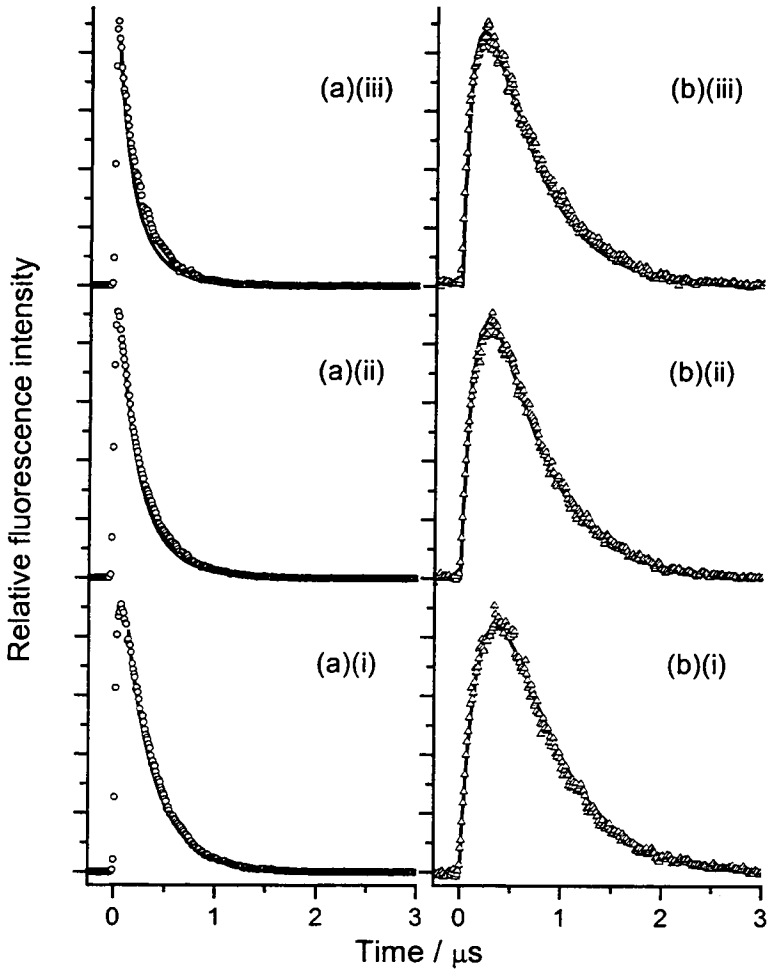

Figure IV.11

Fluorescence decay traces following pumping on the $R_1(3)$ line of the CH B-X(0,0) band in the presence of various pressures of CO_2. Experimental results show (a) directly returning $B^2\Sigma^-$ emission on (○) B-X(0,0) band; (b) collision-induced emission on (Δ) A-X($\Delta v = 0$) band. All traces have been scaled to the same peak value. The solid lines are predictions of the kinetic model.

IV-5 KINETICS

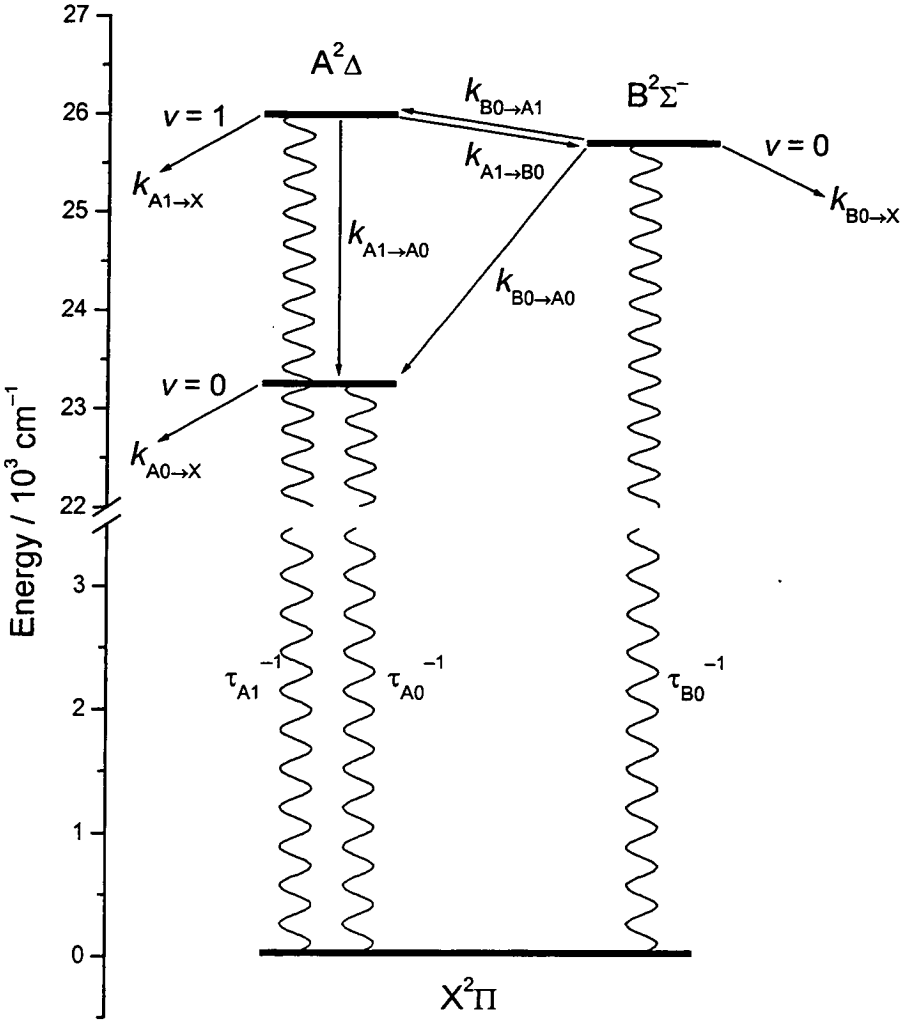

Figure IV.12

Schematic representation of the four-level kinetic model. Collisional and radiative processes are distinguished by straight arrows and wavy lines, respectively.

IV-5.1 Solution of the kinetic scheme

The simplest kinetic scheme required to account for the experimental observations requires the consideration of four vibronic levels. These consist of the only observed vibronic level of the $B^2\Sigma^-$ state, the $v = 0$ level; the $v = 0$ and $v = 1$ vibrational levels of the $A^2\Delta$ state; and all unobserved levels into which population is irreversibly transferred, labelled X. This labelling does not necessarily imply the ground state, but simply any collisionally populated level into which transfer is irreversible.

This scheme is illustrated in Figure IV.12, in which the rate constants for the various processes are defined such that the bimolecular rate constant connecting a level Y to a level Z is denoted $k_{Y\to Z}$. The radiative rate of a level Y is given by the inverse of its radiative lifetime, τ_Y^{-1}. In this case, all levels involved are known to radiate only to the electronic ground state. The time-dependence of the populations, $N_Y(t)$, of the various levels can be written as a set of coupled differential equations:

$$\frac{dN_{B0}(t)}{dt} = -k_{B0}^{T'} N_{B0}(t) + k_{A1\to B0} P_Q N_{A1}(t)$$

Equation IV.1

$$\frac{dN_{A1}(t)}{dt} = -k_{A1}^{T} N_{A1}(t) + k_{B0\to A1} P_Q N_{B0}(t)$$

Equation IV.2

$$\frac{dN_{A0}(t)}{dt} = -k_{A0}^{T} N_{A0}(t) + k_{B0\to A0} P_Q N_{B0}(t) + k_{A1\to A0} P_Q N_{A1}(t)$$

Equation IV.3

in which the pseudo-first order total removal rate constants are given by

$$k_{B0}^{T} = \tau_{B0}^{-1} + \left(k_{B0\rightarrow A1} + k_{B0\rightarrow A0} + k_{B0\rightarrow X}\right)P_Q$$

Equation IV.4

$$k_{A1}^{T} = \tau_{A1}^{-1} + \left(k_{A1\rightarrow B0} + k_{A1\rightarrow A0} + k_{A1\rightarrow X}\right)P_Q$$

Equation IV.5

$$k_{A0}^{T} = \tau_{A0}^{-1} + k_{A0\rightarrow X}P_Q$$

Equation IV.6

and P_Q is the pressure of the quenching gas, limited in this case to CO_2.

The solutions to the differential equations have been calculated using the symbolic mathematical language, *Maple* [13], subject to the initial conditions that either the $A^2\Delta$, $v = 1$ or $B^2\Sigma^-$, $v = 0$ level is populated at $t = 0$. The solutions were subsequently checked analytically.

Taking the case in which the $B^2\Sigma^-$, $v = 0$ level is initially excited, *i.e.* $N_{B0}(0) = N_0$ and $N_{A1}(0) = N_{A0}(0) = 0$, the time-dependence of the $B^2\Sigma^-$, $v = 0$ level is found to be

$$N_{B0}(t) = \frac{N_0}{\lambda_1 - \lambda_2}\left(\left(k_{B0}^{T} + \lambda_1\right)e^{\lambda_2 t} - \left(k_{B0}^{T} + \lambda_2\right)e^{\lambda_1 t}\right)$$

Equation IV.7

The critical parameters λ_1 and λ_2 are defined by

$$\lambda_{1/2} = -\tfrac{1}{2}\left[\left(k_{B0}^{T} + k_{A1}^{T}\right) \mp \sqrt{\left(k_{B0}^{T} - k_{A1}^{T}\right)^2 + 4k_{A1\rightarrow B0}k_{B0\rightarrow A1}P_Q^2}\right]$$

Equation IV.8

The absolute magnitude of λ_2 is greater than λ_1 and both parameters are constrained to be negative. In the low-pressure limit, $\lambda_1 \rightarrow -k_{A1}^T$ and $\lambda_2 \rightarrow -k_{B0}^T$, the total removal rates of the $A^2\Delta$, $v = 1$ and $B^2\Sigma^-$, $v = 0$ levels and ultimately as $P_Q \rightarrow 0$, the inverse of the radiative lifetimes. Thus, it can be seen by inspection of Equation IV.7, that following initial excitation to the $B^2\Sigma^-$, $v = 0$ level, the time-resolved fluorescence decay is only effectively single-exponential in the low-pressure limit with an exponent equal to $-k_{B0}^T$. More generally, since the coefficients $\left(k_{B0}^T + \lambda_1\right)$ and $-\left(k_{B0}^T + \lambda_2\right)$ are positive, the $B^2\Sigma^-$ state decay is given by a sum of two decaying exponentials, with weightings that vary with pressure.

The time-dependence of the $A^2\Delta$, $v = 1$ population is given by

$$N_{A1}(t) = \frac{N_0 k_{B0\rightarrow A1} P_Q}{\lambda_1 - \lambda_2}\left(e^{\lambda_1 t} - e^{\lambda_2 t}\right)$$

Equation IV.9

which can be seen to be the difference of two equally weighted exponentials, producing a rise-and-fall profile typically expected of a collisional product. The exponents λ_1 and λ_2 are as defined above.

The time-dependence of the collisionally populated $A^2\Delta$, $v = 0$ level is given by a more complex function,

$$N_{A0}(t) = \frac{N_0}{\lambda_1 - \lambda_2}\left\{\begin{array}{l}\dfrac{\left(k_{B0\rightarrow A0} P_Q\left(k_{B0}^T + \lambda_1\right) - k_{A1\rightarrow A0} k_{B0\rightarrow A1} P_Q^2\right)}{k_{A0}^T + \lambda_2}\left(e^{\lambda_2 t} - e^{-k_{A0}^T t}\right) \\ -\dfrac{\left(k_{B0\rightarrow A0} P_Q\left(k_{B0}^T + \lambda_2\right) - k_{A1\rightarrow A0} k_{B0\rightarrow A1} P_Q^2\right)}{k_{A0}^T + \lambda_1}\left(e^{\lambda_1 t} - e^{-k_{A0}^T t}\right)\end{array}\right\}$$

Equation IV.10

which can also be expressed as a linear combination of three exponentials in λ_1, λ_2 and k_{A0}^{T}.

The inherent symmetry in the kinetic scheme means that the time-dependencies of the various levels for the reciprocal case in which the $A^2\Delta$, $v = 1$ level is initially populated, *i.e.* $N_{A1}(0) = N_0$ and $N_{B0}(0) = N_{A0}(0) = 0$, can be derived simply by permuting the A1 and B0 labels on all the quantities. The parameters λ_1 and λ_2 are identical, regardless of the particular initial conditions.

The total integrated signal emitted from a specific vibronic level is a further important quantity. For a level Y, the total integrated fluorescence, I_Y, is given by the proportionality

$$I_Y \propto \int_0^\infty \tau_Y^{-1} N_Y(t) dt$$

Equation IV.11

Comparison with experiment requires only that relative signal sizes be known. The integrals were solved numerically at various pressures of the collision partner.

IV-5.2 Determination of kinetic parameters

As Equation IV.7 shows, the time-resolved decay for the direct emission following excitation to either the $A^2\Delta$, $v = 1$ or $B^2\Sigma^-$, $v = 0$ levels should take the form of a weighted sum of two exponential decays. Initial attempts to perform unconstrained fits of the data shown in Figure IV.9 and Figure IV.11 were unsuccessful. The problem arises in the fact that both the exponents and the weighting coefficients are unknown quantities. At lower pressures of CO_2, the problem is exacerbated by the similarity of the values of λ_1 and λ_2 as a result of the similar radiative lifetimes of the $A^2\Delta$ and $B^2\Sigma^-$ states (neglecting the rotational level dependence) of 534 ± 5 and 328 ± 8ns, respectively [11].

The best starting point for the determination of the kinetic parameters is provided by the collision-induced B-X(0,0) decay traces following initial excitation to $A^2\Delta$, $v = 1$. Fitting the experimental data to Equation IV.9, after permutation of the A1 and B0 labels to reflect the alternate excitation scheme, yields the exponents λ_1 and λ_2. The major advantage in fitting to Equation IV.9 is the single scaling coefficient, which applies to both exponentials. Figure IV.9 shows the quality of typical fits to the experimental data. It is possible that there is still a slight problem with ill-conditioning of the parameters at low pressure where λ_1 and λ_2 are similar, but the reproducibility of the fits was found to be good. Values obtained for the parameters λ_1 and λ_2 are shown in Figure IV.13, after conversion of units. Extrapolation to zero pressure shows a plausible agreement with the accepted values of the radiative lifetimes of the $A^2\Delta$ and $B^2\Sigma^-$ states, which were not subsequently treated as variable parameters.

A useful constraint on the rate constants is obtained by summing the λ_1 and λ_2 parameters, thus, according to Equation IV.8

$$-(\lambda_1 + \lambda_2) = k^{\mathrm{T}}_{\mathrm{A1}} + k^{\mathrm{T}}_{\mathrm{B0}}$$

Equation IV.12

This function is also shown plotted in Figure IV.13. Since both $k^{\mathrm{T}}_{\mathrm{A1}}$ and $k^{\mathrm{T}}_{\mathrm{B0}}$ are linear with respect to pressure (see Equation IV.4 and Equation IV.5) the best-fit slope of this function provides a limiting value for the sum of the removal rate constants for the $A^2\Delta$, $v = 1$ and $B^2\Sigma^-$, $v = 0$ levels. After conversion of units, this is found to be $(3.80 \pm 0.05) \times 10^{-11}$ cm^3 molecule^{-1} s^{-1}.

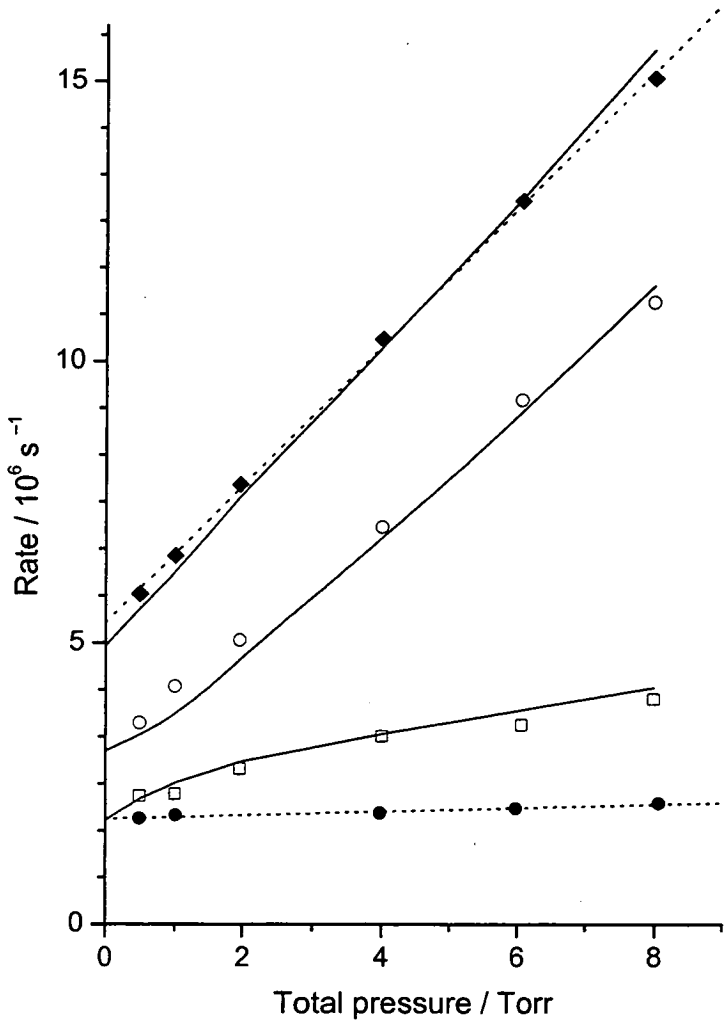

Figure IV.13

Variation of exponential kinetic parameters with pressure of CO_2. Experimental results shown are (□) $|\lambda_1|$, (○)$|\lambda_2|$, and (♦)$|\lambda_1 + \lambda_2|$, all derived from non-linear least squares fits of a rise-and-fall exponential function to B-X(0,0) decay traces following excitation to $A^2\Delta$, v = 1 on the $R_1(1)$ line of the A-X(1,0) band; and (●) the exponent of the smallest magnitude controlling the time-dependence of the extracted A-X(0,0) emission (see Figure IV.10). The dotted lines are linear fits to $|\lambda_1 + \lambda_2|$ and k_{A0}^T; the solid lines are the predictions of the four-level kinetic model.

One further constraint can be deduced from the dispersed fluorescence spectra of the off-diagonal bands. After initial excitation of the $B^2\Sigma^-$, $v = 0$ levels, the total integrated fluorescence ratio, I_{A0}/I_{A1}, can be seen, in Figure IV.8, to have a zero pressure limiting value of ~½. This ratio is entirely due to the relative magnitudes of the rate constants for collisional energy transfer out of the $B^2\Sigma^-$, $v = 0$ level and into each of the two energetically available $A^2\Delta$ vibrational levels. Thus, we can say that $k_{B0\rightarrow A1}$ is twice as large as $k_{B0\rightarrow A0}$.

Using these constraints, the rate constant for each process can be extracted using an iterative procedure to compare experimentally measured quantities with those predicted using the four-level kinetic scheme employed. The kinetic model predicts that the total integrated fluorescence ratio, I_{A0}/I_{A1}, measured after excitation to the $A^2\Delta$, $v = 1$ level is largely determined by the magnitude of the vibrational relaxation rate constant, $k_{A1\rightarrow A0}$. Secondary relaxation, requiring a two-collision process, $A^2\Delta$, $v = 1 \rightarrow B^2\Sigma^-$, $v = 0 \rightarrow A^2\Delta$, $v = 0$, is found to have only a minor influence on the I_{A0}/I_{A1} ratio. A value for $k_{A1\rightarrow A0}$ of ~0.7×10^{-11} cm^3 molecule^{-1} s^{-1} is found to best describe the total integrated fluorescence ratios observed.

The respective ratios of total integrated fluorescence from the product state to the initial state, shown in Figure IV.5, are probably most sensitive to the balance between the total removal rate constants for the $B^2\Sigma^-$, $v = 0$ and $A^2\Delta$, $v = 1$ levels. The *absolute* values of $k_{B0\rightarrow A0}$ combined with $k_{B0\rightarrow A1}$ and $k_{A1\rightarrow B0}$ have the greatest influence on these ratios, reflecting the competition between electronically inelastic collisions and radiative loss. The radiative rates are well known, resulting in estimates for the rate constants of ~1.8×10^{-11} cm^3 molecule^{-1} s^{-1} for $k_{A1\rightarrow B0}$ and ~1.5×10^{-11} cm^3 molecule^{-1} s^{-1} for ($k_{B0\rightarrow A1} + k_{B0\rightarrow A0}$). The constraint on the relative magnitudes of $k_{B0\rightarrow A1}$ and $k_{B0\rightarrow A0}$ deduced from the limiting zero pressure I_{A0}/I_{A1} ratio following initial $B^2\Sigma^-$, $v = 0$ excitation then allows the individual rate constants to be determined.

At this point, we return to the constraint on the sum of the total removal rate constants for the $A^2\Delta$, $v = 1$ and $B^2\Sigma^-$, $v = 0$ levels, given by $|\lambda_1 + \lambda_2|$. For the processes considered already, the sum of the rate constants slightly exceeds the limiting value before the inclusion of any contribution from electronic quenching to dark states, $k_{A1\rightarrow X}$ and $k_{B0\rightarrow X}$. The total loss of the $A^2\Delta$, $v = 1$ and $B^2\Sigma^-$, $v = 0$ levels can therefore be accounted for without recourse to unidentified electronic quenching. We can conclude that the rate constants for such processes are not of comparable magnitude to those for identified electronically inelastic processes and vibrational relaxation in the $A^2\Delta$ state.

The indirectly constructed $A^2\Delta$, $v = 0$ time-resolved decay traces, following initial excitation to the $A^2\Delta$, $v = 1$ level, a typical example of which is shown in Figure IV.10, provide an independent route to the evaluation of $k_{A0\rightarrow X}$. Recalling Equation IV.10, the functional form of the time-dependence of the $A^2\Delta$, $v = 0$ emission has been to shown to be a combination of exponential functions with exponents given by λ_1, λ_2 and k^T_{A0}. The faster components in these traces were found to be irreproducible when fitted, however the smallest exponent, identifiable with k^T_{A0}, which controls the decay at longest times, was well behaved. This shows only a modest variation with pressure, according to Equation IV.6. The result is shown in Figure IV.13. The zero-pressure intercept, corresponding to a radiative lifetime of 533 ± 6 ns agrees with the previously reported value of 534 ± 5 ns for the $A^2\Delta$, $v = 0$ level. The slope yields a quenching rate constant for $k_{A0\rightarrow X}$ of (0.098 ± 0.013) × 10^{-11} cm^3 $molecule^{-1}$ s^{-1}. This value is in reasonable agreement with the previously reported [12] value of (0.04 ± 0.004) × 10^{-11} cm^3 $molecule^{-1}$ s^{-1} for the quenching of the $A^2\Delta$ state by CO_2. Later measurements using 248 nm photolysis made with direct excitation to the $A^2\Delta$, $v = 0$ level on the A-X(0,0) $^RR_{11}(1)$ transition, found the CH fluorescence lifetime to be only weakly dependent on the pressure of CO_2. The collisional removal rate constant was

measured to be $(0.03 \pm 0.003) \times 10^{-11}$ cm^3 molecule^{-1} s^{-1}, with a radiative lifetime of 555 ± 5 ns.

On energetic grounds, the $B^2\Sigma^-$ state is inaccessible to the $A^2\Delta$, $v = 0$ level for a thermal (~295 K) distribution of collision energies. Otherwise, it can be plausibly argued that electronic quenching of the $A^2\Delta$, $v = 0$ and $v = 1$ levels should not differ significantly. The magnitudes of the rate constants for the electronic quenching of the different vibrational levels in the $A^2\Delta$ state should be similar. Hence, throughout the analysis, the value of $k_{A1\rightarrow X}$ has been set equal to $k_{A0\rightarrow X}$, while electronic quenching of the $B^2\Sigma^-$, $v = 0$ level to dark states has been neglected.

IV-5.3 Comparison of predictions with observations

The best rate constants obtained by means of the analysis described above are summarised in Table IV.3. These values are not necessarily unique, since there remains a residual coupling between the rate constants that allows them to be varied co-operatively. The uncertainties quoted give an indication of how much the value of the associated rate constant could be varied independently without causing a clear deterioration in the quality of the agreement with the experimental data. In this section, the extent to which this set of rate constants is capable of fully describing the experimental observations is discussed.

The total integrated fluorescence ratios of product to initial state obtained from the dispersed spectra recorded on the diagonal bands are reproduced satisfactorily, as shown in Figure IV.5. Agreement of the prediction with the observations using these data is essentially by construction, as they were used for the most part to decide on the best values for the rate constants of the electronically inelastic processes $k_{B0\rightarrow A1}$, $k_{B0\rightarrow A0}$, and $k_{A1\rightarrow B0}$. It is pleasing, however, that both the slopes and, especially in the case of initial excitation to $A^2\Delta$, $v = 1$, the degree of curvature are well reproduced.

Table IV.3

Best-fit microscopic rate constants within the four-level kinetic scheme.

Rate constant	Value / 10^{-11} cm^3 molecule^{-1} s^{-1}
$k_{B0\rightarrow A1}$	1.0 ± 0.2
$k_{B0\rightarrow A0}$	0.5 ± 0.2
$k_{B0\rightarrow X}$	0 + 0.1
$k_{A1\rightarrow B0}$	1.8 ± 0.3
$k_{A1\rightarrow A0}$	0.7 ± 0.2
$k_{A1\rightarrow X}$	0.1 ± 0.1
$k_{A0\rightarrow X}$	0.10 ± 0.05

The agreement between the model and the I_{A0}/I_{A1} ratios obtained from the off-diagonal dispersed fluorescence spectra, shown in Figure IV.8, is less good, however. After initial excitation to $B^2\Sigma^-$, $v = 0$, the increase in I_{A0}/I_{A1} with pressure is overestimated, while initial excitation to $A^2\Delta$, $v = 1$ results in an underestimation by the model. It was not found to be possible to resolve this discrepancy to satisfy both initial excitation schemes and the final values for the rate constants reflect a compromise between the two. It should be noted that the integrated fluorescence ratios are subject to systematic difficulties in decomposing the overlapped off-diagonal bands in the spectra in addition to a potential systematic error caused by the uncertainties in the relative transition probabilities of the A-X(1,2) and (0,1) bands, represented by the error bars in Figure IV.8. The measurement of I_{A0}/I_{A1} obtained from the time-resolved A-X($\Delta v = 0$) and A-X(1,2) emission as a function of CO_2 pressure is also shown. The discrepancy between the two independent experimental sets of data is comparable to that between the model predictions and the off-diagonal measurements. There is no similar independent method for determining the ratio following initial excitation to

$B^2\Sigma^-$, $v = 0$. However, applying a correction to the dispersed fluorescence data in Figure IV.8(b) to bring them into line with the model and the time-resolved data, would have a detrimental effect on the agreement in Figure IV.8(a).

The sum of the $A^2\Delta$, $v = 1$ and $B^2\Sigma^-$, $v = 0$ total collisional removal rate constants, $\left(k_{B0}^T + k_{A1}^T\right)$, takes a value of 4.1×10^{-11} cm^3 molecule^{-1} s^{-1}, which only slightly overestimates the limiting value of 3.8×10^{-11} cm^3 molecule^{-1} s^{-1} obtained from the slope of a linear plot of the experimental value of $|\lambda_1 + \lambda_2|$ against the pressure of CO_2. The individual values of λ_1 and λ_2 are also well reproduced by the model predictions, which is illustrated in Figure IV.13. These were not used as separate constraints in the fitting procedure.

The analytical solutions to the four-level kinetic scheme provide the functional forms for the time-dependence of the emission from the various levels, Equation IV.7 – Equation IV.10. The best-fit rate constants can therefore be used to produce predictions for comparison with the measured experimental waveforms. The $B^2\Sigma^-$, $v' = 0$ waveforms recorded following excitation to $A^2\Delta$, $v = 1$ cannot be used in this comparison, since unconstrained fits to them were used to obtain the λ_1 and λ_2 parameters. By default, the model prediction will necessarily agree with the experimental decay traces. The remaining results do provide a genuine means of checking the predictions. The collisionally produced A-X($\Delta v = 0$) waveforms recorded following excitation to $B^2\Sigma^-$, $v = 0$, are very well reproduced by the model predictions, illustrated in Figure IV.11(b). The predicted decays for the initially populated levels, $A^2\Delta$, $v = 1$ and $B^2\Sigma^-$, $v = 0$ agree well at low pressures, see Figure IV.9 and Figure IV.11, but are noticeably different as the pressure of the collision partner is increased. Recalling the function for the time-dependence of the initially populated level, Equation IV.7, this discrepancy is probably due to the need to have both the exponents and the weighting coefficients correct, a factor that becomes more important at higher pressure. The inconsistency between the experimental results and the model's

predictions remains slight, however. A more noticeable discrepancy exists in the case of the A-X($\Delta v = 0$) waveforms recorded following excitation to $A^2\Delta$, $v = 1$, depicted in Figure IV.9. In this situation, too, the quality of the agreement decreases with increasing pressure of CO_2, and the model significantly underestimates the longer-lived A-X(0,0) component of these waveforms at the highest pressures.

IV-5.4 Summary

The four-level kinetic scheme satisfactorily reproduces the experimental observations, although some quantitative discrepancies obviously remain, as discussed above. In addition to the sources of systematic error described, a more fundamental reason for the difficulties in obtaining a good overall agreement with the experimental observations could be limitations in the four-level kinetic scheme. There remains, in principle, the possibility that an underlying electronic state, for example high vibrational levels of the $X^2\Pi$ ground state or the low lying $a^4\Sigma^-$state, could couple reversibly to either the $A^2\Delta$, $v = 1$ or $B^2\Sigma^-$, $v = 0$ levels.

A more obvious, and more likely, explanation is provided by the simplification resulting from the neglect of the rotational structure of the vibronic levels. The method of laser excitation prepares a single rovibronic and/or fine-structure level and this is not necessarily equilibrated to a thermal distribution on the time-scale of the measurements. Indeed, later work, which will be described in detail in Chapter V, shows that the population is not thermally distributed over the rotational levels. In order to produce a model that can quantitatively reproduce the experimental observations it may be necessary to treat rotational levels independently, greatly increasing the number of adjustable parameters. Figure IV.14 shows the rotational structure of the $A^2\Delta$, $v = 1$ and $B^2\Sigma^-$, $v = 0$ levels schematically. Inspection suggests that the value of $k_{B0\rightarrow A1}$ could easily be rotational level dependent,

simply on energetic grounds. In addition, the radiative lifetimes are slightly rotational-level dependent [11], most notably in the $B^2\Sigma^-$, $v = 0$ level.

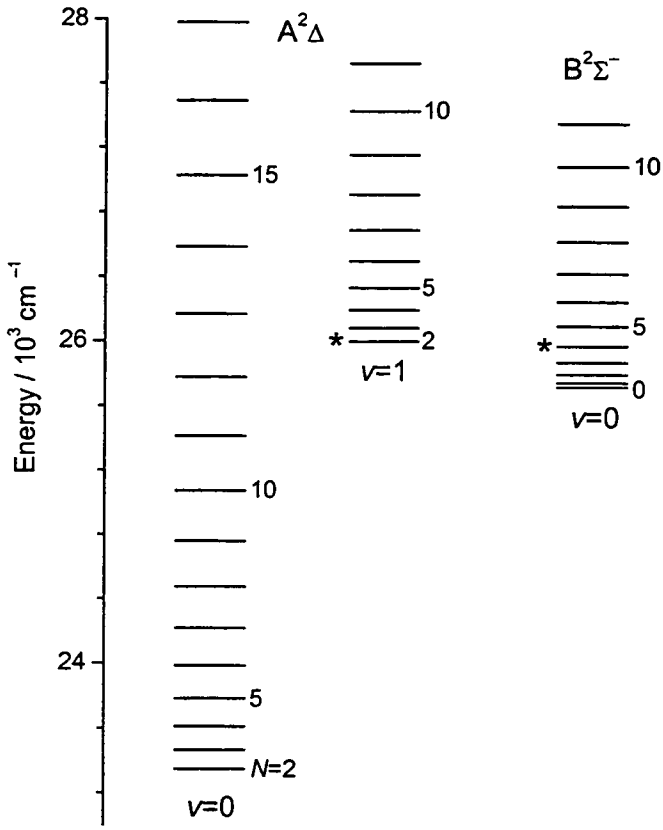

Figure IV.14

Rovibronic energy levels for the $A^2\Delta$, $v = 0$ and 1, and $B^2\Sigma^-$, $v = 0$ states of the CH radical. Additional fine-structure splittings within levels of a given N have been omitted for clarity. The asterisks denote the rotational levels initially populated.

In principle, the rate constants $k_{B0\rightarrow A1}$ and $k_{A1\rightarrow B0}$ should be related by microscopic reversibility, although it is difficult to apply such arguments rigorously without rotationally resolved data. In the analysis described previously, both parameters have been deduced independently. If the rotational structure is neglected and only the vibronic energy

gap and the extra two-fold degeneracy of the $A^2\Delta$ state is taken into account, the ratio $k_{B0\rightarrow A1}/k_{A1\rightarrow B0}$ is predicted to be 0.50 at 295 K. This agrees relatively well with the unconstrained ratio of 0.56 ± 0.15 determined from the four-level kinetic model. If a thermal Boltzmann distribution is assumed over the rotational and fine-structure levels of each state, the ratio decreases to 0.38, impairing the agreement with experiment.

IV-6 IMPLICATIONS FOR QUENCHING MEASUREMENTS

Of greatest significance in this work is the conclusive demonstration that the $A^2\Delta$, $v = 1$ and $B^2\Sigma^-$, $v = 0$ levels of the CH radical are reversibly coupled in collisions with CO_2, and potentially with other collision partners. The efficiencies of other molecules in inducing electronic state changes have not been explored in detailed at this time. Electronic energy transfer between the $A^2\Delta$ and $B^2\Sigma^-$ states has been observed previously in low [2] and atmospheric pressure [1] hydrocarbon flames, but not under controlled conditions with a single collision partner. In contrast to the observations discussed in this chapter, Garland and Crosley [1] reported no $B^2\Sigma^-$, $v = 0 \rightarrow A^2\Delta$, $v' = 0$ energy transfer or vibrational relaxation within the $A^2\Delta$ state. The majority species present in the hydrocarbon flames presumably result in different transfer propensities from CO_2, used in this work.

Recent work by Carter *et al.* [14, 15] has used CH planar laser-induced fluorescence (PLIF) for flamefront imaging. In this work the excitation scheme involves pumping on the B-X(0,0) band and collecting fluorescence in the region of the A-X diagonal and B-X(0,1) bands. Thus, collision-induced electronic energy transfer is essential if a PLIF signal is to be observed. It is essential that care is taken to ensure that the signal intensity is not affected by differences in the temperature or composition of the region of the flame being imaged. In an environment consisting of mixed quenchers, it is possible that the effects of the different collision partners could appear to be non-additive. For example, a

collision partner that effectively quenches $A^2\Delta$, $v = 1$ could enhance the apparent removal rate of $B^2\Sigma^-$, $v = 0$ in the presence of a partner which efficiently interconverts $B^2\Sigma^-$, $v = 0 \leftrightarrow A^2\Delta$, $v = 1$.

The existence of reversible collisional coupling of the $A^2\Delta$ and $B^2\Sigma^-$ states means that it is important that care is taken in the interpretation of rate constants purporting to measure the efficiency of the electronic quenching of these two states. As has been mentioned previously, knowledge of the electronic quenching rate constants is essential in the use of a technique such as LIF as a tool for flame diagnostics, since collisional removal processes affect the quantum yield.

The problem is illustrated in Figure IV.15, for the case of the $B^2\Sigma^-$, $v = 0$ level being initially populated. The predicted variations of the parameters in Equation IV.7 are shown for the best-fit rate constants in Table IV.3. Also shown in Figure IV.15 is the apparent first-order total removal rate constant, k_{B0}^T, obtained by fitting simple single exponential decays to the *calculated* $B^2\Sigma^-$, $v = 0$ time-dependent decay traces at various pressures. This can be seen to significantly underestimate the value of k_{B0}^T used to generate the decay traces as the pressure of the collision partner is increased. Physically, this can be explained by the longer radiative lifetime of the $A^2\Delta$, $v = 1$ level. $B^2\Sigma^-$, $v = 0 \rightarrow A^2\Delta$, $v' = 1$ transfer deposits population in the longer-lived level and under a higher pressure regime, in which collisional processes become more important relative to radiative, a fraction of this population can be transferred back, lengthening the effective $B^2\Sigma^-$, $v = 0$ lifetime.

Single exponential decays were also fitted to the *experimental* $B^2\Sigma^-$, $v = 0$ decay traces. The decay constants obtained show a relatively linear variation with CO_2 pressure, yielding a rate constant of $(0.63 \pm 0.04) \times 10^{-11}$ cm^3 molecule^{-1} s^{-1}. This contrasts markedly with the value of $(1.5 \pm 0.3) \times 10^{-11}$ cm^3 molecule^{-1} s^{-1} required by the four-level model, but is in good agreement with the value of $(0.77 \pm 0.12) \times 10^{-11}$ cm^3 molecule^{-1} s^{-1} reported in

the literature by Cooper and Whitehead [16]. The experimental method they employed measured the variation in the intensity of the $B^2\Sigma^-$ state fluorescence with pressure following production of electronically excited CH radicals by 248 nm photolysis of $CHBr_3$. This effectively measured the phenomenological variation of the lifetime rather than the true microscopic total removal rate constant.

These problems of interpretation are most important when both the $A^2\Delta$ and $B^2\Sigma^-$ states are produced in coincidence, an inevitable situation if UV multiphoton photolysis is used to produce electronically excited CH radicals. In this case, the apparent time-dependence of the $B^2\Sigma^-$ state could be affected by electronic energy transfer from higher vibrational levels ($v \geq 1$) of the photolytically-produced $A^2\Delta$ state. Similarly, in the reverse direction, nascent population in the $B^2\Sigma^-$ state can perturb the $A^2\Delta$ state emission, including the $A^2\Delta$, $v = 0$ level. The $A^2\Delta$, $v = 0$ level does not, however, suffer from this complication if it is prepared in isolation.

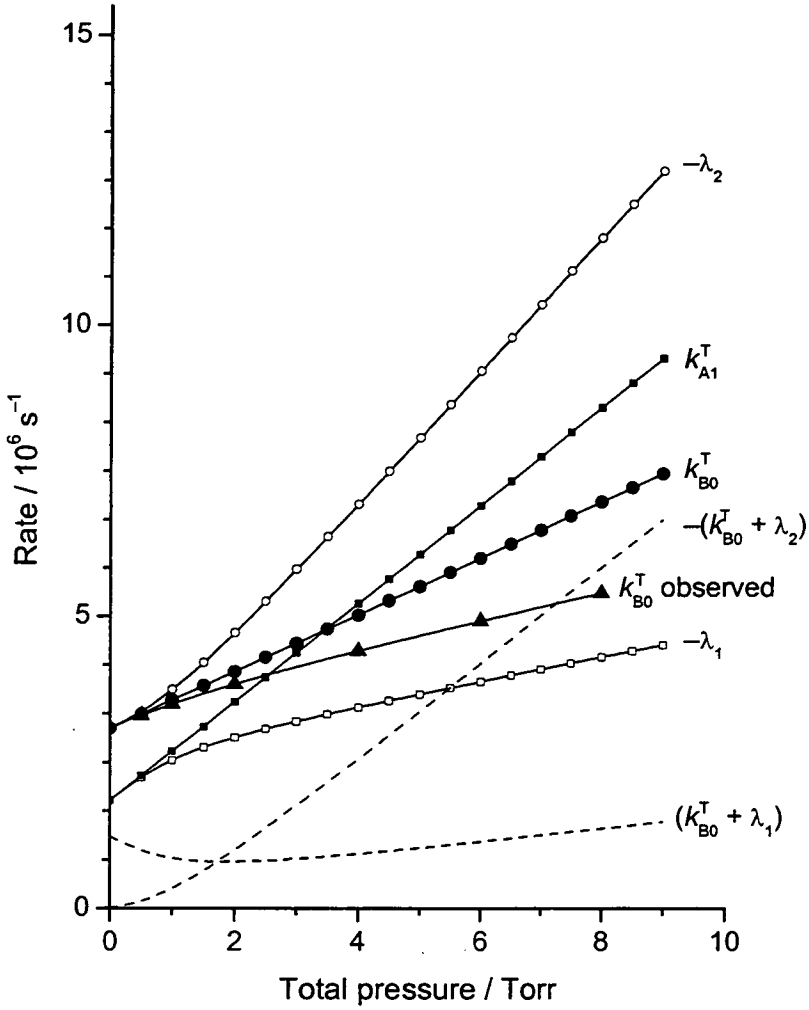

Figure IV.15

Predicted variations with CO_2 pressure of the terms in Equation IV.8 assuming the rate constants in Table IV.3. The symbols correspond to (•) value of k^T_{B0} used in the model, (▲) apparent value of k^T_{B0} obtained by fitting a single exponential decay to the model decays, (□) $-\lambda_1$, (○), $-\lambda_2$, (■) k^T_{A1}. The dashed lines show the variation of the coefficients $\left(k^T_{B0} + \lambda_1\right)$ and $-\left(k^T_{B0} + \lambda_2\right)$ with CO_2 pressure as indicated.

IV-7 REFERENCES

1 N. L. Garland and D. R. Crosley, *Appl. Opt.*, **24**, (1985), 4229

2 K. J. Rensberger, M. J. Dyer and R. A. Copeland, *Appl. Opt.*, **27**, (1988), 3679

3 C. J. Randall, PhD Thesis, University of Edinburgh, 1998

4 J. E. Butler, J. W. Fleming, L. P. Goss and M. C. Lin, *Chem. Phys.*, **56**, (1981), 355

5 M. E. Pillow, *Research Notes*, (1955), 547

6 J. Luque and D. R. Crosley, *J. Chem. Phys.*, **104**, (1996), 3907

7 R. Kępa, A. Para, M. Rytel and M. Zachwieja, *J. Mol. Spectrosc.*, **178**, (1996), 189

8 M. Zachwieja, *J. Mol. Spectrosc.*, **170**, (1995), 285

9 R. N. Zare, A. L. Schmeltekopf, W. J. Harrop and D. L. Albritton, *J. Mol. Spectrosc.*, **46**, (1973), 37

10 J. Luque and D. R. Crosley, *J. Chem. Phys.*, **104**, (1996), 2146

11 J. Brzozowski, P. Bunker, N. Elander and P. Erman, *Astrophys. J.*, **207**, (1976), 414

12 R. D. Kenner, S. Pfannenberg, P. Heinrich and F. Stuhl, *J. Phys. Chem.*, **95**, (1991), 6585

13 Maple V, Release 4.00a, © Waterloo Maple Inc., Ontario, Canada, 1996

14 C. D. Carter, J. M. Donbar and J. F. Driscoll, *Appl. Phys. B*, **66**, (1998), 129

15 K. A. Watson, K. M. Lyons, J. M. Donbar and C. D. Carter, *Combustion and Flame*, **123**, (2000), 252

16 J. L. Cooper and J. C. Whitehead, *J. Chem. Soc., Faraday Trans.*, **88**, (1992), 2323

V ROTATIONALLY-RESOLVED $A^2\Delta \leftrightarrow B^2\Sigma^-$ ENERGY TRANSFER

V-1 INTRODUCTION

In the previous chapter, the inter-conversion of the $A^2\Delta$ and $B^2\Sigma^-$ states of the CH radical induced by collisions with CO_2 was demonstrated. A four-level kinetic scheme was developed which enabled the extraction of the microscopic rate constants for the various collisional processes at *vibronic* resolution. The major advance discussed in this chapter is the extension of the study to collision-induced electronic energy transfer at a fully *rovibronic* state-resolved level. The rotational propensities accompanying $A^2\Delta$, $v = 1 \rightarrow B^2\Sigma^-$, $v' = 0$ and $B^2\Sigma^-$, $v = 0 \rightarrow A^2\Delta$, $v' = 0$ and 1 electronically inelastic collisions have been determined, for several initial rotational levels with CO_2 as collision partner, using time-resolved dispersed fluorescence measurements. Figure V.1 shows the relevant energy level diagram.

To evaluate the effect of rotational excitation in the parent state on the observed distribution in the collisionally populated state requires the determination of the population distributions in both states immediately before and after the electronically inelastic collision. Resolution of individual rotational lines in the dispersed fluorescence spectra is facilitated by the relatively large rotational constant of the CH radical. State-to-state propensities under single-collision conditions are complicated by the relatively long fluorescence lifetimes of the $A^2\Delta$ and $B^2\Sigma^-$ states, and the relatively rapid rates of rotational redistribution compared to the rate of electronic energy transfer. The use of short time gates over the early part of the fluorescence signal, combined with a low pressure of quenching partner is used to minimise the effects of rotationally inelastic collisions smearing out the nascent product state

distribution. It is thus possible to observe the evolution of the population distribution in both the parent and product states over time.

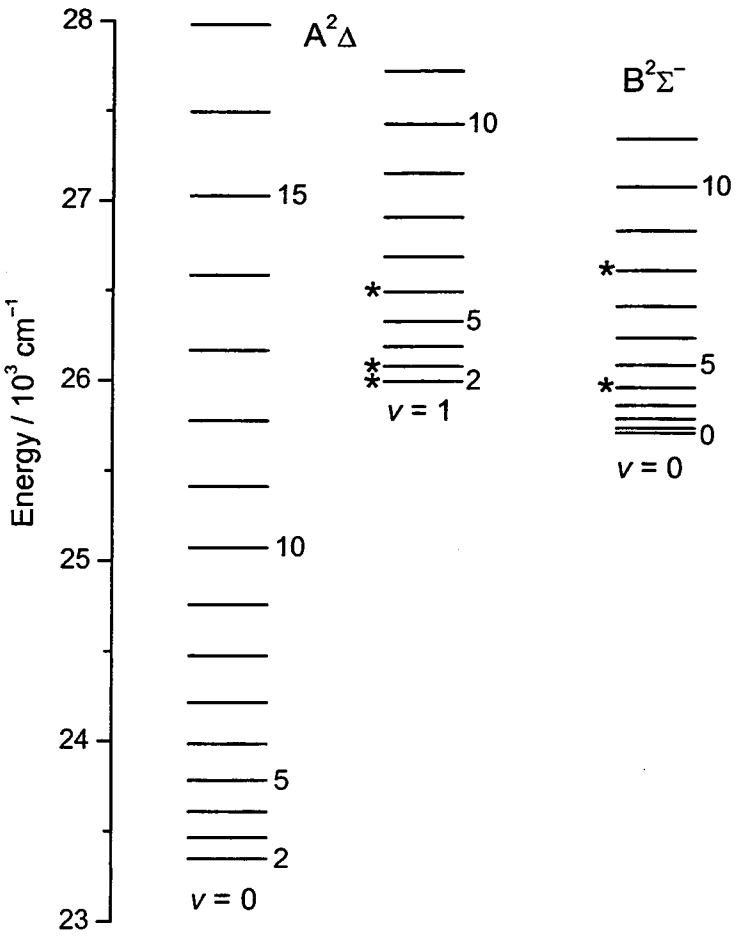

Figure V.1

Rovibronic energy levels for the $A^2\Delta$ and $B^2\Sigma^-$ states of the CH radical of relevance. Levels used for initial excitation are marked by asterisks. Rotational levels are labelled by *N*. Fine-structure and Λ-doublet splittings are not indicated.

V-2 DIRECTLY RETURNING FLUORESCENCE SPECTRA

As mentioned above, it is a pre-requisite for a state-resolved study of electronic energy transfer that the parent state rotational distribution has been characterised. Laser excitation provides a means of preparing a single rotational and fine-structure level, but rotational relaxation, which occurs at near gas-kinetic rates, causes the distribution to be smeared out. High resolution dispersed fluorescence spectra, recorded over a range of time-gates, allow the degree of rotational redistribution as a function of time to be determined. Ideally, the parent state should show as little relaxation as possible, generally achieved in dispersed measurements by using low pressures and short time gates (small pressure-time product). There is however, an obvious trade-off between reducing the average number of collisions and the magnitude of the signal from the product state that can be measured. Although it is secondary to the main interest in this work, the directly returning fluorescence spectra can, in principle, be used to extract absolute state-to-state pure rotational energy transfer (RET) rate constants within the initially populated electronic state.

Throughout this chapter, Hund's case (b) coupling will be assumed for both the $A^2\Delta$ and $B^2\Sigma^-$ states and the rotational levels will be discussed in terms of N rather than J. Case (b) obviously applies to the $B^2\Sigma^-$ state since the electronic orbital angular momentum is zero. In the $A^2\Delta$ state, the spin-orbit coupling is very weak and the transition from case (a) to case (b) occurs with very low rotation.

V-2.1 Initial excitation to $A^2\Delta$, $v = 1$

As described in Chapter IV, the off-diagonal A-X(1,0) band can be conveniently used to selectively populate distinct rotational levels within $A^2\Delta$, $v = 1$. The $R_1(N'' = 1$ and 2) and $R_2(N'' = 1$ and 2) transitions of the A-X(1,0) band were chosen to pump either spin-

orbit state of the lowest lying $N = 2$ and 3 levels. In addition, the $N = 6$ and 8 levels were pumped using the $R_{22ff}(5)$ and $R_{22ee}(7)$ transitions of the same band. For the low-N levels, the individual Λ-doublets could not be resolved within the limit of the excitation laser bandwidth, hence both e and f levels are pumped. However, the use of the $R_{22ff}(5)$ and $R_{22ee}(7)$ transitions allows truly individual quantum states to be initially populated.

Dispersed fluorescence spectra were recorded in the presence of CO_2 as a collision partner (~1.1 Torr) on the diagonal A-X(1,1) band at sufficient resolution to resolve individual rotational levels. The photolysis wavelength was 266 nm. The fine-structure could only be resolved for $N = 2$ and individual Λ-doublets were completely unresolved. The emission on the diagonal band is chosen for the obvious reasons that it carries the bulk of the transition probability and no scattered light from the probe laser is observed. The fluorescence signal was simultaneously integrated over a series of five time-gates of increasing duration (50, 100, 400, 800 and 1600 ns), each of which began coincidentally with the rising edge of the fluorescence signal. In this way, the temporal evolution of the population distribution within the $A^2\Delta$, $v = 1$ level and of the *absolute* magnitude of the signal can be followed. The emission on the A-X(1,1) band isolated by an interference filter was used to normalise the dispersed signal, as described previously in Chapter III.

Figure V.2 shows typical directly returning dispersed fluorescence spectra, recorded following initial excitation to the $A^2\Delta$, $v = 1$, $N = 6$ level, for three of the different time-gates. Best-fit simulations of the experimental spectra, also shown in Figure V.2, were obtained by manually adjusting the populations in each N in the $A^2\Delta$, $v = 1$ level using the spectral simulation program LIFBASE [1] until the agreement was optimised. The insets of the figure show the accompanying best-fit rotational population distributions over N only. Since, in general, the F_1 and F_2 fine-structure levels and Λ-doublets could not be resolved in emission, the distribution for $N \geq 3$ was assumed to be the same over both spin-orbit states and that the populations were not non-statistical. Recent work has been performed by

Dagdigian *et al.* [2,3] and in this laboratory [4] on RET within the $A^2\Delta$, $v = 0$ level in collisions with Ar, in which the spin-orbit states are resolved. Briefly, the fine-structure changing transition for $\Delta N = 0$ dominates, although its propensity decreases with increasing initial N. Transitions with $\Delta N \neq 0$ show an increasing propensity for conservation of the spin-orbit label as the initial N increases. The analysis presented in this work is not adversely affected by the propensities for fine-structure changing/conserving collisions. Population distributions are reported over N only, effectively summing over both spin-orbit states for a given level N. The limited information obtained on fine-structure resolved inelastic collisions will be discussed more fully in Section V-3.

It can be clearly seen in Figure V.2 that for the shortest time gate shown, for which the integration is carried out over the earliest part of the fluorescence signal, the spectrum is dominated by emission from the initially populated level. The other rotational levels contribute more to the spectra recorded over longer gates as the excited state population is relaxed by collisions. The longest gate (1600 ns), which effectively integrates over the entire fluorescence decay, shows that complete rotational equilibration to a distribution which could be represented by a Boltzmann temperature does not occur at this pressure. Qualitatively, the spectra recorded following excitation on the other transitions described above are similar, showing only a small amount of rotational relaxation in the shorter gates, although the fraction remaining in the initial level is N-dependent. This is summarised in Table V.1. Figure V.3 displays the short gate dispersed fluorescence spectra following initial excitation to the F_1 and F_2 levels of $N = 2$ and 3.

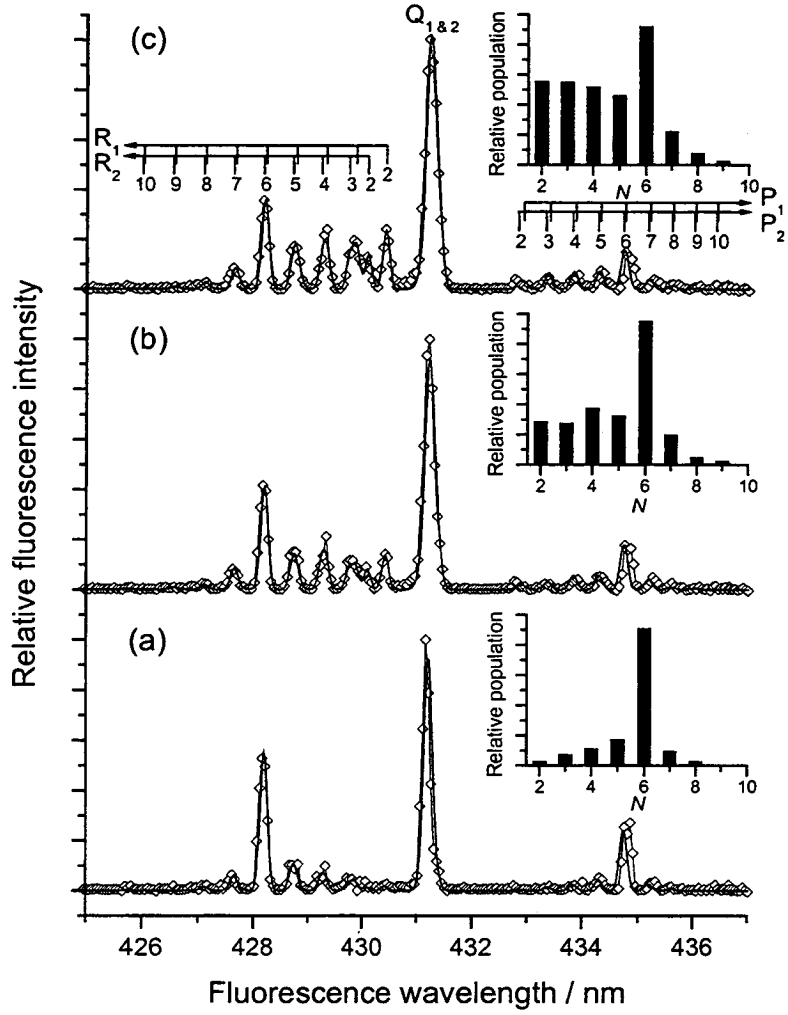

Figure V.2

Dispersed A-X(1,1) fluorescence spectra following excitation of $A^2\Delta$, $v = 1$, $N = 6$ on the A-X(1,0) $R_{22ff}(5)$ line in the presence of 1.1 Torr CO_2. Signal integrated over gates of (a) 100 ns, (b) 400 ns and (c) 1600 ns. The monochromator resolution was 0.16 nm. Experimental spectra (◇) and best-fit simulations (solid lines) are shown. The insets show the corresponding rotational population distributions. Only main branch transitions are indicated and each line consists of two unresolved Λ-doublets.

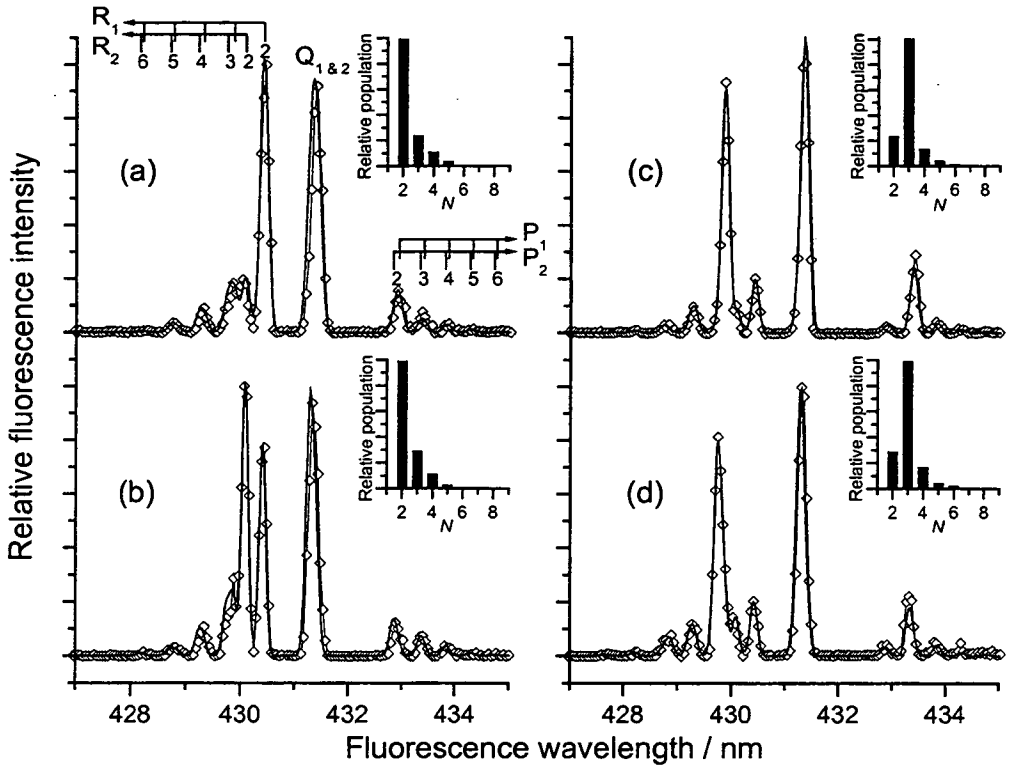

Figure V.3

Dispersed A-X(1,1) fluorescence spectra following excitation of CH $A^2\Delta$, $v = 1$ on the A-X(1,0) (a) $R_1(1)$, (b) $R_1(2)$, (c) $R_2(1)$, and (d) $R_2(2)$ transitions in the presence of 1.1 Torr CO_2. Signal in all cases captured in a gate of 100 ns. The monochromator resolution was 0.16 nm. Experimental spectra (◇) and best-fit simulations (solid lines) are shown. The insets display the associated rotational distributions. The main branch transitions are indicated. Λ-doublets are unresolved.

Recalling that the vibronically resolved study [5] described in the previous chapter established a moderately large rate constant for vibrational relaxation from $v = 1$ to $v' = 0$ by CO_2 of $(0.7 \pm 0.2) \times 10^{-11}$ cm^3 molecule^{-1} s^{-1}, it is important to check that the spectra are not significantly affected by any contribution from the A-X(0,0) band. The highly

diagonal nature of the A-X band system means that even at rotational resolution, the dispersed measurements are unable to resolve A-X(1,1) and (0,0) emission for low N (≤ 7). The kinetic model previously described reassuringly calculates that, during the 100 ns gate which is most significant in the analysis below, only 0.6% of the emission should arise from the A-X(0,0) band at the pressure used. During the longest gate of 1600 ns, the contribution from $A^2\Delta$, $v' = 0$ emission rises to only about 12% and has consequently been neglected during the analysis.

V-2.2 Initial excitation to $B^2\Sigma^-$, $v = 0$

In the complementary experiments, rotational levels with $N = 4$ and 8 were selectively populated by laser excitation using the $R_1(3)$ and $R_2(7)$ transitions of the B-X(0,0) band. Dispersed fluorescence spectra of the B-X(0.0) band were recorded under the same conditions as used to initially populate the $A^2\Delta$, $v = 1$ level. Temporal gates of 50, 100, 200, 400 and 1400 ns were used. Once again, the resolution was sufficient to resolve emission from individual N levels but not the spin-rotation fine-structure components for any N. The populations in the spin-rotation states were assumed to be statistical, in the same way as for the $A^2\Delta$, $v = 1$ level. Recent work in which the different spin states were resolved [6] has found the same trends as for $A^2\Delta$, $v = 0$ [2]. Again, this is not expected to adversely affect the analysis presented. Typical spectra recorded following excitation to $B^2\Sigma^-$, $v = 0$, $N = 8$ are illustrated in Figure V.4, with population distributions over N, obtained from the spectral simulation, shown as insets. The R-branch has been omitted since it contains significant scattered light from the probe laser. The corresponding spectra after initial pumping of $B^2\Sigma^-$, $v = 0$, $N = 4$ show it to be slightly less robust than $N = 8$. The 100 ns gate is shown in Figure V.5(a).

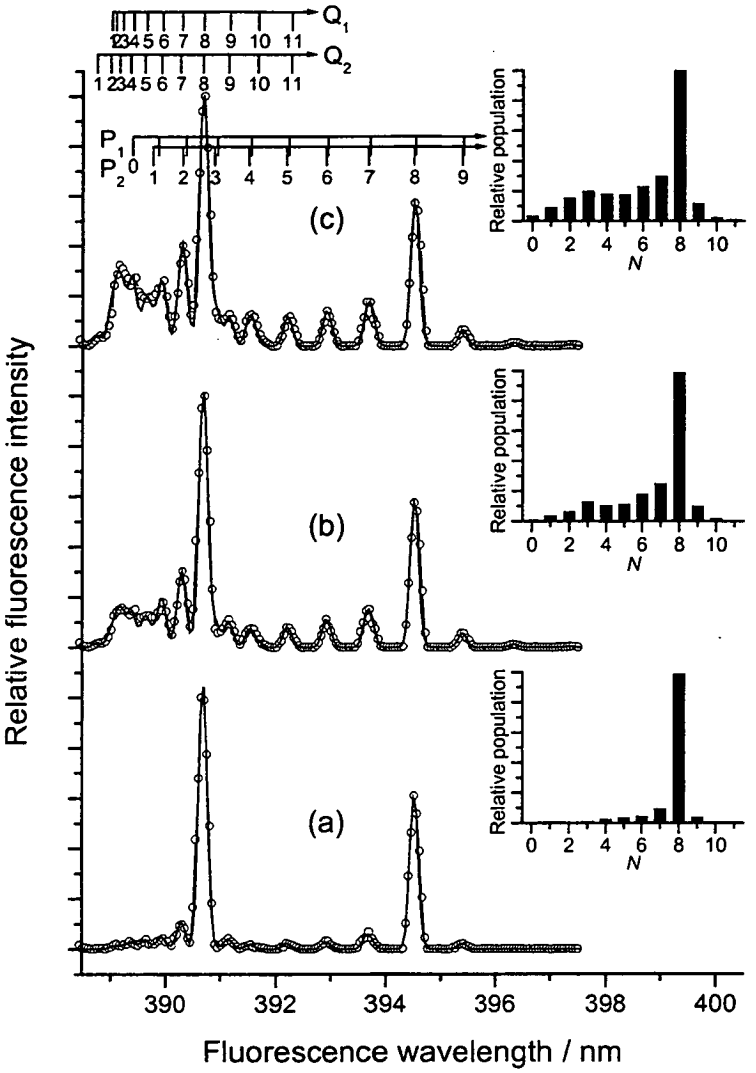

Figure V.4

Dispersed B-X(0,0) fluorescence spectra following excitation of $B^2\Sigma^-$, $v = 0$, $N = 8$ on the B-X(0,0) $R_2(7)$ transition in the presence of 1.1 Torr CO_2. Time gates of (a) 100 ns, (b) 400 ns, and (c) 1400 ns were used to capture the signal. The monochromator resolution was 0.16 nm. Experimental spectra (○) and best-fit simulations (solid lines) are shown. The insets display the rotational population distributions used to produce the simulated spectra. Main branch transitions are indicated.

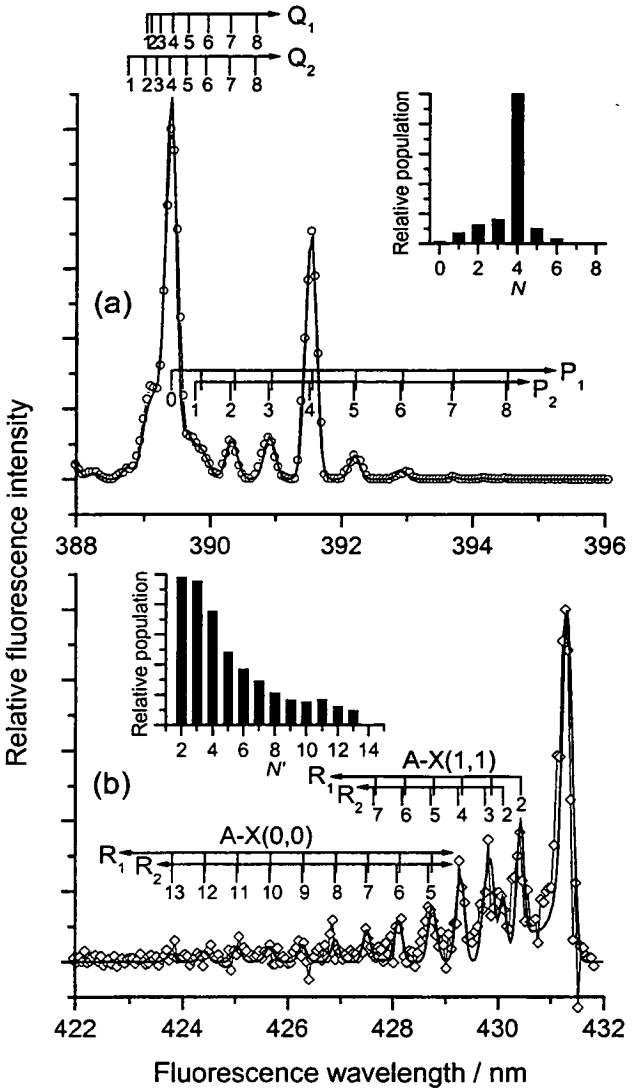

Figure V.5

Dispersed fluorescence spectra recorded on (a) direct B-X(0,0) band and (b) collision-induced A-X(Δv = 0) bands following initial excitation to $B^2\Sigma^-$, v = 0, N = 4 in the presence of 1.1 Torr CO_2. Spectra represent signal captured in 100 ns gate. The monochromator resolution was 0.16 nm. Experimental spectra (○ and ◇) and best-fit simulations (solid lines) are shown, accompanied by the derived population distributions in the insets. Main branch transitions have been indicated.

Table V.1 summarises the fractions of the populations remaining in the initially populated levels in the short (100 ns) gates. The 100 ns gate was found to provide the best compromise between maintaining a significant fraction of the population in the initially pumped rovibronic level and the magnitude of the signal in the collisionally produced state. In the shortest 50 ns gate it was found that there had simply been insufficient population transferred to record spectra with adequate signal-to-noise to derive populations.

Table V.1

Fractions of population[a] remaining in the initially populated rovibronic level, summed over both fine-structure levels, during a 100 ns gate in the presence of 1.1 Torr CO_2.

	Pump $A^2\Delta$, $v = 1$		Pump $B^2\Sigma^-$, $v = 0$
N	F_1	F_2	
2	71%	69%	–
3	69%	65%	–
4	–	–	65%
6	–	61%	–
8	–	71%	79%

V-2.3 Determination of *N*-dependent quenching rates

As described above, the absolute rotational populations as a function of the gate length can be derived from the rotationally resolved spectra. Neglecting rotational transfer, simply summing the population over all observed N for each gate provides the absolute

[a] Typical uncertainties ± 5%, based on reproducibility of fits to experimental data.

populations in the vibronic level. As will be shown below, these can be used to determine the total collisional removal rate constant for that vibronic level, following excitation to a specific initial *N*. The rate constants determined will be directly comparable to those determined in Chapter IV.

Assuming simple first-order kinetics and neglecting any reversible vibronic transfer, the intensity of the fluorescence signal, I_{fl}, as a function of time is given by

$$I_{fl} = c\exp(-k_{tot}t)$$

Equation V.1

where c is a scaling constant and k_{tot}, is the total rate of loss of the initial state, given by

$$k_{tot} = \tau_{rad}^{-1} + k_Q P_Q .$$

Equation V.2

In Equation V.2, τ_{rad}^{-1} is the radiative rate, k_Q is the rate constant for collisional removal and P_Q is the pressure of the collision partner. It follows that the integrated signal, I_{int}, from this vibronic level proportional to the population for a gate of length Δt, can be expressed as

$$I_{\text{int}} = \frac{c}{k_{tot}}(1 - \exp(-k_{tot}\Delta t))$$

Equation V.3

The sum of the rotational population over all observed levels is directly proportional to the total integrated signal and can be fit to Equation V.3. In practice, there are three parameters required for the fit; a scaling constant, equivalent to c/k_{tot}, the

exponent, k_{tot}, and an additional time parameter, required in order to fix the zero-time. This is necessary since, experimentally, positioning the opening of the gates is limited by the temporal resolution of the transient digitiser (10 ns), and the finite duration of the laser pulse (~10 ns) is convoluted with the rising edge of the fluorescence signal. Typical fits to the experimental data are shown in Figure V.6. The rate constants for collisional removal of the vibronic level, k_Q, were obtained from the fitted value of k_{tot} using Equation V.3 and previously reported radiative lifetimes [7, 8]. For $A^2\Delta$, $v = 1$, the lifetime of 534 ± 5 ns is independent of N for all N studied, while a slight N-dependence exists in $B^2\Sigma^-$, $v = 0$, for which lifetimes of 328 ± 8 ns and 360 ± 9 ns were used for $N = 4$ and 8, respectively.

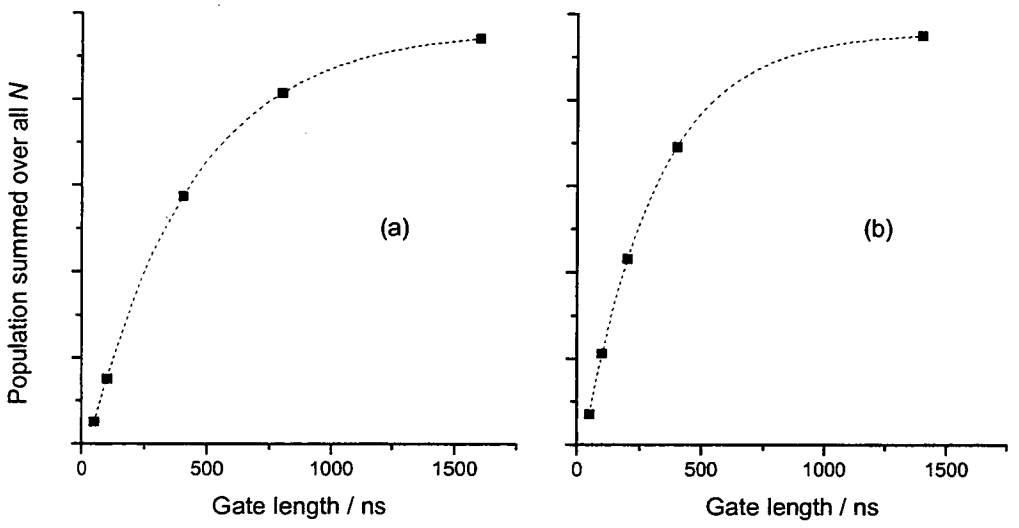

Figure V.6

Representative plots of the total vibronic population (proportional to the integrated signal) against gate length following initial excitation of (a) $A^2\Delta$, $v = 1$, $N = 2$ and (b) $B^2\Sigma^-$, $v = 0$, $N = 8$ in the presence of 1.1 Torr CO_2. Fits to Equation V.3 are shown as dotted lines.

The resulting rate constants and associated uncertainties are presented in Table V.2. Since the equilibration of the spin-orbit components is likely to be the dominant process for the low-N levels in the $A^2\Delta$, $v = 1$ level as is the case for $A^2\Delta$, $v = 0$ [2], the rate constants shown for those levels are averaged over both initial spin states.

Table V.2

Thermal rate constants at 295 K for collisional removal, k_Q, of the initially populated vibronic level in units of 10^{-11} cm^3 molecule^{-1} s^{-1} for CH $A^2\Delta$, $v = 1$ and $B^2\Sigma^-$, $v = 0$ with CO_2.

N	$A^2\Delta$, $v = 1$	$B^2\Sigma^-$, $v = 0$
2[a]	2.4 ± 0.3	–
3[a]	1.6 ± 0.2	–
4	–	1.9 ± 0.6
6	1.9 ± 0.7	–
8	1.2 ± 0.3	1.9 ± 0.4
Ref. 5	$N = 2$ 2.6 ± 0.6	$N = 4$ 1.5 ± 0.4

Values for the total collisional removal rate constants from $A^2\Delta$, $v = 1$, following initial excitation to $N = 2$, and from $B^2\Sigma^-$, $v = 0$, following initial excitation to $N = 4$, have previously been derived by an independent method and discussed in Chapter IV. These values, presented in Table V.2, can be directly compared to those obtained by fitting the

[a] Averaged over both initially populated spin-orbit states.

absolute integrated populations to Equation V.3 since the same rotational levels were initially pumped. As Table V.2 shows, there is favourable agreement between the rate constants obtained *via* the different methods used to determine the rate of collisional loss of population from the entire vibronic level.

It is assumed in applying Equation V.3 that the initial state is not repopulated by secondary collisions, ensuring a fluorescence decay that is described by a single exponential. This is only true in the low-pressure/short time-gate limit [5], under which conditions the effects of secondary vibronic state-changing collisions are negligible. Based on the four-level kinetic model derived in the previous chapter, Figure IV.15 shows that the variation between the observed and the actual total collisional removal rates is marginal at the CO_2 pressure of 1.1 Torr used while recording the rotationally-resolved spectra. Under these conditions, only a minor deviation of the time-resolved fluorescence decay from single exponential behaviour is present, and Equation V.3 should represent the variation of the integrated signal with gate length.

Collisional removal of $A^2\Delta$, $v = 1$ by CO_2, which is mainly attributable to electronic transfer to $B^2\Sigma^-$, $v = 0$ and vibrational relaxation to $A^2\Delta$, $v = 0$, generally appears to become slower with increasing rotational excitation. This trend has also been observed for the quenching of $A^2\Delta$, $v = 0$ by acetone [9, 10] and by CO [11]. This can be interpreted as an anisotropic attractive potential playing a role in the electronic quenching, and therefore $A^2\Delta \rightarrow B^2\Sigma^-$ transfer mechanism, for these collision partners. Hence, greater rotation in the electronically excited CH radical results in a smaller probability of forming a collision complex, necessary to induce the electronic state change. Previous measurements of the total collisional removal rate of the $B^2\Sigma^-$, $v = 0$ level by acetone [10] have found that increasing rotation facilitated removal, suggesting a different mechanism operates and that there could be a barrier in the intermolecular potential. The results obtained for collisional removal of $B^2\Sigma^-$, $v = 0$ by CO_2, which can be accounted for entirely by electronic state

changes to produce the $A^2\Delta$ state, show no dependence on the initial state rotational excitation, although the available data is limited to two rotational levels, both of which are lower than those measured for acetone quenching. It is notable that the rotational levels that show the quenching rate to be *N*-dependent lie close to the predissociation onset. It could be postulated that the perturbation caused by the approach of the collision partner could lead to predissociation rather than transfer to the $A^2\Delta$ state, which accounts for all of the collisionally removed $B^2\Sigma^-$ state at low *N*. Further work to determine the fate of the quenched high-*N* $B^2\Sigma^-$, $v = 0$ radicals is required.

V-3 ROTATIONAL TRANSFER PROPENSITIES

Vibrational relaxation, if possible, and electronic transfer rates, which have already been determined, are the minority collisional processes which remove population from a specific rotational level. This is dominated by rotational energy transfer within the vibronic level, for which typical rate constants are an order of magnitude larger. In principle, the same approach as in Section V-2.3 could be adopted to determine the total collisional removal rate constant for the initial rotational level, since the time-gated high-resolution dispersed fluorescence spectra furnish absolute populations in the initially pumped rotational level. Fitting to Equation V.3, therefore, should yield a value of k_{tot}, which in this case is given by

$$k_{tot} = \tau_{rad}^{-1} + (k_Q + k_{RET})P_Q$$

Equation V.4

where k_Q is the rate constant for processes which remove population from the vibronic level and k_{RET} is the rate constant for all rotational transfer pathways within the initial vibronic

level. In practice, however, application of Equation V.3 in order to obtain the value of k_{RET} is hampered by the increased efficiency of rotationally inelastic collisions over quenching processes. As a result, the rotational population distributions determined, especially from the spectra recorded using longer time gates, are more significantly affected by multiple collisions. Collisional re-population of the initial level results in greater fraction of the population remaining than would be the case if the process was irreversible. This was previously determined at vibronic resolution, for which the fluorescence decay traces for the initially populated level show bi-exponential behaviour. The unsuitability of Equation V.3 is demonstrated by the strong dependence of the magnitude of the k_{tot} parameter on the magnitude of the final point in the data set. The magnitude of k_{tot} increased by up to a factor of two if the longest gate (1400 or 1600 ns) was omitted from the fitting procedure. Overall, the values obtained suggested that rate constants for RET approach gas kinetic rates, but were not thought to be quantitatively reliable.

Time-resolved fluorescence decays with a narrow wavelength resolution, recorded under low-pressure conditions would be more likely to be successful in determining the total rate of loss of the initially populated rotational level. Such measurements have not been made at this stage. The dispersed fluorescence spectra recorded in a short (100 ns) gate, however, are able to furnish the ΔN propensities, displayed in Figure V.7, for rotational energy transfer within the $A^2\Delta$, $v = 1$ or $B^2\Sigma^-$, $v = 0$ vibronic manifolds. The effects of multiple collisions in these spectra can be assumed slight, based on the fraction of population remaining in the initially prepared level. If Poisson statistics are assumed, the ratio of the number of molecules undergoing two state-changing collisions to those suffering only one varies with initial N from ~1:4 to ~1:10.

Since rotationally inelastic collisions, at the level of detail mainly observed in this work, are effecting changes in the nuclear rotation of the CH radical, it is useful to consider the rotational levels in terms of R, rather than N. This is especially the case when

comparing the propensities for rotational transfer in the $A^2\Delta$ and $B^2\Sigma^-$ states. In a Σ state such as the $B^2\Sigma^-$ state of CH, the electronic orbital angular momentum, Λ, is zero and so $N = R$. The $A^2\Delta$ state has $N = R + \Lambda$, where $\Lambda = 2$. The most directly comparable results are therefore the rotational propensities measured following initial excitation to $A^2\Delta$, $v = 1$, $N = 6$ and $B^2\Sigma^-$, $v = 0$, $N = 4$, since for both $R = 4$.

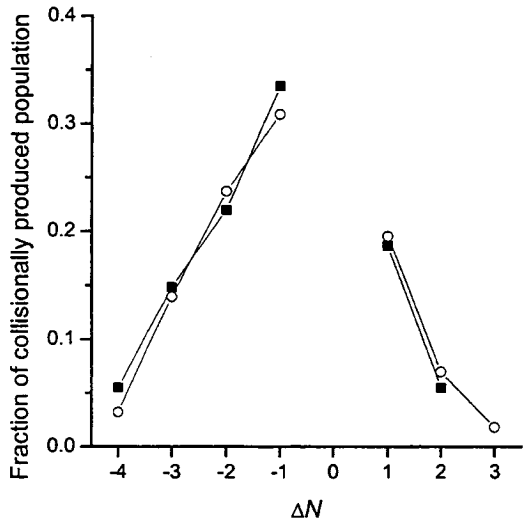

Figure V.7

Propensities for pure rotational energy transfer induced by collisions with CO_2 following excitation to (○) $A^2\Delta$, $v = 1$, $N = 6$, and (■) $B^2\Sigma^-$, $v = 0$, $N = 4$ levels. For both $A^2\Delta$ and $B^2\Sigma^-$, the nuclear rotation quantum number of the initial level is $R = 4$.

The results presented in Figure V.7 show remarkable similarity in the ΔN propensities for rotational transfer in the $A^2\Delta$, $v = 1$ and $B^2\Sigma^-$, $v = 0$ levels induced by CO_2. Although no other rotational levels selected for initial excitation lend themselves so well to direct comparison, there appears to be no significant difference between the $A^2\Delta$ and $B^2\Sigma^-$

states in the range of ΔN observed. This is in contrast to some previous measurements of rotational transfer in the CH radical and will be discussed in more detail below. In all cases, decreasing ΔN propensities are found, with the most probable transfer process being $\Delta N = -1$, where the corresponding product level exists. Discussion of the pure rotational transfer propensities with respect to various fitting laws is reserved until Chapter VI.

V-3.1 Variations in state-to-state rate constants with experimental technique

Previous work on rotational energy transfer in electronically excited CH radicals has followed two different approaches. The first is similar to that adopted in this work and uses a probe laser to prepare electronically excited radicals in specific rotational [12] and, more recently, fine-structure levels with subsequent dispersal of the fluorescence [2, 3, 6]. The second method exploits the spontaneous emission produced when CH radicals are photolytically produced [13, 14, 15, 16]. While both approaches suffer from complications arising from multiple collisions, the difficulties are compounded in the latter experiments since photolysis produces rotationally and vibrationally hot CH. In the absence of any previous results for rotationally inelastic collisions with CO_2, and indeed with any partner for the $A^2\Delta$, $v = 1$ level, discussion of the observed ΔN propensities is limited to contrasting the behaviour of the $A^2\Delta$ and $B^2\Sigma^-$ states with other quenching gases.

Previously, Cooper and Whitehead [14] and Wang *et al.* [15, 16] have used the photolytically produced $B^2\Sigma^- - X^2\Pi$ emission to study RET within $B^2\Sigma^-$, $v = 0$ using Ar and N_2 as the collision partners. In the first instance [14] the state-to-state rate constants were derived from the pressure-dependence of the $B^2\Sigma^-$, $v = 0$ rotational distribution obtained from dispersed fluorescence spectra. In the latter [15, 16], a step-scan Fourier-transform spectrometer was used to record time-resolved fluorescence spectra. Using the same master

equation modelling to account for multiple collisions, both groups found that multiquantum changes up to $\Delta N = \pm 3$ were required to satisfactorily reproduce the experimental spectra.

Most recently, RET within the $B^2\Sigma^-$, $v = 0$ level induced by collisions with Ar has been examined by Kind and Stuhl [6]. These authors prepared specific initial rotational (and fine-structure) levels by laser irradiation of photolytically produced CH $X^2\Pi$. Again, propensities for ΔN up to $\pm$ 3 were observed. This is consistent with the observations of RET in the $B^2\Sigma^-$, $v = 0$ level with CO_2 in this work. Figure V.8 presents a comparison between the ΔN propensities observed for CO_2 and Ar collision partners for rotational transfer out of the $B^2\Sigma^-$, $v = 0$, $N = 4$ level. Decreasing ΔN propensities are observed, although the distribution obtained for collisions with CO_2 appears to be slightly broader than for Ar.

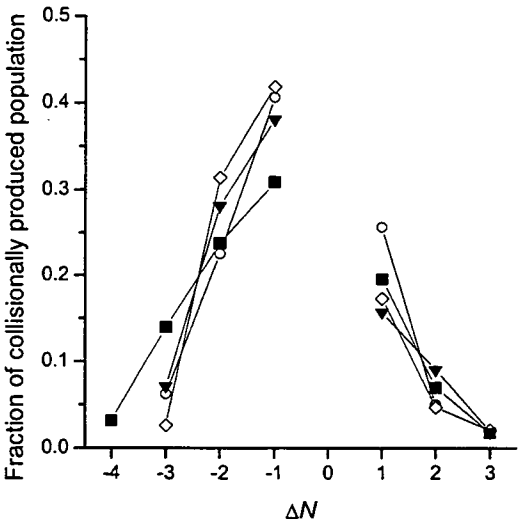

Figure V.8

Comparison of propensities for rotational transfer out of the $B^2\Sigma^-$, $v = 0$, $N = 4$ level in collisions with (■) CO_2 and Ar taken from (○) reference 6, (◇) reference 14 and (▼) reference 16.

Rotational transfer in the $A^2\Delta$, $v = 0$ level was first studied by Dixon *et al.* [12] using He as the collision partner. Laser excitation was used to state-selectively prepare individual rotational levels and the fluorescence was dispersed at rotational resolution. Transitions with $\Delta N = \pm 1$ were found to be dominant, although weaker rotational transfer was observed over a broader range of ΔN. In a similar vein, Dagdigian *et al.* [2] have recently presented a combined experimental and theoretical study on RET in the $A^2\Delta$, $v = 0$ level with Ar as the collision partner. Rotational and fine-structure resolution was achieved. Neglecting for the moment the fine-structure, experimental state-to-state rate constants were found to show Ar capable of causing multiquantum changes, consistent with the observations for He [12]. Measured $N \rightarrow N'$ rate constants decreased with increasing ΔN, as observed for the $B^2\Sigma^-$ state [6, 14, 16]. Good agreement was found between the measured rate constants and the results of quantum scattering calculations based on a recent $CH(A^2\Delta)$-Ar potential surface [17].

Cooper and Whitehead [13] and Wang *et al.* [16] have also measured state-to-state rate constants for rotational transfer within $A^2\Delta$, $v = 0$ with Ar as the collision partner in the same manner as described above for the $B^2\Sigma^-$ state. Cooper and Whitehead [13] found that only $\Delta N = \pm 2$ or ± 1 transitions were required to achieve a satisfactory reproduction of the experimental spectra, with $\Delta N = \pm 1$ dominating at low N. This contrasts with the findings of Dagdigian *et al.* [2] who observed a broader distribution over ΔN. In the work of Wang *et al.* [16] only transitions with $\Delta N = \pm 1$ were included in the model, producing rate constants approximately three times larger than those of Dagdigian *et al.* [2].

The observed ΔN propensities are displayed in Figure V.9, for comparison with the findings of this work for rotational transfer in $A^2\Delta$, $v = 1$ with CO_2 as the collider. The range of ΔN observed for CO_2 can be seen to be slightly broader than for Ar, in accordance with the observations for the $B^2\Sigma^-$ state. These $A^2\Delta$ state propensities with Ar, and those

obtained for collisions with CO_2 in this work, are in marked contrast to those of Cooper and Whitehead [13, 14], as shown in Figure V.9, and Wang *et al.* [15, 16]. Dispersed fluorescence spectra recorded under effectively single-collision conditions following preparation of an individual rotational and fine-structure level should be ideally suited to provide information on the ΔN propensities for a given collision partner. In view of this, and the good agreement between the rate constants measured for $CH(A^2\Delta)$-Ar collisions with the results of the scattering calculations, it appears that the ΔN propensities obtained from analysis of the photolytically produced emission are an artefact of the method.

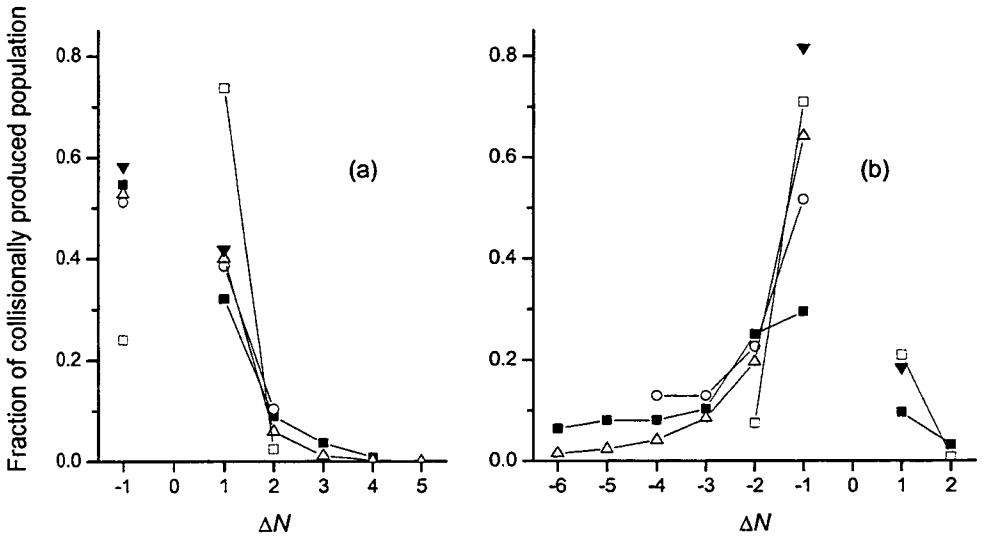

Figure V.9

Comparison of ΔN propensities for rotational transfer in $A^2\Delta$ for initial population in (a) $N = 3$ and (b) $N = 8$. Data shown are from this work (■) for collisions with CO_2. For comparison results for collisions with Ar are also shown. Experimental data taken from (○) reference 2, (□) reference 13, and (▼) reference 16. Theoretical calculations (△) from reference 2 are also included.

V-3.2 Fine-structure conserving/changing propensities

At a higher level of complexity, is the consideration of the fine-structure levels in $A^2\Delta$, $v = 1$, which have been largely neglected up to this point. Initial excitation of $A^2\Delta$, $v = 1$, $N = 2$ allows comparison between the propensities for fine-structure changing transitions with $\Delta N = 0$ and $\Delta N \neq 0$ transitions, although without resolution of the fine-structure in the product levels. This is shown in Figure V.10 for excitation to both fine-structure levels in $N = 2$. For $N = 2$ in $A^2\Delta$, $v = 1$, there is a greater propensity for $F_2 \rightarrow F_1$ transitions than the reverse $F_1 \rightarrow F_2$ process in collisions with CO_2. For $\Delta N \neq 0$ transitions, for which the propensities are summed over both fine-structure levels, the well-known 'exponential-like' decay with increasing ΔN can be clearly seen. Recent results from Dagdigian *et al.* [2] for rotationally inelastic collisions of CH $A^2\Delta$, $v = 0$ with Ar are also shown in Figure V.10. For collisions with Ar, the fine-structure changing transition can be seen to be dominant starting in both F_1 and F_2, an observation supported by quantum scattering calculations. The preference for $F_2 \rightarrow F_1$ transitions over the reverse process observed for CO_2 is mirrored by Ar. This preference is found to decrease with increasing N. It has been suggested [2] that this could be related to the differences in the rotational degeneracy of the F_1 and F_2 levels at low N. According to detailed balance, the rates are

$$(2J_{F_1} + 1)k_{F_1 \rightarrow F_2} = (2J_{F_2} + 1)k_{F_2 \rightarrow F_1}$$

Equation V.5

and the ratio of the rate constants will be inversely proportional to the ratio of the rotational degeneracies. If the total collisional removal rate constants are assumed equal for the F_1 and F_2 manifolds, the ratio $k_{F_1 \rightarrow F_2}/k_{F_2 \rightarrow F_1}$ in this work is 0.77, while the ratio of the degeneracies, is 0.67.

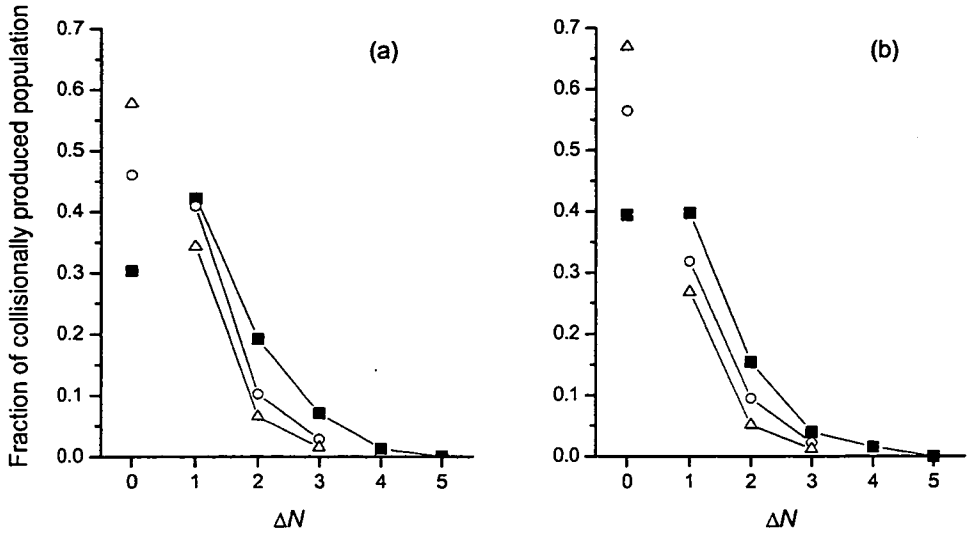

Figure V.10

Experimental ΔN propensities for (■) CH $A^2\Delta$, $v = 1$, $N = 2$ following initial excitation to (a) F_1 level and (b) F_2 level in the presence of CO_2. The data point for $\Delta N = 0$ shows the propensity for the fine-structure changing transition, all other point are summed over both product fine-structure levels. Also shown for comparison are experimental (○) and theoretical (△) propensities following initial excitation to $A^2\Delta$, $v = 0$, $N = 2$ with Ar, adapted from reference 2.

Excitation to $A^2\Delta$, $v = 1$, $N = 3$ provides complementary data on the propensity for conservation (or otherwise) of the fine-structure label for $\Delta N \neq 0$ transitions. The limited resolution of the experiment limits this information to inelastic collisions for which $\Delta N = -1$. Table V.3 presents the results as the ratio of the fine-structure conserving to changing propensities for CO_2 and includes experimental and theoretical results for Ar. For this N, Ar shows a greater propensity to preserve the fine-structure during a $\Delta N \neq 0$ transition.

The propensity to conserve the fine-structure label in $\Delta N \neq 0$ transitions is observed to increase with initial N in collisions with Ar. The interaction potential contains no spin-dependent terms and so cannot directly affect $\boldsymbol{S}$ and the spin is a spectator in the collision. In the Hund's case (b) limit, the magnitude and orientation of $\boldsymbol{N}$, however, can be affected and the subsequent recoupling can lead to a change in the fine-structure label. As $\boldsymbol{N}$ increases, conservation of the orientation is more pronounced following a collision, leading to an increasing propensity for conservation of the fine-structure label.

Table V.3

Ratios of fine-structure conserving to fine-structure changing propensities for $\Delta N = -1$ transitions from $N = 3$ in the $A^2\Delta$, $v = 1$ level for CO_2 and the $A^2\Delta$, $v = 0$ level for Ar.

Collision partner	Pump F_1	Pump F_2
CO_2 [a]	2.0	1.0
Ar [b]	3.9	1.6
Ar [c]	5.8	2.9

[a] This work.

[b] Experimental values for $A^2\Delta$, $v = 0$ taken from reference 2.

[c] Theoretical values for $A^2\Delta$, $v = 0$ taken from reference 2.

V-4 COLLISION-INDUCED FLUORESCENCE SPECTRA

Having characterised the rotational population distribution in the initial state and identified experimental conditions which minimise the extent of relaxation, high resolution dispersed fluorescence spectra of the collisionally populated state were recorded. Gates of length 100 ns were found to result in the best compromise between achieving adequate signal-to-noise in the collisionally produced spectra and the degree of rotational redistribution in the initial state. As described above, Poisson statistics suggest that the initial state distributions be at worst only moderately affected by multiple collisions. The rotational product state distributions can therefore be assumed to represent the effects of single electronic state-changing collisions, with only minimal redistribution in either the initial or product states.

V-4.1 $A^2\Delta$, $v = 1 \rightarrow B^2\Sigma^-$, $v' = 0$ electronic energy transfer

The simplest case to consider, on spectroscopic grounds, is transfer from $A^2\Delta$, $v = 1 \rightarrow B^2\Sigma^-$, $v' = 0$ since the B-X(0,0) band is effectively spectroscopically isolated. Of the other bands in the same region, A-X(2,1) is energetically inaccessible following excitation to $A^2\Delta$, $v = 1$ and A-X(1,0) is exceptionally weak in emission. Thus, emission in this spectral region can, in general, be unambiguously assigned to collisionally produced $B^2\Sigma^-$, $v' = 0$ emission. Dispersed fluorescence spectra on the B-X(0,0) band were recorded under the same experimental conditions used to determine the rotational distribution in the initial $A^2\Delta$, $v = 1$ level.

The time evolution of the B-X(0,0) band following initial excitation to the $A^2\Delta$, $v = 1$, $N = 6$ level is displayed in Figure V.11. In the shortest gate of 100 ns, for which 61% of the population remained in the initial level (see Table V.1), there is a significant asymmetric

peaking of intensity around $N' = 7$. The rotational distribution obtained from the best-fit simulation show in the inset extends over all available N'. The collisional broadening of the distribution is evident in the longer gates. Unfortunately, collision-induced B-X(0,0) dispersed fluorescence spectra could not be recorded with adequate signal-to-noise in the 100 ns gate following initial excitation to $A^2\Delta$, $v = 1$, $N = 8$. Excitation to higher N levels in the $A^2\Delta$ and $B^2\Sigma^-$ states is hampered by the delay between firing the photolysis and probe lasers. This is necessary to allow the spontaneous fluorescence to decay but also results in relaxation of the ground state rotational distribution. In addition, the total collisional removal rate, which transfers population to the $B^2\Sigma^-$, $v = 0$ level, decreases with N as shown in Section V-2.3.

Figure V.12 shows the collision-induced B-X(0,0) spectra and simulations, with associated population distributions, following excitation to the low N levels in $A^2\Delta$, $v = 1$ captured in a gate of length 100 ns. The peak in the product state population distribution is clearly dependent on initial N, a maximum appearing at $N' = N + 1$. Very similar distributions are observed in the collisionally produced $B^2\Sigma^-$, $v = 0$ level following excitation to either initial spin-orbit state. Since the spin-rotation splitting is not resolved in the collisional dispersed fluorescence spectra of the B-X(0,0) band at the current experimental resolution, distributions are given over N only.

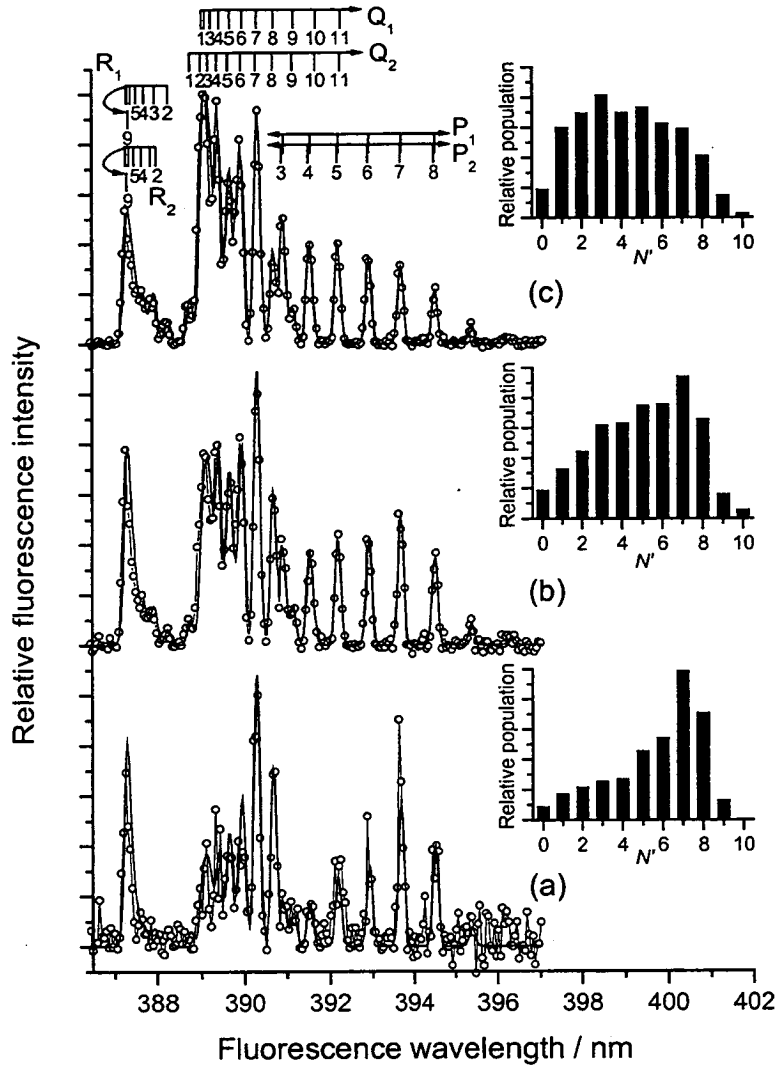

Figure V.11

Collision-induced B-X(0,0) dispersed fluorescence spectra following initial excitation to $A^2\Delta$, $v = 1$, $N = 6$ in the presence of 1.1 Torr CO_2. Gates of length (a) 100 ns, (b) 400 ns, and (c) 1600 ns are shown. The monochromator resolution was 0.16 nm. Symbols (o) represent the experimental spectra while best-fit simulations are displayed using solid lines. The insets display the corresponding rotational population distributions. Main branch transitions have been indicated.

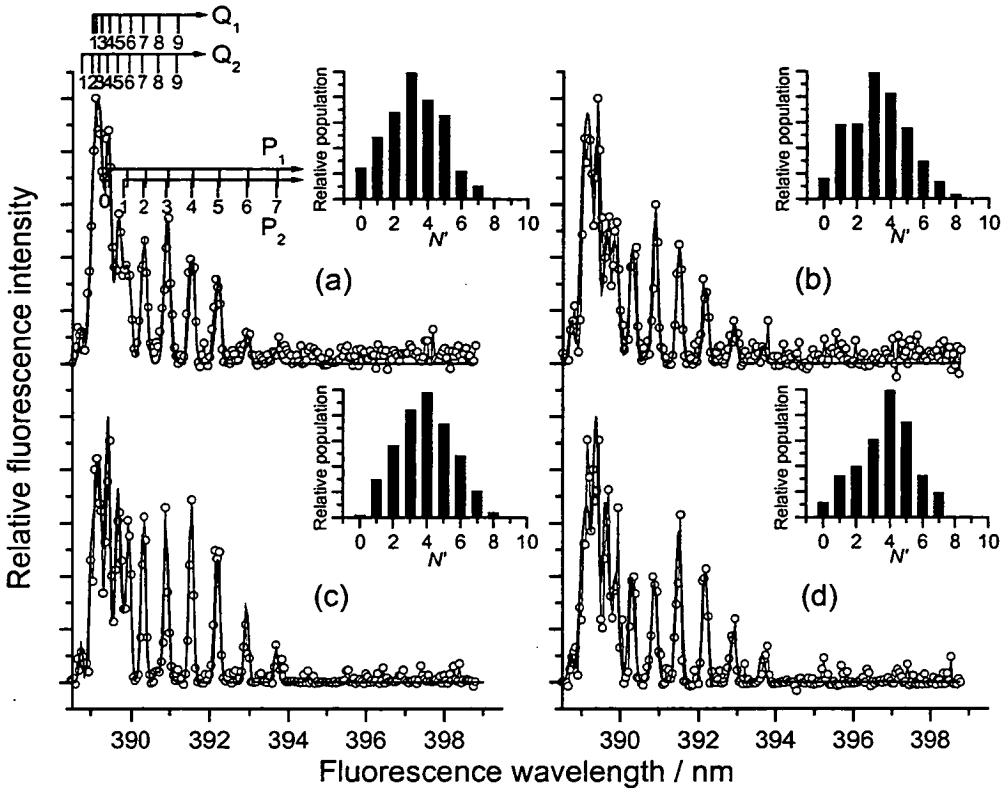

Figure V.12

Collision-induced B-X(0,0) dispersed fluorescence spectra following initial excitation to $A^2\Delta$, $v = 1$ (a) $N = 2$ F_1, (b) $N = 2$ F_2, (c) $N = 3$ F_1, and (d) $N = 3$ F_2 in the presence of 1.1 Torr CO_2. All spectra recorded using gate of 100 ns. The monochromator resolution was 0.16 nm. Experimental spectra (○) and best-fit simulations (solid lines) are shown. The insets show the corresponding population distributions derived from the simulation.

V-4.2 $B^2\Sigma^-$, $v = 0 \rightarrow A^2\Delta$, $v' = 0$ and 1 electronic energy transfer

The electronic energy transfer from $B^2\Sigma^-$, $v = 0$ to $A^2\Delta$ is more complicated than the reverse process described above since, as demonstrated in Chapter 4, collisions can induce transition to both $v' = 0$ and 1, and the aforementioned highly diagonal nature of the A-X band system results in severe overlap of the (0,0) and (1,1) bands. The off-diagonal bands, which are less overlapped, are too weak in emission to resolve at rotational resolution with acceptable signal-to-noise.

Figure V.13 shows collisionally produced A-X spectra on the diagonal bands for three time gates following excitation to $B^2\Sigma^-$, $v = 0$, $N = 8$. The P-branch has been omitted from these spectra since it is overlapped with directly returning emission on the B-X(0,1) which carries about 10% of the fluorescence from $B^2\Sigma^-$, $v = 0$. The spectra have a bimodal appearance, the majority of the intensity appearing in lower N' lines accompanied by a weaker tail extending out to relatively high N' (≤ 14). The collision-induced A-X dispersed fluorescence spectra recorded following excitation to $B^2\Sigma^-$, $v = 0$, $N = 4$ are qualitatively similar. The 100 ns gate spectrum has already been shown in Figure V.5.

The spectral overlap of the A-X(0,0) and (1,1) bands is such that transitions from $A^2\Delta$, $v' = 0$ and 1 can only be distinguished, with the monochromator bandwidth used, for levels with $N' \geq 7$. It is found from the simulation that the emission from the high N' levels can be assigned unambiguously to the A-X(0,0) band. This result is unsurprising since high N' levels in $A^2\Delta$, $v' = 1$ are inaccessible at thermal collision energies (~200 cm^{-1}), as is apparent from Figure V.1. The low N' (≤ 7) section of the R-branch, for which the bands are at best partially resolved, and the Q-branch, which is unresolved for all N', can be satisfactorily simulated by including population in either $A^2\Delta$, $v' = 0$ or 1. The rotational population distributions presented in the insets of Figure V.5 and Figure V.13 are therefore a

total distribution over N', containing a contribution from both vibrational levels. The deconvolution of this distribution into its $A^2\Delta$, $v' = 0$ and 1 components is considered in detail in Chapter VI.

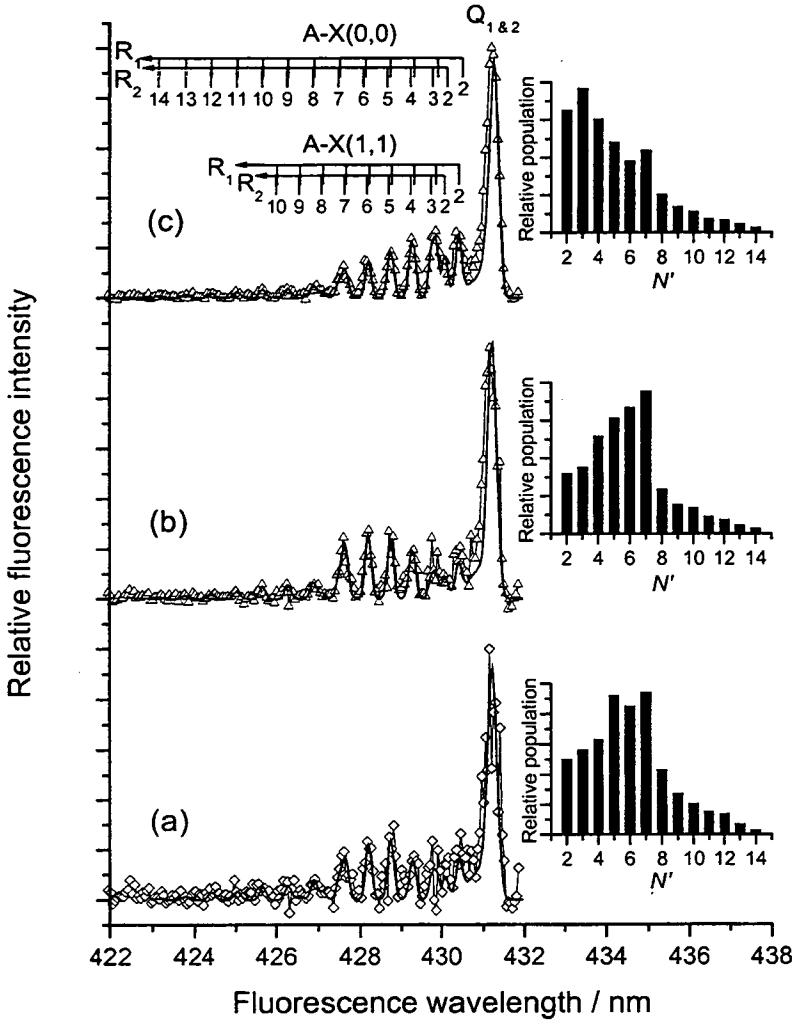

Figure V.13

Collision-induced A-X(Δv = 0) dispersed fluorescence spectra following excitation to $B^2\Sigma^-$, v = 0, N' = 8 in the presence of 1.1 Torr CO_2. The individual panels show (a) 100 ns, (b) 400 ns, and (c) 1600 ns gates. The monochromator resolution was 0.16 nm. Experimental (◇) spectra are displayed along with best-fit simulations (solid lines). The main branch transitions in the A-X(0,0) and (1,1) bands are indicated.

V-5 ELECTRONIC STATE-CHANGING COLLISIONS

The distributions of the population over the product state rotational levels are found, for all initial excitation schemes, to be relatively broad. In general, collisionally transferred population is not constrained to only a few levels centred on the initial level, in terms of either energy or angular momentum. Electronically inelastic collisions most often produce product state rotational distributions which show a distinct propensity for transitions for which $\Delta J \sim 0$ [18]. The distributions observed following $A^2\Delta \leftrightarrow B^2\Sigma^-$ collision-induced transitions in CH clearly do not show a propensity for small changes in angular momentum. There is, however, a residual correlation between the initially populated level and the peak in the product state distribution.

If the N-dependent rate constants for the total rate of electronic transfer were known, absolute state-to-state rate constants, $k(E, v, N) \rightarrow k(E', v', N')$, could, in principle, be determined. However, in previous measurements of the state-to-state rate constants [5], the emission over the complete fluorescence waveforms was used in the analysis. As Figure V.2 and Figure V.4 clearly show, there is substantial, if not complete, rotational equilibration in the long (1600 ns) gate, which covers the entire fluorescence decay trace. The N-dependent quenching rates determined in Section V-2.3 suffer from the same problem. These rate constants are better considered as the rate of removal of the vibronic level, initially peaked in a single N. The absolute ratio of product to parent state emission would have to be known over the short gates used to determine the state-to-state transfer propensities. These measurements have not been performed; hence, only relative N' populations are reported.

The most populated levels are those lying nearby in energy, although the distribution does not necessarily peak in the most isoenergetic level. The most populated product $B^2\Sigma^-$, $v' = 0$ level tends to lie to lower energy than the initially pumped $A^2\Delta$, $v = 1$ level, rather than the most nearly isoenergetic. This is most clearly shown by initial

excitation to the low-N levels in $A^2\Delta$, $v = 1$. Excitation to $A^2\Delta$, $v = 1$, $N = 2$ results in a product state $B^2\Sigma^-$, $v = 0$ distribution which peaks in $N' = 3$, with an exothermic energy gap of -131 cm^{-1}, rather than $N' = 4$, for which ΔE is only -31 cm^{-1}. Similarly, excitation to $N = 3$ yields a product state distribution which peaks in $N' = 4$ ($\Delta E = -115$ cm^{-1}) rather than the nearest level, $N' = 5$ which lies only 10 cm^{-1} above, easily accessible at thermal collision energies. Following excitation to $A^2\Delta$, $v = 1$, $N = 6$, where the rotational energy gaps are larger, the product state population distribution peaks in the $N' = 7$ level. This is the level nearest in energy, with $\Delta E = -80$ cm^{-1}.

The rotational structure of the $A^2\Delta$, $v = 1$ and $B^2\Sigma^-$, $v = 0$ levels is such that levels which have similar energy also have similar values of N. It is useful to again consider the levels in terms of the nuclear rotation, R. $A^2\Delta$, $v = 1 \rightarrow B^2\Sigma^-$, $v = 0$ transfer can therefore be seen to be accompanied by a modest increase in the nuclear rotation. Recalling that for the $A^2\Delta$ state $R = N - 2$, excitation to $N = 2$ ($R = 0$, the rotationless level) the $B^2\Sigma^-$, $v = 0$ distribution peaks in $N' = 3$. The most probable ΔR for all initial $A^2\Delta$, $v = 1$ rotational levels is found to be + 3. This will be discussed more fully in terms of an angular momentum model for electronic transfer [19] in Chapter VI.

Collisional transfer in the $B^2\Sigma^-$, $v = 0 \rightarrow A^2\Delta$ direction is more difficult to interpret. The most populated rotational levels in $A^2\Delta$, $v = 0$ and 1 is masked by the spectral overlap of the A-X(0,0) and (1,1) bands. The high-N' tail of the rotational distribution which can unambiguously be assigned to $A^2\Delta$, $v = 0$, appears to extend to the energetic limit. The product distribution following excitation to $B^2\Sigma^-$, $v = 0$, $N = 8$, however, shows a fairly sharp cut off in the intensity of the lines at $N' = 7$, which is closest in energy, with $\Delta E = 75$ cm^{-1}.

V-6 REFERENCES

1 J. Luque and D. R. Crosley, *"LIFBASE: Database and Spectral Simulation Program (Version 1.6)"*, SRI International Report MP99-009 (1999)

2 M. Kind, F. Stuhl, Y.-Ren Tzeng, M. H. Alexander and P. J. Dagdigian, *J. Chem. Phys.*, **114**, (2001), 4479

3 B. Nizamov, P. J. Dagdigian, Y.-Ren Tzeng and M. H. Alexander, *J. Chem. Phys.*, **115**, (2001), 800

4 C. Murray, H. J. Crichton and K. G. McKendrick, in preparation

5 C. J. Randall, C. Murray and K. G. McKendrick, *Phys. Chem. Chem. Phys.*, **2**, (2000), 471

6 M. Kind and F. Stuhl, *J. Chem. Phys.*, **114**, (2001), 6160

7 J. Brzozowski, P. Bunker, N. Elander and P. Erman, *Astrophys. J.*, **196**, (1976), 414

8 J. Luque and D. R. Crosley, *J. Chem. Phys.*, **104**, (1996), 2146

9 E. Hontzopoulos, Y. P. Vlahoyannis and C. Fotakis, *Chem. Phys. Lett.*, **147**, (1988), 321

10 S. Couris, N. Anastasopoulou and C. Fotakis, *Chem. Phys. Lett.*, **223**, (1994), 561

11 C. Cerezo and M. Martin, *J. Photochem. Photobio. A*, **134**, (2000), 127

12 R. N. Dixon, D. P. Newton and H. Rieley, *J. Chem. Soc., Faraday Trans. 2*, **83**, (1987), 675

13 J. L. Cooper and J. C. Whitehead, *J. Chem. Soc., Faraday Trans.*, **93**, (1993), 1287

14 J. L. Cooper and J. C. Whitehead, *J. Phys. Chem.*, **98**, (1994), 8274

15 C.-C Wang, T.-L. Chin and K.-L. Lin, *J. Chem. Phys.*, **107**, (1997), 10348

16 C.-C. Wang, Y.-P. Chen, T.-L. Chin, H.-Y. Huang and K.-C. Lin, *J. Chem. Phys.*, **112**, (2000), 10204

17 G. Kerenskaya, A. L. Kaledin and M. C. Heaven, *J. Chem. Phys.*, **115**, (2001), 2123

18 P. J. Dagdigian, *Annu. Rev. Phys. Chem.*, **48**, (1997), 95

19 A. J. McCaffery and R. J. Marsh, *J. Chem. Phys.*, **115**, (2001), 9771

VI CONCLUSIONS

VI-1 ROTATIONAL ENERGY TRANSFER WITHIN THE $A^2\Delta$ AND $B^2\Sigma^-$ STATES

A study of rotationally inelastic collisions within the initially prepared vibronic states was not a primary aim in recording the higher resolution dispersed fluorescence spectra discussed in Chapter V. Reliable absolute state-to-state rate constants for rotational transfer within $A^2\Delta$, $v = 1$ and $B^2\Sigma^-$, $v = 0$ induced by collisions with CO_2 were not therefore determined. The results obtained, however, suggest values of the order of 1×10^{-10} cm^3 molecule^{-1} s^{-1}, consistent with previous measurements [1, 2, 3, 4, 5, 6] of rotational energy transfer within the $A^2\Delta$, $v = 0$ and $B^2\Sigma^-$, $v = 0$ levels with other collision partners.

As discussed in Chapter V, studies of rotational transfer in which the electronically excited CH was produced directly in the photolysis process [2, 3, 4] have reported a propensity for a narrower range of ΔN in $A^2\Delta$ than in $B^2\Sigma^-$. In order to explain the apparently greater propensity for multiquantum changing collisions in the $B^2\Sigma^-$ state, it was suggested that the intermolecular potential between it and the collision partner is attractive, leading to formation of a collision complex. The intermolecular potential for the $A^2\Delta$ state was thought to be repulsive, and the propensity for single quantum changing collisions pointed to impulsive energy transfer on a repulsive potential. These findings are contradicted by the results of state-selective techniques [1, 5, 6, 7], which show evidence of multiquantum changes in both the $A^2\Delta$ and $B^2\Sigma^-$ states. Dispersed fluorescence measurements of the evolution of the rotational population distribution following the clean preparation of an individual level are ideally suited to determine ΔN propensities. Thus, it can be concluded that there is no evidence on this basis of the intermolecular potential

between the collision partner and the $B^2\Sigma^-$ state being more attractive than for the $A^2\Delta$ state, in relation to rotational energy transfer.

The propensity for conservation of the fine-structure label accompanying $\Delta N \neq 0$ rotationally inelastic collisions within $A^2\Delta$, $v = 1$ is found to be smaller for CO_2 than for Ar [5], although the data set is very limited. This could suggest that collisions with CO_2 cause a more substantial re-orientation of N, than Ar. A more extensive data set over a greater range of initial N is clearly required before any conclusions can be drawn.

VI-1.1 Applicability of fitting laws

The data obtained can be used to test fitting laws for rotational transfer, assuming the populations in the product rotational levels, N_{j_f}, to be directly proportional to the rate constant for the process, $k_{j_i \to j_f}$. This assumption will hold for a population distribution produced under single collision conditions.

The exponential-gap law (EGL) was first proposed by Polanyi and Woodall [8], following the observation that a non-Boltzmann rotational distribution of HCl relaxes without generating a peak at intermediate J. It can be written as [9]

$$k^{EGL}_{j_i \to j_f} = a \exp\left(-b|\Delta E|\right) N_\Delta R(\Delta E)$$

Equation VI.1

where a and b are free parameters and ΔE is the rotational energy gap. $R(\Delta E)$ is a translational phase space factor [9, 10, 11] and N_Δ is a so-called spin degeneracy factor, which can be calculated for the m_J-randomising case using

$$N_{\Delta} = 2j_f + 1$$

Equation VI.2

and for the m_j-conserving case by

$$N_0 = \frac{2j_< + 1}{2j_i + 1}$$

Equation VI.3

where $j_<$ is the smaller of j_i and j_f.

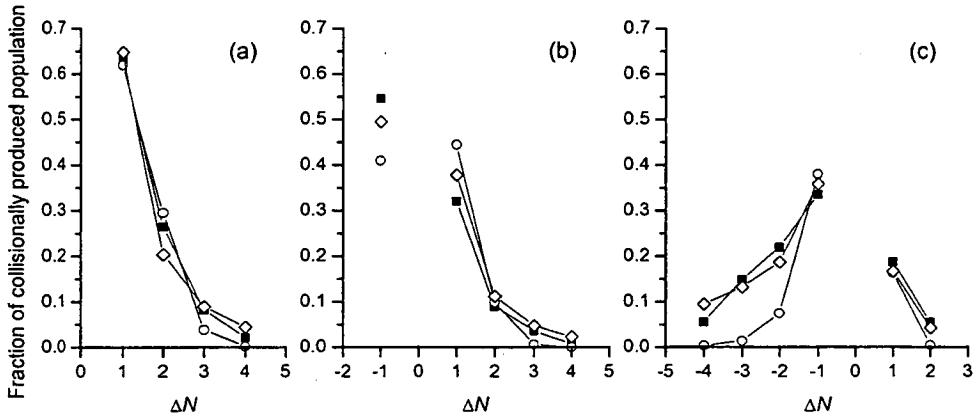

Figure VI.1

Comparison of experimental rotational transfer propensities in $A^2\Delta$, v = 1 induced by collisions with CO_2 (■) with best fits using exponential-gap law (○) and statistical power-gap law with N_{Δ} degeneracy factor (◇). Initial excitation to (a) $N = 2$, (b) $N = 3$, and (c) $N = 6$.

In the statistical power-gap law (SPG), the exponential term is replaced by a power-law dependence on the rotational energy gap. It can be expressed as

$$k^{SPG}_{j_i \to j_f} = a\left|\frac{\Delta E}{B}\right|^{-\alpha} N_\lambda R(\Delta E)$$

Equation VI.4

where B is the rotational constant. The parameters a and α are varied in the fit. N_λ is a generalised form of the degeneracy factor, given by Brunner and Pritchard [9], for which $|\Delta m_j| \leq \lambda$ and provides an additional fitting parameter. In practice, use of N_λ produced physically unrealistic values of λ and fits were carried out using the two extreme cases of the degeneracy factor, N_0 and N_Δ. For both the EGL and SPG laws, fits were carried out globally, using RET data from all rotational levels within a given electronic state.

Typical fits for rotational transfer in the $A^2\Delta$, $v = 1$ level induced by collisions with CO_2 are shown for comparison in Figure VI.1. The results of fitting to the experimental data obtained for the $B^2\Sigma^-$, $v = 0$ level are similarly displayed in Figure VI.2. Since no significant difference was observed in the fits using the SPG law with the N_0 and N_Δ degeneracy factors, only fits obtained using N_Δ are shown for clarity. The best-fit parameters are presented in Table VI-1.

The exponential-gap and statistical power-gap laws can be seen in Figure VI.1 to produce reasonably satisfactory fits to the experimental data for the $A^2\Delta$, $v = 1$ level at low initial N. For higher initial N, however, the SPG law does better as the EGL fit drops off too rapidly for larger ΔN. Both models failed to reproduce the experimental RET data for initial excitation of $A^2\Delta$, $v = 1$, $N = 8$. For RET within the $B^2\Sigma^-$, $v = 0$ level, the EGL and SPG laws can be seen in Figure VI.2 to have only moderate success at reproducing the experimental data.

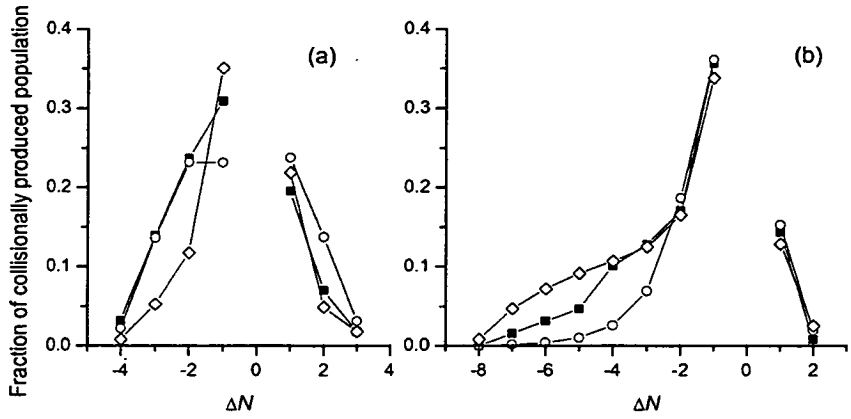

Figure VI.2

Comparison of experimental rotational transfer propensities in $B^2\Sigma^-$, $v = 0$ induced by collisions with CO_2 (■) with best fits using exponential-gap law (○) and statistical power-gap law with N_Δ degeneracy factor (◇). Initial excitation to (a) $N = 4$ and (b) $N = 8$.

Table VI-1

Global best fit parameters obtained from application of exponential and statistical power-gap fitting laws to experimental rotational transfer data for CH $A^2\Delta$, $v = 1$ and $B^2\Sigma^-$, $v = 0$ in collisions with CO_2.

	EGL	SPG-N_0	SPG-N_Δ
	b	α	α
$A^2\Delta$, $v = 1$	4.5	3.1	3.4
$B^2\Sigma^-$, $v = 0$	2.7	3.7	3.7

It would be desirable to use the fitted parameters to predict the rotational re-distribution from levels not initially populated experimentally. In this context, the EGL and SPG fitting laws show only limited applicability. In addition, the use of such empirical fitting laws does not provide much insight into the factors governing the outcome of a rotationally inelastic collision, since it is difficult to attach much physical meaning to the derived fitting parameters.

VI-1.2 Prior distributions in rotational transfer

If the product levels are populated on purely statistical grounds, based only on degeneracy and on the excess energy available for translation, the distribution will be a so-called statistical prior. If angular momentum constraints are neglected, this amounts to a simplified application of phase space theory. For pure rotational transfer, a prior distribution is expected to be a poor representation of the observed distribution. Complete randomisation of the available energy over the rotational levels requires a relatively long interaction with the collision partner. Rotational energy transfer, however, is often expected to occur in the sudden or impulsive limit. Prior distributions are introduced at this point for later comparison with the rotational distributions observed following electronic state changes (Section VI-3.2).

Calculation of prior distributions has been carried out at several levels of complexity, depending on the assumed internal structure of the CO_2 collision partner. At the simplest level, for which the collision partner is assumed to be structureless, the prior probability of forming a given CH(v', j') product level, $P^0(v', j')$, is given by [12]

$$P^0(v', j') \propto (2j'+1)(E - E_{v',j'})^{1/2}$$

Equation VI.5

where $E_{v'j'}$ is the energy of the product level and E is the total available energy. In this 'spherical' prior calculation, E is given by the sum of the energy of the initially populated level plus a contribution from the average relative translational energy of the collision pair, given by $\frac{3}{2}kT$. A temperature of 295 K was used in all calculations.

In contrast, if CO_2 is considered capable of absorbing its statistical share of the total available energy in its internal degrees of freedom, the product CH internal state distribution can be predicted by

$$P^0(v', j') \propto (2j'+1)\sum_{v'',j''}(2j''+1)\left(E - E_{v',j'} - E_{v'',j''}\right)^{1/2}$$

Equation VI.6

where $E_{v''j''}$ is the energy of the post-collision CO_2 rovibrational level (v'', j''). The total available energy, E, is taken to include an additional contribution of kT for the average initial internal energy of the CO_2 linear rotor. Thermal energy in vibration was considered to be negligible and hence was omitted. The more complete treatment of Equation VI.6 includes the CO_2 vibrational, v'', and rotational, j'', structure. If the vibrations are neglected, the summation is carried out only over the rotational levels in the vibrational ground state.

A comparison between the experimentally observed rotational distributions in the initially pumped vibronic level and the calculated priors is presented in Figure VI.3. For initial excitation to low N levels, $A^2\Delta$, $v = 1$, $N = 2$ and $B^2\Sigma^-$, $v = 0$, $N = 4$, the 'rotor' prior distributions are a reasonably satisfactory prediction. However, this is likely to be accidental due to the limited range of N' levels that are available. The deviation from a statistical process is illustrated clearly in Figure VI.3(a) and (c), for which higher N levels were initially populated. For these more discriminatory levels, the prior clearly fails to predict the propensities for negative ΔN.

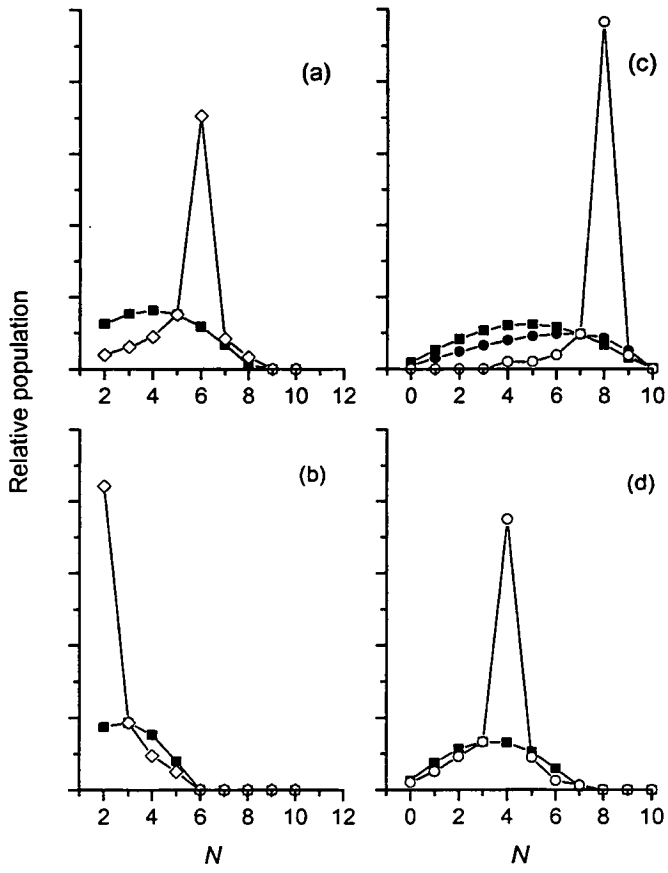

Figure VI.3

Best-fit experimental rotational distributions (◇ and ○) for the vibronic levels in the presence of 1.1 Torr CO_2 in a gate of length 100 ns and calculated prior distributions assuming CO_2 to be structureless (●) and a rigid rotor (■). Panels (a) $N = 6$ and (b) $N = 2$ in $A^2\Delta$, $v = 1$, and (c) $N = 8$ and (d) $N = 4$ in $B^2\Sigma^-$, $v = 0$. Prior distributions have been scaled to match the experiment at $\Delta N = -1$(a, c and d) and +1 (b).

VI-1.3 Kinematic model

In the fitting laws discussed previously, the probability of a state resolved process, $p(j_i \rightarrow j_f)$, has been related to the energy gap, ΔE. McCaffery and co-workers [13,

14] have proposed an alternative model in which $p(j_i \rightarrow j_f)$ is controlled by angular momentum factors within constraints set by energy conservation.

The mechanism for rotational transfer involves the conversion of linear to angular momentum at the repulsive wall of the anisotropic part of the intermolecular potential. In a simple picture, this can be represented as a hard ellipse (or more precisely as a series of hard ellipses [15]). In the classically impulsive limit, the collision of the partner with the surface of the ellipse provides an instantaneous impulse, which can change the rotational angular momentum *via* a torque arm, or effective impact parameter, b_n. This is defined as the perpendicular distance between the centre-of-mass of the molecule and the line of transferred momentum. The orbital angular momentum available in the collision, l_i, is given by

$$l_i = \mu v_n b_n$$

Equation VI.7

where μ is the reduced mass of the collision pair and v_n is the component of the relative velocity perpendicular to the surface. The parallel component is assumed to be unaffected by the collision.

The threshold relative velocity, v_{th}, for opening a specific Δj channel with full utilisation of the available linear momentum is

$$v_{th} = \frac{\Delta j}{\mu b_n^{\max}}$$

Equation VI.8

where b_n^{max} is the maximum available torque arm, determined by the anisotropy of the ellipse. In homonuclear diatoms, this is commonly found to be half the bond length [14]. In a recent investigation into the effects of inelastic collisions on the OH radical, use of a Monte Carlo trajectory calculation [16], suggested two effective torque arms, corresponding approximately to the distance from the centre-of-mass to the O or the H atom, although the exact values were slightly dependent on the assumed shape of the molecule. In this work, the maximum effective impact parameter for CH is assumed equal to the distance from the centre-of-mass to the H atom. Thus, b_n^{max} in the $A^2\Delta$ state is 1.02 Å, while the $B^2\Sigma^-$ state has a slightly larger effective impact parameter of 1.07 Å.

For conversion of all available relative kinetic energy into rotational energy, the channel-opening condition for an initially rotating molecule is given by [13, 14]

$$v_{th} = \sqrt{\frac{2B\Delta j(\Delta j + 2j_i + 1)}{\mu}}$$

Equation VI.9

where B is the rotational constant and j_i is the initial rotational level. Since the model deals only with the nuclear rotation, j in this notation is equivalent to R, as used in Chapter V.

A third equation can be derived which simultaneously conserves both energy and angular momentum. For the case of an initially non-rotating molecule, $j_i = 0$, the threshold channel-opening velocity can be given by [13, 14]

$$v_{th} = \frac{\Delta j\left(\mu b_n^{max\,2} + I\right)}{\mu b_n^{max}}$$

Equation VI.10

where I is the moment of inertia of the diatom.

A useful representation of the predominance of energy or angular momentum constraints is provided by velocity-angular momentum (v_r-Δj) plots [17]. Such plots represent the threshold relative velocities for opening specific Δj (ΔR) channels for the system. If the internal structure of the CO_2 collision partner is neglected, a v_r-Δj plot for CH rotational transfer can be constructed using only the CH equilibrium bond lengths, r_e, atomic masses and the rotational constants. Figure VI.4 shows the v_r-Δj plot for initial excitation to the $R = 4$ level in $A^2\Delta$, $v = 1$ and $B^2\Sigma^-$, $v = 0$.

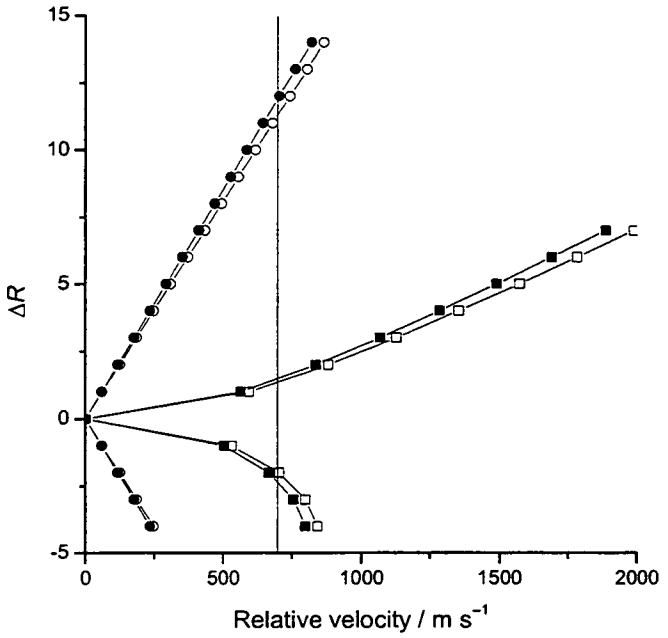

Figure VI.4

Velocity-angular momentum plot showing channel opening velocities for collisions between $R = 4$ CH $A^2\Delta$, $v = 1$ (open symbols) and $B^2\Sigma^-$, $v = 0$ (solid symbols) and CO_2. Threshold velocities calculated using "angular momentum" Equation VI.8 (○, ●) and "energy" Equation VI.9 (□, ■) are shown. The vertical line shows the most probable relative velocity assuming a Maxwell-Boltzmann distribution at 295 K.

Figure VI.4 clearly shows that greater relative velocities are required to satisfy the requirements of energy conservation than of angular momentum conservation and, as for collisions between OH and Ar [16], the system is very strongly energy constrained for all values of ΔR. This is unsurprising for a hydride, which has a relatively long torque arm, facilitating the conversion of linear to angular momentum in Equation VI.9, but a large rotational constant, resulting in large energy gaps between adjacent rotational levels.

The influence of energy constraints can be usefully illustrated if the probability of angular momentum transfer is considered. Given a standard Maxwell-Boltzmann distribution of relative velocities, the angular momentum available, l, is dependent on the effective impact parameter, b_n. This is written as a conditional probability $P(l|b_n)$, for which an analytical expression has been derived [14]. An inverse power law

$$P(b_n) = b_n^{-\gamma}$$

Equation VI.11

has been suggested to provide a reasonable representation of the anisotropic part of the intermolecular potential [13, 14]. The parameter γ provides an indication of the 'hardness' of the repulsive wall. Typical values of γ are around two from best fits to scattering data [///]. A joint probability distribution can be derived as the product of the two distributions,

$$P(l, b_n)db_n dl = P(l|b_n)P(b_n)db_n dl$$

Equation VI.12

and is plotted in Figure VI.5 for positive ΔR in the $A^2\Delta$ state. The energetic constraints can be clearly seen to cut a slice out of the probability density, limiting the range of ΔR. Qualitatively, plots such as Figure VI.4 and Figure VI.5 suggest that only a very limited

range of ΔN should be observable. The decreasing propensities commonly observed in rotational transfer, as they are for $CH(A^2\Delta, B^2\Sigma^-)$-$CO_2$ collisions in this work, can be explained by the exponential decay in the Maxwell-Boltzmann distribution at high relative velocities and the functional form of $P(b_n)$.

According to McCaffery, the effect of the energy constraint is a restriction in the range of values b_n^{max} is able to adopt. A reduced value of the maximum effective impact parameter can be calculated *via* the equation for simultaneous conservation of energy and angular momentum, Equation VI.10. In general, the reduced value of b_n^{max} is calculated for each ΔR channel, although it is independent of ΔR for the case of an initially non-rotating molecule. Low ΔR channels experience the greatest reduction in the maximum allowed torque arm. The reduced value of b_n^{max} plays a key role in a transfer function derived by Osborne and McCaffery [14]. The overall probability of a given rotational transfer channel is controlled by the range of allowed b_n. In effect, the channel-dependent reduced b_n^{max} is an artificial construct, since the maximum effective torque arm is a function of the system, determined by the repulsive anisotropy of the intermolecular potential, rather than a variable parameter. The virtual or apparent reduction in the torque arm effectively prevents trajectories that provide sufficient angular momentum, but fail to satisfy energy conservation, from contributing to that ΔR channel. However, the model does not provide an explanation for what the outcome of such a trajectory would be.

In this model, the $A^2\Delta$ and $B^2\Sigma^-$ state differ only in their bond lengths and, therefore, in the length of the torque arm. Since this difference is small, the rotational transfer propensities are predicted to be similar, as observed experimentally in collisions with CO_2 [7] and with Ar [5, 6]. The reduced mass for the CH-CO_2 system is almost identical to that for CH-Ar. The broader ΔR distribution observed for collisions with CO_2 must therefore be attributed to its internal structure. CO_2 has a small rotational constant in

comparison with CH and so can contribute some rotational angular momentum initially, but probably more significantly absorb a lot during the collision. Since the observed distributions are only slightly broader, it is anticipated that this does not play a very significant role in influencing the CH rotational distribution.

Recently Marsh and McCaffery [18] have extended the kinematic model described above to diatom-diatom collisions. Monte Carlo trajectory calculations on the Na_2-H_2 system showed good agreement with experimental state-to-state cross sections. Such calculations have not yet been attempted for the CH-CO_2 system.

The kinematic model provides a conceptually simple physical explanation for rotational transfer and provides predictive power when coupled with Monte Carlo trajectory calculations. The use of velocity-angular momentum plots clearly illustrates the extent to which energetic considerations provide the dominant constraints for rotational transfer in hydrides. However, the model only deals with the effects of rotationally inelastic collisions on the nuclear rotation. The kinematic model contains no mechanism for explaining the fine-structure changing/conserving propensities observed in this work for collisions with CO_2 and with Ar [5, 6]. A greater test for CH would be provided by a wider range of collision partners with more substantially different reduced masses to explore whether the model can correctly predict the relative efficiencies for rotational energy transfer.

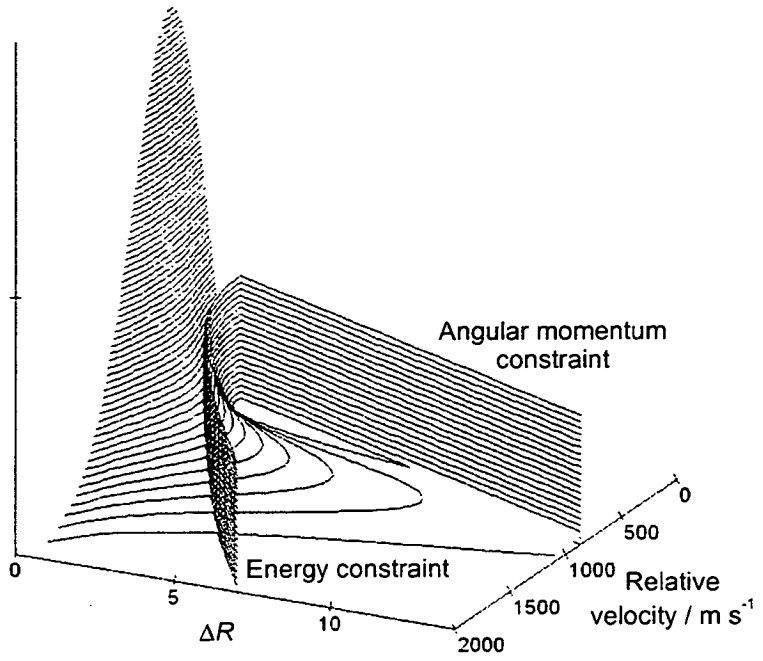

Figure VI.5

Probability density distribution of available angular momentum for collisions between CH($A^2\Delta$, v =1, R = 4) and CO_2 at 295 K, showing angular momentum and energy constraints. Calculations performed using b_n = 1.02 Å and γ = 2. Negative values of ΔR are not shown.

VI-2 VIBRATIONAL RELAXATION WITHIN $A^2\Delta$

Using the four-level kinetic analysis described in Chapter IV, a room temperature (~295 K) rate constant of (0.7 ± 0.2) × 10^{-11} cm^3 $molecule^{-1}$ s^{-1} was determined for $v = 1 \rightarrow 0$ vibrational relaxation within the $A^2\Delta$ state of CH induced by collisions with CO_2. This is of comparable magnitude to the rate constant for total electronic quenching of the $A^2\Delta$, v = 1 level, which is dominated by electronic energy transfer to the $B^2\Sigma^-$ state, of (1.9 ± 0.4) × 10^{-11} cm^3 $molecule^{-1}$ s^{-1}. A rate constant for vibrational relaxation in the $B^2\Sigma^-$ state was not determined in this work.

There are no previously reported rate constants for vibrational relaxation in the $A^2\Delta$ state with CO_2 as the collision partner. Rate constants of 0.50×10^{-11} and 0.15×10^{-11} cm^3 $molecule^{-1}$ s^{-1} for Ar and N_2 colliders, respectively, have been derived from the analysis of photolytically produced CH $A^2\Delta$ by Cooper and Whitehead [2]. Thus, CO_2 shows comparable behaviour to purely physical (that is, structureless) quenchers.

A recent study by Steffens and Crosley [19] has reported rate constants and cross-sections for electronic quenching and vibrational relaxation of the $A^2\Sigma^+$, $v = 1$ level of the OH radical over a range of temperatures. When CO_2 is used as the collision partner, the rate constant for vibrational relaxation at 295 K, measured to be $(22.7 \pm 2) \times 10^{-11}$ cm^3 $molecule^{-1}$ s^{-1}, is approximately a factor of thirty larger than for CH($A^2\Delta$, $v = 1$) measured here. Electronic quenching occurs with a similar efficiency to vibrational relaxation for OH($A^2\Sigma^+$, $v = 1$). The increase in the cross-sections for vibrational transfer with decreasing temperature can be rationalised by a model in which multipole attractive forces dominate [20]. Although the temperature dependence has not been measured in this work for CH($A^2\Delta$, $v = 1 \rightarrow 0$) relaxation, the smaller magnitude of the rate constant could suggest that the intermolecular potential is less attractive than for OH($A^2\Sigma^+$).

Vibrational relaxation in CH($A^2\Delta$) and OH($A^2\Sigma^+$) is generally significantly faster than in the corresponding $X^2\Pi$ electronic ground states. Recently, Blitz *et al.* [21] have presented results for vibrational relaxation of CH($X^2\Pi$, $v = 1, 2$) by He and Ar. A thermal rate constant for $v = 1 \rightarrow 0$ relaxation of $(3.62 \pm 0.32) \times 10^{-14}$ cm^3 $molecule^{-1}$ s^{-1} was reported for collisions with Ar at 295 K, which is two orders of magnitude smaller than that reported for VET in CH($A^2\Delta$) by Cooper and Whitehead [2]. Similarly, the thermal rate constant for $v = 1 \rightarrow 0$ vibrational relaxation in OH($X^2\Pi$) in collisions with CO_2 has been reported by Raiche *et al.* [22] to be 2.2×10^{-13} cm^3 $molecule^{-1}$ s^{-1}, which is a factor of one thousand smaller than for the $A^2\Sigma^+$ state [19]. With Ar as the collision partner, rate constants

for $v = 1 \rightarrow 0$ relaxation of $< 1 \times 10^{-14}$ cm^3 molecule^{-1} s^{-1} for the $X^2\Pi$ state [23] and $(0.41 \pm 0.03) \times 10^{-11}$ cm^3 molecule^{-1} s^{-1} for the $A^2\Sigma^+$ state [24] have been reported.

Ab initio calculations have shown the OH($A^2\Sigma^+$)-Ar potential to be significantly more attractive than that for OH($X^2\Pi$)-Ar [25, 26]. It has been suggested [22] that the greater attraction and closer approach in OH($A^2\Sigma^+$)-Ar facilitates the mixing of the vibrational levels. The intermolecular potentials between CH($A^2\Delta$ and $X^2\Pi$) and Ar, however, have been found to have similar attractive wells [27, 28], implying that other factors may be responsible for the observed differences in the efficiencies of vibrational relaxation in ground and electronically excited states.

VI-3 $A^2\Delta \leftrightarrow B^2\Sigma^-$ ELECTRONIC TRANSFER

In addition to the practical consequences of inter-electronic state collisional energy transfer for quenching measurements and flame diagnostics, discussed in Chapter IV, such processes are also of fundamental interest. In Chapter I, models for electronically inelastic collisions were introduced. The results determined in this work provide further data against which these models can be tested.

VI-3.1 Applicability of Franck-Condon and energy gap model

At the vibronic level, the results presented in Chapter IV provide an opportunity to examine some of the simpler energy transfer models suggested. The vibronic branching ratio between the $A^2\Delta$, $v = 1$ and $v = 0$ levels following initial excitation of $B^2\Sigma^-$, $v = 0$ can be used to test the predictions of a previously suggested scaling law relating to the Franck-Condon overlap, $q_{v,\,v'}$ and the vibronic energy gap, $\Delta E_{v,\,v'}$ [29]. The rate constant, $k_{Ev,E'v'}$, relating a pair of vibronic levels is given by

$$k_{Ev,E'v'} \approx k^{el}_{E,E'} q_{v,v'} \exp\left(-\frac{\Delta E_{Ev,E'v'}}{kT}\right)$$

Equation VI.13

Clearly, the Franck-Condon factors required for the $B^2\Sigma^- - A^2\Delta$ system are not amenable to direct optical measurement on account of the $\Delta\Lambda = 0, \pm 1$ selection rule for electric dipole transitions. Consequently, the standard Rydberg-Klein-Rees (RKR) method was used to construct a potential curve for the $A^2\Delta$ state, based on the molecular constants of Zachwieja [30]. A compound potential for the $B^2\Sigma^-$ state was constructed using a combination of RKR analysis of the two bound vibrational levels with the addition of an artificial barrier to dissociation as has been described previously [31]. The molecular constants for the $B^2\Sigma^-$ state were those of Kepa *et al.* [32]. Radial wavefunctions and Franck-Condon factors were then calculated using LeRoy's LEVEL program [33].

The Franck-Condon factors for the $B^2\Sigma^- - A^2\Delta$ system were calculated to be $q_{00} = 0.812$ and $q_{01} = 0.161$. This gives a q_{00}/q_{01} ratio of ~ 5, which is less than the value of ~ 8 mentioned in passing by other authors previously [34]. Using the lowest rotational levels, the respective vibronic energy gaps are $|\Delta E_{00}| = 2452$ cm^{-1} and $|\Delta E_{01}| = 284$ cm^{-1}. According to Equation VI.13, the electronic energy transfer on the near-degenerate $B^2\Sigma^-$, $v = 0 \rightarrow A^2\Delta$, $v' = 1$ channel should outweigh the $B^2\Sigma^-$, $v = 0 \rightarrow A^2\Delta$, $v' = 0$ channel by a factor of ~ 10^4. This provides a stark contrast to the experimental value of ~ 2 and, regardless of experimental error, the scaling law fails dramatically.

Further examples of the failure of the Franck-Condon energy-gap law are soon found. In SiF, a strong correlation is found [35, 36] between the Franck-Condon factor and the vibrational branching, despite the large energy gaps involved. No such correlation exists for SiCl, however [36, 37]. That the scaling law fails in the SiX systems is unsurprising,

since the point has been made that the Franck-Condon dependence is only valid in the limit of a weak perturbation induced by the collision partner [38]. For collision-induced valence-Rydberg transfer in SiCl and SiF, there is clearly a substantial change in the nature of the electronic state, resulting in a large impulsive energy release in rotation.

The $NH(a^1\Delta \rightarrow X^3\Sigma^-)$ inter-system crossing induced by a range of collision partners provides another example in which the larger energy gap transitions are favoured [39, 40], suggesting that the role of Franck-Condon factors is crucial. For the more common situation, which results in the preferential population of the more nearly isoenergetic vibrational levels, there is an almost universal quantitative failure of the Franck-Condon energy-gap model [41].

VI-3.2 Prior distributions in electronic transfer

At the level of rotational resolution, discussed in Chapter V, the experimentally observed product state distributions were found to be relatively broad. Prior distributions, using the 'spherical', 'rotor' and 'vibrotor' models described in Section VI-1.2, were calculated to assess whether the observed initial-to-final state correlations result from the randomisation of the available energy in electronically inelastic collisions.

The differences between the 'rotor' and 'vibrotor' prior distributions (Equation VI.6) are slight, especially for the smaller energy-gap $A^2\Delta$, $v = 1 \leftrightarrow B^2\Sigma^-$, $v = 0$ transitions. For the larger energy gap $B^2\Sigma^-$, $v = 0 \rightarrow A^2\Delta$, $v' = 0$ transition, the variation in the calculated prior distributions is still only marginal, despite the large excess of energy available. Unsurprisingly, there is a much more significant difference between either of the structured priors and the 'spherical' (Equation VI.5), which predicts much hotter CH internal distributions in the absence of a bath of CO_2 rotational levels.

In calculating prior distributions for comparison with the experimental rotational distributions, the degree of RET in the initially populated vibronic level has been taken into account. Prior distributions were calculated for all rotational levels found to be populated in the initial state. The total available energy, E, reflected the term energy of the 'initial' level. An overall prior distribution was calculated from an average of the individual priors, weighted by the relative populations of the corresponding rotational levels determined experimentally from the directly returning fluorescence spectra.

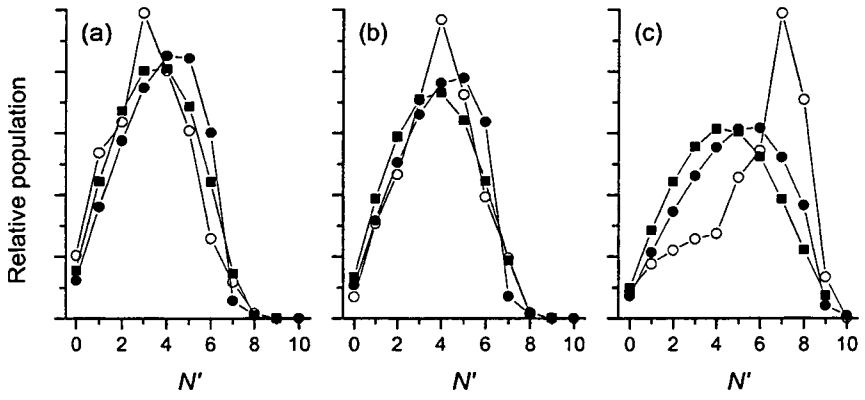

Figure VI.6

$B^2\Sigma^-$, $v' = 0$ product state rotational distributions, N', in 100 ns gate following excitation to $A^2\Delta$, $v = 1$ (a) $N = 2$, (b) $N = 3$, and (c) $N = 6$ in the presence of 1.1 Torr CO_2. Experimental results (○) shown with calculated "spherical" (●) and "rotor" (■) prior distributions. Distributions in each panel are normalised to the same total population.

Collision-induced electronic energy transfer from $A^2\Delta$, $v = 1 \rightarrow B^2\Sigma^-$, $v' = 0$ is simpler to interpret than the reverse process since there is no ambiguity about the product state vibrational level. The experimental $B^2\Sigma^-$, $v = 0$ rotational population distributions from the important 100 ns gate for initial excitation to each N in $A^2\Delta$, $v = 1$ are shown alongside

calculated prior distributions in Figure VI.6. Priors based on the 'spherical' and 'rotor' models of CO_2 are shown for comparison. The experimental product state distributions following excitation to $N = 2$ and 3 have been averaged over both initial spin-orbit states.

Figure VI.6 shows that the calculated priors plausibly reproduce the experimental distributions following excitation to low-N levels of $A^2\Delta$, $v = 1$, the agreement being slightly better when the rotational structure of CO_2 is considered. This apparent agreement between the calculated priors and the $B^2\Sigma^-$, $v' = 0$ experimental distributions could, however be little more than accidental, as was apparently the case for rotational transfer. Since the rotationless energy gap (~ 286 cm^{-1}) between the $A^2\Delta$, $v = 1$ and $B^2\Sigma^-$, $v = 0$ levels is small, it is possible to explain the product state distribution as a propensity for small changes in energy, rather than as the result of a statistical process. Indeed, the product state distribution following excitation to $A^2\Delta$, $v = 1$, $N = 6$, for which a greater range of N' levels are available energetically, is not at all well predicted by the calculated priors. The distribution is significantly peaked in $N' = 7$, the nearest $B^2\Sigma^-$, $v' = 0$ level energetically, and while the distribution extends over the lower N' levels, it does not fill up phase space to the extent predicted by either prior.

Analysis of A-X($\Delta v = 0$) dispersed fluorescence spectra following $B^2\Sigma^-$, $v = 0 \rightarrow A^2\Delta$ collision-induced transitions is complicated by the difficulties in resolving the emission on the A-X diagonal bands, as discussed previously. The calculated prior distributions can be used to provide a means of deconvoluting the product N' distributions into their $A^2\Delta$, $v' = 0$ and 1 contributions. 'Rotor' prior distributions have been calculated independently for $A^2\Delta$, $v' = 0$ and 1 following initial excitation to both $N = 4$ and 8 of $B^2\Sigma^-$, $v = 0$. The prior distributions calculated for $B^2\Sigma^-$, $v = 0 \rightarrow A^2\Delta$, $v' = 1$ transitions, shown in Figure VI.7, predict the maximum energetically allowed N' at thermal collision velocities. This constraint is automatically included by the energy term in Equation VI.5 and is consistent with the maximum observed N' in the reverse $A^2\Delta$, $v = 1 \rightarrow B^2\Sigma^-$, $v' = 0$ transfer process. Hence, all

population with $N' \geq 7$ for initial excitation to $B^2\Sigma^-$, $v = 0$, $N = 4$ and $N' \geq 9$ for excitation to $B^2\Sigma^-$, $v = 0$, $N = 8$ can safely be assigned to emission on the A-X(0,0) band.

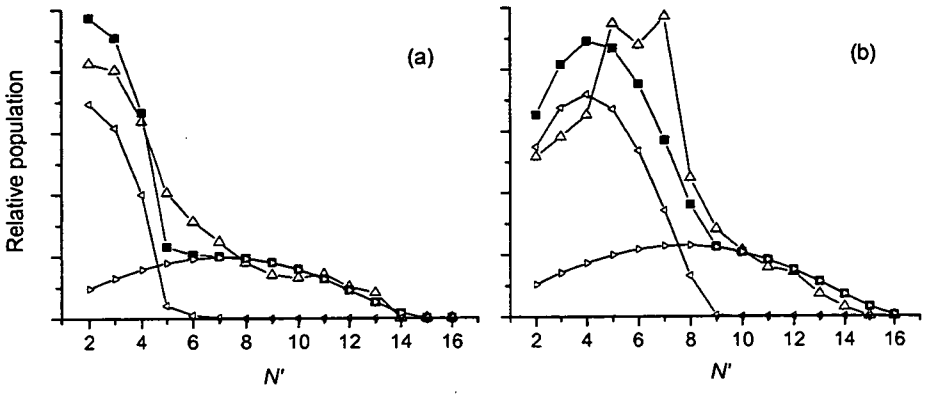

Figure VI.7

Best-fit product state rotational distributions, N', in 100 ns gate following initial excitation to $B^2\Sigma^-$, $v = 0$ (a) $N = 4$ and (b) $N = 8$ in the presence of 1.1 Torr CO_2. Experimental distributions (Δ) are accompanied by overall best-fit "rotor" priors (■) which are given by the sum of the contributions from $A^2\Delta$, $v' = 1$ (◁) and $v' = 0$ (▷) priors as described in the text. Distributions are normalised to the same total population.

The high-N' tails in the product rotational distribution, resulting from emission from $A^2\Delta$, $v' = 0$, are reasonably well reproduced by the prior distributions for both initial excitation schemes. A least squares fit of the rotor prior to the unambiguous $A^2\Delta$, $v' = 0$ portions of the emission spectra was carried out. This allowed the weighting of the $A^2\Delta$, $v' = 1$ contribution to the low-N' region to be determined, in combination with the normalisation of the population. The overall fit is shown in Figure VI.7, accompanied by the individual weighted $A^2\Delta$, $v' = 0$ and 1 contributions.

The ratio of $A^2\Delta$, $v' = 1$ to 0 from the overall combined prior distribution is found to be 1.3 for initial excitation to $B^2\Sigma^-$, $v = 0$, $N = 4$ and 1.6 following pumping of $B^2\Sigma^-$, $v = 0$, $N = 8$. The branching ratio for $B^2\Sigma^-$, $v = 0 \rightarrow A^2\Delta$, $v' = 1$ and $B^2\Sigma^-$, $v = 0 \rightarrow A^2\Delta$, $v' = 0$ has been measured independently previously [42], and discussed in Chapter IV. Using the off-diagonal A-X(0,1) and (1,2) vibrationally-resolved dispersed fluorescence spectra following excitation to $B^2\Sigma^-$, $v = 0$, the low pressure $A^2\Delta$, $v' = 1$ to 0 limiting ratio was found to be 2.0 ± 0.9. This is in plausible agreement with the values determined from the rotationally resolved spectra. It should be noted, however, that the initial state rotational distribution would be considerably thermalised in the vibronic measurements.

The overall quality of the combined prior fit to the experimental data in Figure VI.7 for excitation to $B^2\Sigma^-$, $v = 0$, $N = 4$ is good. The lack of rotational resolution at low-N', however, means that it is not possible to say with any degree of certainty whether the $A^2\Delta$, $v' = 0$ prior accurately describes the true distribution for the spectrally obscured region. The limited distribution over the $A^2\Delta$, $v' = 1$ rotational levels would appear to be reasonable, however since the varying degrees of endothermicity with respect to the initial level restricts the available product levels at thermal collision energies. After initial excitation to $B^2\Sigma^-$, $v = 0$, $N = 8$, the apparent agreement between the combined rotor prior and the experimental $A^2\Delta$ rotational distribution, which peaks to higher N', is poorer. This reflects the situation found for the reverse $A^2\Delta$, $v = 1 \rightarrow B^2\Sigma^-$, $v' = 0$ transfer following excitation to a higher N. The distribution peaks in levels similar in energy to the initial level and while the distribution does extend over the available lower N' levels, it does not reach the statistical limit predicted by the prior.

Recalling Section VI-1.2, it is clear that the prior distributions show better agreement with the rotational distributions observed following electronic state-changing collisions than for pure rotational transfer. It is unsurprising that rotational transfer is non-statistical, since it is generally assumed to be dominated by sudden collisions. Comparison

with the prior distributions does, however serve to illustrate that the degree of redistribution in a rotational state-changing collision is less than for an electronic state-changing collision for which a broader range of ΔN is observed. On this basis, it is possible to conclude that collisions resulting in electronic state changes are those that sample the more strongly interacting regions of the CH···CO_2 potential. For the near isoenergetic $A^2\Delta$, $v = 1 \leftrightarrow B^2\Sigma^-$, $v = 0$ transfer, at least, the rotational energy redistribution in the intermediate complex does not proceed to the statistical limit as predicted by the prior distributions. The branching fraction between $A^2\Delta$, $v' = 0$ and $v' = 1$ of ~1:2 following excitation to $B^2\Sigma^-$, $v = 0$ shows that the collision complex is not sufficiently long-lived to produce a statistical vibrational distribution, which would preferably populate the level lower in energy. The $A^2\Delta$ state product rotational distribution in this interpretation of the data suggests that $B^2\Sigma^-$, $v = 0 \rightarrow$ $A^2\Delta$, $v' = 0$ transfer is accompanied by the greatest range in ΔN, up to the energetic limit. The spectroscopic congestion in the region of the A-X($\Delta v = 0$) bands makes it uncertain whether this distribution extends to low N'.

The broad rotational distributions observed in both $B^2\Sigma^-$, $v' = 0$ and $A^2\Delta$ product states is consistent with the idea that electronic state changing collisions sample the more strongly interacting regions of the intermolecular potential. This would also explain the failure of the Franck-Condon energy-gap law, since the collision can no longer be considered to occur in the weak perturbation limit. Since the entrance channel for $A^2\Delta \rightarrow B^2\Sigma^-$ transfer is the exit channel for $B^2\Sigma^- \rightarrow A^2\Delta$ transfer, the system must inevitably experience the strong interaction at some point during the electronic state-changing collision. Broad distributions are therefore to be expected for collisional transfer in both directions. Unfortunately, at the present time, accurate *ab initio* CH···CO_2 potential surfaces are not available to test these qualitative arguments.

VI-3.3 Kinematic model for electronic transfer

In recent work by McCaffery *et al.*, the kinematic model for rotational transfer has been extended to cover rotational distributions accompanying vibrational [43] and electronic transfer [44]. The mechanism for transfer remains momentum conversion, as discussed above, although in the case of rovibrational transfer, an additional momentum 'gap' must be overcome before a Δj channel may be opened. If this barrier is large in comparison to the typical velocities in the experiment, the low Δj channels are discriminated against [43]. Similarly, an energy barrier exists for collisions that change electronic state, and the use of v_r-Δj plots can be used to provide qualitative predictions for the rotational distribution accompanying an electronic state change. Threshold relative velocities for conversion of all available kinetic energy of relative motion are calculated using an equation similar to Equation VI.8, with the inclusion of an energy barrier. The rotational constants of the $A^2\Delta$ and $B^2\Sigma^-$ states are assumed equal. Again, the internal structure of the CO_2 collision partner will be neglected and it will be treated simply as a hard sphere. The implications of this will be discussed later.

Beginning with the simpler case of $A^2\Delta$, $v = 1 \rightarrow B^2\Sigma^-$, $v' = 0$ transfer, v_r-Δj plots for initial excitation to $N = 2$, 3 and 6 ($R = 0$, 1 and 4) are shown in Figure VI.8. As in the application of the kinematic model to pure rotational transfer, only the nuclear rotation is considered, hence, the rotational levels are best considered in terms of R rather than N. Thus for the $A^2\Delta$ state, $R = N - 2$, while for the $B^2\Sigma^-$ state, $R = N$. As discussed above, an additional momentum barrier must be overcome to open the vibrational channel. According to McCaffery *et al.* [43, 44], the velocity required is the channel-opening condition for $\Delta R = 0$, as shown on the v_r-Δj plot. In this system, the vibrational channel is opened at relative velocities of 710 m s^{-1}, which is slightly higher than the most probable value of the Maxwell-Boltzmann distribution (697 m s^{-1}).

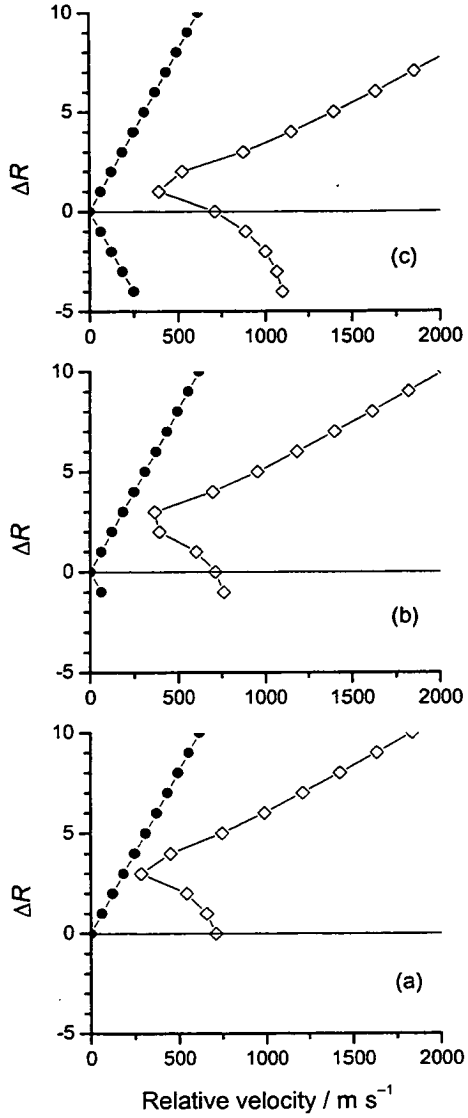

Figure VI.8

Velocity-angular momentum plots for $A^2\Delta$, $v = 1 \rightarrow B^2\Sigma^-$, $v' = 0$ electronic energy transfer induced by collisions with CO_2. Initial excitation to $A^2\Delta$, $v = 1$, (a) $R = 0$, (b) $R = 1$, and (c) $R = 4$. The plots show threshold velocities for (●) angular momentum and (◇) energy constraints for electronic transfer.

For all ΔR, the momentum conversion process is energetically constrained, as was found for rotational transfer within the $A^2\Delta$, $v = 1$ level. The effect of the energetic constraint can be considered as an apparent reduction in the available torque arm for each ΔR channel, as discussed for rotational transfer in Section VI-1.3. It is suggested that the vibrational (or electronic) 'momentum gap' has the effect of causing the greatest (apparent) reduction in the torque arm of the low ΔR channels [16, 43, 44]. This suppression of the low ΔR channels is sufficiently large in vibrotational/electronic transfer to cause significant deviations in the product distribution when superimposed upon the 'natural' or exponential-like distribution of rotational transfer probabilities about $\Delta R = 0$.

An examination of the velocity-angular momentum plots shown in Figure VI.8 allows a qualitative prediction of the $B^2\Sigma^-$, $v = 0$ product level rotational distributions. For all initial R, the low ΔR channels are expected to be most suppressed by energy constraints. In McCaffery's interpretation, these channels experience the greatest apparent reduction in the maximum effective torque arm, while positive ΔR channels will be least constrained. This effectively means that the product state rotational distribution will be biased towards the most nearly isoenergetic levels, as observed experimentally [7]. Whether the product state distribution peaks in the level that is predicted to be least constrained is a matter for a detailed Monte Carlo calculation, not attempted here.

Collisional transfer from $B^2\Sigma^-$, $v = 0$ induced by CO_2 populates both the $A^2\Delta$, $v' =$ 0 and 1 levels [7, 42] and the v_r-Δj plots are shown in Figure VI.9. The angular momentum constraint has been calculated, as before, using the distance from the H atom to the centre-of-mass as the maximum torque arm, determined by the anisotropy of the potential. The threshold velocities for the $\Delta R = 0$ channels, which determine the momentum gap described above, are 710 and 2450 m s^{-1} for transfer to $A^2\Delta$, $v' = 1$ and 0 respectively.

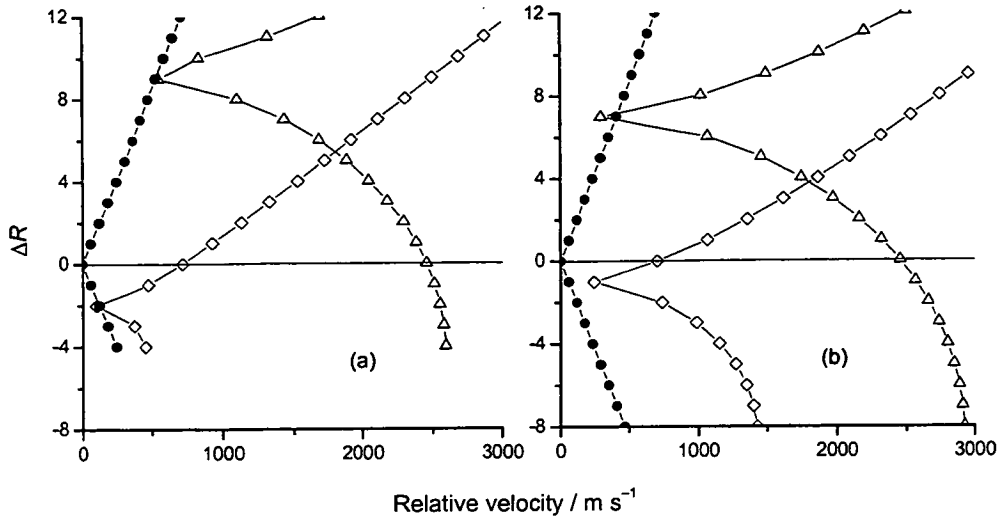

Figure VI.9

Velocity-angular momentum plots for $B^2\Sigma^-$, $v = 0 \rightarrow A^2\Delta$ electronic energy transfer induced by collisions with CO_2. Initial excitation to $B^2\Sigma^-$, $v = 0$, (a) $R = 4$ and (b) $R = 8$. The plots show threshold velocities for (•) angular momentum and $A^2\Delta$, $v' = 1$ (◇) and $v' = 0$ (△) energy constraints for electronic transfer.

For $B^2\Sigma^-$, $v = 0 \rightarrow A^2\Delta$, $v' = 1$ transfer, the product state rotational distribution can qualitatively be predicted to be similar to that for pure rotational transfer, with a moderate enhancement of negative ΔR. As with $A^2\Delta$, $v = 1 \rightarrow B^2\Sigma^-$, $v' = 0$ transfer, this corresponds to a preference for populating the most nearly isoenergetic levels. Again, Monte Carlo calculations would be required to predict the most populated product state rotational levels. Transfer to $A^2\Delta$, $v = 0$ shows a very strong bias towards large, positive ΔR on energetic grounds. Experimentally, a broad rotational distribution, which extended out to high R' was observed in $A^2\Delta$, $v = 0$ following initial excitation of $B^2\Sigma^-$, $v = 0$, as discussed in Chapter V. It should be noted, however, that in the derivation of Equation VI.8 for pure

rotational transfer, and its analogue for rovibrational/electronic transfer, a simple $BN(N+1)$ relationship has been used for the rotational term values. A more accurate representation of the term values, which includes centrifugal distortion, may result in the least constrained ΔR channel shifting slightly.

According to McCaffery *et al.* [44], plots such as Figure VI.9 should also provide a prediction of the branching ratio between $A^2\Delta$, $v = 1$ and 0, by calculating which fraction of the probability density distribution, as represented for pure rotational transfer in Figure VI.5, is excluded by the energetic constraints. A qualitative examination of Figure VI.9 would appear to suggest that the ratio would be more in favour of the $B^2\Sigma^-$, $v = 0 \rightarrow A^2\Delta$, $v' = 1$ channel over the $B^2\Sigma^-$, $v = 0 \rightarrow A^2\Delta$, $v' = 0$ than the 2:1 ratio observed experimentally [42]. In this respect, the model would not appear to be successful, although Monte Carlo calculations would be required to show this rigorously. It should also be borne in mind that the internal structure of the CO_2 collision partner has been neglected, although this could be included in more refined Monte Carlo calculations.

Beyond the points discussed above, however, the model does not recognise any factors upon which the probability of the electronic state change may depend. It is assumed to occur with uniform probability, provided that angular momentum and energy constraints can be satisfied. In the formalism of Alexander and Corey [45] for the collision-induced mixing of $^2\Sigma$ and $^2\Pi$ states, the strength of the V_1 coupling potential, discussed in Chapter I, is dependent on the collision geometry, as displayed in Figure I.1. The probability of mixing the two electronic states would also be expected to depend on the collision velocity, since this causes the non-adiabatic mixing of the adiabatic surfaces. This is also neglected in the McCaffery *et al.* model [44], beyond the 'momentum gap' that must be overcome to open the vibrational channels. While the model is able to qualitatively explain some of the observed features of the experimental data qualitatively, more developments are required to fully assess its quantitative utility.

VI-4 SUMMARY OF CONCLUSIONS

Rotational energy transfer induced by collisions with CO_2 has been observed to be rapid in both the $A^2\Delta$ and $B^2\Sigma^-$ states of the CH radical. Although quantitative measurements were not made, the time-resolved dispersed fluorescence spectra recorded suggest that rates of rotational relaxation are gas-kinetic ($\sim 10^{-10}$ cm^3 molecule^{-1} s^{-1}). Rotational population distributions recorded under single-collision conditions, could be fitted reasonably well using established fitting laws. Most significantly, the results showed there to be no significant differences between the ΔN propensities for rotational transfer in the $A^2\Delta$ state and those in the $B^2\Sigma^-$ state. Thus, there is no evidence that a more attractive CH($B^2\Sigma^-$)-CO_2 potential plays a role in rotational transfer within a vibronic level.

Vibrational relaxation in the $A^2\Delta$ state, induced by collisions with CO_2 was found to be relatively efficient, although significantly slower than for OH($A^2\Sigma^+$) in which attractive forces dominate. This suggests that the CH($A^2\Delta$)-CO_2 intermolecular potential is significantly less attractive than that of OH($A^2\Sigma^+$)-CO_2.

Electronic energy transfer between the $A^2\Delta$ and $B^2\Sigma^-$ states of the CH radical has been demonstrated to be relatively efficient and reversible when CO_2 is used as the collision partner. Collisional transfer from $B^2\Sigma^-$, $v = 0 \rightarrow A^2\Delta$ populates the $v' = 1$ and $v' = 0$ vibrational levels in a 2:1 ratio, contradicting the prediction of the Franck-Condon energy gap scaling law. Observed rotational distributions accompanying an electronic state change are broader than for pure rotational redistribution within a vibronic level and are shifted from $\Delta R = 0$. Collisions between CH and CO_2 most likely do not form a long-lived complex. The observed rotational distributions, while broad, are only reasonably well described by a statistical prior distribution, and could be accounted for on the basis of energetic and angular momentum constraints. Most importantly, $B^2\Sigma^-$, $v = 0 \rightarrow A^2\Delta$ produces a completely non-

statistical distribution over the vibrational levels, favouring transfer to the near-isoenergetic $v' = 1$.

There remains a lack of a theoretical prediction with which to compare the experimentally observed vibrational and rotational distributions observed to accompany collision-induced electronic state changes in CH-CO_2 collisions. Indeed, there is no theoretical model available which can universally even qualitatively predict the vibrational branching fractions in electronically inelastic collisions. Most significantly, accurate *ab initio* CH···CO_2 potential surfaces are required for a more complete interpretation of the experimental data.

VI-5 FUTURE DIRECTIONS

A limited set of data was presented in Chapter V on RET within the $A^2\Delta$, $v = 1$ and $B^2\Sigma^-$, $v = 0$ levels, which was largely obtained as a by-product of measuring the product state rotational distributions accompanying a collision-induced change of electronic state. A more quantitative approach, focussing on rotational transfer within a vibronic level, would enable the extraction of accurate state-to state rate constants within the $A^2\Delta$ and $B^2\Sigma^-$ states following initial preparation of a single rotational and fine-structure level. Laser excitation in the region of the A-X diagonal bands (~430 nm) allows fully quantum state-selective preparation of $A^2\Delta$, $v = 0$ and 1, and $B^2\Sigma^-$, $v = 0$, while dispersed fluorescence spectra enable the determination of the product rotational distributions under single-collision conditions, ideally with resolution of fine-structure and/or Λ-doublet levels. Such work is currently under way utilising Ar, N_2 and CO_2 as collision partners.

As mentioned above, other species have also been observed to cause $A^2\Delta \leftrightarrow B^2\Sigma^-$ transfer. Clearly, there remains a great deal of scope to explore electronic state-changes in CH with a wider range of collision partners. Knowledge of rate constants for interelectronic

state transfer is essential in the interpretation of quenching measurements and flame diagnostics. From a more fundamental point of view, a greater understanding of the collision process would be possible in conjunction with theoretical calculations. In this case, Ar would provide a good model collision partner; although the rate of transfer has not been quantified precisely it is known to be significantly smaller than CO_2 [6]. Dispersed fluorescence measurements at rotational resolution under single-collision conditions are likely to very challenging for Ar, since the rate of electronic transfer is significantly slower than rotational relaxation. Another possible collision partner is N_2, which is of practical significance in atmospheric flames. Preliminary observations of collisions of this species with electronically excited CH radicals suggested that $A^2\Delta \leftrightarrow B^2\Sigma^-$ coupling is of comparable efficiency to CO_2.

One of the major limitations in this work has been the difficulty in obtaining sufficient signal-to-noise in collisional high-resolution spectra *via* the technique of dispersed fluorescence emission through a monochromator. In other systems (especially CN, N_2^+ and CO^+), the rotational population distributions in the collisionally populated electronic states were probed using optical-optical double resonance techniques *via* higher lying excited states. Unfortunately, no suitable states exist for CH. The higher-lying $E^2\Pi$ and $F^2\Pi$ states [46, 47, 48] (referred to as the $D^2\Pi$ and $E^2\Pi$ states in earlier literature), have been observed in only a limited number of experimental studies [49, 50, 51, 52] and are heavily predissociated. Therefore, plans are underway for future work in this laboratory to use the technique of polarisation labelling spectroscopy to study electronically inelastic collisions. In this technique, which will be described only briefly, a linearly or circularly polarised pump laser beam is tuned to be in resonance with a spectroscopic transition, causing the sample to become birefringent and dichroic. A linearly polarised probe beam will become elliptical when it is tuned in resonance with a transition for which either the upper or the lower state has a degree of polarisation. Thus, the degree of retention of polarisation in rotationally,

vibrationally and electronically inelastic collisions can be determined. This should provide further information on the dynamics of the collision.

VI-6 REFERENCES

1 R. N. Dixon, D. P. Newton and H. Rieley, *J. Chem. Soc., Faraday Trans. 2*, **83**, (1987), 675

2 J. L. Cooper and J. C. Whitehead, *J. Chem. Soc., Faraday Trans.*, **89**, (1993), 1287

3 J. L. Cooper and J. C. Whitehead, *J. Phys. Chem*, **98**, (1994), 8274

4 C.-C. Wang, Y.-P. Chen. T.-L. Chin, H.-Y. Huang and K.-C. Lin, *J. Chem. Phys.*, **112**, (2000), 10204

5 M. Kind, F. Stuhl, Y.-R. Tzeng, M. H. Alexander and P. J . Dagdigian, *J. Chem. Phys.*, **114**, (2001), 4479

6 M. Kind and F. Stuhl, *J. Chem. Phys.*, **114**, (2001), 6160

7 C. Murray, C. J. Randall and K. G. McKendrick, *Phys. Chem. Chem. Phys.*, **2**, (2000), 5553

8 Polanyi and Woodall, *J. Chem. Phys.*, **56**, (1972), 1563

9 T. A. Brunner and D. Pritchard, in *Dynamics of the Excited State*, Edited by K. P. Lawley, Wiley, New York, 1982

10 I. Procaccia and R. D. Levine, *Physica (Utrecht) A*, **82**, (1976), 623

11 J. I Steinfeld, P. Ruttenberg, G. Millot, G. Fanjoux and B. Lavorel, *J. Phys. Chem.*, **95**, (1991), 9638

12 R. D. Levine and R. B. Bernstein, *"Molecular Reaction Dynamics and Chemical Reactivity"*, Oxford University Press, New York, 1987

13 A. J. McCaffery, Z. T. Alwahabi, M. A. Osborne and C. J. Williams, *J. Chem. Phys.*, **98**, (1993), 4586

14 M.A. Osborne and A. J. McCaffery, *J. Chem. Phys.*, **101**, (1994), 5604

15 A. J. Marks, *J. Chem. Soc., Faraday Trans.*, **90**, (1994), 2857

16 A. J. McCaffery and R. J. Marsh, *J. Phys. Chem. A.*, **105**, (2001), 7135

17 N. A. Besley, A. J. McCaffery, M. A. Osborne and Z. Rawi, *J. Phys. B: At. Mol. Phys.*, **31**, (1998), 4267

18 R. J. Marsh and A. J. McCaffery, *Chem. Phys. Lett.*, **3335**, (2001), 134

19 K. L. Steffens and D. R. Crosley, *J. Chem. Phys.*, **112**, (2000), 9427

20 P. W. Fairchild, G. P. Smith and D. R. Crosley, *J. Chem. Phys.*, **79**, (1983), 1795

21 M. A. Blitz, M. Pesa, M. J. Pilling and P. W. Seakins, *Chem. Phys Lett.*, **322**, (2000), 280

22 G. A. Raiche, J. B. Jefferies, K. J. Rensberger and D. R. Crosley, *J. Chem. Phys.*, **92**, (1990), 7258

23 K. J. Rensberger, J. B. Jefferies and D. R. Crosley, *J. Chem. Phys.*, **90**, (1989), 2174

24 L. R. Williams and D. R. Crosley, *J. Chem. Phys.*, **104**, (1996), 6507

25 A. Degli Esposti and H.-J. Werner, *J. Chem. Phys.*, **93**, (1990), 3351

26 J. Klos, G. Chalasinski, M. T. Bell, R. A. Kendall, R. Burcl, M. M. Szczesniak and S. M. Cybulski, *J. Chem. Phys.*, **112**, (2000), 4952

27 M. H. Alexander, S. Gregurick, P. J. Dagdigian, G. W. Lemire, M. J. McQuaid and R. C. Sausa, *J. Chem. Phys.*, **101**, (1994), 4547

28 G. Kerenskaya, A. L. Kaledin and M. C. Heaven, *J. Chem. Phys.*, **115**, (2001), 2123

29 D. H. Katayama, T. A. Miller and V. E. Bondybey, *J. Chem. Phys.*, **71**, (1979), 1662

30 M. Zachwieja, *J. Mol. Spectrosc.*, **170**, (1995), 285

31 J. Luque and D. R. Crosley, *J. Chem. Phys.*, **104**, (1996), 3907

32 R. Kepa, A. Para, M. Rytel and M. Zachwieja, *J. Mol. Spectrosc.*, **178**, (1996), 189

33 R. J. Leroy, "*LEVEL*", University of Waterloo Chemical Physics Research Report, C. P.-555, Ontario, Canada, 1995

34 N. L. Garland and D. R. Crosley, *Appl. Opt.*, **24**, (1985), 4229

35 C. W. Watson and K.G. McKendrick, *Chem. Phys.*, **187**, (1994), 79

36 K. G. McKendrick, *J. Chem. Soc., Faraday Trans.*, **94**, (1998), 1921

37 S. Singleton and K. G. McKendrick, *J. Phys. Chem.*, **97**, (1993), 1389

38 M H. Alexander and G. C. Corey, *J. Chem. Phys.*, **84**, (1986), 100

39 J. S. Adams and L. Pasternack, *J. Phys. Chem.*, **95**, (1991), 2975

40 W. Hack and K. Rathmann, *J. Phys. Chem.*, **96**, (1992), 47

41 P. J. Dagdigian, *Annu. Rev. Chem. Phys.*, **48**, (1997), 123

42 C. J. Randall, C. Murray and K. G. McKendrick, *Phys. Chem. Chem. Phys.*, **2**, (2000), 461

43 A. J. McCaffery and R. J. Marsh, *J, Phys. Chem A*, **104**, (2000), 10442

44 A. J. McCaffery and R. J. Marsh, *J. Chem. Phys.*, **115**, (2001), 9771

45 M. H. Alexander and G. C. Corey, *J. Chem. Phys.*, **84**, (1986), 100

46 A. Kalemos, A. Mavridis and A. Metropoulos, *J. Chem. Phys.*, **111**, (1999), 9536

47 A. Metropoulos and A. Mavridis, *Chem. Phys Lett.*, **331**, (2000), 89

48 E. F. van Dishoeck, *J. Chem. Phys.*, **86**, (1987), 196

49 G. Herzberg and J. W. C. Johns, *Astrophys. J.*, **158**, (1969), 399

50 P. Chen, W. A. Chupka and S. D. Colson, *Chem. Phys Lett.*, **121**, (1985), 405

51 P. Chen, J. B. Pallix, W. A; Chupka and S. D. Colson, *J. Chem. Phys.*, **86**, (1987), 516

52 X. Li and Y.-P. Lee, *J. Chem. Phys.*, **111**, (1999), 4942

APPENDIX A COURSES ATTENDED

Molecular Quantum Mechanics

Modern Optics

Laser Physics

APPENDIX B CONFERENCES ATTENDED

Annual Northern Universities Meeting on Chemical Physics (ANUMOCP-8), University of Manchester, June 1998

16th International Symposium on Gas Kinetics, Cambridge University, July 2000.

European Conference on the Dynamics of Molecular Collisions (MOLEC XIII), Jerusalem, Israel, September 2000

Stereochemistry and Energy Landscapes, Joint Meeting of the Molecular Beams and Dynamics Group and the Theoretical Chemistry Group of the RSC, Warwick University, March 2001

APPENDIX C PUBLISHED PAPERS

C. J. Randall, C. Murray and K. G. McKendrick, *Phys. Chem. Chem. Phys.*, **2**, (2000), 461

C. Murray, C. J. Randall and K. G. McKendrick, *Phys. Chem. Chem. Phys.*, **2**, (2000), 5553

State-specific collisional coupling of the CH $A\,^2\Delta$ and $B\,^2\Sigma^-$ states

Colin J. Randall, Craig Murray and Kenneth G. McKendrick*

Department of Chemistry, The University of Edinburgh, Edinburgh, UK EH9 3JJ

Received 25th October 1999, Accepted 26th November 1999

Electronically excited CH radicals have been prepared in chosen vibrational levels of the $A\,^2\Delta$ and $B\,^2\Sigma^-$ states by selective laser excitation. The evolution of the populations in the initial and collisionally produced vibronic levels has been followed by time- and wavelength-resolved fluorescence spectroscopy. It is found that CO_2, as a model collision partner, efficiently promotes the coupling of the $A\,^2\Delta$ and $B\,^2\Sigma^-$ states at room temperature (~295 K). CH $A\,^2\Delta$, $v = 1$ is reversibly transferred to the near-degenerate $B\,^2\Sigma^-$, $v = 0$ level, and irreversibly vibrationally relaxed to $A\,^2\Delta$, $v = 0$, with comparable probabilities for these competing processes. CH $B\,^2\Sigma^-$, $v = 0$ is correspondingly reversibly transferred to $A\,^2\Delta$, $v = 1$ and irreversibly transferred to $A\,^2\Delta$, $v = 0$. The branching ratio for these two product vibrational states is *ca.* 2 : 1, which contrasts markedly with the predictions of energy-gap scaling laws. The $A\,^2\Delta$, $v = 0$ level is found to be only weakly quenched by CO_2, in agreement with previous measurements. These observations have important consequences for the use of laser-induced fluorescence spectroscopy as a tool for monitoring the density of CH in collisional environments, and in the interpretation of previously measured quenching rate constants for electronically excited CH.

Introduction

It has been known for many years that molecules in electronically excited states can be removed through bimolecular collisions.[1] There have subsequently been numerous investigations of the rates of total removal or "quenching". Various models have been proposed which attempt to explain the dependence of the quenching efficiency on molecular properties and on temperature.[2–7]

However, it is much rarer for the fate of the quenched molecules to have been established. The current state of this field for the simplest molecular systems, diatomic molecules, was reviewed recently by Dagdigian.[8] The number of systems for which the rotational or even vibrational state distribution in the products of electronic quenching has been determined is still quite limited. However, an important conclusion that has emerged is that a universal quantitative understanding of electronically inelastic processes is still lacking. In particular, appealing but simplistic models of energy disposal[9,10] have been shown to be of poor general applicability.[8,11]

In addition to being of fundamental interest because of the remaining challenges they present to both experiment and theory, these processes are of considerable practical significance. Electronically excited molecules are formed spontaneously as minority species in high-energy environments such as combustion and technological plasmas. Collision degradation of their excitation energy to thermal energy competes with spontaneous emission. Probably even more importantly, electronically inelastic collisions will often directly influence the measurement of concentrations of the majority ground electronic state species in the same environments. For methods based on optical electronic spectroscopy, such as laser-induced fluorescence, quenching of the excited state affects the relationship between the ground state population and signal strength.[12,13]

The subject of the current paper is state-specific electronic quenching of the CH radical. This molecule occurs widely in nature, including solar and other stellar atmospheres, comets and interstellar space. It is ubiquitous in combustion, and is responsible for the familiar violet colouration of hydrocarbon flames. The electronic spectroscopy of the visible and UV systems has been extensively investigated, and remains a topic of contemporary interest.[14–20] In the current work we focus on the near-degenerate $A\,^2\Delta$ and $B\,^2\Sigma^-$ states. The relevant potential curves are illustrated in Fig. 1, based partly on existing extensive *ab initio* studies.[21]

The total quenching of the CH $A\,^2\Delta$ state has been the subject of particularly thorough examination for a wide range of identified quenchers.[22–33] Several aspects of these studies indicate an activated process involving a significant energy

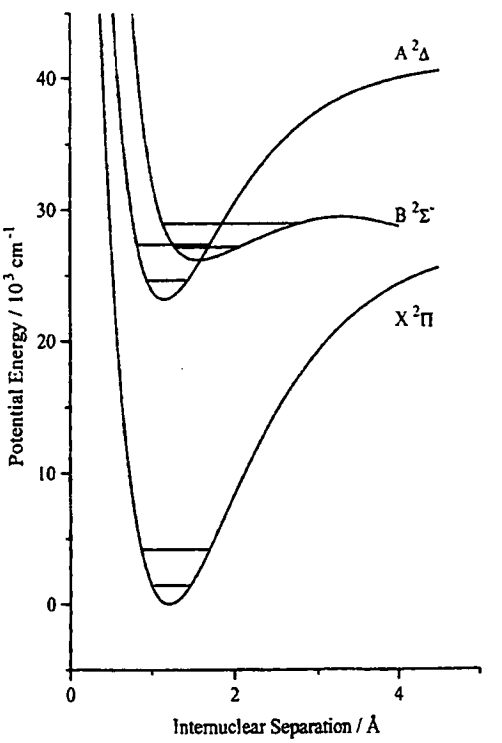

Fig. 1 Potential energy curves for the states of CH of interest in this work. The two lowest vibrational levels in each state are indicated.

DOI: 10.1039/a908494k

This journal is © The Owner Societies 2000

barrier. There has also been some work on the intra-electronic state vibrational and rotational relaxation.[34,35]

Somewhat in contrast, the total removal of the $B\,^2\Sigma^-$ state has been less studied.[32,36] The work that has been done suggests that removal by most partners is through chemical reaction, more analogous to the $X\,^2\Pi$ electronic ground state. Rovibrational relaxation within the $B\,^2\Sigma^-$ state has also been investigated.[37]

Probably the most direct stimulus to the current work is reports of specific transfer between the CH $A\,^2\Delta$ and $B\,^2\Sigma^-$ states in both high[38] and low[39] pressure flames. These studies establish the existence of the basic phenomenon, although under conditions where there is inevitably a complex mixture of collision partners and a range of temperatures and densities. Our aim here, therefore, was to implement a more selective approach in which collisions of specifically excited CH radicals with a single, defined partner could be investigated.

Experimental

The experiments were carried out in a stainless-steel vacuum system, indicated schematically in Fig. 2. The chamber was evacuated by a liquid-N_2 trapped diffusion pump, backed by a rotary pump. CH radicals were produced by the established technique of UV multiphoton photolysis of $CHBr_3$. For practical reasons, the $CHBr_3$ was diluted in Ar in a ratio of 1 : 5. This mixture was flowed steadily into the chamber to create a total partial pressure of $\leqslant$40 mTorr (consisting therefore of $\leqslant$7 mTorr of $CHBr_3$: our preliminary measurements below confirmed that the small quantity of Ar had no significant influence on the remainder of the results.) The quenching gas, which was CO_2 in most experiments, was admitted separately. The flow of gases was matched by partially throttling the diffusion pump to give total pressures typically in the range 0.5–10 Torr. All measurements were carried out at room temperature, estimated typically at ~295 K but which was not controlled.

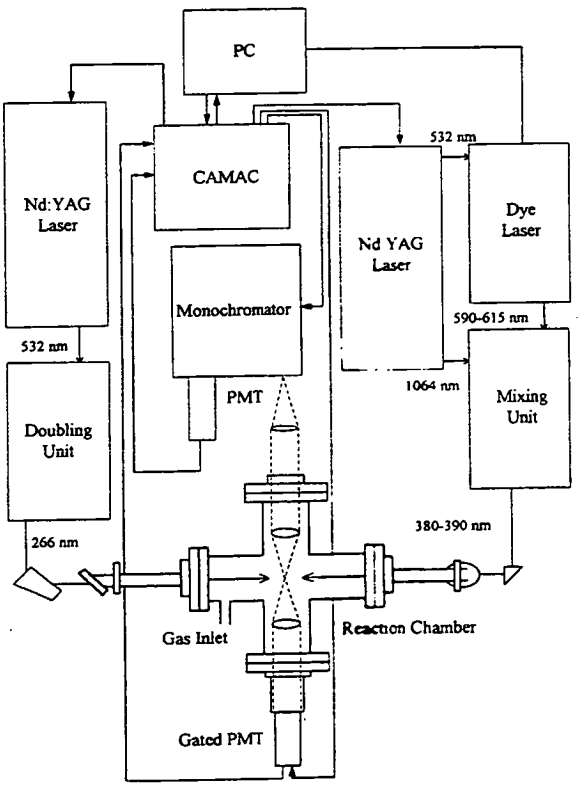

Fig. 2 Schematic diagram of the experimental apparatus. The reaction chamber was evacuated from below by a diffusion pump (not shown).

The UV photolysis wavelength was either 266 nm (4th harmonic of a Nd : YAG laser: Spectron Laser Systems SL803) or 193 nm (ArF excimer laser: Questek Series 2000 or Lambda Physik COMPex 200). The results were found not to be dependent on the choice of wavelength or the photolysis pulse energy (typically 40–60 mJ). The yield of CH was enhanced by mild focusing of the photolysis beam.

As is well documented,[40] the multiphoton photolysis process produces CH in a range of electronic states, including the $A\,^2\Delta$ and $B\,^2\Sigma^-$ states of interest in the present work. It was therefore necessary to let this initial population decay before attempting to excite and observe the desired vibronic levels in isolation. A delay of typically 2–5 μs was introduced between the photolysis pulse and counterpropagating selective pump pulse. Both pulses had a nominal duration of ~10 ns. The pump pulse was generated by a tunable Nd : YAG laser-pumped dye laser system (Spectron Laser Systems, SL803S + SL400G + SL400EX). The necessary wavelengths in the 380–395 nm region were produced by 532 nm pumping of a red dye (590–630 nm) and mixing the output (KD*P crystal) with residual Nd : YAG 1064 nm fundamental.

Fluorescence was collected by two independent systems of lenses mounted in opposite directions perpendicular to the laser axis. The light from one passed through an interference filter, selected to isolate a particular vibronic emission band, and then to a photomultiplier tube (EMI 9813QB). The light from the other was focused onto the entrance slit of a monochromator (1 m, Hilger and Watts, Monospek 1000), which allowed full (ro)vibronic resolution of the emission, before being detected by a second photomultiplier tube (EMI 9789QB).

The signals were processed by a computer-controlled CAMAC (IEEE 583) modular data acquisition system. The time dependence of the fluorescence waveforms could be captured with a transient digitiser (100 MHz, DSP 2001A), or gated-integrated signals could be recorded (SRS SR250 boxcar integrator fed to Hytec 520 ADC converter). This configuration provided the capability to normalise spectrally resolved signals to the total fluorescence signal on a shot-wise basis. Other experimental parameters, such as the delay between the laser pulses and the scanning of the dye laser and monochromator, were controlled electronically *via* CAMAC modules.

Gases were used as provided by the manufacturers and without further purification apart from the usual freeze–pump–thaw cycling to remove dissolved air: $CHBr_3$ (Fisons, Laboratory grade); Ar (BOC, 99.99%), CO_2 (BOC, 99.995%), CH_4 (Distillers MG, 99.5%).

Results

Fluorescence excitation spectra

An essential preliminary task was the identification of suitable spectroscopic transitions which could be used to prepare the initial levels of interest. We have limited our attention in the present study to preparation of the CH $A\,^2\Delta$, $v = 1$ and $B\,^2\Sigma^-$, $v = 0$ levels. As indicated in Fig. 1 and shown in more detail in Fig. 3, these levels are nearly degenerate. The lower-lying $A\,^2\Delta$, $v = 0$ level is also observed as a collisional product. For the sake of brevity in what follows, we have adopted the previously suggested[38] notation A0, A1, B0 to refer to the CH $A\,^2\Delta$, $v = 0$ and 1 and $B\,^2\Sigma^-$, $v = 0$ levels, respectively.

At first sight, it might seem straightforward to prepare molecules selectively in B0 using the strong, near-diagonal B–X(0, 0) band. In the conventional absorption spectrum or low-power LIF excitation spectrum, this band appears isolated, as

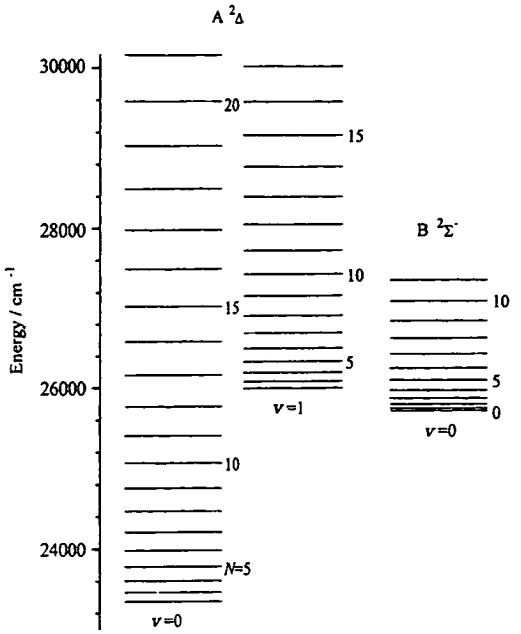

Fig. 3 Rovibronic energy levels for CH $A\,^2\Delta$, $v = 0$ and 1, and $B\,^2\Sigma^-$, $v = 0$. Additional fine-structure splittings within levels of a given N are not indicated.

illustrated for the R-branch region in Fig. 4a. However, with much higher laser powers as might be used in an attempt to maximise the population transferred to the excited state, additional features appear in the spectrum (see Fig. 4b).

We have successfully assigned[41] all the additional lines to either the A–X(1,0) or (2,1) bands. (The observation of A–X(2,1) obviously indicates that vibrationally excited CH $X\,^2\Pi$ persists on the timescale of the measurement.) Although these off-diagonal A–X bands have very weak transition probabilities,[19] the B–X(0,0) band can be so heavily saturated with the available laser pulse energies that comparable amounts of population are transferred to the $A\,^2\Delta$ and $B\,^2\Sigma^-$ states. Fortunately, there are individual rotational lines within the B–X(0,0) band which remain suitable for clean excitation of B0, but clearly they have to be selected with care. We have used the $R_1(3)$ line throughout the present study.

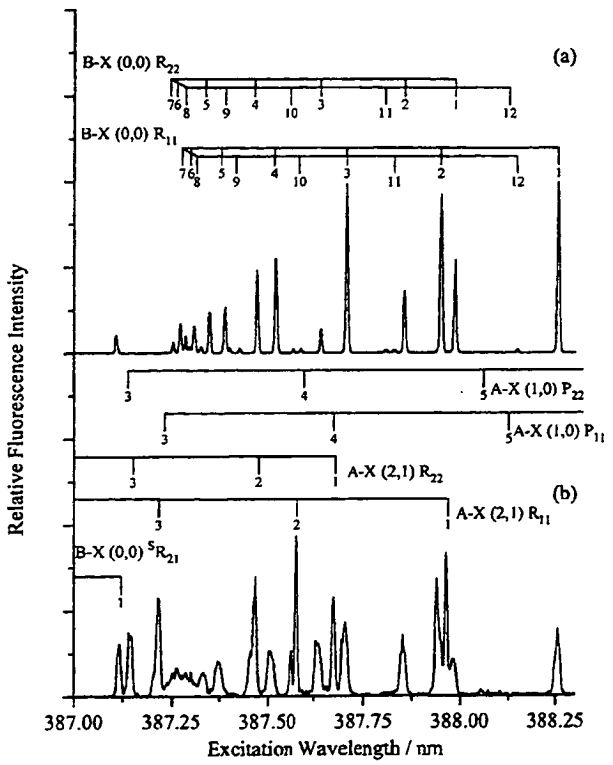

Fig. 4 LIF excitation spectra of CH produced by UV photolysis of $CHBr_3$ in the presence of CO_2 (0.5 Torr). Photolysis-pump delay = 5 μs. (a) Relatively low power (pump pulse energy 20 μJ), dominated by B–X(0,0) lines. (b) High power (pump pulse energy ~15 mJ), showing heavily saturated B–X(0,0) lines and additional A–X(2,1) and (1,0) lines.

The identification of the A–X(1,0) band can be turned to positive advantage, however, when it comes to selective preparation of A1. The diagonal A–X(1,1) band carries almost all the vibrational transition probability connecting A1 to the ground state.[19] It might therefore seem the obvious choice given that a significant population of $X\,^2\Pi$, $v = 1$ is known to be present. However, the A–X system is, in fact, so diagonal that the (0,0) and (1,1) bands are almost perfectly overlapped. It is consequently much more convenient to use isolated lines in the R-branch region of the A–X(1,0) band to shorter wavelengths. These can again be chosen carefully to be free from A–X(2,1) and B–X(0,0) contamination. We have selected the $R_1(1)$ line throughout.

Preliminary confirmation of CH A ↔ B collisional coupling

To establish that CH B ↔ A transfer does indeed take place for particular collision partners, we carried out a series of preliminary measurements in which B0 was selectively prepared. The component of the fluorescent emission in the region of 430 nm was isolated simply using an interference filter (FWHM 10 nm). This effectively selects a combination of the A–X($\Delta v = 0$) diagonal bands and the comparatively weak, but easily measurable, B–X(0,1) band.[20]

The time dependence of this emission was examined using the transient digitiser. In the low-pressure limit, a simple exponential decay was observed, as expected for the directly excited B–X(0,1) emission. The effects of adding a number of collision partners, including $CHBr_3$ (our selected precursor), CH_4 (an alternative precursor and typically present in flames as a fuel), Ar (a model physical quencher) and CO_2 (a known $B\,^2\Sigma^-$ state quencher[36] and typical combustion end product) were then determined. In all cases, but with varying efficiencies, an additional contribution to the signal grew in with pressure. This exhibited the characteristic rise-and-fall profile of a collisional product, and is diagnostic of collision-induced B0 → $A\,^2\Delta$ transfer. At this stage it could not be distinguished whether the population was transferred to A0 or A1.

In the remainder of the detailed study of this phenomenon which we report below, we concentrate entirely on CO_2 as collision partner. It was found to be substantially more efficient than Ar in promoting CH B → A transfer. It meanwhile had the advantage over CH_4 of not reacting rapidly with the CH $X\,^2\Pi$ ground state[42,43] and therefore not depleting the signal during the necessary delay between photolysis and pump laser pulses.

Dispersed fluorescence spectra

(a) Diagonal bands. That CH B ↔ A conversion is induced in both directions by collisions with CO_2 was confirmed conclusively through a series of measurements on the strong B–X and A–X diagonal bands. Dispersed fluorescence spectra were collected by scanning the monochromator with a fixed pump-laser wavelength and integrating the total fluorescence signal over the entire waveform. These spectra were normalised using time-integrated, undispersed B–X(0,0) fluorescence signals observed simultaneously through an interference filter by the other PMT (see Experimental section), compensating for fluctuations in the experimental conditions.

Representative spectra following excitation of B0 are shown in Fig. 5. The collision-induced A–X($\Delta v = 0$) bands clearly grow in with increasing CO_2 pressure. Conversely, when A1 was populated initially the corresponding time-integrated spectra contained strong, collision-induced B–X emission. This could unambiguously be assigned to the B–X(0,0) band because it is the only strong feature in emission in this region (and, in any case, $v = 0$ is effectively guaranteed to be the only $B\,^2\Sigma^-$ state product level by energy conservation).

The ratio of A–X to B–X signals following B0 pumping exhibited a quite distinct pressure dependence to the converse B–X to A–X ratio from A1 pumping. This is quantified in Fig. 6. Clearly, I_A/I_B continues to grow roughly linearly over the range 0–6 Torr following B0 pumping. Over the same range for A1 pumping, I_B/I_A rises more rapidly initially but shows significant curvature.

Because the B–X(0,0) band and both the A–X(0,0) and (1,1) bands carry almost all of the transition probability from the respective upper states, the data in Fig. 6 closely reflect true relative emission intensities. Any correction required for the relative vibrational transition probabilities is negligible (at most a few percent). Probably more significant is the relative detection sensitivity of the experimental apparatus (primarily monochromator transmission and PMT response) at ~390 and ~430 nm. We have not yet characterised this exactly and have therefore not applied a correction, but do not anticipate a large variation over this limited interval.

(b) Off-diagonal bands. It is worth reiterating that the contributions from the A–X(1,1) and (0,0) bands are not resolved in Fig. 5. To be able to distinguish between A0 and A1, we recorded two additional series of integrated spectra in the region of the off-diagonal A–X(0,1) and (1,2) bands. The much

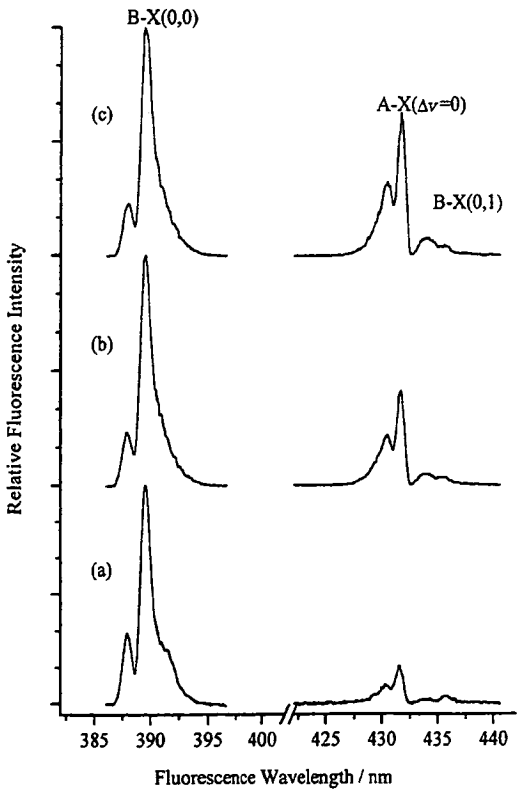

Fig. 5 Dispersed fluorescence spectra on the CH B–X(0,0) and A–X($\Delta v = 0$) diagonal bands following pumping of the $R_1(3)$ line of the B–X(0,0) band in the presence of CO_2 at pressures of (a) 1.24 Torr; (b) 4.08 Torr; (c) 6.07 Torr. Signals have been scaled to the B–X(0,0) band at each pressure. Experimental bandwidth = 0.93 nm.

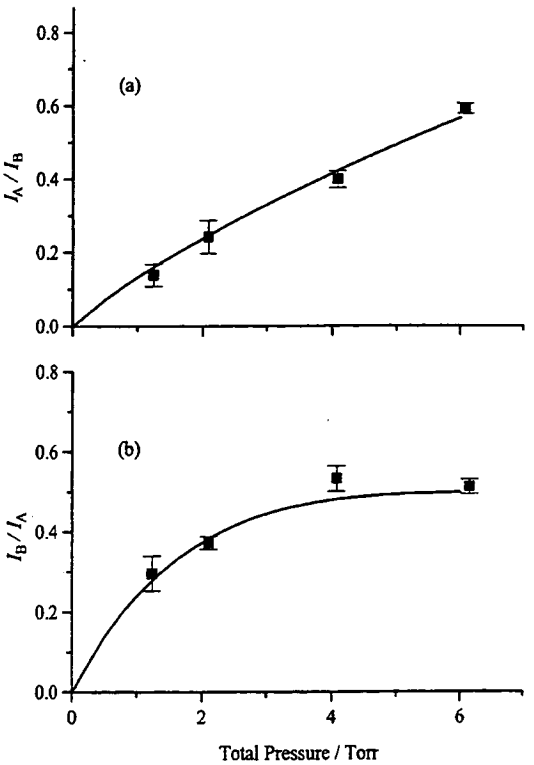

Fig. 6 Variation with pressure of CO_2 of CH product state: initial state ratios of integrated signals on the A–X (I_A) and B–X (I_B) diagonal bands. Initial excitation of (a) $B\,^2\Sigma^-$, $v = 0$; (b) $A\,^2\Delta$, $v = 1$. In each case, (squares) experimental results, with error bars (1σ) estimated from variations in repeated measurements; (solid lines) predictions of the 4-level kinetic model described in the text.

weaker band strengths (approximately two orders of magnitude down on the diagonal bands[19]) obviously carry a significant penalty in terms of signal-to-noise. The B–X(0,2) band, which is even weaker by another order of magnitude,[20] happens to fall in the same region.

Representative spectra recorded following the excitation of B0 in the presence of varying pressures of CO_2 are shown in Fig. 7. The partially overlapping A–X(1,2) and (0,1) bands grow in, as expected, relative to the weak B–X(0,2) band originating in the initially pumped level. Notably, even at the lowest pressures, both A1 and A0 are clearly populated.

In the reciprocal spectra produced by exciting A1, the A–X(0,1) band was seen to grow in with CO_2 pressure. This implies that vibrational relaxation of A1 competes effectively with its removal through other processes. The B–X(0,2) band also increased as expected, but was less prominent simply as a result of its bandstrength.

At a more quantitative level, the relative contributions of the A–X(1,2) and (0,1) bands in the off-diagonal spectra were extracted by an iterative simulation procedure.[41] Typical best-fit decompositions are indicated in Fig. 7 for comparison. There is some degree of subjectivity in the fit because a rotational band contour has to be assumed for each of the three bands prior to convolution with the experimental bandwidth. The procedure we used was to start with a thermal rotational distribution in the collisionally populated levels and a sharp distribution peaked in the pumped state of the initially populated level. The fits were only marginally improved by a slight broadening of the distributions in the product levels. They were more noticeably improved by spreading population into adjacent rotational states in the initially populated level. However, some preliminary higher resolution spectra indicated that rotational thermalisation was not complete, particularly at lower pressures.[44] Incomplete rotational relaxation

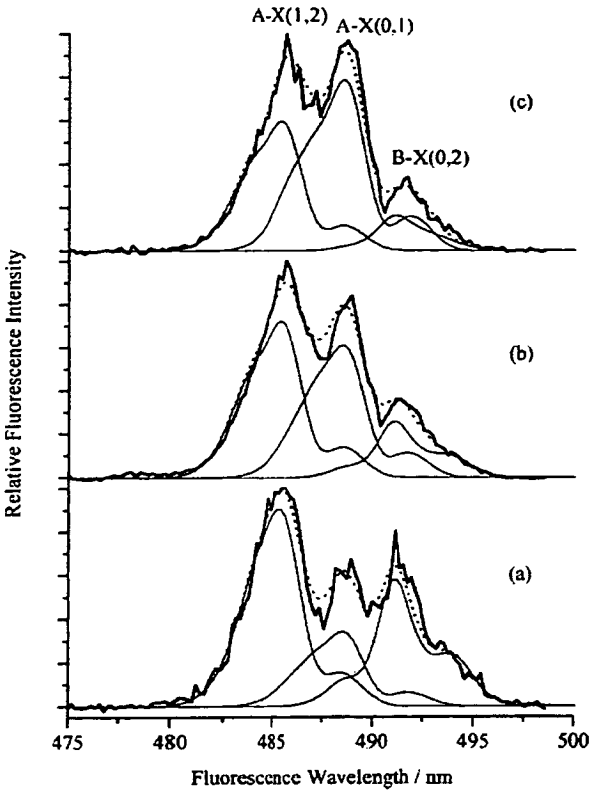

Fig. 7 Dispersed fluorescence spectra on the CH A–X(1,2) and (0,1) and B–X(0,2) off-diagonal bands following pumping of the $R_1(3)$ line of the B–X(0,0) band in the presence of CO_2 at pressures of (a) 1.06 Torr; (b) 4.03 Torr; (c) 8.13 Torr. Signals have been scaled to the A–X(1,2) band at each pressure. Experimental bandwidth = 1.86 nm. (Bold lines) experimental results; (fine lines) best-fit decompositions into component bands; (dotted lines) sum of the best-fit components.

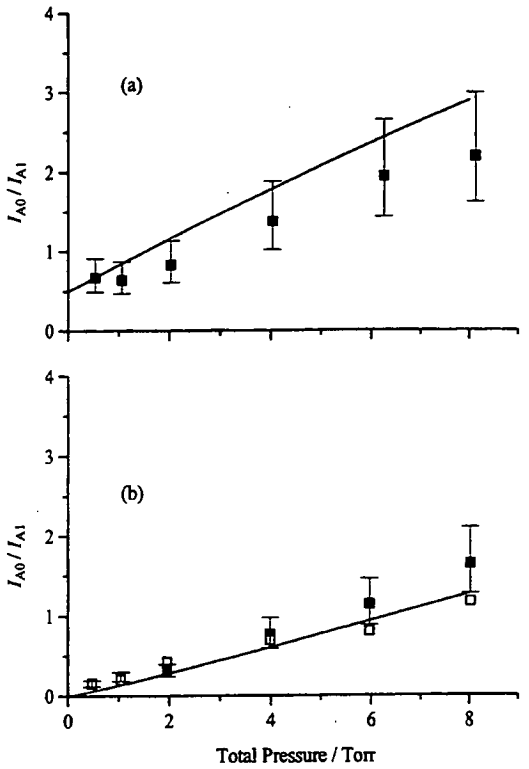

Fig. 8 Variation with CO_2 pressure of the ratio of integrated emission intensities, I_{A0}/I_{A1}, from the CH $A\,^2\Delta$, $v = 0$ and 1 levels. Excitation of (a) $B\,^2\Sigma^-$; $v = 0$; (b) $A\,^2\Delta$, $v = 1$. (Filled squares) experimental measurements on the off-diagonal bands, corrected for the relative vibrational transition probabilities of the A–X(0,1) and (1,2) bands: error bars indicate the systematic uncertainty in the correction factor. (Open squares) alternative measurements derived from the integration of time-dependent waveforms following $A\,^2\Delta$, $v = 1$ pumping, as described in the text. (Solid lines) predictions of the 4-level kinetic model.

was also observed in the related studies at high temperatures in flames,[38] implying that the rate constants for electronic (and in some cases vibrational) transfer are a significant fraction of gas-kinetic values. Room temperature measurements have produced a compatible difference of only a single order of magnitude between the rates of rotational and vibrational relaxation of the $A\,^2\Delta$ state in collisions with partners such as N_2 and Ar.[35]

The integrated signals were then corrected for the known relative bandstrengths of the A–X(0,1) and (1,2) bands.[19] The resulting ratios I_{A0}/I_{A1} are plotted as a function of CO_2 pressure in Fig. 8. A moderately large systematic uncertainty is introduced by the correction because of the uncertainties in the measured bandstrengths for these weak bands.[19] This uncertainty is indicated by the error bars in Fig. 8, which in this case we believe exceeds the statistical scatter in the results or the systematic errors in determining the best-fit decompositions. Any minor variation of the detection sensitivity with wavelength has again been neglected. A useful way of thinking of the quantities in Fig. 8 for later comparison with kinetic models is as a measure of the relative number of molecules which emitted while in a given level. Because the radiative rates are very similar for A0 and A1,[19,45–47] they also closely reflect relative populations in the two levels integrated over time.

The off-diagonal measurements could, in principle, also be used to determine relative A and B state populations because the contribution from the B–X(0,2) band is generated in the fit to the spectra. However, the results would be subject to even more significant systematic uncertainties due to the compounding of errors in all three small vibrational transition probabilities.[19,20] It was also not a realistic proposition in most cases, particularly following A1 pumping, because the B–X(0,2) band is hard to distinguish with any degree of accuracy and the statistical uncertainties in the fits were found to be very large.

Time-resolved fluorescence waveforms

Having established the form of the various integrated fluorescence spectra, the time dependence of emission from particular initial and product CH levels could be examined. This was achieved by fixing the pump-laser and monochromator wavelengths while capturing the time dependence of the fluorescence signal with the transient digitiser.

(a) Initial population of CH $A\,^2\Delta$, $v = 1$. Experimentally, the most straightforward measurement following A1 excitation is to monitor the strong, diagonal A–X fluorescence. At the experimental resolution used the A–X(0,0) and (1,1) bands are detected with effectively equal sensitivity. Representative waveforms for different CO_2 pressures are included in Fig. 9. The A–X($\Delta v = 0$) decay appears at least approximately single-exponential at low pressures. It becomes increasingly bimodal at higher pressure, acquiring a relatively long-lived tail in addition to an increasingly rapid initial decay. Qualitatively, this is supporting evidence for A1 → A0 collisional relaxation and an indication of the 'pooling' of population in a relatively robust A0 level.

Alternatively, at the cost of weaker signals but with the advantage of isolating emission from A1 alone, the monochromator was set to the short-wavelength side of the A–X off-diagonal (1,2) band at 485 nm. Although there is some

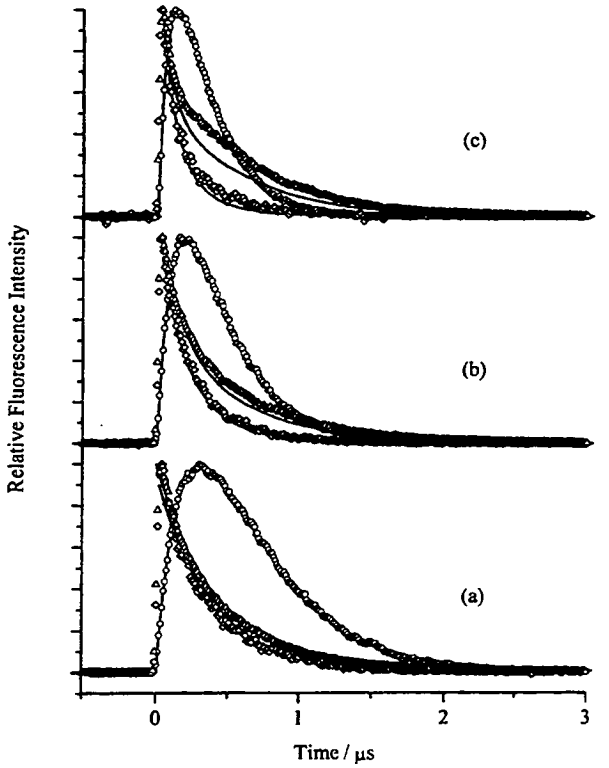

Fig. 9 Fluorescence decay traces following pumping of the $R_1(1)$ line of the CH A–X(1,0) band in the presence of CO_2 at pressures of (a) 1.0 Torr; (b) 4.0 Torr; (c) 8.0 Torr. All traces have been scaled to the same peak value. Experimental results: (triangles) combined A–X($\Delta v = 0$) diagonal bands; (diamonds) isolated A–X(1,2) off-diagonal band; (circles) collisionally produced B–X(0,0) diagonal band. The solid lines through the B–X(0,0) traces are non-linear least-squares fits of a difference of exponentials function (compare eqn. (8) with a transposition of B0 and A1 labels). The lines through the A–X traces are predictions of the 4-level kinetic model.

residual uncertainty in the best-fit decomposition of the spectra, any underlying contribution at this wavelength from the A–X(0,1) or B–X(0,2) bands can reasonably be assumed to be insignificant. The resulting waveforms are also shown in Fig. 9, where the behaviour at longer times contrasts markedly with the combined A state diagonal emission.

Unfortunately, as can be seen from Fig. 7, it is not possible to choose a wavelength which would isolate the emission solely from A0. However, an *indirect* route to the time-dependence of A0 is provided by using a combination of the waveforms in Fig. 9. The procedure is to subtract a multiple of the observed A–X(1,2) decay, suitably scaled to match the intensity at early times when only A1 is populated, from the observed decay on the diagonal bands. This leaves a residual trace which should consist only of A–X(0,0) emission, as illustrated in Fig. 10. Despite the reduced signal-to-noise ratio, the resulting A0 waveform clearly shows the characteristic rise-and-fall profile of a collisional product.

An interesting by-product of this analysis is that an independent estimate of the A0 to A1 ratio is generated by integrating the two component waveforms over time. The results are compared in Fig. 8(b) with the values obtained from integration of the off-diagonal A–X(1,2) and (0,1) bands. The agreement is reasonable but not perfect (~30% discrepancy in the slope of a linear fit forced to pass through the origin). The time-integrated data fall just within the error limits defined by the systematic uncertainty in the relative band strengths used in processing the off-diagonal results.

The final sets of experimental data in Fig. 9 are the corresponding, collisionally produced B–X(0,0) decays resulting

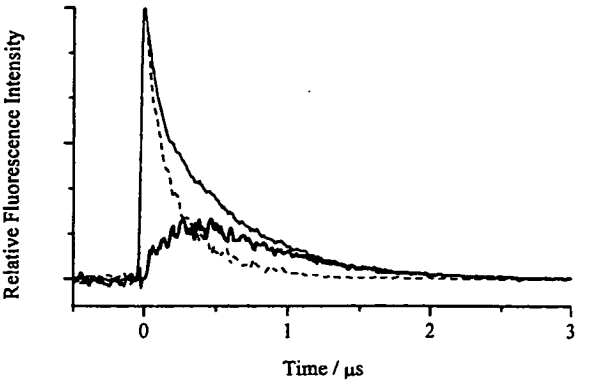

Fig. 10 Extraction of the time-dependent CH A–X(0,0) emission (bold line) following pumping of the $R_1(1)$ line of the A–X(1,0) band in the presence of CO_2 at a pressure of 6.0 Torr. A scaled multiple of the A–X(1,2) emission (dashed line) has been subtracted from the A–X($\Delta v = 0$) diagonal emission (fine line).

from A1 excitation. This strong emission is observed with excellent signal-to-noise and without any problems of spectral overlap. It is qualitatively obvious that the rates of both the rising and falling portions of the profile increase with CO_2 pressure.

(b) Initial population of CH $B\,^2\Sigma^-$, $v = 0$. The directly returning B–X(0,0) fluorescence waveforms following initial population of B0 are shown in Fig. 11. Their qualitative appearance is plausibly single-exponential, with lifetimes decreasing with pressure, but the extent to which they are truly represented by this form is considered further below.

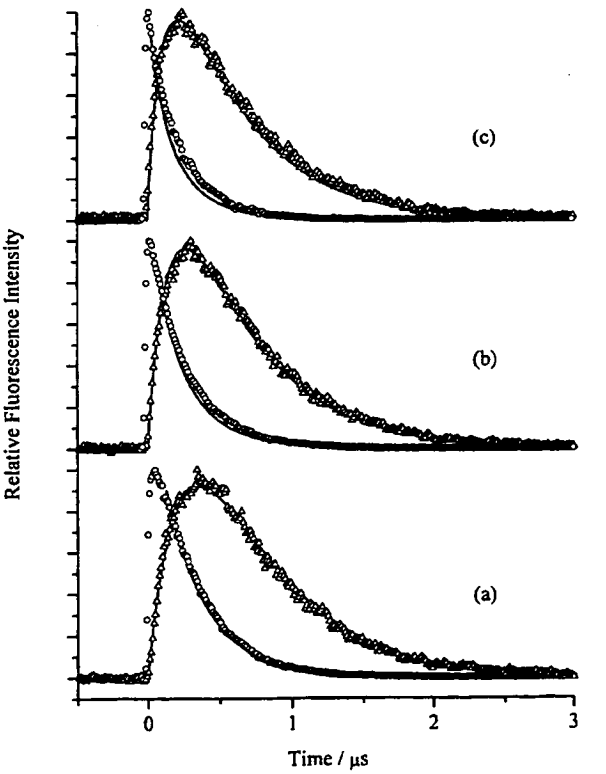

Fig. 11 Fluorescence decay traces following pumping of the $R_1(3)$ line of the CH B–X(0,0) diagonal band in the presence of CO_2 at pressures of (a) 1.0 Torr; (b) 4.0 Torr; (c) 8.0 Torr. Traces have been scaled to the peak signal in each case. Experimental results: (circles) directly excited B–X(0,0) band; (triangles) combined collisionally produced A–X($\Delta v = 0$) diagonal bands. The solid lines are predictions of the 4-level kinetic model.

The corresponding time-resolved total emission on the A–X diagonal bands is also shown in Fig. 11. The growth and decay curves include a persistent component at long times associated with the A0 level. Further measurements on the off-diagonal bands would potentially allow the diagonal emission to be decomposed into its constituents. However, the recovery of the A0 waveform would, in practice, be problematical because the signals from both levels now have very similar forms. It would therefore not be so straightforward to carry out a correctly scaled subtraction of the type described above when A1 is the initially populated level. There should, in any case, be sufficient redundancy in the existing measurements to allow a kinetic analysis (see below) without the need for these additional data so we have not pursued them at this stage.

Kinetic analysis

Solution of the kinetic scheme

The minimum number of levels required in the most basic kinetic scheme that might realistically be expected to reproduce the experimental data is four. These consist of the two observed vibronic levels of the $A\,^2\Delta$ state, A0 and A1; the single observed level of the $B\,^2\Sigma^-$ state, B0; and all unobserved levels in which population is irreversibly deposited, labelled X. This does not necessarily imply that unobserved products are in the electronic ground state, but only that the process is irreversible.

Such a mechanism is illustrated schematically in Fig. 12, where the rate constants for the various processes are defined. The bimolecular rate constant connecting a given pair of levels Y and Z is denoted k_{YZ}. The total radiative rate from level Y (in this case known unambiguously to populate the electronic ground state) is equal to the inverse of the radiative lifetime, τ_Y^{-1}.

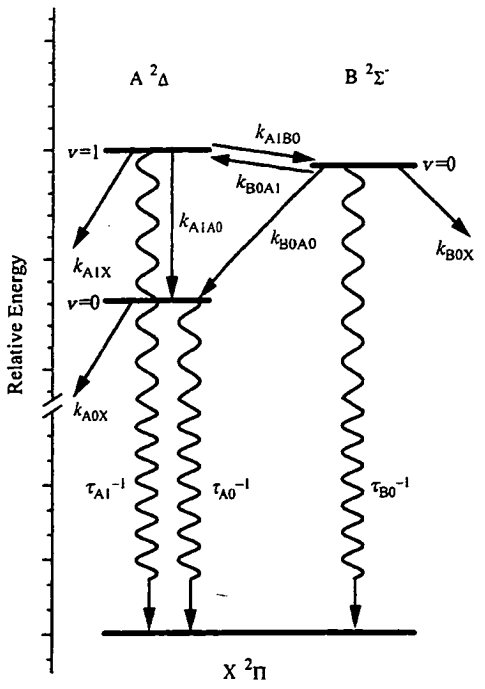

Fig. 12 Schematic representation of the 4-level kinetic model. Collisional and radiative processes are distinguished by straight and wavy lines, respectively.

The scheme of coupled differential equations connecting the time-dependent populations, $N(t)$, of the various levels is:

$$\frac{dN_{B0}(t)}{dt} = -k^T_{B0}N_{B0}(t) + k_{A1B0}P_Q N_{A1}(t) \quad (1)$$

$$\frac{dN_{A1}(t)}{dt} = -k^T_{A1}N_{A1}(t) + k_{B0A1}P_Q N_{B0}(t) \quad (2)$$

$$\frac{dN_{A0}(t)}{dt} = -k^T_{A0}N_{A0}(t) + k_{B0A0}P_Q N_{B0}(t) + k_{A1A0}P_Q N_{A1}(t) \quad (3)$$

where the pseudo-first order total removal rate constants are

$$k^T_{B0} = \tau^{-1}_{B0} + (k_{B0A1} + k_{B0A0} + k_{B0X})P_Q \quad (4)$$

$$k^T_{A1} = \tau^{-1}_{A1} + (k_{A1B0} + k_{A1A0} + k_{A1X})P_Q \quad (5)$$

$$k^T_{A0} = \tau^{-1}_{A0} + k_{A0X}P_Q \quad (6)$$

and P_Q is the pressure of quencher (in the present case, limited to CO_2).

We are interested in the solutions to this scheme subject to the boundary condition that either B0 or A1, respectively, is initially populated. They have conveniently been calculated using the *Maple*[48] symbolic programming language, but the results have also been checked analytically.

Taking the case where B0 is populated, *i.e.* $N_{B0}(0) = N_0$ and $N_{A1}(0) = N_{A0}(0) = 0$, the time-dependences of the reversibly coupled B0 and A1 levels are

$$N_{B0}(t) = \frac{N_0}{\lambda_1 - \lambda_2}((k^T_{B0} + \lambda_1)e^{\lambda_2 t} - (k^T_{B0} + \lambda_2)e^{\lambda_1 t}) \quad (7)$$

and

$$N_{A1}(t) = \frac{N_0 k_{B0A1}P_Q}{\lambda_1 - \lambda_2}(e^{\lambda_1 t} - e^{\lambda_2 t}) \quad (8)$$

The critical parameters λ_1 and λ_2 are defined by

$$\lambda_1 = -\tfrac{1}{2}[(k^T_{B0} + k^T_{A1}) - \sqrt{(k^T_{B0} - k^T_{A1})^2 + 4k_{A1B0}k_{B0A1}P_Q^2}] \quad (9)$$

and

$$\lambda_2 = -\tfrac{1}{2}[(k^T_{B0} + k^T_{A1}) + \sqrt{(k^T_{B0} - k^T_{A1})^2 + 4k_{A1B0}k_{B0A1}P_Q^2}] \quad (10)$$

Both λ_1 and λ_2 are constrained to be negative, with λ_2 having the larger absolute magnitude.

At low pressure, as $P_Q \to 0$, the limiting values of these parameters are $\lambda_1 \to -k^T_{A1}$ and $\lambda_2 \to -k^T_{B0}$, *i.e.* the respective total removal rates of the two levels. It can therefore be seen that only in this limit is the decay of B0 a simple, single-exponential with an exponent equal to $-k^T_{B0}$. The coefficients $(k^T_{B0} + \lambda_1)$ and $-(k^T_{B0} + \lambda_2)$ are both positive, so $N_{B0}(t)$ is more generally a sum of two decaying exponentials in λ_1 and λ_2 with weightings that vary with pressure.

As might be anticipated, $N_{A1}(t)$ has the rise-and-fall profile of a difference of (equally but oppositely weighted) exponentials in the same pair of exponents, λ_1 and λ_2. The population of the irreversibly produced A0 level is also described by a more complex rise-and-fall function:

$$N_{A0}(t) = \frac{N_0}{\lambda_1 - \lambda_2} \times \left\{ \frac{(k_{B0A0}P_Q(k^T_{B0} + \lambda_1) - k_{A1A0}k_{B0A1}P_Q^2)}{k^T_{A0} + \lambda_2}(e^{\lambda_2 t} - e^{-k^T_{A0}t}) - \frac{(k_{B0A0}P_Q(k^T_{B0} + \lambda_2) - k_{A1A0}k_{B0A1}P_Q^2)}{k^T_{A0} + \lambda_1}(e^{\lambda_1 t}e^{-k^T_{A0}t}) \right\} \quad (11)$$

If desired, this could equivalently be re-expressed as a linear function of exponentials in λ_1, λ_2 and the total removal rate from this level, $-k^T_{A0}$, with pressure-dependent weighting coefficients.

In the alternative case when level A1 is initially populated, the corresponding boundary condition $N_{A1}(0) = N_0$, $N_{B0}(0) = N_{A0}(0) = 0$ applies. Because of the inherent symmetry of the kinetic scheme the solutions can be generated from those in eqns. (7)–(11) simply by permuting the B0 and A1 labels on all the quantities. It is worth noting, in particular, that the expressions for λ_1 and λ_2 in eqns. (9) and (10) are identical regardless of which level is populated initially. The A1 level now decays monotonically as a sum of exponentials while the B0 level is an exponential rise-and-fall.

A further useful quantity is the total integrated signal from each level. For level Y, the result, I_Y, is determined by the proportionality

$$I_Y \propto \int_0^\infty \tau_Y^{-1} N_Y(t) dt \qquad (12)$$

The necessary integrals were solved analytically. Only the relative signals from different levels at a given quencher pressure were required for comparison with experiment.

Extraction of kinetic parameters from the experimental data

We found that initial attempts at unconstrained fits of sums of decaying exponentials to the observed decay curves (see *e.g.* Figs. 9 and 11) from either of the initially populated levels, B0 or A1, were not very successful. In essence, the problem is that both the values of the exponents and the coefficients weighting the contributions are unknown quantities. The situation is worst at low pressures, when the values of λ_1 and λ_2 are not particularly well separated because of the roughly similar $A\,^2\Delta$ and $B\,^2\Sigma^-$ radiative lifetimes.

A much more successful strategy was to fit the exponential rise-and-fall profile of the collisionally populated B0 level following A1 pumping (see Fig. 9). The main advantage is that, according to eqn. (8), there is only one overall scaling coefficient. There may still be a slight problem with ill-conditioning[49] at low pressures, where there is some correlation in the fitted parameters, but on the whole the fits were satisfactory and reproducible. The quality of typical fits is illustrated in Fig. 9. The values of λ_1 and λ_2 obtained in this way are presented in Fig. 13. Realistic extrapolations of λ_1 and λ_2, respectively, to zero pressure are in plausible agreement with the known radiative rates of 1.85×10^6 and 3.08×10^6 s^{-1} of the A1 and B0 levels.[19,20,45]

A very useful constraint on the overall scheme of rate constants is generated by summing the values of λ_1 and λ_2. This yields, according to eqns. (9) and (10)

$$-(\lambda_1 + \lambda_2) = k^T_{A1} + k^T_{B0} \qquad (13)$$

This function is also plotted in Fig. 13. The best-fit linear slope (after conversion of units) of $(3.80 \pm 0.05) \times 10^{-11}$ cm^3 molecule^{-1} s^{-1} should encompass the sum of all rate constants for collisional removal from levels A1 and B0 combined, as expressed in eqns. (4) and (5).

The next stage was to try to divide this constrained sum between the rate constants for the elementary steps. An additional constraint can straightforwardly be deduced from the low-pressure I_{A0}/I_{A1} ratio in the experiments when B0 was initially populated (see Fig. 8a). The limiting ratio is apparently $\sim 1/2$. This is entirely determined by k_{B0A0}/k_{B0A1}.

We turned next to the I_{A0}/I_{A1} ratio in the complementary experiments when A1 was prepared initially (Fig. 8b). The predictions of the kinetic model confirm that the rate of increase with pressure is mainly determined by the value of k_{A1A0}. There is only a relatively minor influence from secondary "relaxation" in two cascading steps, A1 → B0 → A0, for any realistic overall combination of rate constants. Based on this

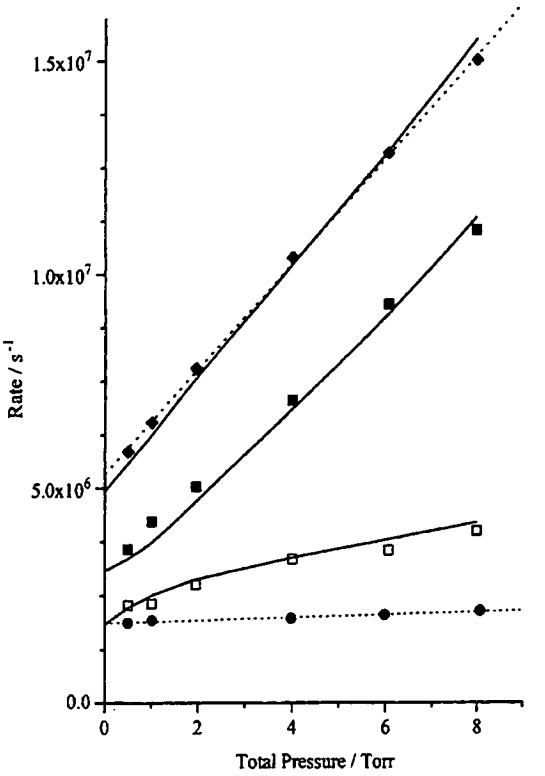

Fig. 13 Variation of exponential kinetic parameters with pressure of CO_2. Experimental results (open squares) $|-\lambda_1|$; (filled squares) $|-\lambda_2|$; and (filled diamonds) $|\lambda_1 + \lambda_2|$, all derived from fits of an exponential rise-and-fall function to observed B–X(0,0) decays following pumping of the $R_1(1)$ line of the CH A–X(1,0) band (compare Fig. 9). (Filled circles) the exponent of smallest magnitude, identified with k^T_{A0}, controlling the time-dependence of the extracted CH A–X(0,0) emission following pumping of the $R_1(1)$ line of the A–X(1,0) band (compare Fig. 10 and discussion in the text). (Dotted lines) linear fits to the $|\lambda_1 + \lambda_2|$ and k^T_{A0} data; (solid lines) predictions of the 4-level kinetic model.

criterion we conclude that k_{A1A0} has a value of $\sim 0.7 \times 10^{-11}$ cm^3 molecule^{-1} s^{-1}.

The remaining major decision is the balance between the total removal rate constants for the B0 and A1 levels. The observations which are probably most sensitive to the *absolute* values of $(k_{B0A1} + k_{B0A0})$ combined and k_{A1B0} are the respective ratios of total integrated signals from product and initial levels in Fig. 6. These largely reflect the competition between electronically inelastic collisions and radiative loss. The absolute radiative rates should be quite well known.[19,20] The rate constants estimated on this basis are $(k_{B0A1} + k_{B0A0}) \sim 1.5 \times 10^{-11}$ and $k_{A1B0} \sim 1.8 \times 10^{-11}$ cm^3 molecule^{-1} s^{-1}.

Taken in conjunction with the value of k_{A1A0} deduced above, these values already marginally exceed the overall constraint on the sum of removal processes based on eqn. (13). The total loss from B0 and A1 therefore appears to be accounted for before including *any* contribution due to unobserved states through k_{B0X} and k_{A1X}. We therefore conclude that it is highly unlikely that k_{B0X} has a comparable value to k_{B0A1} and k_{B0A0}, or that k_{A1X} is competitive with k_{A1A0} and k_{A1B0}.

In further support of a relatively small k_{A1X} is the plausible (but not rigorous) argument that the A0 and A1 levels do not differ markedly in their coupling to states other than the $B\,^2\Sigma^-$ state. We note from Figs. 1 and 3 that A → B transfer only becomes energetically feasible at the A1 level.

Our own measurements provide an independent route to the evaluation of k_{A0X}. The indirectly constructed A0 decays, as shown in Fig. 10, should obey eqn. (11). We found that fits to these traces gave irreproducible results for the more rapid

components. However, the smallest exponent which controls the decay at longest times was well behaved. Its value may be identified with k^{T}_{A0}. Its variation with pressure, given simply by eqn. (6), was found to be modest. The results are included in Fig. 13. The zero-pressure intercept agrees well with the accepted radiative lifetime (535 ns)[19] of the A0 level. The slope yields $(0.098 \pm 0.013) \times 10^{-11}$ cm^3 molecule^{-1} s^{-1} for k_{A0X}. This is also in reasonable agreement with the previously reported[29] relatively small value of $(0.04 \pm 0.004) \times 10^{-11}$ cm^3 molecule^{-1} s^{-1} for the quenching of the A $^2\Delta$ state by CO_2. We have set $k_{B0X} = 0$ and k_{A1X} equal to our result for k_{A0X} throughout.

The "best" values of the rate constants derived from our iterative fitting procedure are collected in Table 1. We do not propose that the results are entirely unique. There remains some coupling which allows the values to be varied co-operatively. The uncertainty limits quoted in Table 1 attempt to quantify ranges within which they may be varied *independently* without leading to a clear deterioration in the quality of the predictions. In any case, as we now summarise, even the "best" values are only partially successful in reproducing some aspects of the results.

Essentially by construction, the ratios of total integrated signals in Fig. 6 are predicted rather well. This reassuringly includes the distinct qualitative differences in the initial slope and degree of curvature in Figs. 6a and 6b.

As already noted, the combined value of $(k^{T}_{A1} + k^{T}_{B0}) = 4.1 \times 10^{-11}$ cm^3 molecule^{-1} s^{-1} only slightly overestimates the slope of 3.8×10^{-11} cm^3 molecule^{-1} s^{-1} of a linear fit to the experimental values of $|\lambda_1 + \lambda_2|$ in Fig. 13. Furthermore, the individual λ_1 and λ_2 values are also very satisfactorily reproduced, as also shown in Fig. 13. This is encouraging because they were not used as separate constraints.

In contrast, the experimental results for I_{A0}/I_{A1} in Fig. 8 are not so well predicted. The best-fit rate constants represent a compromise. The increase in I_{A0}/I_{A1} with pressure is *overestimated* in Fig. 8a for B0 pumping, but *underestimated* in Fig. 8b for A1 pumping. We have not found it possible to resolve this conflict. Nevertheless, although significant, the remaining discrepancy is not extreme. We have already noted that there are systematic difficulties in decomposing the off-diagonal spectra and a potential systematic error in the vibrational band strengths for the A–X(1,2) and (0,1) bands. The discrepancy between the two independent experimental estimates of I_{A0}/I_{A1} in Fig. 8b is comparable to that between the off-diagonal experimental values and the model predictions. (We note, though, that a corresponding "correction" to the experimental data in Fig. 8a would in fact make the prediction worse.)

Turning to the time-resolved fluorescence data, the B0 waveforms following A1 pumping in Fig. 9 are not an independent measure because they were the original source of λ_1 and λ_2 in Fig. 13. The remaining results do provide a genuine check of the predictions. Gratifyingly, the collisionally produced A1 + A0 waveforms from B0 pumping are also very well reproduced, as shown in Fig. 11. On the other hand, none of the predicted decays for the initially excited levels are entirely satisfactory. The increase in the rate of decay with pressure is overestimated for all the A state decays in Fig. 9 and, to a lesser extent, for the B state in Fig. 11. This may partly reflect the point made above that, unlike (single) collisional product waveforms, both the decay constants and their weightings need to be correct. For example, the underestimate of the contribution from the longer-lived component in the A–X diagonal emission in Fig. 9c is consistent with the underprediction of the A0 : A1 ratio at higher pressures in Fig. 8b.

In summary, we feel that the basic four-level scheme reproduces quite satisfactorily the main features of the observations. However, some quantitative discrepancies clearly remain. Some possible sources of systematic error have already been identified. More fundamentally, though, the difficulty in achieving satisfactory overall agreement could be due to the limitations of the kinetic scheme itself. Four levels may simply not be sufficient. This could, in principle, be because of an additional, unidentified *reversible* coupling to an underlying electronic state (either high levels of the X $^2\Pi$ ground state or of the a $^4\Sigma^-$ state[50]).

However, an obvious and more likely cause is the major oversimplification resulting from the neglect of the *rotational* structure of the vibronic levels. As we have described, our experimental method creates a single initial rovibronic level and this is not necessarily fully equilibrated on the timescale of the measurements. Consequently, it may be necessary to treat the population and the corresponding rate constants for each rotational level independently, greatly increasing the number of adjustable parameters. Inspection of Fig. 3 suggests that it is quite likely, for example, that the value of k_{B0A1} will be a sensitive function of B0 rotational level simply on energetic grounds. There may also be dynamical reasons why the other rate constants are rotational-level dependent. Indeed, even the radiative lifetimes are level dependent, although only weakly for the lower-lying levels well below the region where predissociation becomes significant.[19,20,51]

In the absence of rotational-level resolved data, it is difficult to apply microscopic reversibility arguments rigorously to the results. In principle, the parameters k_{B0A1} and k_{A1B0} which we have treated as independent should, of course, be related in this way. Neglecting entirely the rotational structure of the levels and accounting only for the vibronic energy gap and the additional two-fold electronic degeneracy of the A $^2\Delta$ state, k_{B0A1}/k_{A1B0} is predicted to be 0.50 at 295 K. This compares rather satisfactorily with the unconstrained ratio of (0.56 ± 0.15) in Table 1. On the other hand, assuming complete rotational equilibration over the fine-structure levels of both A1 and B0, the prediction decreases (because B0 has the smaller rotational constant) to 0.38, slightly impairing the agreement with experiment.

Table 1 Best-fit microscopic rate constants within the four-level kinetic scheme

Rate constant	Value[a]/10^{-11} cm^3 molecule^{-1} s^{-1}
k_{B0A1}	1.0 ± 0.2
k_{B0A0}	0.5 ± 0.2
k_{B0X}	$0 + 0.1$
k_{A1B0}	1.8 ± 0.3
k_{A1A0}	0.7 ± 0.2
k_{A1X}	0.1 ± 0.1
k_{A0X}	0.10 ± 0.05

[a] Uncertainty limits are estimates of the ranges within which the parameters may be *independently* varied without leading to a clear deterioration of the overall fit, as discussed in the text.

Discussion

The main significance of our observations from a practical point of view is the clear demonstration that the CH B0 and A1 levels are reversibly coupled in collisions with CO_2, at least, and potentially with a wide range of other quenchers. This reinforces the previous observations of the B ↔ A coupling process in flames.[38,39] The details of the product branching differ from the flame studies, however, because Garland and Crosley[38] reported no significant A1 → A0 vibrational relaxation, nor B0 → A0 inelastic transfer. This presumably reflects differences in these propensities between CO_2 and the majority collision partners present in the flames.

These observations mean that considerable care must be taken in the interpretation of rate constants which apparently measure the efficiency of collisional removal of CH A $^2\Delta$ and

$B\,^2\Sigma^-$ states. Similar caution is required in their subsequent use to correct the magnitudes of fluorescence signals for excited state quenching.

The essence of the problem is illustrated in Fig. 14, which refers to the situation when B0 is populated initially. The predicted variation with pressure of the various terms in eqn. (7) is shown for the rate constants in Table 1. Also shown is the phenomenological best-fit decay constant for the forced fit of a single exponential function to the corresponding *synthesised* B0 data. If taken at face value, these decay constants could be misinterpreted as k^T_{B0}, measuring the total removal from B0. However, as can be seen from Fig. 14, they actually significantly underestimate the true value of k^T_{B0} which was used to generate them. The main physical reason for this is that the B0 → A1 process populates a level which has a significantly lower radiative rate. A fraction of this A1 population returns to the B0 level and subsequently emits, apparently lengthening the B0 lifetime.

In pursuit of this point, we have also forced single-exponential fits to our *experimental* B0 decays. The reasonably linear variation with CO_2 pressure which is found yields an apparent B0 total removal rate constant of $(0.63 \pm 0.04) \times 10^{-11}$ cm^3 molecule^{-1} s^{-1}. This contrasts with the higher value of $k^T_{B0} = (k_{B0A1} + k_{B0A0}) = (1.5 \pm 0.3) \times 10^{-11}$ cm^3 molecule^{-1} s^{-1} deduced from the four-level model results in Table 1. Interestingly, however, it agrees more closely with the value of $(0.77 \pm 0.12) \times 10^{-11}$ cm^3 molecule^{-1} s^{-1} reported by Cooper and Whitehead.[36] These authors used an experimental method based on the variation of the fluorescence intensity with pressure, which also effectively measures the phenomenological variation in the $B\,^2\Sigma^-$ state lifetime rather than the microscopic total removal rate constant.

An interesting consequence of the collisional coupling could readily arise in environments consisting of mixed quenchers,

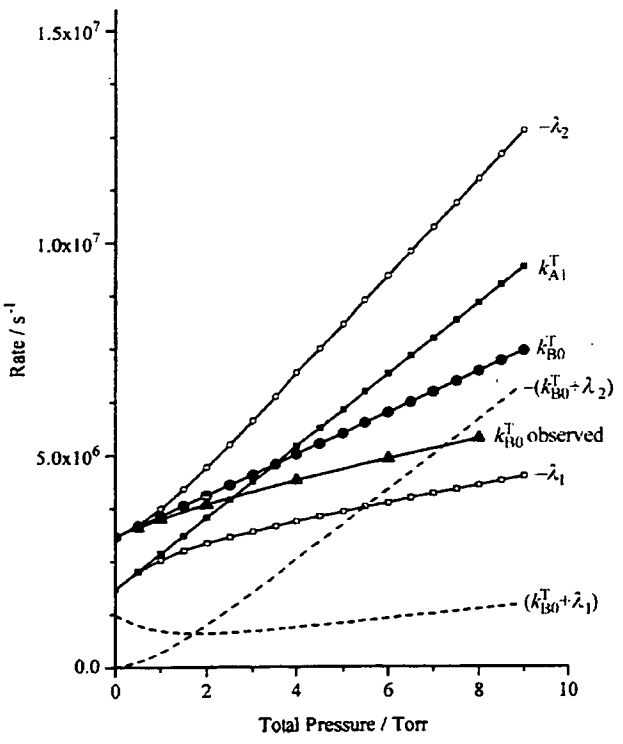

Fig. 14 Predicted variations with CO_2 pressure of the terms in eqn. (7) assuming the rate constants in Table 1. The symbols correspond to: (filled circles) true value of k^T_{B0} used in the model; (filled triangles) apparent value of k^T_{B0} obtained from a forced single-exponential fit to predicted B0 decays; (open squares) $-\lambda_1$; (open circles) $-\lambda_2$; (filled squares) k^T_{A1}; (dashed lines) coefficients $(k^T_{B0} + \lambda_1)$ and $-(k^T_{B0} + \lambda_2)$, as indicated.

as will indeed often be the case in those of applied practical interest. The effects of the different quenchers could appear to be non-additive. For example, an effective A1 quencher could enhance the apparent total quenching of B0 by a second partner which efficiently interconverts B0 and A1.

The problems of interpretation are compounded in systems where the $A\,^2\Delta$ and $B\,^2\Sigma^-$ states are produced together, as will often be the case in practice when UV multiphoton photolysis is used. Nascent A1 population (and, potentially, higher $A\,^2\Delta$ vibrational levels) can, in principle, influence the apparent decay of the $B\,^2\Sigma^-$ state. Conversely, cascading of nascent $B\,^2\Sigma^-$ state population can perturb the emission from the $A\,^2\Delta$ state, including A0. This lowest level is notably immune from any of the present problems, however, provided it is prepared by a method which produces it in isolation. Rate constants for A0 measured in this way should remain reliable.

One specific way in which the present results provide a test of theoretical models is in the branching of population between the A1 and A0 levels in the products of B0 collisions. As discussed in the Introduction, there have been attempts to propose scaling laws for the prediction of these branching ratios. One such empirical expression[9,10] combines the effects of Franck–Condon overlap, $q_{v,v'}$, and the vibronic energy gap, $\Delta E_{v,v'}$ on the rate constant, $k_Q^{Ev,E'v'}$, connecting a pair of vibronic levels:

$$k_Q^{Ev,E'v'} = k_Q^{E,E'} q_{v,v'} \exp\left(\frac{-\Delta E_{v,v'}}{kT}\right) \qquad (14)$$

The CH $B\,^2\Sigma^-$–$A\,^2\Delta$ Franck–Condon factors needed to test eqn. (14) are clearly not amenable to direct optical measurement. We are not aware that they have been published previously, other than a brief statement[38] that $q_{00}/q_{01} \sim 8$. Consequently, we have derived the potential curve for the $A\,^2\Delta$ state using standard Rydberg–Klein–Rees (RKR) methods. A compound curve was constructed for the $B\,^2\Sigma^-$ state based on an RKR analysis of the only two bound vibrational levels extrapolated with a realistic barrier to dissociation, as has been described previously.[20] Radial wavefunctions and Franck–Condon factors were then calculated in the normal way.[52] As a check, we computed Franck–Condon factors for the B–X system, which agreed well with previous results.[18]

For the B–A system, we obtained $q_{00} = 0.812$ and $q_{01} = 0.161$, implying $q_{00}/q_{01} = 5.0$, slightly smaller than reported in passing previously.[38] The respective energy gaps for the lowest rotational levels are $|\Delta E_{00}| = 2452$ cm^{-1} and $|\Delta E_{01}| = 284$ cm^{-1}. According to eqn. (14), transfer on the near-degenerate B0 → A1 channel should therefore outweigh B0 → A0 by a factor of $\sim 10^4$. This contrasts starkly with the experimental k_{B0A1}/k_{B0A0} ratio of ~ 2. Regardless of some uncertainty in the experimental value, this clearly adds to the list of examples where the empirical scaling law fails dramatically.[8,11]

From a more fundamental point of view, it is notable that CO_2, at least, is reasonably efficient in promoting the interconversion of the $A\,^2\Delta$ and $B\,^2\Sigma^-$ states (measured by $k_Q^{E,E'}$ in eqn. (14)). *Ab initio* studies[21] of CH indicate that the predominant electronic configurations in the region of the equilibrium internuclear separation are $A\,^2\Delta$: $1\sigma^2\,2\sigma^2\,3\sigma^1\,(1\pi^2,\,^1\Delta)$ and $B\,^2\Sigma^-$: $1\sigma^2\,2\sigma^2\,3\sigma^1\,(1\pi^2,\,^3\Sigma^-)$. The rearrangement involved in B ↔ A interconversion therefore amounts essentially to a recoupling of the spins of the pair of electrons in the π-orbitals. It would be interesting to see whether this is predicted to be a probable process by first-principle calculations.

Conclusions

We have established conclusively that collisional interconversion of certain vibronic levels of the CH $A\,^2\Delta$ and $B\,^2\Sigma^-$

states takes place, and have pursued this quantitatively for CO_2 as a test-case collision partner. The near-degenerate $A\,^2\Delta$, $v = 1$ and $B\,^2\Sigma^-$, $v = 0$ levels are efficiently reversibly coupled. Direct vibrational relaxation of the $A\,^2\Delta$, $v = 1$ level proceeds at a competitive rate. The $A\,^2\Delta$ state plausibly accounts for all the population removed from $B\,^2\Sigma^-$, $v = 0$, which is distributed in a ratio of $\sim 2 : 1$ between $A\,^2\Delta$, $v = 1$ and 0. This is not predicted by an energy gap-scaling law. A four-level kinetic model is reasonably successful in describing the majority of the observations. Some quantitative discrepancies remain, which may partly be due to unaccounted rotational level-dependent effects. The results have potentially important consequences for the interpretation and application of measured quenching rate constants for the $A\,^2\Delta$ and $B\,^2\Sigma^-$ states.

Acknowledgements

We acknowledge the contributions of Florian Ausfelder and Iain R. Hesketh to early phases of the experimental work.

We are grateful to the EPSRC for an equipment grant, studentships for CJR and CM, and the provision of equipment from the LSF Laser Loan Pool. We also thank Shell Research Ltd for additional financial support.

References

1 R. W. Wood, *Philos. Mag.*, 1911, **21**, 309.
2 J. E. Selwyn and J. I. Steinfeld, *Chem. Phys. Lett.*, 1969, **4**, 217.
3 C. A. Thayer and J. T. Yardley, *J. Chem. Phys.*, 1972, **57**, 3992.
4 H.-M. Lin, M. Seaver, K. Y. Tang, A. E. W. Knight and C. S. Parmenter, *J. Chem. Phys.*, 1979, **70**, 5442.
5 P. W. Fairchild, G. P. Smith and D. R. Crosley, *J. Chem. Phys.*, 1983, **79**, 1795.
6 P. H. Paul, J. A. Gray, J. L. Durant and J. W. Thoman, *Appl. Phys. B*, 1993, **57**, 249.
7 P. H. Paul, *J. Quant. Spectrosc. Radiat. Transfer*, 1994, **51**, 511.
8 P. J. Dagdigian, *Annu. Rev. Phys. Chem.*, 1997, **48**, 95.
9 V. E. Bondybey and T. A. Miller, *J. Chem. Phys.*, 1978, **69**, 3597.
10 D. H. Katayama, T. A. Miller and V. E. Bondybey, *J. Chem. Phys.*, 1979, **71**, 1662.
11 K. G. McKendrick, *J. Chem. Soc., Faraday Trans.*, 1998, **94**, 1921.
12 K. Kohse-Höinghaus, *Prog. Energy Combust. Sci.*, 1994, **20**, 203.
13 D. R. Crosley, in *Current Problems and Progress in Atmospheric Chemistry*, ed. J. R. Barker, World Scientific, Singapore, 1996, p. 256.
14 P. F. Bernath, *J. Chem. Phys.*, 1987, **86**, 4838.
15 P. F. Bernath, C. R. Brazier, T. Olsen, R. Hailey, W. T. M. L. Fernando, C. Woods and J. L. Hardwick, *J. Mol. Spectrosc.*, 1991, **147**, 16.
16 Z. Bembenek, R. Kepa, A. Para, M. Rytel and M. Zachwieja, *J. Mol. Spectrosc*, 1990, **139**, 1.
17 M. Zachwieja, *J. Mol. Spectrosc.*, 1995, **170**, 285.
18 R. Kepa, A. Para, M. Rytel and M. Zachwieja, *J. Mol. Spectrosc.*, 1996, **178**, 189.
19 J. Luque and D. R. Crosley, *J. Chem. Phys.*, 1996, **104**, 2146.
20 J. Luque and D. R. Crosley, *J. Chem. Phys.*, 1996, **104**, 3907.
21 E. F. van Dishoeck, *J. Chem. Phys.*, 1987, **86**, 196.
22 C. Nokes and R. J. Donovan, *Chem. Phys. Lett.*, 1983, **99**, 491.
23 C. Nokes and R. J. Donovan, *Chem. Phys.*, 1984, **90**, 167.
24 C. Chen, Y. Sheng, S. Yu and X. Ma, *J. Chem. Phys.*, 1984, **101**, 5727.
25 N. L. Garland and D. R. Crosley, *Chem. Phys. Lett.*, 1987, **134**, 189.
26 P. Heinrich, R. D. Kenner and F. Stuhl, *Chem. Phys. Lett.*, 1988, **147**, 575.
27 E. Hontzopoulos, Y. P. Vlahoyannis and C. Fotakis, *Chem. Phys. Lett.*, 1988, **147**, 321.
28 D. R. Crosley, *J. Phys. Chem.*, 1989, **93**, 6282.
29 R. D. Kenner, S. Pfannenberg, P. Heinrich and F. Stuhl, *J. Phys. Chem.*, 1991, **95**, 6585.
30 C. Cheng, X. Wang, S. Yu, Q. Lu and X. Ma, *Chem. Phys. Lett.*, 1992, **197**, 286.
31 C. Chen, Q. Ran, S. Yu and X. Ma, *J. Chem. Phys.*, 1993, **99**, 1070.
32 S. Couris, N. Anastopoulou and C. Fotakis, *Chem. Phys. Lett.*, 1994, **223**, 561.
33 P. Heinrich and F. Stuhl, *Chem. Phys.*, 1995, **199**, 105.
34 R. N. Dixon, D. P. Newton and H. Rieley, *J. Chem. Soc., Faraday Trans.*, 1987, **83**, 675.
35 J. L. Cooper and J. C. Whitehead, *J. Chem. Soc., Faraday Trans.*, 1993, **89**, 1287.
36 J. L. Cooper and J. C. Whitehead, *J. Chem. Soc., Faraday Trans.*, 1992, **88**, 2323.
37 J. L. Cooper and J. C. Whitehead, *J. Phys. Chem.*, 1994, **98**, 8274.
38 N. L. Garland and D. R. Crosley, *Appl. Opt.*, 1985, **24**, 4229.
39 K. J. Rensberger, M. J. Dyer and R. A. Copeland, *Appl. Opt.*, 1988, **27**, 3679.
40 D. A. Lichtin, M. R. Berman and M. C. Lin, *Chem. Phys. Lett.*, 1984, **108**, 18.
41 Spectral line positions and linestrengths were calculated from the known molecular constants[14–18] according to the methods described in R. N. Zare, A. L. Schmeltekopf, W. J. Harrop and D. J. Albritton, *J. Mol. Spectrosc.*, 1973, **46**, 37.
42 J. E. Butler, J. W. Fleming, L. P. Goss and M. C. Lin, *Chem. Phys.*, 1981, **56**, 355.
43 M. R. Berman and M. C. Lin, *Chem. Phys.*, 1983, **82**, 435.
44 C. J. Randall, PhD Thesis, The University of Edinburgh, UK, 1998.
45 J. Brzozowski, P. Bunker, N. Elander and P. Erman, *Astrophys. J.*, 1976, **207**, 414.
46 K. H. Becker, H. H. Breing and T. Tartaczyk, *Chem. Phys. Lett.*, 1980, **71**, 242.
47 W. Bauer, B. Engelhard, P. Wiesen and K. H. Becker, *Chem. Phys. Lett.*, 1989, **158**, 321.
48 Maple V, Release 4.00a, copyright (©) Waterloo Maple Inc., Ontario, Canada, 1996.
49 P. R. Bevington, in *Data Reduction and Error Analysis for the Physical Sciences*, McGraw-Hill, New York, 1969, ch. 11.
50 T. Neils, J. M. Brown and K. M. Evenson, *J. Chem. Phys.*, 1988, **88**, 2087.
51 J. Luque and D. R. Crosley, *Chem. Phys.*, 1996, **206**, 185.
52 Radial wavefunctions and transition moment integrals were calculated using the program Level, distributed by R. J. Leroy, University of Waterloo Chemical Physics Research Report, C.P.-555, Ontario, Canada, 1995.

Paper a908494k

Rotational-state resolved coupling of CH $A\,^2\Delta$ and $B\,^2\Sigma^-$ in collisions with CO_2

Craig Murray,[a] Colin J. Randall[a] and Kenneth G. McKendrick*[b]

[a] *Department of Chemistry, The University of Edinburgh, Edinburgh, UK EH9 3JJ*
[b] *Department of Chemistry, Heriot-Watt University, Edinburgh, UK EH14 4AS. E-mail: k.g.mckendrick@hw.ac.uk*

Received 8th September 2000, Accepted 18th October 2000
First published as an Advance Article on the web 22nd November 2000

Inelastic collisions of selected rovibronic levels of the CH $A\,^2\Delta$ and $B\,^2\Sigma^-$ states with CO_2 have been investigated experimentally. Initial levels in $A\,^2\Delta$, $v = 1$ and $B\,^2\Sigma^-$, $v = 0$ were prepared by selective laser excitation. Time-gated emission from the initial and product levels was dispersed at rotational resolution for the first time. Conditions were established where 60–80% of the population remained in the initially populated rovibronic level. The rotational state propensities were established for electronically inelastic collisional transfer from $A\,^2\Delta$, $v = 1$ to $B\,^2\Sigma^-$, $v = 0$. The reverse transfer is complicated by the spectral overlap of the A–X(1,1) and (0,0) bands. A high N' component can unambiguously be assigned to $A\,^2\Delta$, $v = 0$. The distributions of ΔN for inter-electronic state transfer are generally broader than for pure rotational energy transfer within either state, particularly at higher N where the results are more clear-cut. For these levels the redistribution of rotational population during electronic transfer is, however, less complete than implied by a statistical prior distribution. This suggests that the electronic state-changing collisions sample more strongly interacting regions of the CH···CO_2 excited state potentials than are required to cause pure rotational relaxation. These interactions are not sufficiently strong, however, to promote complete rotational (or vibrational) energy redistribution during the collision.

Introduction

Inelastic collisions of electronically excited molecules are important in many contexts. In the gas phase, electronically excited states of stable molecules and radical fragments are created in high-energy environments such as combustion, plasmas, laser gain media, stellar atmospheres, *etc.* They may also be formed photolytically, for example in the Earth's atmosphere. The fate of these species is generally determined by the various collision processes that they might undergo in competition with spontaneous emission to lower-lying electronic states. This competition is also crucial to the interpretation of signal strengths in the applied use of optical spectroscopy to monitor the majority ground state species.

On the whole, it is relatively straightforward to measure the total removal rate of a selected electronically excited state, and many studies of this type and their interpretation have been reported.[1–6] It is also often possible to monitor the rates of rotational energy transfer (RET) or vibrational energy transfer (VET) within a particular electronic state, typically because the optical transition used to excite the initial level is also allowed for emission in the reverse direction.[7]

It is generally a greater challenge to detect the products of electronically inelastic collisions, especially at a vibrational or even rotational state-resolved level. As reviewed recently by Dagdigian,[8] only a few molecular systems have been studied at this level of detail. They tend to be those which have an accidentally favourable combination of excited state energies and symmetries, either allowing spontaneous emission to be observed from both an initial and a product state, or being amenable to optical–optical double resonance methods.

The work compiled so far has, however, highlighted the lack of a general theoretical understanding of electronically inelastic processes. Simplistic models, such as energy gap scaling laws,[9,10] have poor predictive ability.[8,11] Rigorous *ab initio* calculations are very challenging for electronically excited systems, even for relatively simple parent molecules and collision partners. Some notable progress has been made in explaining the detailed product state propensities for a few specific systems, particularly the isoelectronic CN and N_2^+ excited states.[8,12–16] Even in these cases, however, there remain some quantitative difficulties and the results are not necessarily transferable to other systems.

In this paper we extend our previous studies[17] of state-selective electronically inelastic collisions of the CH radical. This radical plays a central role in hydrocarbon combustion, is present in plasmas used for chemical deposition of diamond-like carbon, and has also been detected in various astrophysical sources. It is well known from extensive spectroscopic studies[18–24] to have near-degenerate $A\,^2\Delta$ and $B\,^2\Sigma^-$ excited states located $\sim$25 000 cm^{-1} above the ground $X\,^2\Pi$ state. It therefore falls into the category of systems for which there are two excited states both connected to the ground state. That these two states could be coupled collisionally was first demonstrated in high[25] and low[26] pressure flames. There is also quite a sizeable literature on the total quenching of these states,[27–39] and some work on RET and VET processes within each of them.[40–43]

In our previous work,[17] we confirmed the interconversion of certain vibronic levels of the CH $A\,^2\Delta$ and $B\,^2\Sigma^-$ states with CO_2 as a test case collision partner. Fig. 1 shows the arrangement of the relevant energy levels. We will continue for the sake of brevity to use the contracted notation[17,25] A1, A0 and B0 to represent the $A\,^2\Delta$, $v = 1$, 0 and $B\,^2\Sigma^-$, $v = 0$ levels, respectively. We found that the near-degenerate A1 and B0 levels are efficiently reversibly coupled. Direct A1 → A0

DOI: 10.1039/b007309l

This journal is © The Owner Societies 2000

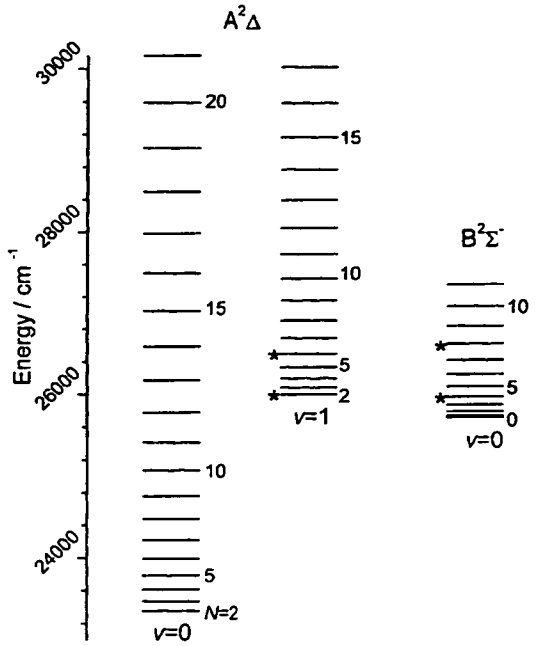

Fig. 1 Rovibronic energy levels for the CH $A^2\Delta$ and $B^2\Sigma^-$ states relevant to this work. The respective initially populated levels are indicated by stars. Levels are labelled by N. Fine-structure and Λ-doublet splittings are not indicated.

VET proceeds at a competitive rate. The $A^2\Delta$ state appears to account for all the population removed from B0. This is distributed in a ratio of ~2 : 1 between A1 and A0, which differs dramatically from the predictions of an energy gap scaling law. Quantitative rate constants for the various elementary steps could be extracted reasonably successfully through a four-level kinetic model.

The main advance we present in the current paper is a study of the inter-electronic state propensities at the level of *rotational* resolution. We have continued with CO_2 as a convenient and efficient collision partner. Individual rotational levels in both the A1 and B0 states have been prepared. The inter-state transfer in both directions has been studied under conditions of relatively few collisions so that the correlation between initial and final rotational states could be determined.

Experimental

The method has been described in detail previously,[17] so will only be summarised here. The main difference from our previous work is that emission spectra were recorded under higher optical resolution and with time-gating.

Experiments were carried out in a stainless steel vacuum system. All measurements were made at ambient temperature (~295 K). CH radicals were created by photolysis of $CHBr_3$ using the mildly focussed fourth harmonic of a Nd : YAG laser at 266 nm. The CH is produced in a range of electronically excited states[35,44] as well as the ground state. Therefore, this initially excited population was allowed to relax by emission (and possibly some quenching) by introducing a delay of a few microseconds before the selective excitation step. As a secondary precaution, we recorded any residual signal caused by the photolysis laser and subtracted it from the desired, selectively excited emission.

A second, tunable Nd : YAG-pumped dye laser was used to pump a selected transition in either the B–X or A–X bands. Sufficient lines in the B–X(0,0) band are spectroscopically isolated and suitable for preparing B0 cleanly. However, because of the highly diagonal nature of the A–X system, the A–X(0,0) and (1,1) bands are almost perfectly overlapped. Therefore, as in our previous work,[17] the A–X(1,0) band was used to excite selected rotational levels in A1 by using larger pump powers to overcome the relatively weak bandstrength.

The laser-induced fluorescence excited by the dye laser was detected by two separate photomultiplier tubes (PMTs). The primary signal was first dispersed by a monochromator and the time-resolved output of the PMT was captured by a transient digitiser. Portions of the fluorescence decay could be gated in software. The second PMT observed the signal on a particular vibronic band, isolated by an appropriate interference filter. This signal was generally used to normalise the primary signal.

Gases were used as provided by the manufacturers and without further purification apart from the usual freeze–pump–thaw cycling to remove dissolved air: $CHBr_3$ (Fisons, Laboratory grade); Ar (BOC, 99.99%), CO_2 (BOC, 99.995%).

Results

(a) Directly returning fluorescence spectra

Our primary aim in this work was to study the rotational level-dependent propensities for inter-electronic state transfer. Consequently, it was necessary to establish the conditions under which a sufficiently large fraction of the population would remain in the initially populated rovibronic level. The first stage of the measurements was therefore designed to monitor inelastic processes within the initial vibronic level.

(i) Excitation of A1. Selected A–X(1,0) lines were used to prepare two distinct rotational levels, $N = 2$ and 6, in the A1 level. The emission on the A–X diagonal bands from population remaining in this vibronic level was dispersed at rotational resolution. A series of time gates of increasing duration, each starting coincident with the dye-laser pulse, was used to monitor rotational relaxation within the initial level at a fixed pressure of CO_2 (typically 1.1 Torr). Typical results for gates of length 100, 400 and 1600 ns following pumping of A1, $N = 6$ are shown in Fig. 2. We have also recorded signals with additional gates of shorter and intermediate duration and observed sensible smooth continuations of the trends shown here.

The spectra in Fig. 2 have been analysed by iterative simulations[45] to extract the best-fit population distributions shown as insets. Only contributions from the A–X(1,1) band have been considered (see below). With the current experimental resolution we are effectively limited to knowing the distribution over N. The F_1 and F_2 fine-structure levels are at best only partially resolved for the lowest values of N, and the Λ-doublet levels are completely unresolved.

It can be seen in Fig. 2 that for the shortest of the gates shown (100 ns) the emission spectrum is dominated by lines from the pumped $N = 6$ level. The contributions from other levels grow in as expected for the longer gates. Qualitatively similar results were found for pumping A1, $N = 2$, but with a slightly higher fraction of the emission from the initial level. The respective slightly relaxed rotational distributions are shown in Figs. 3(a) and (b) for further comparison below. The fractions of the population remaining in the initial levels are collected in Table 1. In subsequent measurements of the inter-electronic state transfer, we have adopted a gate length of 100 ns as a compromise between a reasonably large value for this fraction (in the range 60–80%) and sufficient signal-to-noise in the collision-induced emission spectra.

In our previous[17] work we established a moderately large value of $(0.7 \pm 0.2) \times 10^{-11}$ cm^3 molecule^{-1} s^{-1} for the rate constant for A1 → A0 VET by CO_2. It is therefore worth checking that the results are not affected significantly by emission from A0 following A1 → A0 transfer because of the much-noted chance overlap of the A–X(1,1) and (0,0) bands. Using

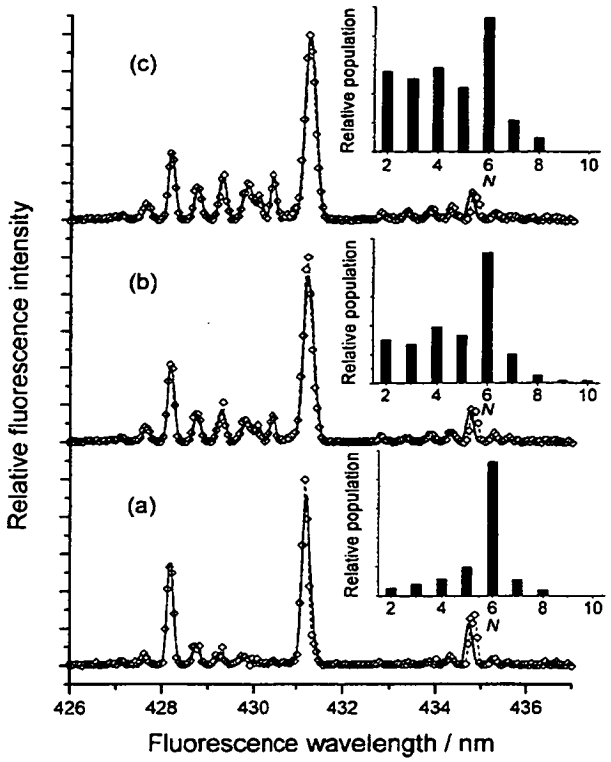

Fig. 2 Dispersed A–X(1,1) emission spectra following excitation of CH A $^2\Delta$, $v = 1$, $N = 6$ on the A–X(1,0) $R_{22}(5)$ line in the presence of CO_2 (1.1 Torr). Signal was captured in gates of length (a) 100 ns, (b) 400 ns, (c) 1600 ns. The monochromator resolution was 0.16 nm. Symbols (◇) represent the experimental signal. Best-fit simulations are shown as bold lines, with the corresponding rotational populations shown in the insets.

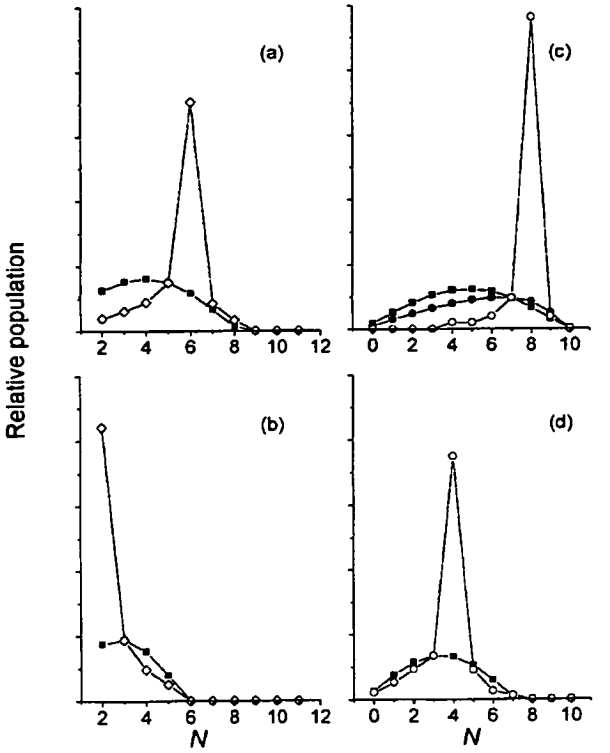

Fig. 3 Best-fit rotational populations for the initially excited vibronic levels in the presence of CO_2 (1.1 Torr) in a gate length of 100 ns. (a) $N = 6$ and (b) $N = 2$ in CH A $^2\Delta$, $v = 1$. (c) $N = 8$ and (d) $N = 4$ in CH B $^2\Sigma^-$, $v = 0$. Open symbols are the experimental results. Closed symbols are the predictions of prior distributions: (●) structureless CO_2, eqn. (1); (■) rotor CO_2, eqn. (2). Experimental distributions are on the same relative scale. Prior distributions are scaled to match at $\Delta N = -1$ (a, c, d) and $+1$ (b).

the kinetic model developed previously, we reassuringly calculate that only 0.6% of the emission will have come from collisionally produced A0 levels during the most important 100 ns gate. Its effects have therefore been neglected in the analysis. The fraction only rises to 12% for a gate over the entire course of the emission at this pressure.

(ii) Excitation of B0. The results of the converse experiment in which selected levels of the B state were excited and the directly returned B–X(0,0) fluorescence was dispersed are illustrated in Fig. 4 for B0, $N = 8$. (The R-branch region contains scattered light from the excitation laser and is therefore not shown.) Qualitatively similar results were obtained for B0, $N = 4$. As expected, most of the population remains in the initially populated N level, particularly for the shortest gates. It is again not possible on the whole to distinguish between transitions from the fine-structure levels and we do not attempt to report these populations separately. The distributions for the 100 ns gate are presented in Fig. 3. The higher initial N level is in this case slightly more collisionally robust. The fractions of the population remaining in the initial levels are collected in Table 1.

Table 1 Fractions of population[a] remaining in the initially pumped rovibronic level during a 100 ns gate

N	Pump A1[b]	Pump B0[c]
2	72%	
4		64%
6	61%	
8		82%

[a] Typical uncertainty ±5%, estimated from the reproducibility of fits to spectra such as those in Figs. 2 and 4. [b] Excitation of selected lines in the A–X(1,0) band. [c] Excitation of selected lines in the B–X(0,0) band.

(b) Spectra from the products of inter-electronic state transfer

Having characterised the initial state rovibronic distributions, we proceeded to record spectra from the product electronic states not directly populated in the excitation step.

(i) B–X(0,0) spectra from preparation of A1. The corresponding B–X(0,0) spectra from B0 molecules produced in electronically inelastic collisions of the selectively excited A1, $N = 6$ level are shown in Fig. 5. Even for the shortest 100 ns gates there is significant intensity on a range of lines around a broad, asymmetric peak at $N' = 7$. The peak is successively smeared out for the longer gates. The best-fit population distributions shown in the insets extend over the full range of available N'.

There were quite noticeable differences between the results in Fig. 5 and the equivalent collisionally produced B–X spectra following pumping of A1, $N = 2$. The respective product distributions are compared in Figs. 6(a) and (b), illustrating the colder B0 population following pumping of the lower A1 rotational level.

(ii) A–X($\Delta v = 0$) spectra from preparation of B0. Fig. 7 shows the complementary collisionally produced A–X spectra following excitation of B0, $N = 8$. (The P-branch region is overlapped by emission on the B–X(0,1) band and is therefore

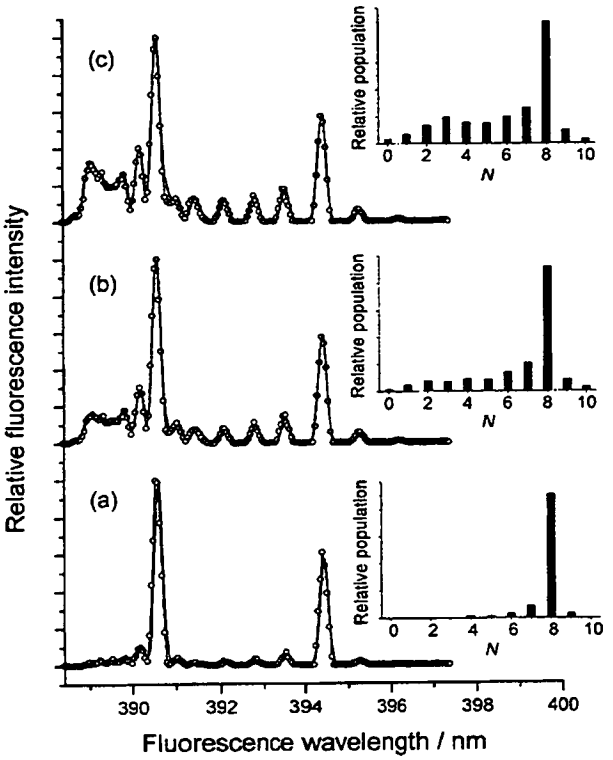

Fig. 4 Dispersed B–X(0,0) emission spectra following excitation of CH $B\,^2\Sigma^-$, $v = 0$, $N = 8$ on the B–X(0,0) $R_{22}(7)$ line in the presence of CO_2 (1.1 Torr). Signal was captured in gates of length (a) 100 ns, (b) 400 ns, (c) 1400 ns. The monochromator resolution was 0.16 nm. Symbols (○) represent the experimental signal. Best-fit simulations are shown as bold lines, with the corresponding rotational populations shown in the insets.

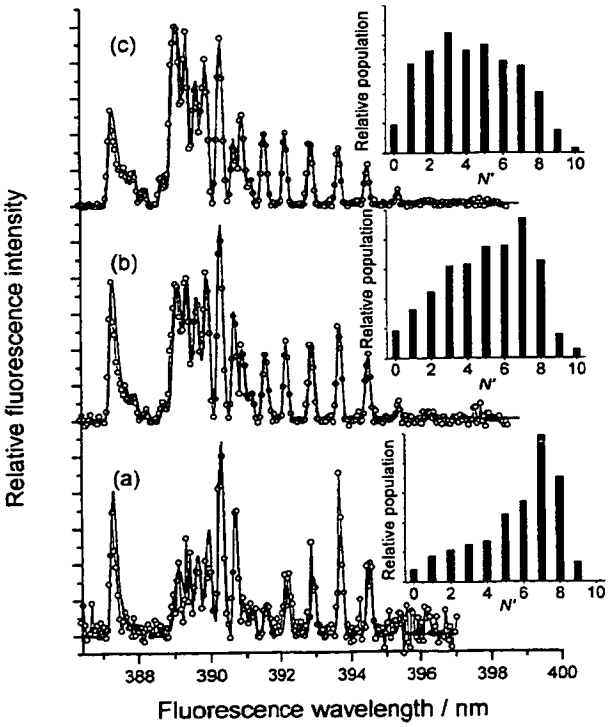

Fig. 5 Collisionally produced B–X(0,0) emission spectra following excitation of CH $A\,^2\Delta$, $v = 1$, $N = 6$ in the presence of CO_2 (1.1 Torr). Gate lengths (a) 100 ns, (b) 400 ns, (c) 1600 ns, as in Fig. 2, where the other conditions are defined. Best-fit product rotational populations, N', are indicated.

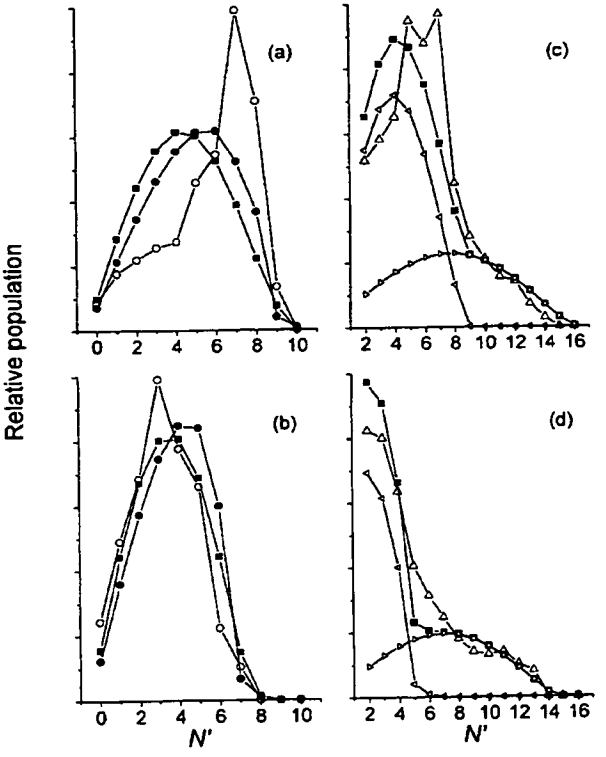

Fig. 6 Best-fit product rotational populations, N'. Initially populated levels and other conditions as in Fig. 3. CH $B\,^2\Sigma^-$, $v = 0$ products from (a) $N = 6$ and (b) $N = 2$ of $A\,^2\Delta$, $v = 1$. CH $A\,^2\Delta$ products from (c) $N = 8$ and (d) $N = 4$ of $B\,^2\Sigma^-$, $v = 0$, for which the product vibrational level is not distinguished experimentally as described in the text. Open symbols are experimental results. For (a) and (b), closed symbols are the predictions of prior distributions: (●) structureless CO_2, eqn. (1); (■) rotor CO_2, eqn. (2). For (c) and (d), the overall rotor prior prediction (■) is the sum of the separate contributions shown for $A\,^2\Delta$, $v = 1$ (◅) and 0 (▻). Distributions in a given panel are normalised to the same total population.

omitted.) Qualitatively similar but again distinct spectra were obtained from B0, $N = 4$. The spectra have a bimodal appearance, with the majority of the intensity in the lower N' lines but with a weaker tail extending out to quite high N' ($\leqslant 14$).

Only for higher N' lines (roughly $N' \geqslant 7$) in the R branch can transitions in the A–X(1,1) and (0,0) bands be distinguished with the current experimental resolution. The result is that essentially all the emission in this region can unambiguously be assigned to the (0,0) band. This is, of course, not surprising because such high N' levels in the A1 state are inaccessible for thermal collision energies (see Fig. 1). The lower N' lines in the two bands are spectroscopically unresolved. An equally satisfactory fit is obtained to the Q-branch and low-N' R-branch regions with the same rotational distribution in either A0 or A1. At this stage we therefore present in Fig. 7 and Figs. 6(c) and (d) only the total distributions in N' summed over the two vibrational levels. We consider further below how these might be deconvoluted into the separate A0 and A1 contributions.

Discussion

Although it is secondary to our main purpose in this article, the data in Fig. 3 clearly contain information on RET processes within the A1 and B0 levels in collisions with CO_2. The absolute rate constants do not appear substantially different for the A1 and B0 levels, judging from the trends in the fractions of population remaining in the pumped level (see Table 1). Our results imply rate constants of order $\sim 1 \times 10^{-10}$ cm^3 molecule^{-1} s^{-1}, consistent with the typically near gas kinetic

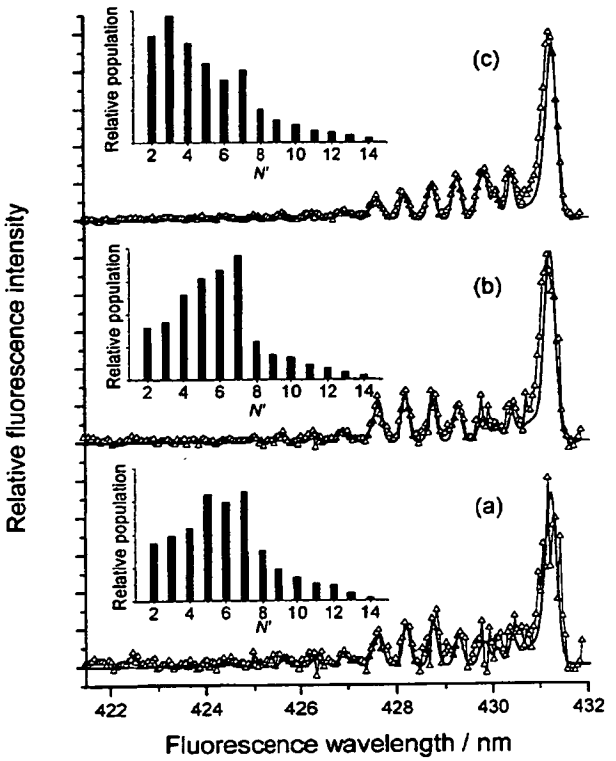

Fig. 7 Collisionally produced A–X($\Delta v = 0$) emission spectra following excitation of CH B $^2\Sigma^-$, $v = 0$, $N = 8$ in the presence of CO_2 (1.1 Torr). Gate lengths (a) 100 ns, (b) 400 ns, (c) 1600 ns. Other conditions as in Fig. 4. Best-fit product rotational populations, N', are indicated in the insets. The simulated spectra assume that the rotational population is exclusively in A $^2\Delta$, $v = 1$ for $N' \leqslant 6$, switching to $v = 0$ for higher N', as explained in the text.

rate constants for RET in both the A0 and B0 levels with other quenchers reported previously.[41–43]

In the A1 state, the $N = 2$ level seems to be slightly more resistant to RET than $N = 6$. This observation is also supported by independently derived[41,43] anomalously small rate constants for the lowest levels with other quenchers. The reported values increase initially and then drop at higher N. We appear to see this decline between $N = 4$ and 8 in the B0 state, which fits in with the conventional idea of a decrease in the rate of RET as the rotational energy gaps increase.

It is probably not sensible to attempt a systematic comparison of RET in the A1 and B0 states on the basis of this limited data set, especially since we did not pump the same N levels in each case. We also need to be alert to the possibility of a contribution of multiple collisions during the finite observation gate. The fractions of population remaining in the initial levels (Table 1) range from 60 to 80%. Assuming Poisson statistics, this implies that the ratio of molecules suffering one state-changing collision to those making two correspondingly ranges from $\sim 4:1$ to $\sim 10:1$. We therefore conclude that the apparent ΔN propensities in Fig. 3 are at worst only modestly affected by secondary collisions.

It is still notable, though, that the A1 and B0 states do not appear to show any particularly marked differences in their ΔN propensities during RET. For the A1 state, the $N = 2$ ground level can, by definition, only undergo positive ΔN. (This may partly be the origin of its relative resistance to RET.) It shows significant probability for transitions up to $\Delta N = +3$ [see Fig. 3(b)]. For the higher level $N = 6$, ΔN spans roughly -4 to $+2$ [see Figs. 2(a) and 3(a)]. This is fairly comparable to B0, $N = 4$ [Fig. 3(d)]. The higher B0 level, $N = 8$, shows a similar range of negative ΔN, but is more curtailed on the positive side [Figs. 3(c) and 4(a)], presumably for energetic reasons.

There are no equivalent data on RET with CO_2 as collision partner with which to make a direct comparison. However, in contrast to the similarity we observe, it has been reported previously[40–43] for the simpler colliders He, Ar and, to a less extreme extent, N_2, that the A0 level displays a more restricted range of ΔN than the B0 level. These observations have been interpreted[42,43] as evidence for differences in the intermolecular potentials, implying a more attractive interaction between the quencher and the B state than with the A state. We note, though, that there are complications of deconvolution inherent in most of the previous work because of the broad distribution of initially populated N states.[41–43] It is also conceivable that the A1 level studied here differs in its RET propensities from the A0 level examined in the previous work. One possible reason for this is the coupling to the B0 level itself. However, the rate constants for A1 $\leftrightarrow$ B0 electronic transfer by CO_2 are roughly an order of magnitude[17] lower than the typical values for RET. We therefore do not think it likely that a "double transfer" mechanism, where the system starts and finishes on the A state surface but is temporarily transferred to the B state, contributes significantly to the observed rate of RET in the A1 level. We conclude that the RET propensities may well be a profitable area for further study using state-selective methods to prepare a single initial N level, such as in Dixon *et al.*'s report[40] of A state relaxation by He.

Returning to our main aim, the ΔN propensities during the transfer between electronic states, we find in all cases a reasonably broad product state rotational distribution (see Fig. 6). Population is generally not very tightly constrained to a few levels around the initial level, in terms of either energy or angular momentum. There is, however, a residual correlation with the pumped level in terms of the peak in the product distribution and the highest level populated. Distributions centred on $\Delta J \sim 0$ are known to be the most common behaviour for processes of this type.[8]

In principle, the relative N' populations could be converted to absolute state-to-state rate constants $k(E, v, N \rightarrow E', v', N')$ if the N-dependent rate constants for total transfer between electronic states were known. Our previous measurements[17] of the total inter-state rate constants were derived from an analysis of the emission over the whole course of the fluorescence waveforms. Under these conditions there is considerable thermalisation of the initial rotational distribution. To derive N-dependent results, the absolute ratios of A–X and B–X fluorescence signals would have to be known during the short initial gate where there is negligible RET. We have not yet attempted these measurements, so only report the relative N' populations at this stage.

To assess whether our observed initial-to-final state correlations simply result from the complete randomisation of different total available energies, we have calculated statistical prior distributions for comparison. There are several levels at which this can be done, depending on the assumed participation of the CO_2 internal degrees of freedom. For a structureless collision partner, in the absence of angular momentum constraints, the prior probability, $P^0(v', j')$, of forming a particular product CH(v', j') rovibrational level is given simply by[46]

$$P^0(v', j') \propto (2j' + 1)(E - E_{v', j'})^{1/2} \quad (1)$$

where $E_{v', j'}$ is the energy of the product level (including its electronic energy). In this case, the total energy, E, is taken to be that of the pumped level plus $\frac{3}{2}kT$ for the average thermal energy in relative translation of the partners.

On the other hand, recognising that the collision partner, CO_2, has internal structure capable of absorbing its statistical share of the available energy, the prior CH internal state distribution is predicted by

$$P^0(v', j') \propto (2j' + 1) \sum_{v'', j''} (2j'' + 1)(E - E_{v', j'} - E_{v'', j''})^{1/2} \quad (2)$$

where $E_{v'',j''}$ is the energy of the CO_2 rovibrational level (v'', j''). The total energy, E, is taken to include a further contribution of kT for the average initial thermal energy of a linear rotor. (The thermal energy in vibration is assumed to be negligible.) The full treatment in eqn. (2) includes the CO_2 vibrations, v''. If these are neglected, the summation is only over the rotational levels, j'', of its vibrational ground state. In practice, the prior predictions for a rigid rotor and vibrotor are very similar, particularly for A1 ↔ B0 transfer where the energy defect is small. Even for the exothermic B0 ↔ A0 transfer, these distributions are only marginally different. There is a more noticeable difference between either of them and structureless CO_2, eqn. (1), which naturally tends to predict hotter CH internal distributions in the absence of a bath of CO_2 rotational levels.

In comparing the experimental distributions with the prior predictions, we have taken into account the effects of the slightly dispersed experimental distribution of initial N levels (Fig. 3). The overall prior distribution was taken to be the average of the prior distributions from each contributing initial N, weighted by its known population.

The simpler case to interpret is A1 ↔ B0 transfer, which is not complicated by any ambiguity about the identity of the product vibrational state. The calculated B0 prior distributions for A1 initial levels $N = 6$ and 2 are included in Figs. 6(a) and (b), respectively. The distinct prior distributions obtained *via* eqns. (1) and (2) are shown for comparison.

For the lower level A1, $N = 2$, the prior distributions quite plausibly reproduce the experimental distributions. The predictions of eqn. (2), including the rotational degrees of freedom of CO_2, are slightly superior. However, it is not conclusive that the agreement between prior and experiment is more than accidental. A1, $N = 2$ is roughly degenerate with B0, $N' = 4$. The observed product state distribution could also be explained reasonably well as a propensity for transfer to the most nearly isoenergetic levels, with the probability falling off in some way proportionately to the energy defect.

The observed B0, N' distribution for A1, $N = 6$ is probably a more incisive test of this point. The comparison with the prior distributions is shown in Fig. 6(a). The slightly hotter prediction resulting from structureless CO_2, eqn. (1), is now in marginally better agreement. However, neither prior is a very satisfactory prediction of the experimental distribution. This is peaked at $N' = 7$, which is the B0 level most nearly isoenergetic with the pumped A1 level. Although the experimental distribution does extend significantly over the lower N' levels, it does not fill up "phase space" to the full extent of either prior prediction.

As a further point of comparison, we have calculated prior distributions for the pure RET process *within* the initial A1 state [see Figs. 3(a) and (b) and the discussion above]. For the lower level, $N = 2$, the prior distribution [only the rotor predictions of eqn. (2) are shown for clarity] is once again quite a satisfactory prediction [Fig. 3(b)]. However, this probably only illustrates the accidental agreement when the distribution is restricted to a small range of ΔN. The deviation from a statistically determined process is obvious for $N = 6$ in Fig. 3(a).

The case of pumping B0 and observing the A state emission is complicated by the difficulties in resolving emission on the A–X(0,0) and (1,1) bands, as identified and discussed above. One way to attempt to resolve the overall A state N' distribution into its A0 and A1 components is to use the prior distributions as a starting point. For each initial B0 level, we have calculated separate rotor prior distributions for the A0 and A1 levels. These are shown in Figs. 6(c) and (d), with weightings that will shortly be justified. As noted above, it is obvious on energetic grounds that the highest populated N' levels must belong to A0. This constraint is automatically included in the prior distributions. Inspection of Fig. 6(c) suggests that all population in $N' \geqslant 9$ can safely be assigned to A0 when pumping B0, $N = 8$. The equivalent cut-off is $N' \geqslant 7$ for B0, $N = 4$ in Fig. 6(d).

These A0, high-N' tails in both cases plausibly resemble the qualitative shapes of the A0 prior distributions. We have therefore proceeded by carrying out a least-squares fit of the relevant A0 prior distribution to the experiment in the range of N' above the respective cut-off. In combination with the normalisation of the populations, this defines the complementary weighting of the A1 prior in the low-N' region. For B0, $N = 4$ and 8 we find A1/A0 = 1.3 and 1.6, respectively.

An independent test of the validity of the overall division of populations is available from our previous work.[17] This was carried out under conditions where the B0 rotational distribution would be at least partially thermalised. Dispersion of the emission on the A–X(0,1) and (1,2) off-diagonal bands at vibronic resolution allowed the low-pressure limiting ratio of probabilities for B0 → A0 and B0 → A1 transfer to be determined. The resulting ratio of A1/A0 = 2.0 ± 0.9 is in plausible agreement with the values just deduced above.

Returning to the rotational distributions, the overall synthesised N' distribution in Fig. 6(d) for B0, $N = 4$ is in fair agreement with experiment. It is not possible to say with any certainty whether the A0 minority contribution to the low-N' levels has been predicted correctly by the prior distribution. It does suggest, though, that the prediction of the A1 majority contribution is reasonable. However, the initial level lies marginally below the A1 ground level, so only a relatively small range of product levels is accessible at thermal collision energies. The agreement is apparently poorer in Fig. 6(c) for the higher initial level, B0, $N = 8$. The experimental distribution peaks around $N' = 5$–7, to higher N' than in the prior distribution. This is reminiscent of the behaviour for the reverse transfer A1 → B0 in Fig. 6(a), with less redistribution of population away from the isoenergetic levels in the experiment than in the prior prediction.

This behaviour may again be contrasted with the corresponding results for pure RET within the initial B0 state in Figs. 3(c) and (d). For B0, $N = 4$, a prior distribution simulates rather well the slightly asymmetric distribution of decaying ΔN values around the initial level. However, for the higher-lying B0, $N = 8$ level, the prior distribution is a patently very poor prediction of the propensities for negative ΔN.

Summary and conclusions

In summary of the observed ΔN propensities for inter-electronic state transfer, we find that for higher initial levels, where the results are more discriminatory, the product distributions are generally more sharply peaked near the initial energy level than the prior predictions. For these same levels, there is, however, a broader range of ΔN than in pure RET. We therefore conclude that the CH···CO_2 collisions which lead to electronic energy transfer are those that sample the more strongly interacting regions of the intermolecular potential. The products carry the signature of relatively large ΔN, but at least for the relatively isoenergetic B0 ↔ A1 coupling, rotational energy redistribution in the intermediate complex does not proceed to the statistical limit.

It was already clear from our previous measurement[17] of the inverted A state vibrational distribution (A1/A0 ~ 2) produced from the B0 level that the coupling in the collision complex is not sufficiently strong to achieve complete vibrational energy redistribution. Interestingly, our interpretation of the A state rotational distribution is that those collisions which do result in B0 → A0 transfer are accompanied by the largest range in ΔN. The larger positive values are sufficient to populate levels up to the energetic limit (with correspondingly small ΔE). Unfortunately, we cannot be sure for experimental

reasons whether this distribution extends to the low rotational states with small (or negative) ΔN and large ΔE.

As noted above, previous workers have concluded[42,43] that the CH B state generally experiences a more strongly attractive interaction with the collision partner than the A state. There may be a question of whether our limited RET data support this conclusion for CO_2. Regardless of that, for the collisional interconversion between electronic states, the entrance channel of the $B \rightarrow A$ process is obviously the exit channel for $A \rightarrow B$, and *vice versa*. Therefore, for transfer in either direction, the system will inevitably experience the more strongly attractive potential at some stage. It is therefore reasonable that both show the relatively broad range of ΔN that is observed. We repeat the call[17,43] that it would be highly desirable to have rigorous *ab initio* intermolecular potentials for CH excited states with CO_2 and other simple quenchers to allow more quantitative tests of these qualitative arguments.

Acknowledgements

We acknowledge the contributions of Florian Ausfelder and Hilary Crichton to some aspects of the experimental work. We are grateful to the EPSRC for an equipment grant and studentships for CM and CJR.

References

1 J. E. Selwyn and J. I. Steinfeld, *Chem. Phys. Lett.*, 1969, **4**, 217.
2 C. A. Thayer and J. T. Yardley, *J. Chem. Phys.*, 1972, **57**, 3992.
3 H.-M. Lin, M. Seaver, K. Y. Tang, A. E. W. Knight and C. S. Parmenter, *J. Chem. Phys.*, 1979, **70**, 5442.
4 P. W. Fairchild, G. P. Smith and D. R. Crosley, *J. Chem. Phys.*, 1983, **79**, 1795.
5 P. H. Paul, J. A. Gray, J. L. Durant and J. W. Thoman, *Appl. Phys. B*, 1993, **57**, 249.
6 P. H. Paul, *J. Quant. Spectrosc. Radiat. Transfer*, 1994, **51**, 511.
7 P. J. Dagdigian, in *The Chemical Kinetics and Dynamics of Small Radicals*, ed. K. Liu and A. Wagner, World Scientific, Singapore, 1995, Part I, p. 315.
8 P. J. Dagdigian, *Annu. Rev. Phys. Chem.*, 1997, **48**, 95.
9 V. E. Bondybey and T. A. Miller, *J. Chem. Phys.*, 1978, **69**, 3597.
10 D. H. Katayama, T. A. Miller and V. E. Bondybey, *J. Chem. Phys.*, 1979, **71**, 1662.
11 K. G. McKendrick, *J. Chem. Soc., Faraday Trans.*, 1998, **94**, 1921.
12 H.-J. Werner, B. Follmeg and M. H. Alexander, *J. Chem. Phys.*, 1988, **89**, 3139.
13 H.-J. Werner, B. Follmeg, M. H. Alexander and D. Lemoine, *J. Chem. Phys.*, 1989, **91**, 5425.
14 P. J. Dagdigian, D. Patel-Misra, A. Berning, H.-J. Werner and M. H. Alexander, *J. Chem. Phys.*, 1993, **98**, 8580.
15 A. Berning and H.-J. Werner, *J. Chem. Phys.*, 1994, **100**, 1953.
16 M. Yang and M. H. Alexander, *J. Chem. Phys.*, 1997, **107**, 7148.
17 C. J. Randall, C. Murray and K. G. McKendrick, *Phys. Chem. Chem. Phys.*, 2000, **2**, 461.
18 P. F. Bernath, *J. Chem. Phys.*, 1987, **86**, 4838.
19 P. F. Bernath, C. R. Brazier, T. Olsen, R. Hailey, W. T. M. L. Fernando, C. Woods and J. L. Hardwick, *J. Mol. Spectrosc.*, 1991, **147**, 16.
20 Z. Bembenek, R. Kepa, A. Para, M. Rytel and M. Zachwieja, *J. Mol. Spectrosc.*, 1990, **139**, 1.
21 M. Zachwieja, *J. Mol. Spectrosc.*, 1995, **170**, 285.
22 R. Kepa, A. Para, M. Rytel and M. Zachwieja, *J. Mol. Spectrosc.*, 1996, **178**, 189.
23 J. Luque and D. R. Crosley, *J. Chem. Phys.*, 1996, **104**, 2146.
24 J. Luque and D. R. Crosley, *J. Chem. Phys.*, 1996, **104**, 3907.
25 N. L. Garland and D. R. Crosley, *Appl. Opt.*, 1985, **24**, 4229.
26 K. J. Rensberger, M. J. Dyer and R. A. Copeland, *Appl. Opt.*, 1988, **27**, 3679.
27 C. Nokes and R. J. Donovan, *Chem. Phys. Lett.*, 1983, **99**, 491.
28 C. Nokes and R. J. Donovan, *Chem. Phys.*, 1984, **90**, 167.
29 C. Chen, Y. Sheng, S. Yu and X. Ma, *J. Chem. Phys.*, 1984, **101**, 5727.
30 N. L. Garland and D. R. Crosley, *Chem. Phys. Lett.*, 1987, **134**, 189.
31 P. Heinrich, R. D. Kenner and F. Stuhl, *Chem. Phys. Lett.*, 1988, **147**, 575.
32 E. Hontzopoulos, Y. P. Vlahoyannis and C. Fotakis, *Chem. Phys. Lett.*, 1988, **147**, 321.
33 D. R. Crosley, *J. Phys. Chem.*, 1989, **93**, 6282.
34 R. D. Kenner, S. Pfannenberg, P. Heinrich and F. Stuhl, *J. Phys. Chem.*, 1991, **95**, 6585.
35 J. L. Cooper and J. C. Whitehead, *J. Chem. Soc., Faraday Trans.*, 1992, **88**, 2323.
36 C. Cheng, X. Wang, S. Yu, Q. Lu and X. Ma, *Chem. Phys. Lett.*, 1992, **197**, 286.
37 C. Chen, Q. Ran, S. Yu and X. Ma, *J. Chem. Phys.*, 1993, **99**, 1070.
38 S. Couris, N. Anastopoulou and C. Fotakis, *Chem. Phys. Lett.*, 1994, **223**, 561.
39 P. Heinrich and F. Stuhl, *Chem. Phys.*, 1995, **199**, 105.
40 R. N. Dixon, D. P. Newton and H. Rieley, *J. Chem. Soc., Faraday Trans.*, 1987, **83**, 675.
41 J. L. Cooper and J. C. Whitehead, *J. Chem. Soc., Faraday Trans.*, 1993, **89**, 1287.
42 J. L. Cooper and J. C. Whitehead, *J. Phys. Chem.*, 1994, **98**, 8274.
43 C.-C. Wang, Y.-P. Chen, T.-L. Chin, H.-Y. Huang and K.-C. Lin, *J. Chem. Phys.*, 2000, **112**, 10204.
44 D. A. Lichtin, M. R. Berman and M. C. Lin, *Chem. Phys. Lett.*, 1984, **108**, 18.
45 Line positions and intensities were simulated using the program LIFBASE, distributed by J. Luque and D. R. Crosley, SRI International report MP-99-0099, 1999.
46 R. D. Levine and R. B. Bernstein, *Molecular Reaction Dynamics and Chemical Reactivity*, Oxford University Press, New York, 1987, p. 267.